UNIVERSITÉ DE STRASBOURG

ÉCOLE DOCTORALE SCIENCES CHIMIQUES

Institut de Chimie et Procédés pour l'Energie, l'Environnement et la Santé (ICPEES)

THÈSE présentée par :

Basma Mewafy

soutenue le : 5 November **2019**

pour obtenir le grade de : **Docteur de l'Université de Strasbourg**

Discipline/ Spécialité : Chimie / Chimie Physique

Etude de surface d'électrodes Ni-cermet dans des conditions d'électrolyse à vapeur à température intermédiaire

Surface study of Ni-cermet electrodes under intermediate temperature steam electrolysis conditions

THÈSE dirigée par :

M. ZAFEIRATOS Spyridon	Directeur de recherche CNRS, ICPEES

RAPPORTEURS :

M. Dimitrios T. Tsiplakides	Professeur, Université de Thessaloniki (GR)
M. Laurent Piccolo	Chargé de recherche CNRS, IRCELYON

AUTRES MEMBRES DU JURY :

Mme. Elena Savinova	Professeur, Université de Strasbourg
M. Jean-Jacques Gallet	Maître de conférences, Université de Sorbonne
Mme. Petit Corinne	Professeur, Université de Strasbourg

To My Mother

To My father

To Fouad Elgendy

Basma Mewafy

Etude de surface d'électrodes Ni-cermet dans des conditions d'électrolyse à vapeur à température intermédiaire

Abstract

Solid Oxide Electrolysis Cells (SOEC) are high temperature electrochemical devices where water dissociates to hydrogen and oxygen under an applied potential. SOEC technology has a huge potential for future mass production of hydrogen and shows great dynamics to become commercially competitive against other electrolysis technologies (e.g. alkaline or polymer membrane electrolysis), which are better established but more expensive and less efficient. This is mainly due to the fact that by increasing the operating temperature the demand in electrical energy is significantly reduced, allowing high electrical-to-chemical energy conversion efficiencies. On the downside, up to now SOECs devices are still not commercially viable mainly due to the difficulty to find materials that fulfill the high-performance and durability requirements at high operating temperatures. The general objective of this thesis is to deal with the two major drawbacks that hamper the penetration of SOEC technology in the energy market, namely high *degradation* rates and device *cost*. Voltage degradation during the ageing of the cell is the performance indicator which is translated in an increase on the overpotential that has to be applied to an electrolysis cell in order to maintain constant hydrogen production.

Résumé

Les cellules d'électrolyse à oxyde solide (SOEC) sont des dispositifs électrochimiques à haute température dans lesquels l'eau se dissocie en hydrogène et en oxygène sous un potentiel appliqué. La technologie SOEC offre un potentiel énorme pour la production future massive d'hydrogène et montre une grande dynamique pour devenir compétitive sur le plan commercial par rapport à d'autres technologies d'électrolyse (par exemple, l'électrolyse à membrane polymère ou alcaline), mieux établies mais plus coûteuses et moins efficaces. Ceci est principalement dû au fait que l'augmentation de la température de fonctionnement permet de réduire considérablement la demande en énergie électrique, ce qui permet des rendements de conversion d'énergie électrique à chimique élevés. À la baisse, les dispositifs des pays de l'Europe centrale et orientale jusqu'à présent ne sont toujours pas viables commercialement, principalement en raison de la difficulté à trouver des matériaux qui répondent aux exigences de haute performance et de durabilité aux températures de fonctionnement élevées. L'objectif général de cette thèse est de traiter les deux inconvénients majeurs qui entravent la pénétration de la technologie SOEC sur le marché de l'énergie, à savoir les taux de dégradation élevés et le coût des équipements. La dégradation de la voltage au cours du vieillissement de la cellule est l'indicateur de performance qui se traduit par une augmentation du overpotential qu'il faut appliquer à une cellule d'électrolyse afin de maintenir une production constante d'hydrogène.

Acknowledgements

I would like to express my gratitude to all the people who supported me during my study in Europe. I was very lucky to have you all on this journey. I would like to thank the **Selysos European project** for the financial support during these three years.

I will be always grateful to my PhD supervisor **Dr. Spiros Zafeiratos**, for his scientific guidance, fruitful discussion and his patience with me during my PhD. He always provided me a great atmosphere for conducting my research and made our lab my favorite place. He is a good leader who made me find my target for my PhD.

I would like to thank **Dr. Fotis Paloukis** and **Dr. Wassila Derafa** for teaching me a lot during their postdoc in our lab and their generous scientific and technical help. I am very thankful for **Dr. Vasiliki Papaefthymiou** for her continuous support and help; I do not remember how many times she helped me in solving my problems in lab or in my daily life**.**

I would like to thank our colleagues in Selysos European project **Dr. Stella Balomenou** (CERTH) and **Dr. Dimitrios K. Niakolas** (FORTH/ICE-HT) for providing us with the samples used in this thesis and for fruitful discussions.

I would like to thank **Dr. Detre Teschner** and **Dr. Michael Hävecker** at ISISS beamline of HZB/BESSY II; The synchrotron experiments presented in this thesis would not be possible without their help and support.

I would like to thank **Prof. Olivier JOUBERT** and **Dr. Annie Le Gal La Salle** from the university of Nantes, Institut des Materiaux Jean Rouxel for their collaboration in fitting the Impedance spectra discussed in this thesis and their generous discussions and support.

I would like to thank all my colleagues from the administration department in ICPEES **Véronique Verkruysse, Michèle Thomas, Francine Jacky** and **Sylvia**. Special thanks to **Dr.**

Thierry Dintzer for helping me with SEM experiments and **Dr. Christophe Mélart** for helping me with Raman experiments.

I am very grateful to have the opportunity to meet brilliant and hard-working students in the last three years. Special thanks to my colleagues in the lab **Liping Zhong, Chen Dingkai**, **Alexandr**, **Sébastien**, **Anna**, **Ivan.**

Above all, I would like to thank **my parents and my sister,** for their enormous support and love especially during my PhD. Special thanks to **Ahmed Elgendy** for being my family in Europe in the last five years and his continuous support.

Table of Content

Résumé

a) Introduction

La demande en énergie augmente de plus en plus rapidement avec la mondialisation. Le charbon, le pétrole et le gaz naturel sont les principaux fournisseurs d'énergie actuellement, Cependant, les problèmes liés aux émissions de gaz à effet de serre, aux sources d'énergie et à leurs coûts, tels que la diminution de la qualité des réserves de combustibles fossiles, les maladies humaines et environnementales et les risques climatiques sont de forts arguments en faveur du passage à des ressources énergétiques plus écologiques basées sur les énergies renouvelables. . Les sources d'électricité renouvelables, telles que l'énergie éolienne et solaire, sont généralement intermittentes car non disponibles en permanence et doivent être combinées à une énergie plus stable sur sa production dans le temps. Il s'avère nécessaire de développer des technologies efficaces pour stocker l'énergie en la convertissant en une autre forme d'énergie[1]. Ceci est le cas en particulier l'électricité, afin de la rendre disponible lors des pics de consommation.

L'hydrogène est considéré comme un vecteur d'énergie et de stockage attrayant pour le développement d'une source d'énergie propre et durable. La principale production d'hydrogène provient du reformage à la vapeur et de la gazéification du charbon. Ces deux réactions créent un gaz de synthèse (un mélange composé principalement de CO et de H_2). Ces produits peuvent ensuite être valorisés par la réaction du gaz à l'eau (ou **water-gas shift reaction en anglais** (WGSR)) pour produire plus d'hydrogène[2]–[5]. Une autre voie, l'électrolyse de l'eau est une voie assez couteuse sauf pour les pays disposant d'énergie hydraulique. L'utilisation de l'électrolyse pour la production d'hydrogène a fait un bref retour sur la scène scientifique après les chocs pétroliers des années 1970[6].Actuellement en utilisant l'énergie produite à partir de sources renouvelables, telles que le soleil et le vent, l'électrolyse fait l'objet d'une attention particulière pour générer de l'hydrogène propre et exempt de CO et de CO_2.

L'intérêt actuel pour la génération future d'hydrogène concerne les électrolyseurs alcalins, à membrane polymère échangeuse de protons et à oxyde solide. L'électrolyse alcaline est la technologie la plus ancienne et la seule disponible sur le marché. Cette technologie est la plus énergivore et produit de l'hydrogène de la plus basse pureté. Les électrolyseurs à membrane

polymère échangeuse (PEM), ou comme on les appelle souvent électrolyseurs à polymère solide (SPE), sont basés sur la technologie de la pile à combustible à PEM inversée. Ils peuvent fonctionner une température au moins égale à celle des électrolyseurs alcalins ou à une température supérieure (dans le cas de PEM à haute température) et ont généralement un meilleur rendement. Ils sont sur le point de devenir disponibles dans le commerce. Les électrolyseurs PEM peuvent être considérés comme un développement incrémental d'électrolyseurs alcalins. La principale différence est qu'ils utilisent un système plus avancé technologiquement, à savoir une membrane polymère. Comme l'iridium est l'un des éléments les plus rares de la croûte terrestre, la quantité élevée d'iridium dans les ensembles d'électrodes à membrane (MEA), dans lequel se produit la séparation de l'eau, est un des facteurs qui en empêche son application à grande échelle.

L'électrolyse de l'eau utilisant des cellules d'électrolyse à oxyde solide à haute température (SOEC) a été considérée comme une voie efficace pour ce processus en raison d'une cinétique et d'une thermodynamique favorables à températures élevées[7]–[18]. En plus du rendement élevé, cette voie conduit également à l'utilisation d'oxygène pur, améliorant de manière significative l'économie globale du processus[19]. Cependant, en raison du fonctionnement à haute température, des matériaux spéciaux sont nécessaires pour résister aux conditions dures du processus. Cette technologie, offre la plus haute efficacité faradique, mais aussi en raison d'une possibilité d'électrolyse directe du CO_2la technologie peut s'étendre à la co-électrolyse simultanée de H_2O et de CO_2. Le produit de cette co-électrolyse conduit à l'obtention du gaz de synthèse (CO, H_2) , qui peut ensuite être retraité pour obtenir un carburant synthétique par la réaction de Fischer-Tropsch[20], [21].

Pour cette raison, les électrolyseurs à oxyde solide offrent la possibilité de stocker et de transporter de l'énergie chimique provenant d'énergie renouvelable et/ou d'énergie excédentaire provenant de centrales à combustibles fossils.

Les dispositifs SOECs ne sont toujours pas viables sur le plan commercial jusqu'à présent, principalement en raison de la difficulté à trouver des matériaux qui répondent aux exigences performance et de durabilité aux hautes températures de fonctionnement. Les cermets sont des matériaux composites composés de céramique (cer) et de nickel (met). Les cermets à base de Ni, sont actuellement les électrodes cathodiques de SOEC les plus largement utilisés.

Ceci est principalement dû à leur faible coût et à leur activité électrocatalytique élevée. Cependant, la dégradation des performances des électrodes en cours d'exploitation demeure un problème critique qui entrave la pénétration de la technologie SOEC sur le marché de l'énergie. L'oxydation du nickel induite par la vapeur a été accusée d'être le facteur de dégradation majeur. Ce vieillissement est dû à la conductivité électronique et à l'efficacité de dissociation de l'eau de l'oxyde de nickel inférieures à celles du métal.

Dans ce travail, nous nous focalisons sur deux électrodes cathodiques à base de nickel, la première composée de nickel sur de l'oxyde de cérium dopé au gadolinium (Ni/GDC) et la seconde constituée de nickel sur de l'oxyde de zirconium-yttria stabilisé (Ni/YSZ). Notre étude porte sur la mise en relation de l'état d'oxydation du nickel et de la réponse électrochimique de cellules SOEC. Nous cherchons également à développer des dispositifs SOEC par modification de surface d'électrodes Ni/YSZ en utilisant des nanoparticules de cérium à substitution métallique (notées MCeOx NPs) comme promoteurs électrocatalytiques. Cette manière de doper, favorise une introduction localisée de sites d'oxyde de cérium et de nickel dans la zone électrochimique active, sans affecter la stabilité mécanique de l'électrode. Ces études ont été réalisées en utilisant des données expérimentales fiables obtenues par la spectroscopie d' absorption étendue des rayons X pour les structures fines et par la spectroscopie de photoélectrons à rayons X proche de la pression ambiante dans des installations de synchrotron, ainsi que par des méthodes de pointe standard au laboratoire (XPS, XRD, TEM, SEM, RAMAN).

b) Résultats et discussions

Les électrodes Ni/GDC et Ni/YSZ ont été testées dans les conditions initiales de mélanges gazeux (25% H2 + 75% H_2O) sous un courant constant de -20 mA et à 630 ° C, ce qui correspond à une densité de courant de -100 ± 5 mA / cm^2.Les spectres XPS obtenus de divers éléments ont été analysés à l'aide du logiciel CasaXPS. Un spectre typique de Ni2p et Ce3d qui se situe dans la BE (850-920) eV montre des phénomènes de recouvrement (multisplitting) qui nous incitent à les analyser avec des spectres de référence par dé sommation. Une amélioration des performances électrochimiques a été constatée au cours de l'expérience, et pour comprendre la raison de cette amélioration, les données NAP-XPS ont été analysées.

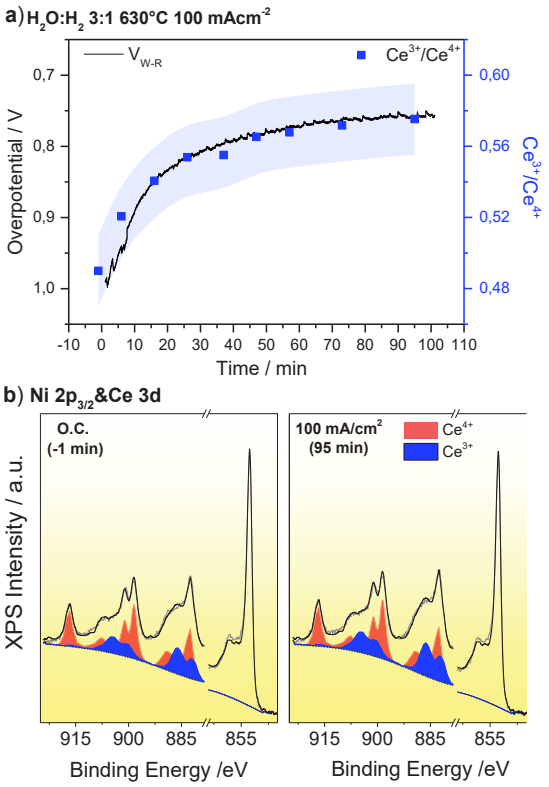

Figure 1. Réduction de l'électrode Ni-GDC a) Évolution dans le temps du surpotentiel de cellules Ni-GDC / YSZ / Pt (ligne noire continue) et évolution du rapport des composants Ce^{3+} / Ce^{4+} (points bleus), déduite de l'analyse des spectres 3d correspondants de NAP-XPS Ce. Les mesures ont été effectuées sur des cathodes Ni-GDC pré-oxydées dans un mélange gazeux H_2O / H_2 3: 1 à 640 ° C et à courant constant de -100 mA / cm^2. Le fond bleu représente l'incertitude dans le calcul du ratio Ce^{3+} / Ce^{4+} principalement lié à la procédure de désommation. b) Spectres NAP-XPS caractéristiques de $Ni2p_{3/2}$ et Ce 3d dans H_2O / H_2 avant et après l'application en cours. Deux composantes de Ce 3d ont été utilisées pour ajuster les spectres correspondant aux états d'oxydation Ce^{3+} (bleu) et Ce^{4+} (rouge) de l'oxyde de cérium.

On observe une corrélation entre la réduction de la consommation de surpotentiel et la réduction de l'oxyde de cérium (Ce^{4+} → Ce^{3+}), comme indiqué dans la figure.1a. Le spectre Ni $2p_{3/2}$ obtenu avec le mélange H_2O / H_2en début d'expérience montre le pic caractéristique du Ni métallique (fig. 1b). La corrélation entre la réduction du l'oxyde de cérium et l'amélioration des performances électrochimiques est également montrée par le retour des conditions

expérimentales de température et la pression partielle de l'eau à l'état initial. Ceci sans changement morphologique de l'électrode Ni/Ce, comme le montre la figure.2.

Afin d'accélérer l'oxydation du nickel, des impulsions d'oxygène ont été introduites dans les mélanges gazeux à 25% H_2 + 75% H_2O sous un courant constant de -20 mA et à 630 ° C, comme indiqué sur la figure (fig.2). Les modifications morphologiques de l'électrode sont examinées par microscopie électronique à balayage ex situ. Les résultats suggèrent que, avec un degré d'oxydation du nickel similaire, les cellules SOEC contenant des électrodes Ni/YSZ présentent des surpotentiels jusqu'à 40% supérieurs, tandis que pour Ni/GDC, elles ne dépassent pas 4% comme indiqué dans la figure (fig.3). Ceci est une preuve directe que le mécanisme de dégradation des cermets contenant GDC et YSZ est différent.

Cela suggère également que GDC participe activement à l'électrolyse de l'eau en trouvant les sites actifs et les chemins de transfert de charge ioniques et électroniques nécessaires. L'incorporation de courant continu à la surface des électrodes conventionnelles en Ni-YSZ pourrait constituer un moyen efficace d'améliorer les performances électrochimiques. L'observation de ce résultat à savoir qu'un impact mineur de la stabilité thermique et mécanique de la cellule permet l'augmentation significatives des performances et la stabilité des cellules SOEC pour l'électrode Ni-YSZ nous a conduit à envisager une autre voie de modification. Celle –ci s'envisage comme une modification des électrodes de cermet avec l'imprégnation de nanoparticules de cérium à substitution Ni ($Ni_{0,1}Ce_{0,9}O_{2-x}$ NPs). Cette approche permet d'obtenir du cérium hautement réductible et d'abondants sites d'interface Ni / oxyde de cérium dans un seul matériau. De plus, en raison de leur petite taille, les NP peuvent être facilement incorporés sur des électrodes Ni-YSZ standard [squelette] avec un minimum d'empreinte sur les caractéristiques globales de la cellule.

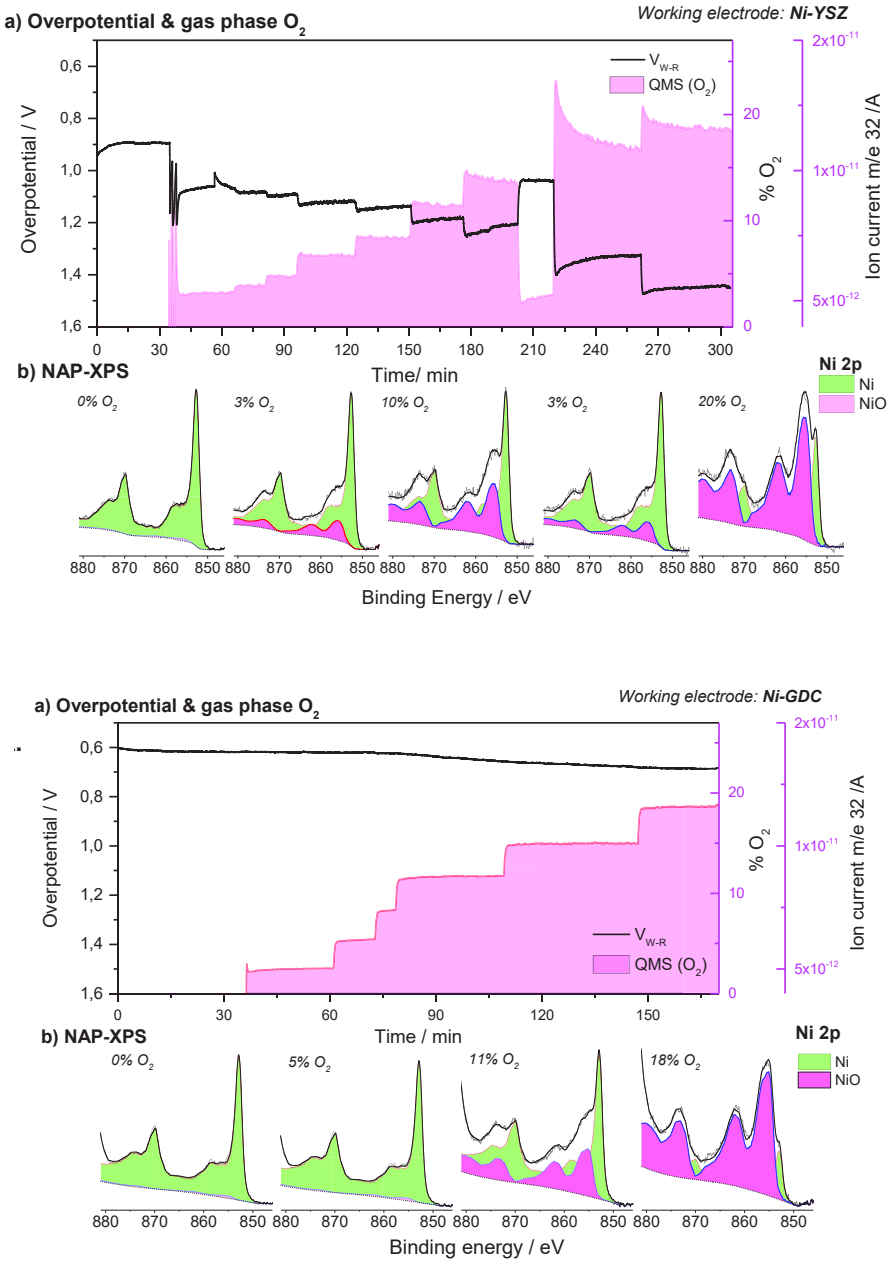

Figure 2. a) Évolution dans le temps du surpotentiel (cathode Ni-GDC à droite et cathode Ni-YSZ à gauche) (ligne noire) et signal du spectromètre de masse en ligne de l'oxygène (ligne rose) mesuré à courant constant de 100 mA/cm^2 alors que différentes concentrations de O_2 ont été introduites dans la charge H_2O/H_2. La température a été maintenue constante à 640 °C. b) Spectres Ni2p NAP-XPS enregistrés aux moments caractéristiques des conditions apparaissant

en a. Deux composants de Ni2p ont été utilisés pour ajuster les spectres correspondant au Ni métallique (vert) et au NiO oxydé (rose).

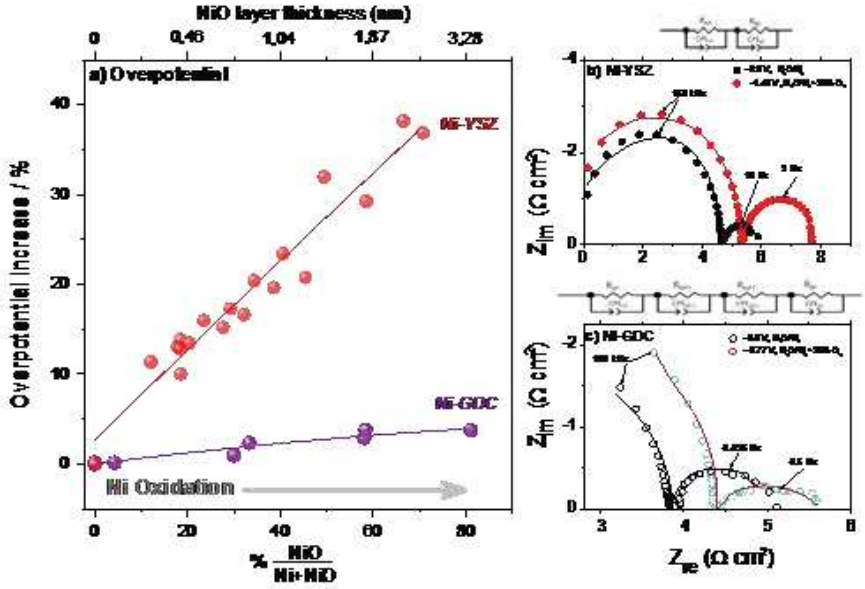

Figure 3. a) Comparaison de l'augmentation en% du surpotentiel des cellules avec des électrodes de cathode Ni-YSZ et Ni-GDC en fonction de la quantité relative de NiO et de l'épaisseur moyenne du film de NiO (déduite de l'analyse du NAP-XPS correspondant) Spectres Ni 2p enregistrés avec une énergie photonique de 1320 eV). Les mesures ont été effectuées à 640 ° C et à un courant constant de -100 mA / cm^2 tandis que différentes concentrations de O2 ont été introduites dans l'alimentation H_2O/H_2. Spectres d'impédance présentés sous forme de Nyquist, obtenus avec un courant appliqué constant de -100 mA cm^{-2} à 640 °C dans H_2O/H_2 (3/1) et $H_2O/H_2/O_2$ (3/1/1) à une pression totale de 0,5 mbar de deux cellules électrochimiques avec des électrodes de travail b) Ni-GDC et c) Ni-YSZ. Les circuits équivalents utilisés pour l'ajustement des données d'impédance sont indiqués ci-dessus de chaque graphique. Les données mesurées sont données par des symboles, tandis que les résultats d'ajustement sont montrés par des lignes. Dans les 2 cellules, des électrodes de compteur de Pt et de référence de géométrie identique ont été utilisées.

Des nanoparticules de cérium dopées au nickel ($Ni_{0,1}Ce_{0,9}O_{2-x}$ NP) ont été fabriquées à partir de complexes à base de Schiff et caractérisées par diverses méthodes microscopiques et spectroscopiques[22]. Les NPs $Ni_{0,1}Ce_{0,9}O_{2-x}$ présentent une réductibilité accrue sous flux d' H_2

comparés aux particules classiques de Ni supportées sur de l'oxyde de cérium et sous flux d' O_2 les cations nickel dopants sont oxydés à une valence supérieure à celle des particules supportées[23]. Dans les deux conditions, à basse température, le pic Ni $2p_{3/2}$ des NP $Ni_{0,1}Ce_{0,9}O_{2-x}$ estattribué à l' espèce Ni^{3+}. Dans le cas de Ni déposé sur CeO_2, le pic principal de Ni $2p_{3/2}$ à 854.1 eV est accompagné d'un épaulement autour de 855,3 eV et intense (50 ± 5% de la hauteur de pic principale Ni $2p_{3/2}$) décalée de 6.9 eV du pic principal (Fig. 4a), caractéristique de NiO en vrac[24]–[27].

Ces différences d'état Ni^{3+} pour les NPs et Ni^{2+} pour Ni/CeO_2révèle une interaction forte du nickel dans le réseau d'oxyde de cérium pour $Ni_{0,1}Ce_{0,9}O_{2-x}$. Le degré d'oxydation du nickel reste inchangé jusqu'à 200 °C sousH_2, tandis qu'à 400 °C d le déplacement de Ni $2p_{3/2}$ à 852.7 eV et l'intensité maximale du satellite chutent considérablement. Ceci est une indication claire de la réduction du nickel à l'état métallique pour les deux types d'échantillons. Les contributions obtenues après désommation du pic Ce3d en composants Ce^{3+} et Ce^{4+} (figure 4b) sont présentées dans le tableau 1. Ce tableau montre clairement que, dans des conditions de traitement par H_2 identiques, la quantité d'espèce Ce^{3+} pour les NP $Ni_{0,1}Ce_{0,9}O_{2-x}$ est jusqu'à 7 fois plus élevée que celle présente pour Ni/CeO_2.

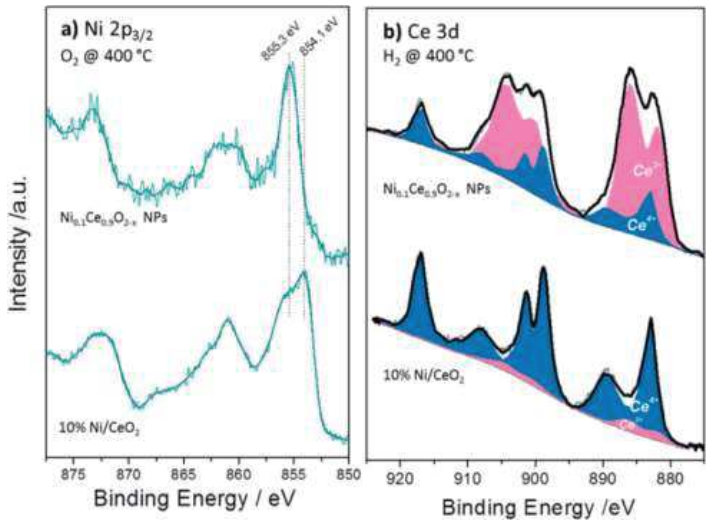

Figure 4. (a) Comparaison des spectres Ni $2p_{3/2}$ entre des échantillons NPs $Ni_{0,1}Ce_{0,9}O_{2-x}$ et 10% Ni/CeO_2enregistrés après calcination à 400 °C échantillons de référence enregistrés dans des conditions de réduction identiques (400 °C dans H_2).

Tableau 1. Concentration en% des espèces Ce^{3+} issue des spectres XPS du Ce 3d pour différents traitements de gaz.

Conditions	% Ce^{3+}	
	$Ni_{0.1}Ce_{0.9}O_{2-x}$	$10\%Ni/CeO_2$
calcined	**0**	**0**
200 °C in H_2	**27**	**5**
400 °C in H_2	**74**	**10**
200 °C in O_2	**31**	**10**
400 °C in O_2	**0**	**0**

Après avoir montré que les NPs $Ni_{0,1}Ce_{0,9}O_{2-x}$ sont relativement stables en taille et forme et capables de conduire à la formation vacants d'oxygène, nous explorons leur potentiel sur l'activité électrochimique des électrodes Ni-YSZ pendant l'électrolyse à la vapeur. A cette fin, la solution de $Ni_{0,1}Ce_{0,9}O_{2-x}$ a été coulée directement sur le WE (Ni-YSZ) d'une cellule Ni-YSZ/YSZ/Pt préformée et soumise à des traitements d'oxydation et de réduction pour éliminer les résidus organiques. La cellule Ni-YSZ/YSZ/Pt modifiée avec l'imprégnation des NPs $Ni_{0,1}Ce_{0,9}O_{2-x}$ est désignée ci-après par l'abréviation NiCe@NiYSZ.

Ces performances sont comparées avec la cellule Ni-YSZ/YSZ/Pt (en abrégé, Ni-YSZ) avant modification dont les performances ont été évaluées dans des conditions identiques. Les tests électrochimiques ont été réalisés en présence de vapeur d'eau à 100% et non dans un mélange H_2O/H_2 comme il est d'usage, afin de simplifier l'interprétation des résultats et d'éviter les

complications liées à l'H_2. La même cellule est utilisée pour les tests électrochimiques avant et après modification. Afin d'éviter une dégradation irréversible de la cellule, les conditions des tests sont maintenues dans des conditions relativement douces (température basse, pression et densités de courant faibles) et ceci afin de ne pas masquer l'effet des NPs $Ni_{0,1}Ce_{0,9}O_{2-x}$. Les courbes de polarisation de l'électrode Ni-YSZ en mode SOEC sous 0.5 mbar H_2O, avant et après l'ajout de NPs $Ni_{0,1}Ce_{0,9}O_{2-x}$, sont représentées sur la figure 5a. Il est clair que les performances de polarisation sont améliorées pour la cellule dopée NiCe@NiYSZ.

En particulier, après l'ajout des NPs $Ni_{0,1}Ce_{0,9}O_{2-x}$, le surpotentiel total, y compris les pertes d'activation, ohmiques et de concentration, est considérablement réduit. Il est également clair que l'augmentation de la charge de NPs $Ni_{0,1}Ce_{0,9}O_{2-x}$ dès 100µL/cm^2 et au-delà 200, 300, 400 et 500 µL/cm^2 est bénéfique pour la performance car elle conduit à une diminution significative du surpotentiel. Pour soutenir cet effet important des NPs $Ni_{0,1}Ce_{0,9}O_{2-x}$ dans des conditions d'électrolyse plus réalistes, les performances du Ni-YSZ et des cellules d'électrode NiCe@NiYSZ à forte charge ont également été étudiées à 23 mbar H_2O (ce qui correspond à environ 77% d'humidité relative) et à région i-V plus étendus, en utilisant 2 cellules distinctes mais identiques en formulation. Comme le montrent les courbes i-V de (Fig. 5c) pour la cellule non dopée Ni-YSZ, le surpotentiel augmente presque linéairement avec la densité de courant appliquée, ce qui est une indication de la détérioration des performances de l'électrode, attribuée à l'oxydation du nickel comme proposée précédemment.

L'électrode modifiée aux NPs $Ni_{0,1}Ce_{0,9}O_{2-x}$ présente une performance supérieure sans dégradation évidente jusqu'à des densités de courant beaucoup plus élevées que celles testées pour la cellule de référence. Des diagrammes de Nyquist des données d'impédance mesurées à -20 mA en mode électrolyse sont représentés sur (figure 5b) avant et après chaque chargement des gouttes. La résistance ohmique Rel (valeur d'axe réel à l'interception haute fréquence), est liée à la conductivité de l'électrolyte et la résistance de polarisation RP (diamètre du demi-cercle). Cette résistance liée à la cinétique des réactions et à la diffusion externe de l'eau à l'électrode indique la diminution de ces deux grandeurs après l'addition des NPs $Ni_{0,1}Ce_{0,9}O_{2-x}$ indépendamment de la pression de l'eau. La valeur réelle de l'axe à l'interception basse fréquence est la somme de la résistance de polarisation et de la résistance de l'électrolyte. Comme on le voit sur la figure 5d, la résistance ohmique de l'électrode et la résistance de polarisation à 23 mbar de

vapeur diminuent considérablement, ce qui indique une amélioration de la conductivité de l'électrode NiYSZ par addition de $Ni_{0,1}Ce_{0,9}O_{2-x}$.

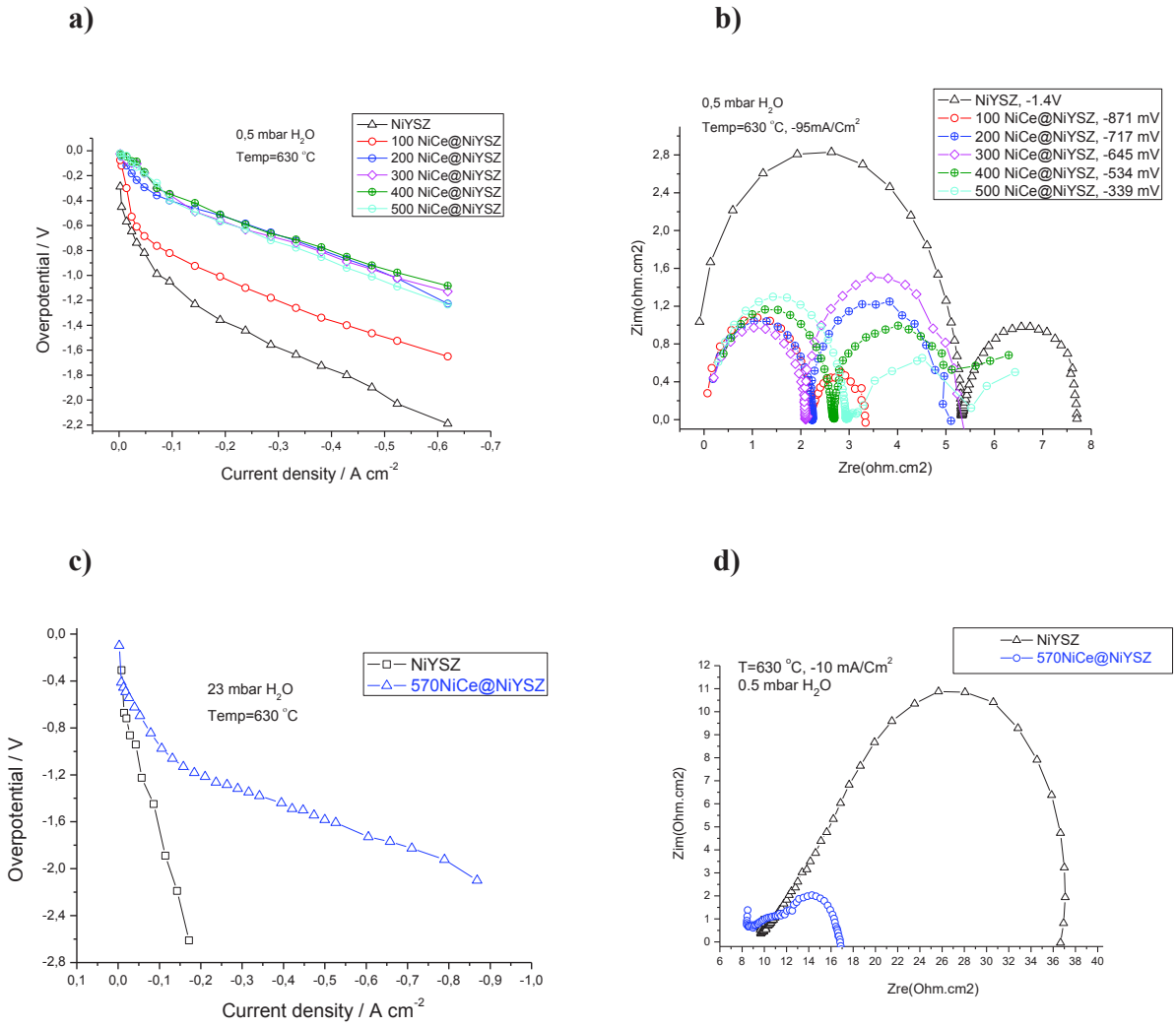

Figure 5. a) Courbes de densité de surtension du courant mesurées dans des conditions d'électrolyse à la vapeur (à 650 °C sous 0.5 mbar de 100% H_2O) sur des électrodes Ni-YSZ avant et après l'addition de deux imprégnations de NPs $Ni_{0,1}Ce_{0,9}O_{2-x}$ (100, 200,300,400, et 500 et 570 µL). b) Les données d'impédance sont indiquées ci-dessus pour chaque charge d'électrodes de travail Ni-YSZ et NiCe@NiYSZ. c) Courbes de densité de surtension du courant mesurées sur des électrodes de travail NiYSZ et 570NiCe@NiYSZ (pour une imprégnation de 570 µL lors d'une électrolyse de tige à 650 °C à 23 mbar 100% H_2O. d) Données d'impédance correspondantes des électrodes de travail. Une électrodeUn compteur de Pt et des électrodes de référence de géométrie identique ont été utilisés dans toutes les mesures.

c) Conclusion générale

La relation entre les performances de la cellule et l'état d'oxydation de la surface de la cathode pour les électrodes de cermet Ni-YSZ et Ni-GDC au cours de l'électrolyse à la vapeur a été mise en évidence. Il a été constaté qu'une couche de NiO de quelques nm d'épaisseur sur une électrode Ni-YSZ augmentait de manière significative le surpotentiel pour une réaction d'électrolyse, mais dans le cas du Ni-GDC, son effet était mineur. De fortes démonstrations sont faites sur l'influence de l'état d'oxydation de la surface du GDC sur le surpotentiel de la cathode pendant l'électrolyse et en particulier sur l'amélioration des performances avec le degré de réduction de la surface du GDC. Dans l'ensemble, nous avons démontré que de petites modifications réversibles sur les quelques nm extérieurs des électrodes cathodiques ont une influence majeure sur les performances électrochimiques de la cellule pendant l'électrolyse à la vapeur pour des ajouts bien choisis.

L'imprégnation d'électrodes de cermet Ni-YSZ standard avec des nanoparticules de cérium dopées au Ni notés $Ni_{0,1}Ce_{0,9}O_{2-x}$ a amélioré les performances électrochimiques. Cette méthode permet ainsi d'introduire une grande population de sites d'oxyde de cérium facilement réductibles et hautement interfacés à la surface du Ni-YSZ avec une empreinte digitale négligeable sur l'ensemble de la morphologie de la cellule, propriétés mécaniques ou porosité des électrodes. La caractérisation électrochimique dans des conditions d'électrolyse de l'eau à basse température a montré que les électrodes Ni-YSZ modifiées sont considérablement améliorées, et en particulier les pertes de polarisation sont beaucoup plus faibles par rapport à la cellule d'origine non modifiée. De plus, après modification, les électrodes Ni-YSZ conservent leur activité même dans des conditions d'électrolyse hautement oxydantes, sans qu'il soit nécessaire d'introduire un agent réducteur (par exemple H_2). La caractérisation de la surface a suggéré que l'amélioration de la performance est liée à une population importante de sites Ce^{3+} et Ni^{3+} maintenus sur une surface de Ni-YSZ pendant l'électrolyse.

List of Abbreviations

WGS	Water Gas Shift
PEM	Proton Exchange Membrane
AEL	Alkaline Electrolysis
SOEC	Solid Oxide Electrolysis Cell
SOFC	Solid Oxide Fuel cell
RSOFC	Reversible Solid Oxide Fuel cell
FTIR	Fourier Transform Infrared
DRIFT	Diffuse Reflectance Infrared Fourier Transform Spectroscopy
HT	High Temperature
YSZ	Yttria-Stabilized Zirconia
GDC	Gadolinia doped Ceria
BV	Butler Volmer Equation
XANES	X-Ray Absorption Near Edge Structure
XAS	X-Ray Absorption Spectroscopy
XPS	X-Ray Photoelectron Spectroscopy
XRD	X-Ray Powder Diffraction
NEXAFES	Near Edge Absorption Fine Structure Spectroscopy
AEY	Auger Electron Yield
TEY	Total Electron Yield
UHV	Ultra High Vacuum
UPS	Ultraviolet Photoelectron Spectroscopy
FY	Fluorescence-Yield
BE	Binding Energy
IMFP	Inelastic Mean Free Path
KE	Kinetic Energy
VB	Valence Band

WE	Working Electrode
RE	Reference Electrode
CE	Counter Electrode
IV	Current-Voltage
NAP	Near Ambient Pressure
EDX	Energy-Dispersive X-Ray Spectroscopy
EIS	Electrochemical Impedance Spectroscopy
R_p	Polarization resistance
R_{el}	Ohmic Resistance
FC	Fuel Cell
FWHM	Full Width At Half Maximum
OCP	Open Circuit potential
PE	Pass Energy
QMS	Quadrupole Mass Spectrometer
SEM	Scanning Electron Microscopy
STEM	Scanning Transmission Electron Microscopy
SUT	Sample Under Test
NPs	Nickel Doped Ceria Nanoparticles
DC	Doped Ceria
MIEC	Mixed Ionic-Electronic Conductor

List of Figures

Figure 1.14. SEM micrograph of the electrolyte-hydrogen electrode interface from the cell used for the "high current density"[37].

Figure 1.15. Illustration of the possible mechanism for the changes in the microstructure at the YSZ-Ni/YSZ interface observed for the high current density, a) The YSZ-Ni/YSZ interface at OCV prior to degradation at high current density electrolysis testing, 3PB are marked by blue squares, b) The YSZ-Ni/YSZ interface upon degradation at high current density electrolysis testing. The electrical potential gradient in the YSZ particles is illustrated by $\uparrow\Delta_{\varphi}$ and the 3PB marked by red squares will be more reducing points than those 3PB marked by blue squares and the reduction of nickel hydroxide will take place at the red marked 3PB leading to a dense Ni-YSZ layer[37].

Figure 1.16. a) Area specific resistance vs. Temperature for different electrolyte materials: yttria-stabilized zirconia (8YSZ), yttria-partially-stabilized zirconia (3YSZ), scandia- stabilized zirconia(ScSZ), scandia-ceria-stabilized zirconia (ScCSZ), samaria-doped ceria (SDC), gadolinia-doped ceria (GDC), lanthanum strontium gadoliniumman- ganite (LSGM), lanthanum strontium gadolinium manganite cobaltite (LSGMC), yttria-doped bariumcerate-zirconate (BCZY), $Ce_{0.43}Zr_{0.43}Gd_{0.1}Y_{0.04}O_{2-\delta}$ (CZGY), b) Selected data on the ionic conductivity of electrolyte materials [21].

Figure 1.17. Scheme of the infiltrated nano-structured electrodes on pre-sintered porous electrode or electrolyte scaffold/ skeleton[38].

Figure 1.18. Typical process for the infiltration of metal salt nitrate solution or nanoparticle suspension into pre-sintered electrode or electrolyte porous structure[39].

Figure 1.19. Diagram showing the steps used to fabricate an SOFC in which the electrodes are produced by infiltration of active components into a porous YSZ scaffold[40].

Figure 1.20. Schematic representation of (top) conventional infiltration method and (bottom) layer-by-layer (LbL) assembled polyelectrolyte multilayer-assisted infiltration for a SOFC electrode.

Figure 1.21. Nyquist plots for symmetric anode cells tested at 600 °C. The size of the arc indicates the magnitude of the polarisation losses. The infiltrated cell showed much lower polarisation losses than the reference both before and after 50 h aging.

Figure 1.22. A) Normalized intensities of the a) NiO and b) CGO Raman peaks monitored as a function of time from pure NiO and CGO samples exposed to dry and wet 75% N_2:25% H_2 flowing at 100 cm^3 m^{-1} . The reduction of NiO is unchanged by the presence of water in the reduction gas, while the CGO appears to be strongly stabilized B) Normalized intensities of the CGO peak monitored from pure and NiO-CGO composites under a) dry and b) wet 75% N_2:25% H_2 flowing at 100 cm^3 min^{-1} over long timescales. CGO within the cermet appears to reduce more rapidly, and without intermediate phases when exposed to dry H_2. It is also more strongly reduced. When exposed to wet H_2, the CGO within the composite is reduced relatively quickly before recovering on longer timescales, tending to the same oxidation state observed for pure CGO[41].

Figure 1.23. Common setups used for the characterization of catalytic samples using infrared absorption spectroscopy. Top, left: transmission (TIR) mode, where the IR beam is directed through a self-sustained sample placed inside the catalytic reactor and collected after exiting for analysis. Top, right: diffuse reflectance (DRIFTS) mode, where powder samples are radiated by a focused IR beam and the scattered light collected using a high-area parabolic mirror. Bottom, left: attenuated total reflection (ATR) mode, where the sample is placed on the outside of the flat surface of the prism used to direct the beam. Bottom, right: reflection–absorption (RAIRS) mode, where the beam is bounced from a flat reflective surface before collection[42].

Figure 1.24. Schematic drawing the evolution of the base unit design and the optical path through the DRIFTS apparatus. (A) As purchased Spectra-Tech configuration. (B) Modification to reduce gas leak in the chamber. (C) SOC operation configuration. (D) Full schematic view of DRIFTS rig showing mirror assembly and beam path[43].

Figure 1.25. Schematic of the processes occurring during photoemission and absorption spectroscopies[44]. Survey spectrum for Ni-YSZ cathode electrode after heating under 0.5 mbar O_2 to remove carbon.

Figure 1.26. O K-edge spectra of $Ce_{1-x}Co_xO_2(0 \leq X \leq 0.07)$ nanoparticles along with reference spectrum of Ce_2O_3[45].

Figure 1.27. O 1s, Fe 2p, Co 2p, and Sr 3d core level XPS spectra of LSC (black), STF (blue), and LSF (red) thin films under polarization (indicated voltage)[46].

Figure 1.28. Valence band and Fe 2p XPS spectra of STF (a, c) and LSF (b, d) polarized by different overpotentials in H_2/H_2O atmosphere. Each spectrum is plotted with the same scale. The applied overpotentials are indicated for each spectrum. (e) DC-characteristics of LSF (red squares) and STF (blue circles)[46].

Figure 1.29. Current–overpotential curve (I_{dc} vs.) of LSF in a humid reducing atmosphere (0.25 mbar H_2+0.25 mbar H_2O).The reaction proceeding on the surface of the LSF working electrode is given on the top right. For selected points of the curve (indicated by arrows), the Fe2p XPS spectra are shown as insets. The sketches indicate the situation for the LSF surface and the resulting reactivity, respectively[47].

Figure 1.30. (*left*) Operando Ni $2p_{3/2}$ XPS spectra and fitted synthetic deconvolutions of very oxidized (A) and partially oxidized (B) Ni electrodes. Of the three peaks of metallic Ni only the main metallic peak (Ni pk1) could be resolved in (A)[48]. (*right*) Operando O 1s XPS spectra acquired from Ni electrode at three different oxidation conditions: no oxidation (black), partially oxidized (blue), and very oxidized (magenta). [NiO]OH and NiO[OH] represent the oxygen components present in NiOOH and do not appear in the metallic Ni. (B) Bar chart comparing the areas of the synthetic peaks shown in (A)[48].

Figure 1.31. (A) Spatially resolved cerium redox changes (Ce^{3+} fraction) calculated from fitted Ce 4d spectra under OCV and ±1.2 V applied biases. (B) Spatially resolved binding energy separations (i.e., surface potential steps) between surface adsorbates (OH^-) and solid surface (O^{2-}) derived from O 1s spectra under OCV and ±1.2 V applied biases. (C) Example of Ce 4d peak fitting. (D) Correlation between Ce^{3+} fraction changes and surface potential step changes under +1.2 V applied bias versus OCV. The Ce^{3+} positions were corrected for a 50 μm experimental shift associated with using different beam energies in different XPS measurements[49].

Figure 1.32. Left spectra (a) Ce 3d-Ni 2p (hν=1065 eV) NAP-XPS spectra (b) Ni $L_{3,2}$-and Ce $M_{5,4}$-edges NEXAFS spectra. The measurement conditions were 0.2 mbar O_2at 700 °C (top) and 500 °C (middle). The measured Ce 3d&Ni2p spectrum (open symbols) is well fitted (black solid line) by a linear combination of the reference CeO_2 and NiO spectra shown at the bottom of the figure and measured under similar acquisition conditions over standard powder samples. **Right spectra** (a) Ce 3d-Ni 2p (hν=1065 eV) NAP-XPS spectra (b) Ni $L_{3,2}$-and Ce $M_{5,4}$-edges NEXAFS spectra. The Ni $L_{3,2}$ edge is magnified 4 times. The measurement conditions were 0.2 mbar H_2at 700 °C (top) and 500 °C (middle). The measured Ce3d&Ni2p spectrum (open symbols) is well fitted (black solid line) by a linear combination of the reference $CeO_{1.5}$ and metallic Ni spectra shown at the bottom of the figure and measured under similar acquisition conditions over standard powder samples[50].

Figure 1.33. (a) Ce 3d and Ni $2p_{3/2}$ (hν=1065 eV) NAP-XPS spectra of the NiGDC electrode recorded at 700 °C at various H_2O exposure periods a) electrode pre-treated in H_2, (b) electrode pre-treated in O_2[50].

Figure 1.34. (a) I–V polarization curves for Ni/GDC electrode under H_2O feed recorded in potential step-up and down cycles. The green star represents the cell current measured in H_2O after 8 h of operation. The current density for various applied potentials as a function of: (b) NiO_x valence and c) Ni/Ce AR measured by APXPS. The color zones represent the applied potentials. Prior to the potential application the sample was pretreated in H_2 and remained at O.C. in the feed gas for about 30 min. The voltage was applied directly between the working (Ni/GDC) and the counter (Pt) electrodes[1].

Figure 1.35. (a) Ce 3d and (b) Ni 2p3/2 APXPS spectra in two information depths (i.d.) under H_2O at 500 °C and -1 V bias. The reference spectra recorded on CeO_2, $CeO_{1.5}$, NiO and Ni are shown in the bottom of the graph. c) The Ni 2p to Ce 3d APXPS area ratio of the overall (Ni/Ce) peak and only the metallic Ni and $CeO_{1.5}$ components (Ni^0/Ce^{3+}) for the two i.d.s. The conditions where the spectra were recorded are indicated in the graph[1].

Figure 2.1. (a) Top view for the Ni-YSZ/YSZ/Pt cell for NiYSZ cathode electrode, (b) Schematic diagrams of cell configuration and setup, (c) Bottom view of the Countering& Reference electrodes Pt**.**

Figure 2.2. SEM micrograph for the Pt electrode after firing procedure, **(top)** prepared with the fast baking procedure (980°C), these images illustrate high density of fractures. (**Bottom**) prepared with the slow baking procedure (800 °C). These images illustrate some fractures and aggregations much less than the above.

Figure 2.3. The NAP-XPS Pt4f spectra measured on the Pt countering electrode (hv =255 eV) in a) 0.5 mbar H_2O,b) 0.5 mbarO_2, c) 0.5 mbar H_2 and d) 0.5 mbar H_2/H_2O under +3mA, prepared with the slow baking procedure (800 °C).

Figure 2.4. Measurement setup configurations used in EIS featuring (a) two electrodes, (b) three electrodes and (c) four electrodes[51].

Figure 2.5. (top) Left panel: detailed photograph of the Laboratory set-up for the electrochemical tests of the cells under the gas-phase conditions. Right panel: Laboratory set-up. (**middle**) a)The primary setup sample holder connected in the setup, b) sketch for the lamp showing the focal point, C) Infra-red lamp64635 HLX, Halogen lamps with reflector MR16; temperature at the focal point, approximately 1300 °C. (**bottom**) a) The three electrode configuration connection in primary setup sample holder containing the electrochemical cell, b) The bottom stainless steel current collector sample holder which is similar to synchrotron setup, c) The top stainless steel current collector sample holder used to fix the cell.

Figure 2.6. XPS laboratory setup and its Schematic drawing for the operation process at (ICPEES, France).

Figure 2.7. a) The sample holder inside the variable pressure chamber. b) Variable pressure chamber of the advanced Laboratory set-up for the electrochemical tests of the cells under the gas-phase conditions. c) The three electrode configuration connection setup sample holder containing the electrochemical cell. d) Mass flow controllers which control the gas flow into the reaction cell and quadrupole mass spectrometer (QMS) to monitor the gas phase.

Figure 2.8. a) The principle of high-pressure x-ray photoelectron spectroscopy (HP-XPS). The sample is placed in a high-pressure chamber that is separated from the x-ray source by an x-ray–transparent window. Electrons and gas escape through a differentially pumped aperture. b) A conventional HP-XPS setup. Several differential pumping stages are needed to keep the electron

analyzer under vacuum when the pressure in the sample cell is close to 1 Torr or higher. There is a tradeoff between the pumping efficiency, given by aperture sizes and spacings, and the solid angle of transmission of electrons through the differential pumping stages. c) The principle of HP-XPS using a differentially pumped electrostatic lens system. The electrons are focused onto the apertures using electrostatic lenses in the differential pumping stages, which increases the efficiency of electron collection and allows for a reduction of the size of the apertures for improved differential pumping. d) Differentially pumped electrostatic lens system and hemispherical analyzer (Phoibos 150, Specs GmbH, Berlin) of the HP-XPS instruments at BESSY, taken from [52].

Figure 2.9. (**top**) Schematic diagram of the in-situ NAP-XPS set-up under the electrochemical gas-phase conditions, at the right side the detailed design of the NAP-XPS set-up in HZB/BESSY II (Berlin, Germany). (**bottom**) The sample holder in detail in mounted inside the NAP-XPS chamber.

Figure 2.10. a) Sketch of the sample holder used to fix the SOEC in the NAP-XPS chamber.

Figure 2.11. Incident photon flux vs kinetic energy recorded at ISISS.

Figure 2.12. (top) Example of the peak fitting procedure used for the estimation of ceria and nickel stoichiometry a) NiGDC cathode electrode, b) NiYSZ cathode electrode for *ex-situ XPS* measurements after exposure to polarization under 0.5 mbar H_2O electrolysis condition at 630 °C. **(bottom)** Example of the peak fitting procedure used for the estimation of ceria and nickel stoichiometry, left) NiGDC cathode electrode, right) NiYSZ cathode electrode for *in-situ XPS* measurements under negative polarization in 0.5 mbar H_2O electrolysis condition at 630 °C.

Figure 2.13. Left IV Curve: Before normalization, Right IV Curve: After normalization Current density-overpotential curves measured under steam electrolysis conditions at 630 °C in3 vapour pressure regimes (0.5, 10 and 23 mbar).

Figure 2.14. Left EIS: Before normalization, Right EIS: After normalization, Nyquist plot by galvanostat EIS obtained on NiYSZ cathode under 0.5 mbar water vapor and 630 °Cat different currents at the advanced laboratory setup (ICPEES, France).

Figure 3.1. a) Time evolution of the Ni-YSZ cathode overpotential (*black line*) and the on line mass spectrometer signal of oxygen (*pink line*) measured at constant current of -100 mA/cm^2 while different concentrations of O_2 were introduced in the H_2O/H_2 feed. The temperature was kept constant at 640 °C. b) Ni 2p NAP-XPS spectra recorded during characteristic moments of the conditions appearing in a. Two Ni 2p components were used to fit the spectra corresponding to metallic Ni (green) and oxidized NiO (pink).

Figure 3.2. a) Time evolution of the Ni-GDC cathode overpotential (*black line*) and the *on line* mass spectrometer signal of oxygen (*pink line*) measured at constant current of -100 mA/cm^2 while different concentrations of O_2 were introduced in the H_2O/H_2 feed. The temperature was kept constant at 640 °C. b) Ni 2p NAP-XPS spectra recorded during characteristic moments of the conditions appearing in a. Two Ni 2p components were used to fit the spectra corresponding to metallic Ni (green) and oxidized NiO (pink).

Figure 3.3. The NAP-XPS Pt 4f peak measured on the counter electrode of the Ni-YSZ/YSZ/Pt cell in 0.5 mbar (*from bottom to the top*) H_2 at 500 °C, H_2O/H_2 at 640 °C and application of +15 mA between Pt and Ni-YSZ electrodes, O_2 at 500 °C. The Pt 4f peak is identical in all cases and corresponds to that of the metallic Pt without any evident peak of PtO_x. The peak of Al 2p is due to traces of alumina visible through the pores of the Pt electrode. Alumina remained on the YSZ electrolyte after the sandblaster cleaning procedure and before application of the platinum paste.

Figure 3.4. Time evolution of the Pt cathode overpotential (*black line*) and the on line mass spectrometer signal of oxygen (*pink line*) measured at constant current of 40 mA/cm^2 while different concentrations of O_2 were introduced in the H_2O/H_2 feed. The temperature was kept constant at 650 °C.

Figure 3.5. The NAP-XPS Zr 3d peak measured on the Ni-YSZ cathode electrode in 0.5 mbar H_2O/H_2 at 640 °C (*from bottom to the top*) at open circuit, application of 100 mA/cm^2 and application of 100 mA/cm^2 and co-feed of O_2.

Figure 3.6. The NAP-XPS Ce 3d spectra measured on the Ni-GDC cathode electrode in 0.5 mbar H_2O/H_2 at 640 °C (*from bottom to the top*) at open circuit, application of -100 mA/cm^2 and application of -100 mA/cm^2 and co-feed of O_2. Two Ce 3d components were used to fit the spectra corresponding to Ce^{3+} (blue) and Ce^{4+} (red) oxidation states.

Figure 3.7. Ce M_5-edge NEXAFS spectra measured on the Ni-GDC electrode in 0.5 mbar H_2O/H_2 at 640 °C and at a current of -100 mA/cm^2 before and during co-feed of O_2. The mathematical difference between the two curves is shown in blue line, while the reference spectrum of Ce_2O is included for comparison.

Figure 3.8. Reduction of Ni-GDC electrode a) Time evolution of the Ni-GDC/YSZ/Pt cell overpotential (*solid black line*), and the evolution of Ce^{3+}/Ce^{4+} components ratio (*blue points*) as derived by the analysis of the corresponding NAP-XPS Ce 3d spectra. Measurements were performed on pre-oxidized Ni-GDC cathodes in 3:1 H_2O/H_2 gas mixture at 640 °C and at constant current of -100 mA/cm^2. The blue color background represents the uncertainty in the calculation of the Ce^{3+}/Ce^{4+} ratio mainly related to the deconvolution procedure. b) Characteristic Ni2$p_{3/2}$ and Ce 3d NAP-XPS spectra in H_2O/H_2 before and after current application. Two Ce 3d components were used to fit the spectra corresponding to Ce^{3+} (*blue*) and Ce^{4+} (*red*) oxidation states of ceria.

Figure 3.9. Ce 3d NAP-XPS spectra measured on the Ni-GDC cathode electrode in H_2O/H_2 before the current application (O.C.) and after 95 min in electrolysis conditions. The difference curve as well as the reference spectrum of $CeO_{1.5}$ is included for comparison.

Figure 3.10. Time evolution of the Ni2p/Ce 3d peak area ratio derived by the analysis of the corresponding NAP-XPS spectra. Measurements were performed on preoxidized Ni-GDC cathode electrodes in 3:1 H_2O/H_2 gas mixture at 640 °C and at constant current of -100 mA/cm^2.

Figure 3.11. Correlation of GDC oxidation state as expressed by the Ce^{3+}/Ce^{4+} ratio and the corresponding Ni 2p/Ce 3d peak area ratio obtained by the analysis of Ce 3d NAP XPS peak as a function of the overpotential. The measurements were performed on Ni-GDC cathodes in 3:1 H_2O/H_2 gas mixture at 640 °C and at constant -100 mA/cm^{2}current after cell pre-treatment at the indicated conditions.

Figure 3.12. Characteristic SEM micrographs of the surface of a) Ni-YSZ and b) Ni-GDC cathode electrodes recorded after the oxidation tests.

Figure 3.13. a) Comparison of the % overpotential increase of cells with Ni-YSZ and Ni-GDC cathode electrodes as a function of the relative amount of NiO and the average NiO film

thickness (derived by the analysis of the corresponding NAP-XPS Ni 2p spectra recorded using 1320 eV photon energy). Measurements were performed at 640 °C and at constant current of -100 mA/cm^2 while different concentrations of O_2 were introduced in the H_2O/H_2 feed. Impedance spectra presented in Nyquist form, obtained under constant applied current of -100 mA cm^{-2} at 640 °C in H_2O/H_2*(3/1)* and $H_2O/H_2/O_2$*(3/1/1)* at total pressure of 0.5 mbar from two electrochemical cells with b) Ni-YSZ and c) Ni-GDC working electrodes. The equivalent circuits used for the fitting of impedance data are shown above of each graph. Measured data are given by symbols, whereas fit results are shown by lines. In both cells Pt counter and reference electrodes with identical geometry were used.

Figure 3.14. Simplified schematic illustration of steam electrolysis pathways over Ni/YSZ and Ni/GDC electrode surfaces in a) reduced and b) partially oxidized states. The specific sites that electrochemical reaction takes place are not shown in this figure.

Figure 4.1. Schematic illustration of the preparation of the $Ni_{0.1}Ce_{0.9}O_{2-x}$nanoparticles.

Figure 4.2. Synthesis step of Ce^{III}-(N,N'-bis(3-methoxysalicylidene)-propylene-1,3-diamine).

Figure 4.3. Synthesis step of Ni^{II}-Ce^{III} (N,N'-bis(3-methoxysalicylidene)-propylene-1,3-diamine).

Figure 4.4. (a) XRD patterns b)Raman spectra and c) XPS spectra d) Auger spectrum of$Ni_{0.1}Ce_{0.9}O_{2-x}$particles as synthesized (red) and after calcination at 400 °C in O_2 (black).

Figure 4.5. SEM images of a $Ni_{0.1}Ce_{0.9}O_{2-x}$ layer (a) fresh after drop casting the solution on a SiO_2/Si wafer (b) after calcination at 400 °C on a SiO_2/Si wafer and (c) after calcination at 400 °C on a Au polycrystalline foil.

Figure 4.6. High resolution bright field STEM image and the corresponding FFT diffraction pattern of $Ni_{0.1}Ce_{0.9}O_{2-x}$formed after calcination at 400 °C.

Figure 4.7. Temperature profiles.

Figure 4.8. In situ XRD patterns of $Ni_{0.1}Ce_{0.9}O_{2-x}$ NPs (left) and 10%Ni/CeO_2 (middle) upon treatment up to 400 °C in O_2 and H_2 atmospheres. Whatever the samples, all Bragg peaks are

singly indexed on to the CeO_2-like fluorite cubic sub cell. An enlarged view of the 42-46 degrees region is also given at the right or the figure.

Figure 4.9. Ni 2p and Ce 3d XPS specta of $Ni_{0.1}Ce_{0.9}O_{2-x}$ NPs (a) and 10%Ni/CeO_2 (b) upon treatment up to 400 °C in O_2 and H_2 atmospheres.

Figure 4.10. (a) Comparison of the Ni $2p_{3/2}$ spectra between 10% Ni/CeO_2 and NiCe NPs samples recorded after calcination at 400 °C (b) deconvolution procedure of two characteristic Ce 3d XPS spectra using Ce^{4+} and Ce^{3+} line shapes derived from reference samples recorded under identical reduction conditions (400 °C in H_2).

Figure 5.1. Schematics of the $Ni_{0.1}Ce_{0.9}O_{2-x}$ modified Ni-YSZ sample preparation.

Figure 5.2. Current density-overpotential curves measured under steam electrolysis conditions at 630 °C in3 vapour pressure regimes (0.5, 10 and 23 mbar).

Figure 5.3. Ce 3d and Ni 2p spectra of the recorded over Ni-YSZ and 570NiCe@NIYSZ electrodes after reduction in 7 mbar H_2 at 400 °C.

Figure 5.4. Ce 3d and Ni 2p spectra of the recorded over Ni-YSZ and 570NiCe@NIYSZ electrodes after reduction in H_2 at 400 °C.

Figure 5.5. a) Current-overpotential curves measured under steam electrolysis conditions over Ni-YSZ electrodes and 570NiCe@NiYSZ electrodes during stem electrolysis at 650°C in 0.5 mbar of 100% H_2O and 23 mbar 100% H_2O. b) Ex-situ Ce 3d and Ni 2p XPS spectra from the conventional and impregnated electrodes in (a) measured after electrolysis.

Figure 5.6. a) Ce 3d XPS spectra of 21 % NiCe@NiYSZ electrodes measured after steam electrolysis. The Ni $2p_{1/2}$ contribution has been properly subtracted and the spectra are deconvoluted using reference peaks measured on pure Ce^{3+} and Ce^{4+} ceria states b) Ni $2p_{3/2}$ XPS spectra measured on NiYSZ and NiCe@NiYSZ electrodes. The reference peak measured on $Ni_{0.1}Ce_{0.9}O_{2-x}$ NPs is included for comparison.

Figure 5.7. Ni $2p_{3/2}$ spectra recorded on NiCe-modified Ni-YSZ electrode (top) and NiCe NPs (middle). The product of the mathematical subtraction of the two spectra after proper background subtraction and intensity normalization (10% of the overal Ni 2p peak area), is shown at the

bottom curve. From this curve it is clear that about 10% of nickel in the surface of 570NiCe@NiYSZ electrode originates from Ni^{3+} species of the NiCe NPs.

Figure 5.8. SEM micrographs of the Ni-YSZ electrodes before and after addition of $Ni_{0.1}Ce_{0.9}O_{2-x}$ NPs measured after water electrolysis conditions (at 650◦°C in 0.5 mbar of 100% H_2O)

Figure 5.9. a) Raman spectra of the 570NiCe@NiYSZ and Ni-YSZ electrodes recorded after electrolysis experiment. b) Cross sectional SEM micrographs of the 570NiCe@NiYSZ electrode after electrolysis experiment**.**

Figure 5.10. a) Current-overpotential curves measured under steam electrolysis conditions over Ni-YSZ conventional electrode and 100NiCe@NiYSZ, 200NiCe@NiYSZ, 300NiCe@NiYSZ, 400NiCe@NiYSZ and 500NiCe@NiYSZ impregnated electrodes (from bottom to top) during stem electrolysis at 630°C in 0.5 mbar of 100% H_2O. b) Impedance spectra presented in Nyquist form, obtained under constant applies current density of -95 mA/cm^2 at 630°C in 0.5 mbar of 100% H_2O from Ni-YSZ conventional electrode and 100NiCe@NiYSZ, 200NiCe@NiYSZ, 300NiCe@NiYSZ, 400NiCe@NiYSZ and 500NiCe@NiYSZ impregnated electrodes.

Figure 5.11. a) Current-overpotential curves measured under steam electrolysis conditions over Ni-YSZ conventional electrode, 100Hexane@NiYSZ and 200Hexane@NiYSZ impregnated electrodes (from bottom to top) during steam electrolysis at 630°C in 0.5 mbar of 100% H_2O. b) Impedance spectra presented in Nyquist form, obtained at OCP. C) Impedance spectra presented in Nyquist form, obtained under constant applies current density of -35 mA/cm^2, both impedance for Ni-YSZ conventional electrode, 100Hexane@NiYSZ and 200Hexane@NiYSZ impregnated electrodes during stem electrolysis at 630°C in 0.5 mbar of 100% H_2O.

Figure 5.12. a) Current-overpotential curves measured under steam electrolysis conditions over Ni-GDC and Ni-YSZ conventional electrodes and 100NiCe@NiYSZ, 200NiCe@NiYSZ, 300NiCe@NiYSZ, 400NiCe@NiYSZ and 500NiCe@NiYSZ impregnated electrodes (from bottom to top) during steam electrolysis at 630°C in 0.5 mbar of 100% H_2O.

Figure 5.13. a) Characteristic Ni $2p_{3/2}$ and Ce 3d XPS spectra after exposing to steam electrolysis in 0.5 mbar H_2O at 630°C for Ni-GDC electrode, b) 500NiCe@NiYSZ and C)

200Hexane@NiYSZ. Two Ce 3d components were used to fit the spectra corresponding to Ce^{3+} (*red*) and Ce^{4+} (*grey*) oxidation states of ceria and NiO (blue) for Ni 2p.

Figure 5.14. SEM micrographs of the Ni-YSZ electrodes after addition of 500 μL/cm^2 $Ni_{0.1}Ce_{0.9}O_{2-x}$ NPs measured after water electrolysis conditions (at 630◦°C in 0.5 mbar of 100% H_2O).

Figure 5.15. Comparison of the % overpotential increase of cells with Ni-YSZ and Ni-GDC cathode and 20NiCe@Ni-YSZ electrodes as a function of the relative amount of NiO and the average NiO film thickness (derived by the analysis of the corresponding NAP-XPS Ni 2p spectra recorded using 1320 eV photon energy). Measurements were performed at 640 °C and at constant current of -100 mA/cm^2 while different concentrations of O_2 were introduced in the H_2O/H_2 feed. Impedance spectra presented in Nyquist form, obtained under constant applied current of -100 mA cm^{-2} at 640 °C in H_2O/H_2*(3/1)* and $H_2O/H_2/O_2$*(3/1/1)* at total pressure of 0.5 mbar from two electrochemical cells with a) Ni-YSZ, b) 20NiCe@Ni-YSZ and c) Ni-GDC working electrodes.

Figure 5.16. The NAP-XPS Ce 3d Ni 2p spectra measured on the 20NiCe@Ni-YSZ cathode electrode in 0.5 mbar H_2O/H_2 at 640 °C under -100 mA/cm^2 and co-feed of O_2(*from bottom to the top*). b) The evolution of Ce^{3+}/Ce^{4+} components ratio as derived by the analysis of the corresponding NAP-XPS Ce 3d spectra.

List of Tables

.

Chapter 1. Literature Review

I. Chapter 1. Literature Introduction

Problems related to greenhouse gas emissions, energy supplies and their costs, health issues and climate change are strong motives to shift towards environmentally friendly and sustainable energy resources. The current major energy suppliers are based mainly on non renewable fuel sources like coal, petrol and natural gas. Their high consumption rate threatens their availability for future generations as mentioned on the 2018 BP Energy Outlook fig. 1.1a. Nevertheless, in an optimistic scenario it is predicted that in the coming 20 years the consumption of renewable energy sources will reach about 20% of the global energy consumption as shown in fig. 1.1b. However, renewable energy sources, such as wind and solar, are usually intermittent in the sense that they are not continuously available. This fact points to the necessity of efficient technologies to store energy during power peak loads by converting it into another energy form easy to store and transfer[1]. Imperial College of London predicates that up to 10 gigawatts of new storage capacity is needed by 2030 if we targeting to lower-carbon consumption economies.

a) b)

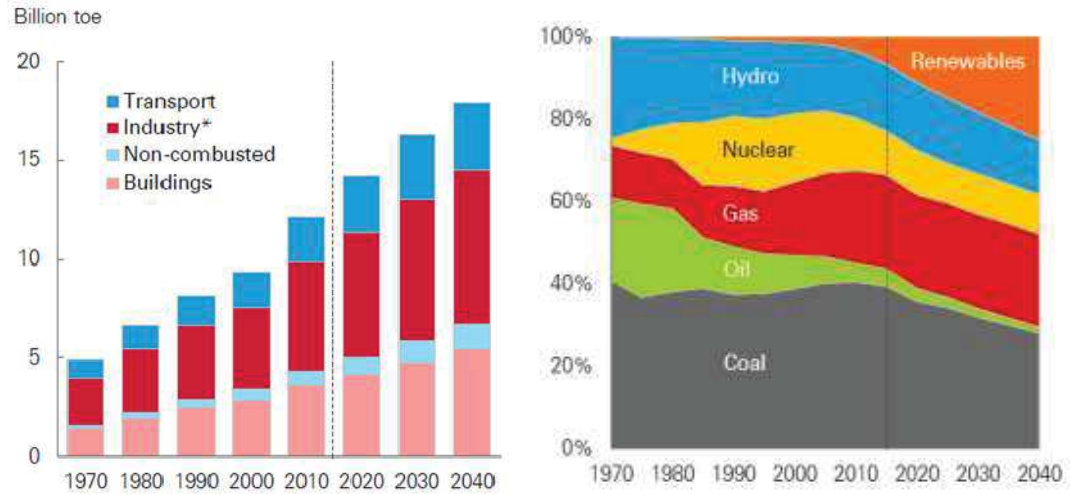

Figure 1.1. a) Primary energy consumption by end use sector expected scenario, b) The global energy consumption prediction from 2018 BP Energy Outlook©BP p.l.c.[28].

Hydrogen is considered as an attractive energy carrier and storage medium for intermitted energy sources. Additionally, as compared to other fuels, hydrogen has the highest calorific value, which is the amount of heat released during the combustion of a specified amount of it, as shown in table1.1[31], [54], [55]. Hydrogen is barely found as pure element in nature but it is a main component of other compounds. The global production of hydrogen is mainly based on fossil

fuels (i.e. by using steam reforming and coal gasification processes). Synthesis gas (syngas, i.e. a mixture primarily of CO and H_2) is the result of steam reforming and coal gasification reactions, which is usually followed by the water gas shift (WGS) reaction to produce more hydrogen[2]–[5].

Table1.1. Comparison of properties of synthetic fuels [31]**.**

Fuel	Relative amount of fuel needed to match the weight composition of H_2 [Heat of combustion / Heat of combustion of H_2]	Hydrogen density in fuel [g/dm^3]	Net Calorific value [kJ/g]	Storage
Hydrogen	**1**	**70.5**	**120.0**	**Very difficult**
Methane	**2.4**	**104.1**	**50.0**	**Difficult**
Methanol	**6.0**	**113.7**	**20.1**	**Easy**
Ethanol	**4.4**	**104.1**	**26.8**	**Easy**
Gasoline	**2.7**	**112.1**	**46.7**	**Easy**

In the 1970s, after the oil crisis also called the first oil shock, there was a transformative step toward hydrogen production from water electrolysis, using renewable electricity sources coming from the sun or the wind[6]. Nowadays, two types of electrolysis technologies, the alkaline (AEL) and Polymer Exchange Membrane electrolyzers (PEM) (see fig. 1.2), both performed at low temperature are commercially available. However, there are several disadvantages for both AEL and PEM, and also numerous infrastructure challenges in the areas of production, distribution, storage and delivery must be solved before hydrogen to play a central role in future energy systems.

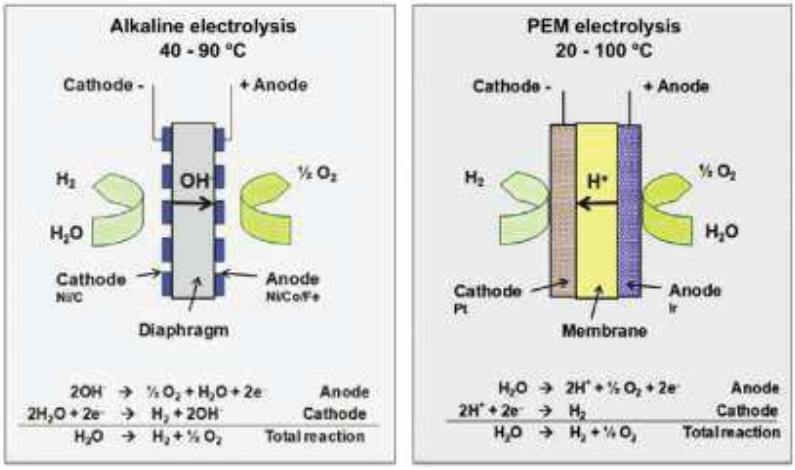

Figure 1.2: Schematic of the operating principle of the low temperature electrolysis technology (alkaline and PEM water electrolysis cell), taken from[29].

Despite the fact that AEL electrolysis is the most well established technology with long term stability, it still has some key problems, related to the low partial load range, limited current density, and low operating temperature. On the other hand PEM electrolyzers, or as they are often called solid polymer electrolyzers (SPE), show better efficiency related to their ability to operate at high current density, high voltage efficiency and high gas purity production. The main drawback of PEM technology is the high cost due to the use of rare and expensive materials as electrocatalysts (e.g. Pt and IrO_2). In addition other problems are related to the corrosive acidic environment caused by the proton exchange membranes that force the use of expensive materials in such operational condition. Both AEL and PEMEL are taking place at low temperature (up to 100 °C) which requires higher electrical energy consumption as compared to high temperature electrolysis cells[29].

Water electrolysis using high-temperature solid oxide electrolysis cells (SOECs) has been considered as an efficient route for this process because of the favorable kinetics and thermodynamics of electrolysis at elevated temperatures[7]–[17], [56]. In addition to high efficiency, this route also leads to the evolution of pure oxygen, significantly enhancing the overall economics of the process[19]. The technology, besides offering the highest faradic efficiency, also offers a possibility of direct electrolyzing of CO_2, or co-electrolyzing H_2O and CO_2. The product of such co-electrolysis is syngas, which can then be reprocessed to yield synthetic fuel[20], [21]. For this reason, solid oxide electrolyzers offer the possibility of chemical

energy storage/carrier when converting renewable energy or excess energy from fossil power plants to hydrogen or syngas. On the downside, up to now SOECs devices are still not commercially viable mainly due to the difficulty to find materials that fulfill the high-performance and durability requirements at high operating temperatures. Due to high temperature operation, special materials are required to withstand the conditions of the process.

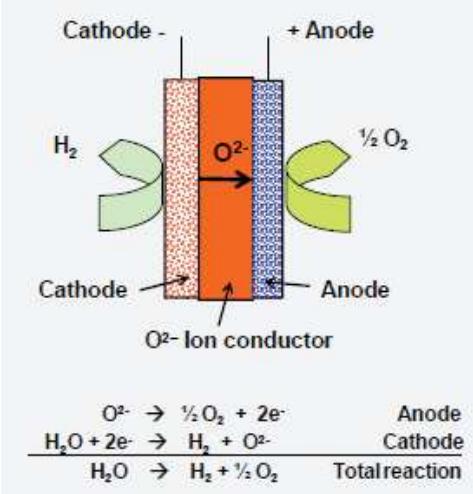

Figure 1.3. Schematic of the operating principle of the high temperature electrolysis technology (SOECs), taken from[29].

1.1. Current methods of hydrogen production

In the coming section as shown in fig. 1.4, the global sources for hydrogen production using renewable and non-renewable sources will be presented and then appraise each production technology from their state of art, commercialization applicability, environmental impact and energy efficiency points of view..

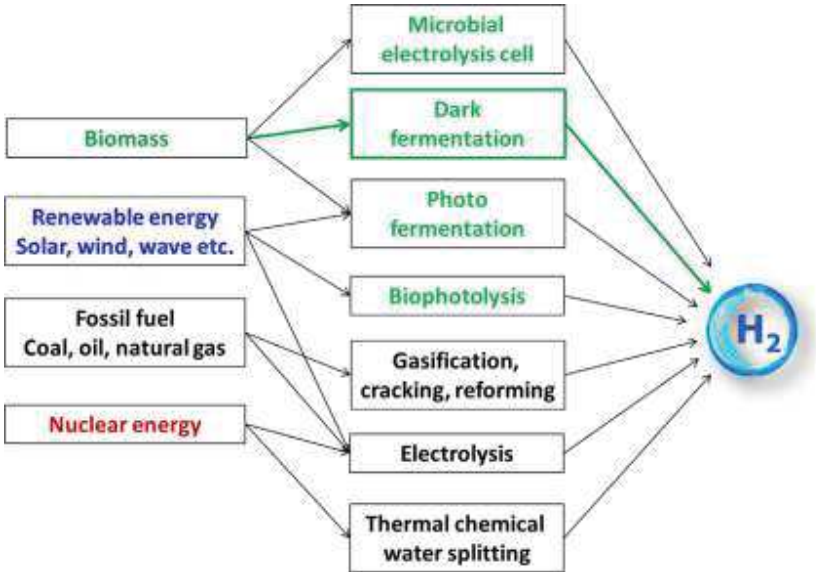

Figure 1.4. Sources and production methods of Hydrogen, taken from[30].

1.1.1. Fossil fuels

Natural gas reforming is the major source for hydrogen production, almost 48% of the global hydrogen production followed by 30% from heavy oils and 18% from coal gasification, as is shown in fig. 1.5 [57]. U.S. Department of Energy (DOE) announced that 95% of the hydrogen produced in the United States is made by natural gas reforming in large central plants. In France, hydrogen production amounts to about 900,000 tonnes per year, with more than 99% originating from fossil fuels according to Durville et al. [58]. The steam reforming of methane (SRM, Eq. 1) is currently the most cost effective and highly mature production process that builds upon the existing natural gas pipeline delivery infrastructure at relatively low cost and high H_2/CO ratios as desired for hydrogen production. SRM products can further react through the water gas shift reaction (WGS, Eq. 2) to produce more hydrogen[59]:

$$CH_4 + H_2O \leftrightarrow CO + 3H_2 \qquad \Delta H°_{298°C} = +206 KJ.mol^{-1} \text{ (Eq.1)}$$

$$CO + H_2O \leftrightarrow CO_2 + H_2 \qquad \Delta H°_{298°C} = -41 KJ.mol^{-1} \text{ (Eq.2)}$$

Methane reacts with steam under 3–25 bar pressure in the presence of a catalyst to produce hydrogen, carbon monoxide, and a relatively small amount of carbon dioxide. Steam reforming is endothermic as shown in reaction (1) as heat must be supplied to the process for the reaction to proceed. In the subsequent WGS reaction carbon monoxide and steam react to produce carbon

dioxide and more hydrogen at lower temperature. In the final step a hydrogen purification process called "pressure-swing adsorption" follows, where carbon dioxide and other impurities are removed from the gas stream. Steam reforming can also be used to produce hydrogen from other fuels, such as ethanol, propane, or even gasoline[2], [5], [57].

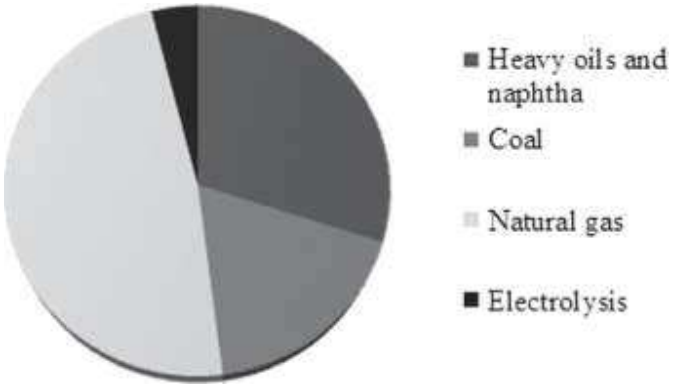

Figure 1.5. Global sources of Hydrogen production, 48% natural gas reforming, 30% from heavy oils, 18% from coal gasification and 4% electrolysis[31].

The big challenge that faces most of the petroleum industries is how to minimize the CO_2 and C formation to achieve the total conversion of methane into syngas by steam and the key solution is to improve the catalysts used during the reaction. One main family of catalysts for this is based on precious metals[60], [61]. On the other hand, other studies proposed the use of metal oxide catalysts and control of their activity by creating defects and/or oxygen vacancies in their structure or by adding dopants [2].

The most commonly used metal oxide catalyst for the WGS reaction at high temperatures is iron oxide, due to its very low cost[2]. At high temperature operation iron deactivates fast, and therefore it is usually promoted with chromium oxides, [62] which prevents sintering of iron crystals. Fe_3O_4/Cr_2O_3 catalysts lose activity rapidly at first but can last up to 10 years in an industrial setting without needing replacement. Alternatively, cobalt/molybdenum catalysts can be used also at such high operating temperatures to remove H_2S from sour gas and oil streams in petroleum refining. Cu supported on alumina catalysts, promoted with ZnO for a longer lifetime, were also used for low temperature WGS reaction [63].

Recently WGS reaction catalysts based on precious metals like gold and platinum supported on rare earth supports, mainly CeO_2, have shown very promising results, for the effective production of hydrogen with low concentrations of CO[63]. The cost of the catalyst is the key point for the petroleum industries and catalysts based on rare earth supports are very expensive, especially when supporting a precious metal, which is economically not sustainable for large scale hydrogen production[2], [63], [64]. There is still a lot of work going on in order to develop convenient catalysts to produce hydrogen from fossil fuels that give a good compromise between, stability, performance and cost for sustainable hydrogen production industrial processes.

1.1.2. Biomass

Hydrogen production from biomass waste has dual benefits of clean energy generation and waste management since agricultural and urban wastes can be disposed at the same time. The major biomass feedstock resources are mainly municipal solid waste, agriculture crops and residues, forestry crops and residues, animal residues, industrial residues, algae biomass and sewage sludge. Bio-hydrogen production processes from biomass can be divided into two main technologies: thermochemical and biological processes fig. 1.6. Biomass gasification and pyrolysis are the thermochemical processes. Direct biophotolysis, indirect biophotolysis, biological water–gas shift reaction, photo fermentation and dark-fermentation are the biological processes. The thermochemical conversion requires large energy input in which biomass gasification is realized at high temperature (600-1000 ^{o}C) but it has the advantage of its possibility to be applied to various types of biomass[31], [32]. The biological technologies using microorganisms to generate hydrogen as a result of the metabolic process include different methods as mentioned before in presence and in absence of light but the most promising method is dark fermentation[30], [31], [65].

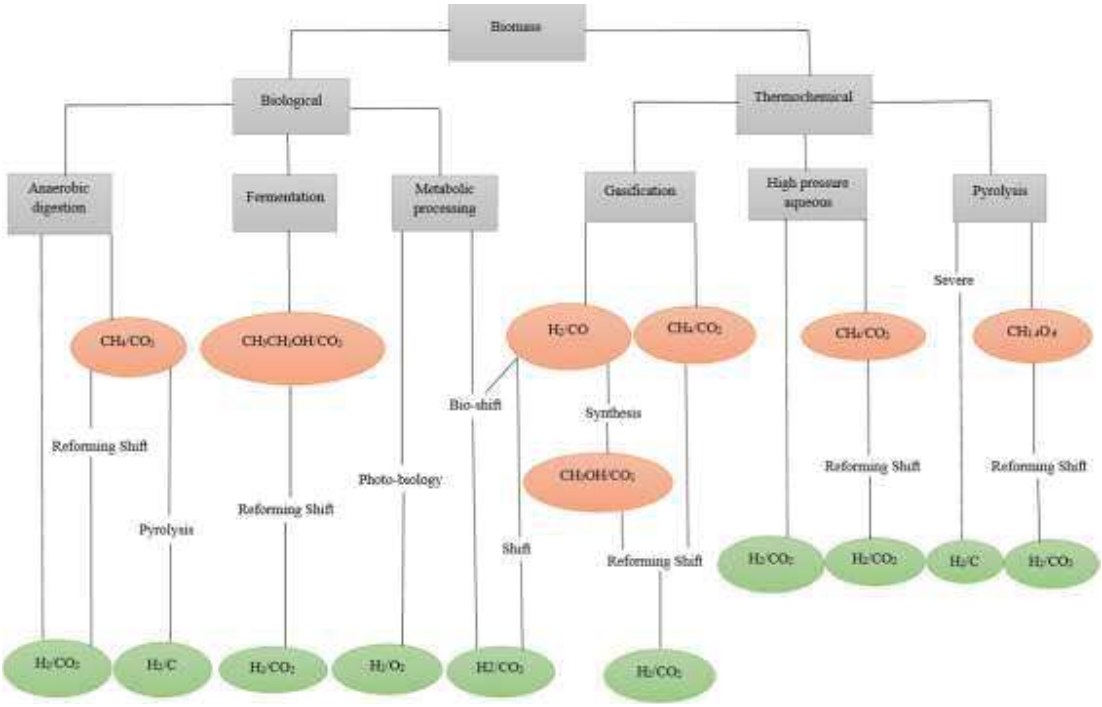

Figure 1.6. Pathways of biomass based hydrogen production [32].

Biomass pretreatment affects the accuracy of conversion process. The amount and nature of the degradation products could be the reasons of the inhibitory to downstream biocatalytic process. Additionally, the substrate type and concentration, inoculums source, fermentation temperature, PH and hydraulic retention time are also important factors to the fermentative bio-hydrogen process[30], [31]. The fermentative hydrogen production occurs in several steps. The first process is disintegration in which the feedstock is firstly disintegrated into soluble matters including proteins, carbohydrates and lipids[30], [32], [66], [67]. Then Hydrolysis occurs to the resulting molecules in which they are further hydrolyzed to smaller molecules like amino acids, monosaccharaides and long chain fatty acids. Finally, acidogenesis and acetogenesis take place, with resulting products H_2, CO_2 and soluble metabolites byproducts[30], [68]–[70]. Biomass energy has high potential for future hydrogen production and huge efforts and research are spent to achieve high conversion efficiency. Globally the awareness of people and politicians is increasing and much concern and efforts are directed towards the biological hydrogen production process due to its mild reaction condition, economic feasibility and environmental benefits[30].

1.1.3. Nuclear Energy

As stated in the International Energy Association (IEA) report (2018), around 11% of the world's electricity is generated by about 450 nuclear power reactors fig. 1.7a. IAEA Power Reactor Information Service (PRIS) revealed that in 2017 nuclear plants supplied 2487 TWh of electricity, which is about 150 TWh higher than in 2012. France has 58 operable nuclear reactors, with a combined net capacity of 63.1 GWe. In 2017, nuclear energy generated 72% of the country's electricity. A 2015 energy policy had aimed to reduce the country's share of nuclear generation to 50% by 2025. In November 2017, the French government postponed this target. The country's energy minister said that the target was not realistic, and that it would increase the country's carbon dioxide emissions, endanger security of supply and put jobs at risk. Thirteen countries in 2017 produced at least one-quarter of their electricity from nuclear energy fig. 1.7b.

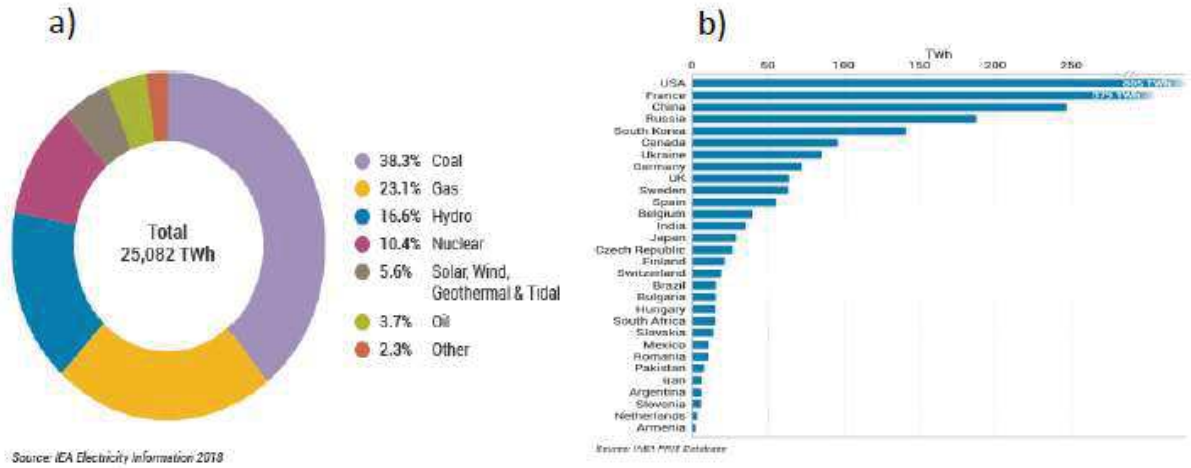

Figure 1.7. a) World Electricity Production by Source 2016, IEA Electricity information (2018), b) Nuclear Generation by Country 2017, IAEA PRIS database.

Hydrogen production from nuclear energy is done by two methods: electrolysis and high temperature water splitting. After the universal Paris agreement to combat climate change signed in December 2015 lots of studies analyzed the correspondence between the deployment of hydrogen markets by 2050 and the potential hydrogen supply that the French nuclear fleet could provide from its excess power available[71]–[73] Recently, Camille and Gilles (2017)[74] proposed a methodology to utilize the nuclear energy for hydrogen production. The model includes two switches for the power output: the first switch goes directly to the electricity grid

and the second to hydrogen power plants. The nuclear fleet will transfer the excess power to the hydrogen plants, and then the produced hydrogen will be stored and delivered to the market. Apart from nuclear, this study also includes power plants based on renewable energy sources (eg: wind and solar) which their electrical output switched to the conventional grid. Electrolysis is the principal process to convert water into hydrogen and oxygen using electricity produced by nuclear energy.

1.1.4. Electrolysis

The world electricity production dependence on fossil fuels is changing in the last 20 years and it is expected to be partially replaced by renewable energy resources such as solar and wind in the future. However, these renewable energy sources are usually intermittent and their electrical output should be stored or converted to another form of energy, especially during the power peak loads[1]. Electrolysis is the most convenient option for the conversion of electricity to chemical energy and in particular H_2. The produced hydrogen is then compressed and stored in tanks, which can be further used for fuel cells to generate electricity (fig. 1.8). Electrolyzers are used to produce hydrogen at levels ranging from a few cm^3/min to several thousand m^3/hour[75]. Water electrolysis can be carried out at low temperature, where H_2O is in its liquid form, using alkaline or proton exchange membrane electrolysers [34]. Alternatively, it can be also performed at high temperature (above 500 °C) with steam, by using Solid Oxide Electrolysis Cells (SOECs). Although low temperature electrolysis is a well-established technology [4], SOEC devices have strong potential for future mass production of hydrogen and show great dynamics to become commercially competitive to other available technologies[6],[7],[9].

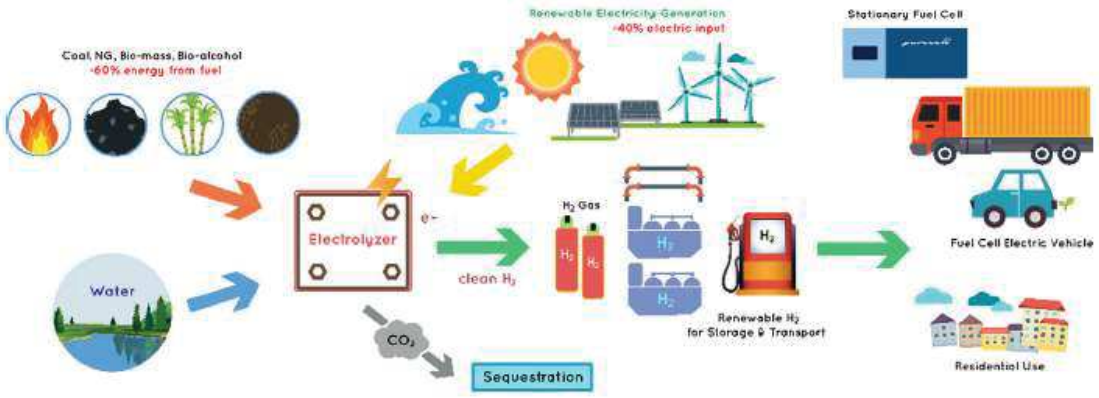

Figure 1.8. Hydrogen production by electrolysis and its applications[33].

The electrolyzer is an electrochemical cell where a potential difference is applied between two electrodes placed on an electrolyte (fig. 1.9). The conversion of electrical energy to chemical energy takes place at the electrode-electrolyte interface through charge transfer reactions. Both hydrogen gas at the negatively biased electrode and oxygen gas at the positively biased electrode are produced as shown in (eq.3):

$$H_2O_{(liq/g)} \rightarrow H_{2(g)} + ½\ O_{2(g)} \text{ (Eq. 3)}$$

At standard ambient temperature and pressure, the change in Gibb's free energy ΔG for the water splitting reaction is positive and hence the reaction is non-spontaneous; which means electrical energy must be supplied equivalent to the change in the Gibb's free energy ΔG of the reaction [34], [75]. The energy required for the water electrolysis reaction is determined by the change of enthalpy ΔH, the Gibbs free energy ΔG and TΔS (T is the temperature and ΔS is the entropy change) as shown in (eq.4).

$$\Delta H = \Delta G + T\Delta S \text{ (Eq. 4)}$$

The minimum required voltage to be applied between the electrodes in order to drive the reaction can be used to do maximum work of nFE, where F is the Faraday constant and n is the number of electrons involved in the reaction per 1 mole of hydrogen which is equal to 2. At 25 °C and 1 bar, the ΔG^0 for the water-splitting reaction is 237.178 kJ/mol as is expressed by (eq.5). The reaction is endothermic at this voltage (1.23 V) and hence at isothermal conditions heat energy must be absorbed from the surrounding environment for the increase in entropy associated with water dissociation as shown in (eq.6)[75].

$$\Delta G^0 = nFE^0 \text{ (Eq. 5)}$$

$$E^0 = \Delta G^0/nF = 1.229V \text{ (Eq. 6)}$$

The situation is different for commercial electrolyzers because the thermal energy TΔS required for electrolysis is provided by electricity. When energy equal to the enthalpy ΔH = ΔG + TΔS (= 285.83 kJ/mol at 1 bar and 25 °C) is supplied for water splitting, no heat is absorbed or evolved by the system[75]. The voltage corresponding to this condition, the thermo-neutral voltage Vtn is expressed in (eq.7).

$$E_{tn} = \Delta H/nF = 1.482V \text{ (Eq.7)}$$

At Vtn the electrolysis generates enough heat to compensate for TΔS. When the cell is operated above Vtn, the reaction becomes exothermic. However energy losses, associated with reaction kinetics as well as charge transport through electrical leads and the electrolyte, necessitate electrolyzer operation in this voltage regime. In the case of practical devices the operating voltage can be expressed as:

$$Eop = E^\circ + \eta a + |\eta c| + \eta \Omega \text{ (Eq.8)}$$

where η_a is the anodic overpotential, associated with the reaction kinetics (electrode polarization effects),

η_c is the cathodic overpotential, associated with the reaction kinetics (electrode polarization effects),

η_Ω is the Ohmic overpotential, generated due to the resistive losses in the cell.

The overvoltage represents the voltage in excess of the thermodynamic voltage, required to overcome the losses in the cell and obtain the desired output in terms of current density or amount of hydrogen from the cell. Slow reactions kinetics and large ohmic losses result in high overpotentials. The electrode, both anodic and cathodic, overpotential arises as a result of several polarization effects. These include low electrocatalytic activity of the electrodes (known as activation overpotential) leading to slow-charge transfer processes and reactants deficiency at the electrode active sites due to the poor mass transport through diffusion (diffusion overpotential), migration or convection electron transfers at anode/electrolyte and cathode/electrolyte interfaces. Chemical kinetics was applied by Butler and Volmer to electrochemical processes, and the expression of charge transfer kinetics at such interfaces was then derived.

The so-called Butler Volmer (BV) equation (eq.9) prevails for mono-electronic transfers. This is a hyperbolic function of the charge transfer overvoltage η, defined as the algebraic difference.

$$j = jo\left\{\exp\left[\frac{\beta nF}{RT}\ \eta\right] - \exp\left[\frac{(1-\beta)nF}{RT}\ \eta\right]\right\} \text{ (Eq.9)}$$

where j is the current density across the interface in $A.cm^{-2}$,

j_0 is the apparent exchange current density across the interface in $A.cm^{-2}$,

β is the geometry or symmetry factor, experimentally close to 0.5 is most experiments,

F is the Faraday constant (96,485.33 $C.mol^{-1}$),

R is the constant of ideal gases (8.134 $Pa.m^3.mol^{-1}.K^{-1}$),

T is the thermodynamic temperature in K,

η is the overvoltage in V,

The overpotential interpreted from (eq.9) is shown in (eq.10):

$$\eta = \frac{RT}{\beta_n F} \log(j_0) - \frac{RT}{(1-\beta)_n F} \log(j) \quad \text{(Eq.10)}$$

and it is simplified by the Tafel relation in (eq.11), where the electrode overpotential increases logarithmically with current density:

$$\eta = a + b \log (j) \text{ (Eq.11)}$$

The constant 'a' provides information about the electrocatalytic activity of the electrodes, and 'b' the slope of the Tafel plot (η Vs log j) carries information regarding the electrode reaction mechanisms.

The (BV) equation which was originally derived for mono-electronic transfers without chemical bond rupture or formation has been generalized to the case of multistep heterogeneous processes, in which both chemical and electrochemical steps occur:

$$j = jo \left\{ \exp\left[\frac{\alpha \leftarrow F}{RT}\ \eta\right] - \exp\left[\frac{\alpha \rightarrow F}{RT}\ \eta\right] \right\} \text{(Eq.12)}$$

The transfer coefficients ($\alpha^{\leftarrow}$ and $\alpha^{\rightarrow}$) are physical parameters that characterize multistep reactions such as the stoichiometry factor of the reaction, the number of steps, the number of electrons transferred during the rate-determining step (rds), and the number of electron-transfer steps before the rds. When applied to the hydrogen evolution reaction (HER) and oxygen evolution reaction (OER) half-cell reactions found in PEM water electrolysis cells, one obtains the two following equations (eq.13,14):

$$jHER = (jo)HER\left\{\exp\left[\frac{\alpha HER\leftarrow F}{RT}\,\eta HER\right] - \exp\left[\frac{\alpha HER\rightarrow F}{RT}\,\eta HER\right]\right\} \quad \text{(Eq.13)}$$

$$jOER = (jo)OER\left\{\exp\left[\frac{\alpha OER\leftarrow F}{RT}\,\eta OER\right] - \exp\left[\frac{\alpha OER\rightarrow F}{RT}\,\eta OER\right]\right\} \quad \text{(Eq.14)}$$

The cell voltage ranges differ in (AEL), (PEM) and (SOECs) due to the factors affecting the energy consumption in each electrolyzer fig. 1.9b. However, increasing the temperature results in a decrease in ΔG and cell voltage.

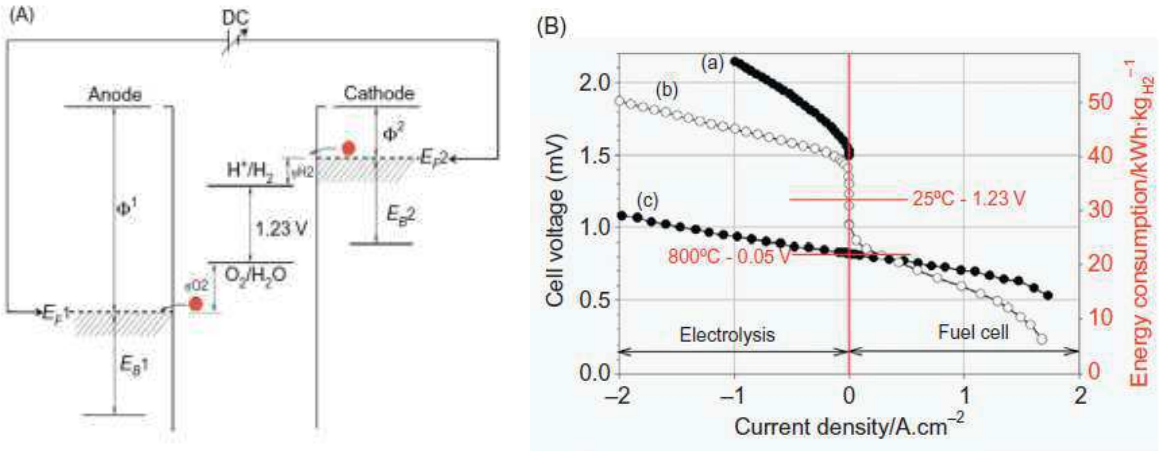

Figure 1.9. (A) Schematic diagram of a water electrolysis cell. (B) Typical I-V curves (water electrolysis mode, left, and fuel cell mode, right) obtained for (a) alkaline, (b) PEM, and (c) solid oxide water electrolysis[34].

Temperature is the key operating parameter that dictates the magnitude of internal dissipation and reaction efficiency of water dissociation reaction as shown in Fig. 1.10. In particular, it should be highlighted that the kinetics of the water/oxygen redox increases with operating temperature. As a result, the system becomes fully reversible at >700 ^{o}C.

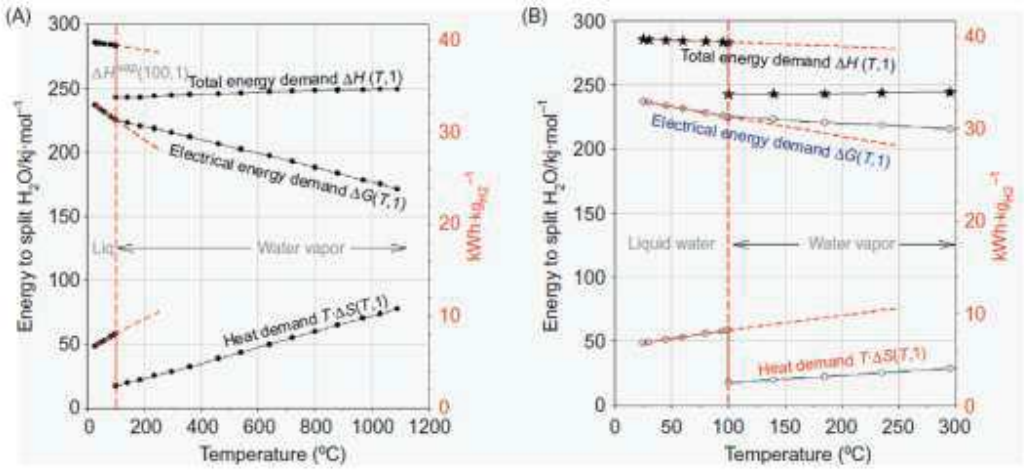

Figure 1.10. Energy required for the electrolysis reaction as a function of temperature[34].

One advantage of high-temperature Solid oxide technology which is used to electrolyze water vapor over near-ambient temperature technologies (Alkaline and proton-exchange membrane (PEM)) is that, at 1000 ^{o}C, approximately one third of the total energy demand is required as heat. Since the kWh of heat is usually said to be less expensive than the kWh of electricity, it would be less expensive to split 1 mole of water at 1000 ^{o}C than at around room temperature. Such heat is potentially available in nuclear and solar plants[75]–[78].

As thermodynamically, the electrical energy demand drops from 225 kJ/mol at 100 ^{o}C to 185 kJ/mol at 1000 ^{o}C. In addition, high temperature electrolysis is advantageous also from the electrochemical perspective because kinetics for electrode reactions improve and the ohmic conductivity increases with temperature, leading to the decrease of the cell`s internal resistance. In conclusion, by increasing the operating temperature, a smaller amount of electricity and a larger portion of corresponding heat are needed for the dissociation reactions.

1.2. Solid oxide water electrolysis

The challenges which face the energy sector to fulfill the consumption increase make the deployment of renewable energy sources necessary in order to decrease the dependence on non-renewable energy sources (Fossil fuel). Today, the three main types of electrolysers are; alkaline (AEL) which is a mature and commercialized technology, proton exchange membrane (PEM) which is in its early commercial phase, and high temperature steam electrolysis (HTSE) which is

very convenient for this application since it can also use the waste heat produced from the nuclear plants in addition to the produced electricity. Current developments in both Solid oxide electrolysis cells (SOECs) and solid oxide fuel cells (SOFCs) increase their potential in the energy market and it is expected to be one of the main sources for energy generation sources. In the coming section, the state of the art about SOECs will be discussed, together with their operation conditions, their competitive points parallel to their weakness point. In table 1.2 the key strong and weakness points of each electrolysis technology, and also the challenges which are facing these technologies are given.

Table1.2. Typical characteristics of main electrolysis technologies[53].

	Low Temperature Electrolysis			High Temperature Electrolysis		
	Alkaline (OH^-) electrolysis		Proton Exchange (H^+) electrolysis	Oxygen ion(O^{2-}) electrolysis		
	Liquid	Polymer Electrolyte Membrane		Solid Oxide Electrolysis (SOE)		
	Conventional	Solid alkaline	H^+ - PEM	H^+ - SOE	O^{2-} - SOE	Co-electrolysis
Operation principles	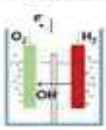	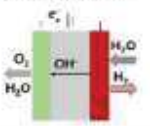	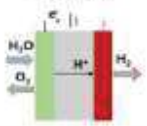	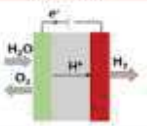	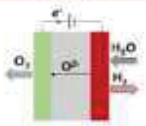	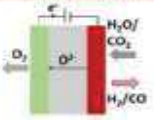
Charge carrier	OH^-	OH^-	H^+	H^+	O^{2-}	O^{2-}
Temperature	20-80°C	20-200°C	20-200°C	500-1000°C	500-1000°C	750-900°C
Electrolyte	liquid	solid (polymeric)	solid (polymeric)	solid (ceramic)	solid (ceramic)	solid (ceramic)
Anodic Reaction (OER)	$4OH^- \rightarrow 2H_2O + O_2 + 4e^-$	$4OH^- \rightarrow 2H_2O + O_2 + 4e^-$	$2H_2O \rightarrow 4H^+ + O_2 + 4e^-$	$2H_2O \rightarrow 4H^+ + 4e^- + O_2$	$O^{2-} \rightarrow {}^1/_2O_2 + 2e^-$	$O^{2-} \rightarrow {}^1/_2O_2 + 2e^-$
Anodes	Ni > Co > Fe (oxides) Perovskites: $Ba_{0.5}Sr_{0.5}Co_{0.8}Fe_{0.2}O_{3-\delta}$, $LaCoO_3$	Ni-based	IrO_2, RuO_2, $Ir_xRu_{1-x}O_2$ Supports: TiO_2, ITO, TiC	Perovskites with protonic-electronic conductivity	$La_xSr_{1-x}MnO_3$ + Y-Stabilized ZrO_2 (LSM-YSZ)	$La_xSr_{1-x}MnO_3$ + Y-Stabilized ZrO_2 (LSM-YSZ)
Cathodic Reaction (HER)	$2H_2O + 4e^- \rightarrow 4OH^- + 2H_2$	$2H_2O + 4e^- \rightarrow 4OH^- + 2H_2$	$4H^+ + 4e^- \rightarrow 2H_2$	$4H^+ + 4e^- \rightarrow 2H_2$	$H_2O + 2e^- \rightarrow H_2 + O^{2-}$	$H_2O + 2e^- \rightarrow H_2 + O^{2-}$ $CO_2 + 2e^- \rightarrow CO + O^{2-}$
Cathodes	Ni alloys	Ni, Ni-Fe, $NiFe_2O_4$	Pt/C MoS_2	Ni-cermets	Ni-YSZ Subst. $LaCrO_3$	Ni-YSZ perovskites
Efficiency	59-70%		65-82%	up to 100%	up to 100%	-
Applicability	commercial	laboratory scale	near-term commercialization	laboratory scale	demonstration	laboratory scale
Advantages	low capital cost, relatively stable, mature technology	combination of alkaline and H^+-PEM electrolysis	compact design, fast response/start-up, high-purity H_2	enhanced kinetics, thermodynamics: lower energy demands, low capital cost		+ direct production of syngas
Disadvantages	corrosive electrolyte, gas permeation, slow dynamics	low OH^- conductivity in polymeric membranes	high cost polymeric membranes; acidic: noble metals	mechanically unstable electrodes (cracking), safety issues: improper sealing		
Challenges	Improve durability/reliability; and Oxygen Evolution	Improve electrolyte	Reduce noble-metal utilization	microstructural changes in the electrodes: delamination, blocking of TPBs, passivation		C deposition, microstructural change electrodes

1.2.1. Theoretical aspects

Solid oxide electrolysis cells (SOECs) and solid oxide fuel cells (SOFCs) have the same configuration but reverse operation, as is shown in fig. 1.11. As discussed before, high temperature electrolysis technology is considered to be the best future challenge for future energy market. Compared to AEL and PEMEL which are better established but more expensive

and less efficient, it shows great dynamics to become commercially competitive[6], [12], [17], [21], [77]. Additionally, SOECs can be used for carbon dioxide electrolysis to carbon monoxide and oxygen which creates a great interest for syngas production.

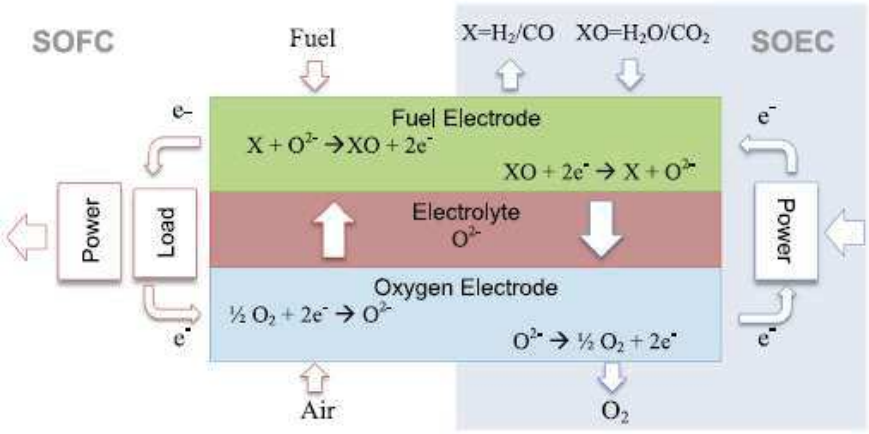

Figure 1.11. SOEC and SOFC operating modes[21].

A SOEC consists of three main components: an electrolyte and two electrodes. The electrolyte is a ceramic membrane that can conduct ions and is sandwiched between two porous electrodes that can conduct electrons: the steam/hydrogen electrode (or anode in fuel cell mode) and the air/oxygen electrode (or cathode in the fuel cell mode). An example is a Ni-YSZ/GDC/LSCF cell shown in fig. 1.12.

In the former electrode water and/or carbon dioxide molecules react with electrons, which are supplied through an external power source, to produce hydrogen and/or carbon monoxide and oxygen anions. In the anode compartment the oxygen ions, which are driven through the electrolyte, are combined to produce oxygen gas. The latest progress in the SOFC technology changed the above described cell concept from an electrolyte supported to a fuel electrode supported cell, comprising a thick mechanically stable cermet layer as actual electrode on which a very thin YSZ electrolyte is supported. Both the electrode and the electrolyte are about 10 μm thick. The latter configuration allows even lower operating temperatures, due to the substantially lower ohmic resistance of the electrolyte.

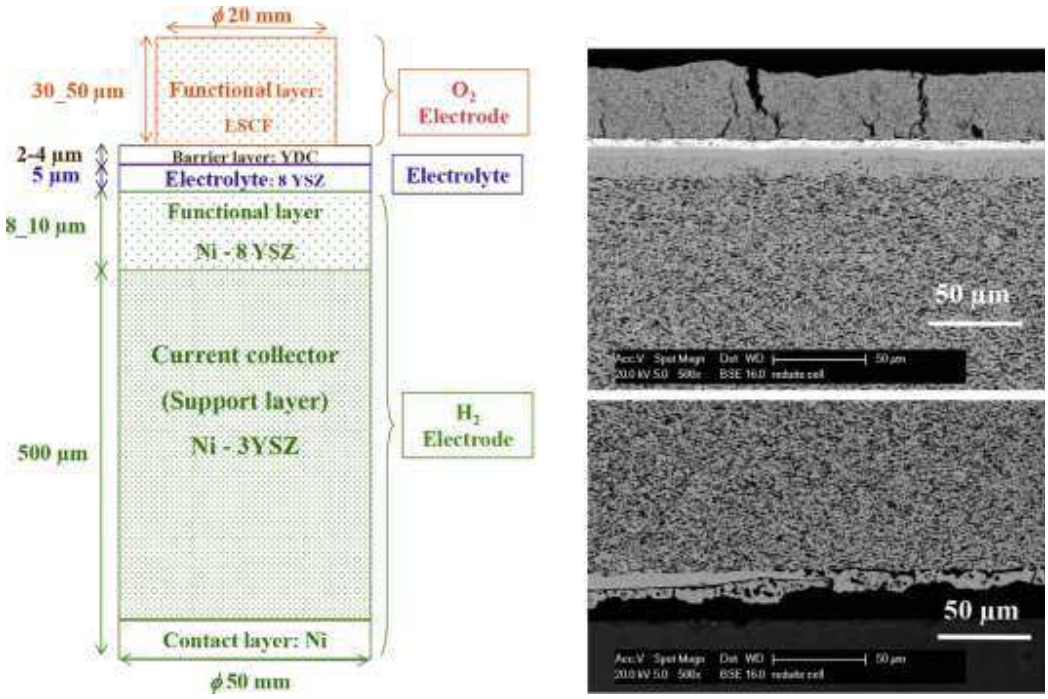

Figure 1.12. Schematic representation of the cell structure. The global view of cell layers are illustrated by two polished cross section images obtained with a Scanning Electron Microscope (SEM) in Back Scattering Electron (BSE) mode[35].

The commonly used materials in SOECs are basically the same like those for SOFCs and they have to fulfill similar requirements such as: thermal stability at high operating temperature, chemical and mechanical compatibility, chemical and microstructural stability in the operating atmosphere and temperature and redox stability[17], [79]. The electrodes must additionally present some other properties such as high electrocatalytic activity and high electronic conductivity. They must also present high porosity for the promotion of mass transfer in the gas phase, while maintaining sufficient electrical percolation and ionic conductivity that may allow the geometric extension of the electrochemical reaction zone in the entire volume of the electrode.

High temperature co-electrolysis could be one of the most practical solutions in reducing CO_2 emissions. Consequently, this gives SOECs the dual benefit of producing energy source and mitigation of CO_2. High temperature co-electrolysis of H_2O and CO_2 shows very efficient use of electricity and heat (near 100% electricity-to-syngas efficiency), high reaction rates and direct production of syngas with proper composition for use in conventional Fischer-Tropsch catalytic

fuel synthesis reactors[20], [80]. Syngas can be converted into electrical energy by using SOFCs or into hydrocarbon fuels (e.g. CH_4) through the Fischer–Tropsch process[81]. This cycle can be described as a "gas-to-liquid" (GTL) process in agreement with the conventional process for the production of syngas from natural gas feedstock. The process may also be referred to as a renewable-to-liquids (RTL) process, when RES provides the required energy for the electrolysis step[2]. This process can be considered as an alternative route for the production of hydrogen and synthesis gas, without consuming fossil fuels or emitting green-house gases, realizing a CO_2-recycled synthetic fuel cycle.

However, the dissociation of H_2O and CO_2 requires larger energy consumption because the minimum energy demand is the sum of the reactions enthalpy of the corresponding reactions (eq.15) and (eq.16):

H_2O + electrical energy + heat → H_2 + ½ O_2, ΔH_f = 286 kJ/mol – ΔG = 188 kJ/mol (Eq.15)

CO_2 + electrical energy + heat → CO + ½ O_2, ΔH_f = 283 kJ/mol – ΔG = 189.2 kJ/mol (Eq.16)

From the thermodynamic point of view the higher electrical efficiencies result from the decrease in the molar Gibbs energy of the reaction (ΔG), with increasing temperature, while the molar enthalpy (Total Energy demand, ΔH) remains essentially unchanged[20] and the heat energy demand ($T\Delta S$) increases as shown in fig. 1.13. That is why Solid Oxide electrolysis has gained particular interest for the electrical energy demand reduction for electrolysis as result from increasing the operating temperature[17], [79].

From the kinetics point of view the reaction rates of the high temperature electrolysis are faster. However the ohmic conductivity increases with temperature which causes decreasing in the cell`s internal resistance and in total to an increased efficiency. In conclusion, by increasing the operating temperature, a smaller amount of electricity and a larger portion of corresponding heat are needed for the dissociation reactions.

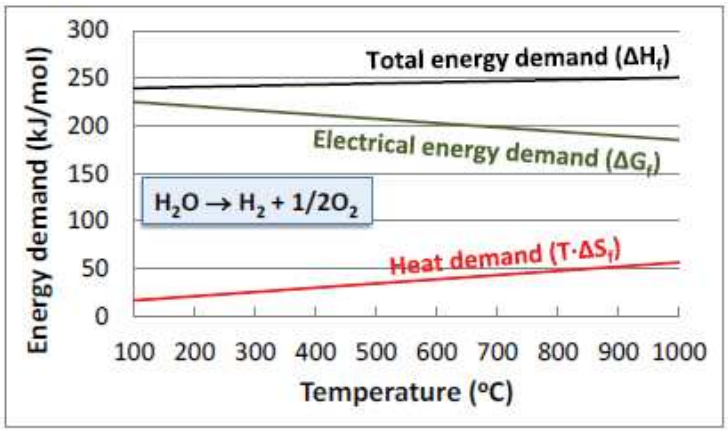

Figure 1.13. Operational principle for water electrolysis and CO_2/H_2O Co-electrolysis SOEC[36].

Electrolysis is a relatively expensive technology due to high electricity demand which part of it is consumed as heat for the process to occur. SOEC technology compensates the decrease of this electrical demand by heat demand. During the electrolysis operation, the increased demand on heat energy can be covered either from an external source or it can be the Joule heat that is inevitably produced by the internal electrical resistance of the cell. The potential value, at which the generated Joule heat in the cell and the heat consumption for the electrolysis reactions are equal, is defined as the thermoneutral potential V_{tn} of operation as we discussed before in the electrolysis section. Indicatively, for an SOEC operating at 900 – 950 °C, the thermoneutral potential V_{tn} is around 1.29V and the SOEC can be theoretically operated at thermal equilibrium with an electrical efficiency of 100%. If the cell operates below the thermoneutral voltage (endothermic mode), the electric energy is lower than the enthalpy of the reaction and heat must be supplied to the cell, in order to maintain the operating temperature. In this case the thermal needs are partly covered by the Joule heating and electrical efficiencies above 100% can be achieved. Moreover, the thermal needs are complementarily covered by thermal energy from the environment, particularly from the reaction gases, which leads to a temperature decrease. Alternatively, by operating above the thermoneutral potential (exothermic mode) the thermal needs are entirely covered by the Joule heating, which is in excess, and the achieved electrical efficiencies are below 100%. The excess heat is dismissed as thermal energy to the environment, particularly to the reaction gases, leading thus to a temperature increase. On the other hand, low temperature electrolysis is always performed in the exothermic mode and at much higher

voltages from the thermoneutral value, thus achieving quite lower cell efficiencies and production rates[17], [79], [82].

1.2.2. Main problems (degradation)

Obtaining high performance and durability are currently the most important factors for SOECs commercialization. The requirements for commercial electrolysis cells are long term operation stability for a period of approximately 3 – 5 years, degradation rates below ≈1%/1000 h, high performance (high H_2 production rates i.e., ≈ 40 $mgH_2/cm^2/h$ or ≈ -1A/cm^2), and sufficient materials durability[80], [83]–[87]. Electrolysis testing at high current density (1−2 A/cm^2), high temperature (800-950°C), and a high partial pressure of steam (pH_2O ≈ 1atm), showed that the cells could withstand at least 1300 h of electrolysis testing without significant loss of their performance [87], [88]. However, impurities in the hydrogen electrode of tested solid oxide electrolysis cells lead to significant microstructural changes at the hydrogen electrode-electrolyte interface.

Most of the latest data show that SOECs performance decrease of about 2% after 1000 h of operation for the H_2O electrolysis reaction, whereas for the co-electrolysis processes the situation is even worse. A degradation test on a Ni/YSZ electrode under operation conditions in high current density (current density of −1.5 A/cm^2, 950 °C and at pH_2O= 0.9 atm and pH_2= 0.1 atm) was done and then the electrode was analyzed. In this context the high current density test is interesting even though it can hardly be considered as a long-term electrolysis test. Fig.1.14 shows irreversible microstructural changes of the YSZ-Ni/YSZ interface observed for the cell used for this test that correspond well to the very large increase in the ohmic resistance, R_s, observed during testing.

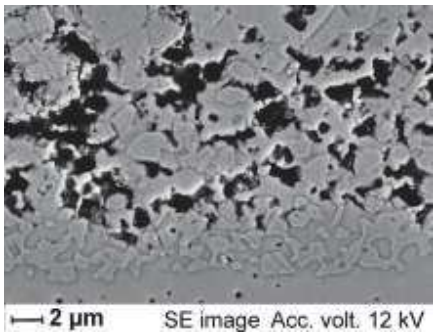

Figure 1.14. SEM micrograph of the electrolyte-hydrogen electrode interface from the cell used for the "high current density"[37].

A possible degradation mechanism is suggested by A. Hauch[37] for the microstructure at the YSZ-Ni/YSZ interface after high current density tests, as illustrated in fig. 1.15a. Under the high steam partial pressure and high temperature conditions the electrode surface is suggested to be surrounded by a relatively high partial pressure of nickel hydroxide, $Ni(OH)_2$. When external voltage is applied, the steam electrolysis starts and oxygen ions are conducted in the YSZ toward the oxygen electrode, as is shown in fig. 1.15b. They suggested that Ni particles are equipotentials, and an electrical resistance in the YSZ particles of the Ni/YSZ electrode is raised together with an electrical potential gradient outwards in the YSZ, as indicated by $\uparrow\Delta_{\varphi}$ in fig. 1.15b. In addition, Ni reduction occurs, in which the 3PB closest to the electrolyte (marked by red squares) is more strongly reducing (high current density) than the blue marked 3PB (lower current density) and nickel hydroxide Ni(II) is most likely reduced to metallic at the strongly reducing points as in (eq.17).

$$Ni(OH)_{2\,(g)} + 4e- \rightarrow Ni(s) + 2O^{2-} + H_{2(g)} \quad \text{(Eq.17)}$$

They illustrated that such relocation of Ni will consequently lead to a dense Ni-YSZ layer as observed in the SEM image in fig. 1.14. However, there will be a large potential difference near the electrode/electrolyte interface during electrolysis testing that is the "driving force" for the electrochemical reduction of Ni(II) to metallic Ni at this interface. SEM image shows some parts of reduced nickel and other parts of the cell that may contain Ni(II) species. Further studies of SOECs operated at current densities (above -1.5 A/cm^2) are necessary to verify the proposed hypothesis for the observed microstructural changes of the YSZ-Ni/YSZ interface put forward here.

Short term degradation was originally observed during operation at high current densities (<-1.75 A/cm^2) and high steam concentration. On the other hand, the long-term H_2O electrolysis studies on single cells attributed the observed decrease in performance to the increasing polarization resistance and to the degradation on both electrodes[79]. Generally, one of the biggest reasons for the increase in overpotential consumption is nickel oxidation, nickel agglomeration and/or re-oxidation which usually occur during typical operation conditions. Moreover, significant

degradation has been also observed on the oxygen electrode, mainly caused by its delamination due to high oxygen partial pressures at the electrolyte/anode interface[79], [89]. Additionally, after long-term operational conditions, fracture and large cracks can be seen even by naked eye.

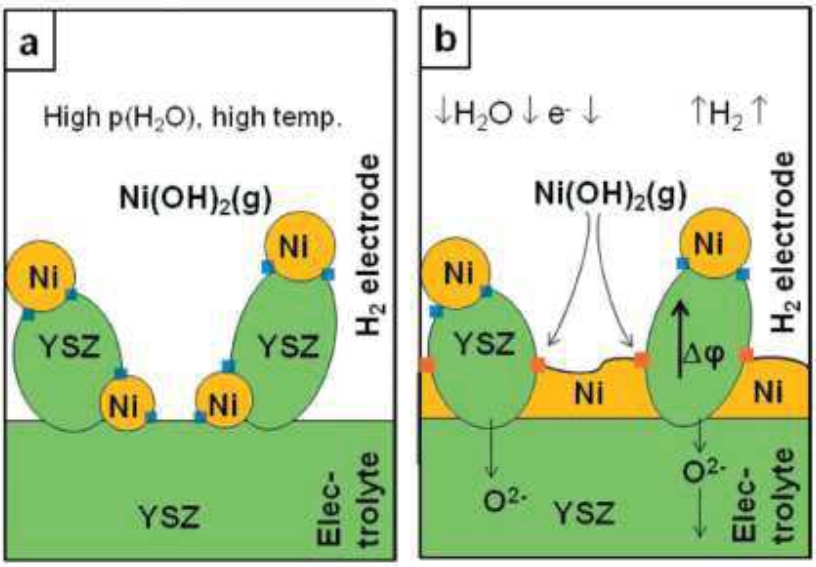

Figure 1.15. Illustration of the possible mechanism for the changes in the microstructure at the YSZ-Ni/YSZ interface observed for the high current density, a) The YSZ-Ni/YSZ interface at OCV prior to degradation at high current density electrolysis testing, 3PB are marked by blue squares, b) The YSZ-Ni/YSZ interface upon degradation at high current density electrolysis testing. The electrical potential gradient in the YSZ particles is illustrated by $\uparrow\Delta_{\varphi}$ and the 3PB marked by red squares will be more reducing points than those 3PB marked by blue squares and the reduction of nickel hydroxide will take place at the red marked 3PB leading to a dense Ni-YSZ layer[37].

Stack degradation tends to be faster compared to single cell degradation as a consequence of contact degradation of the interconnections and accelerated cell degradation due to thermal stresses and contamination from tubing, interconnects and sealing materials[90]–[92]. Therefore, it is a common belief that operation at lower temperature could be beneficial, resulting in minimization of interconnects corrosion and of the interactions between the stack components, thus providing the ability of using inexpensive metallic interconnects.

1.2.3. Type of SOEC and operation modes

SOECs or SOFCs are fabricated in several specific types which are manly (i) electrode supported cells or (ii) electrolyte-supported cells or (iii) Reversible solid oxide fuel cells[21], [89], [93]. Electrode-supported cells have a relatively thin electrolyte (~10 μm) with thick electrodes as support (~ 300 - 500 μm). On the other hand, electrolyte-supported cells use a thick electrolyte as a support with thin electrodes coated on both sides of it. In general, it is believed that the electrochemical reaction occurs in the part of the electrode which is within roughly 10μm from the electrolyte[40]. SOC can also work in dual mode, (RSOFC) both fuel cell and electrolysis mode, fulfilling both requirements in a single device[21].

1.2.4. State of the art materials for SOC

Currently the most convenient materials used for SOECs are Ni/YSZ or Ni/GDC as fuel electrode, YSZ as electrolyte, and LSM as oxygen electrode. However, Ni/YSZ fuel electrode suffers from different degradation reasons such as agglomeration of Ni particles due to either thermal or overpotential sintering, redox instability of the cermet when exposed to oxidizing atmosphere (especially under only steam content), carbon deposition onto nickel under H_2O/CO_2 co-electrolysis, or poisoning from trace impurities, chromium poisoning from the connectors and delamination of the electrode. In addition, it was found that Ni/YSZ cathodes are always in need of adding a small quantity of hydrogen in fuel (steam) in order to assist the instability of cathode materials during start up when it experiences low hydrogen conditions (high steam content). The need of hydrogen to produce hydrogen increases SOEC complexity. Both families of materials which were used herein are expected to attain high redox stability. On the other hand, perovskites of the type LSCM are redox stable and could be used without the need of hydrogen in fuel.

(i) **Fuel (steam) Electrode for SOECs**

The fuel SOEC electrode should fulfill some requirements such as high electronic conductivity, high thermal and mechanical stability, low cost and facile manufacturing, high electrocatalytic activity towards electro-oxidation of H_2O and/or CO_2, high ionic conductivity, high porosity that allows the fuel molecules to easily flow towards the active sites, durability and compatibility with other SOEC components during cell fabrication and operation electrolysis conditions [6, 28].

The material that fulfills most of the above properties and is perfectly utilized in several cell/stack studies is the Ni/YSZ cermets. In response to the degradation issues and the poor durability of Ni/YSZ fuel electrode under electrolysis applications, either in the form of single cell measurements or in stacks, novel materials are nominated as candidates. Some of these materials include cermets that contain nickel in their formulation, while others are related to perovskite-based materials with or without nickel. However up to now, there are not many published studies with significant progress regarding the performance, improvement and/or development of alternative Ni/based or Ni/free SOEC fuel electrodes. Modifications to the traditional Ni/YSZ cermets are focused in increasing the 3 phase boundaries (TPB) by introducing new reaction sites. For instance, Ni/YSZ infiltration with perovskite ($BaZr_{0.9}Yb_{0.1}O_{3-\delta}$) increased the structural stability and poisoning resistance[94]; coating with samaria-doped ceria (SDC, $Sm_{0.2}Ce_{0.8}O_2$) resulted in four times lower polarization; substitution of YSZ by gadolinia doped ceria (GDC) made a more stable cell during CO_2 electrolysis and reduced ASR values from 1.3 to 0.9 Ω cm² (at 25% CO_2, 1000 °C) due to improved ionic- electronic conductivity and TPB enlargement. Perovskites such as $La_{0.7}Sr_{0.3}VO_3$ (LSV), $La_{0.8}Sr_{0.2}Cr_{0.5}Mn_{0.5}O_3$ (LSCM), $La_{0.3}Sr_{0.7}TiO_3$ (LST), $La_{0.3}Sr_{0.3}Cr_{0.3}Fe_{0.7}O_3$ (LSCrF) and $La_{0.3}Ca_{0.7}Cr_{0.3}Fe_{0.7}O_3$ (LCFCr) became scope of research for their low ASR, low polarization resistance, high chemical stabilities against carbon coking and sulfur poisoning[95].

$(La_{0.75}Sr_{0.25})_{0.95}Mn0.5Cr_{0.5}O_3$ (LSCM)-electrode cells present higher performance with lower ASR compared to other fuel electrode materials using YSZ as electrolyte at 700 °C and lower polarization resistance in air and hydrogen; at 900°C: 0.29–0.59 Ω cm^2 and at 850 °C: 0.27–0.34 Ω cm^2[96] .Yang et al. developed solid oxide electrolysis cells with $(La_{0.75}Sr_{0.25})_{0.95}Mn0.5Cr_{0.5}O_3$ cathodes and LSM/YSZ anode[97]. The performance compared to Ni-based electrodes was improved in low hydrogen conditions. In another study, materials of the type $Ce_xLa_{0.75-x}Sr_{0.25}Cr_{0.5}Mn_{0.5}O_3$, x=0, 0.1, 0.25 and 0.375, were synthesized and tested as fuel electrodes under SOFC and SOEC conditions[98]. All materials were stable under neutral and wet environments, while for the cerium containing materials ($Ce_xLa_{0.75-x}Sr_{0.25}Cr_{0.5}Mn_{0.5}O_3$, x=0.1, 0.25 and 0.375) exposure to air led to the formation of CeO_2 and decomposition into a chromo-manganite phase in dry H_2 for all compounds. It was found that under dry and wet argon and wet hydrogen, these materials behave like p-type semiconductors.

The perovskite-type ABO_3 titanate composites doped with Sr are alternative materials for solid oxide fuel cell electrodes. To increase the low conductivity displayed by $Sr^{+2}Ti^{+4}O_3$, $Sr^{2+}$is partially substituted by a trivalent ion such as La^{3+}(LST)[95].A study on a similar ceramic composite cathode $La_{0.4}Sr_{0.4}TiO_{3-\delta}$ (LST)/$Ce_{0.8}Gd_{0.2}O_{2-\delta}$ (GDC) loaded with Ni nanoparticles by impregnation method showed an improve performance for direct steam electrolysis[99]. The current efficiency with the Ni-loaded cathode electrode was enhanced by 3% and 17% compared to a bare LSTO/SDC at 2 V load and 800 °C operation temperature in 3% H_2O/5% H_2/Ar and 3% H_2O/Ar, respectively. However, the major concern of this material is instability which is related to the agglomeration of the nickel particles occurred at these high operating temperatures. A perovskite titanate in an oxygen-ion conducting electrolyzer was also studied by Qin et al[100]. The doping of this perovskite with Fe, $(La_{0.2}Sr_{0.8})_{0.9}Ti_{0.9}Fe_{0.1}O_{3-\delta}$ (LSTFO), which can be reduced to in-situ grown iron nanocatalyst on substrate, was investigated as a cathode for direct steam electrolysis. According to the physicochemical analysis results, the exsolution and dissolution of the iron nanoparticles from the A-site deficient and B-sited doped titanate is a reversible redox process. LSTFO/SDC led to improved electrochemical performance and current efficiency for direct steam electrolysis. It was clearly observed that, even without H_2 reducing gas over the electrode, LSTFO performed better (175 mA cm^{-2}) compared to bare LSTO (110 mA cm^{-2}) at 2 V load and 800°C. Another study on a potential cathode steam electrolysis perovskite material $(La_{0.2}Sr_{0.8})_{0.9}Ti_{0.9}Cu_{0.1}O_{3-\delta}$ (LSTCO) with A-site deficiency and B-site excess was designed to anchor copper nanoparticles on the LSTO surface through a reversible exsolution of copper nanoparticles via a treatment in a high-temperature reducing atmosphere[101]. The LSTCO/GDC composite material revealed significant improvement in terms of performance and current efficiency for steam electrolysis. The faradaic efficiency for steam electrolysis reached a value of about 93 and 96% with and without reducing gas (H_2), respectively.

Xu et al synthesized a composite fuel electrode of Fe-$La_{0.75}Sr_{0.25}Cr_{0.5}Mn_{0.5}O_{3-\delta}$/$Ce_{0.8}Sm_{0.2}O_{2-\delta}$ (Fe-LSCM/SDC) and studied its performance under direct steam electrolysis[102]. The electrode performance was evaluated under different temperatures and oxygen partial pressures. It was found that by increasing the Fe loading of LSCM/SDC, the electrode performance was significantly improved as well as the faradaic efficiency even without H_2 reducing gas flowing. The current efficiency of Fe-LSCM/SDC electrode was enhanced by 30 and 40% compared to

pure LSCM/SDC at 800°C in 3% H_2O/5% H_2/Ar and 3% H_2O /Ar, respectively, indicating a synergetic effect of catalytic-active Fe and redox-stable LSCM. In another study on perovskite composite material LSCM-SDC, Ni particles (10% mol) were loaded by impregnation and tested under steam electrolysis with and without flowing of H_2 reducing gas[95]. The current density enhanced by loading Ni on LSCM/SDC cathodes both in 4.96% H_2/Ar/3% H_2O and 97% Ar/3% H_2O, with the enhancement being more considerable at the latter case, compared to LSCM/SDC electrode. Moreover recently, Pd and CeO_2 were added to the composite cathode of Sr-doped $LaVO_3$ (LSV) with YSZ and studied under fuel cell, steam electrolysis, co-electrolysis of H_2O and CO_2 and dry CO_2 electrolysis conditions[103]. It was concluded that at 800°C, if the fuel electrode was infiltrated with both Pd and CeO_2 in co-electrolysis conditions, steam was electrolyzed into H_2 and CO_2 was reduced to CO through the RWGS reaction. In the case of the electrode infiltrated with only CeO_2, CO_2 was electrolyzed directly into CO and this was followed by the decomposition of steam to H_2 through the RWGS.

Electrolyte for SOECs

ZrO_2 doped with 8 mol% Y_2O_3 (YSZ) is the most commonly reported composition that is used as a SOEC electrolyte[17], [19], [21], [79], [104]. This material exhibits high ionic conductivity as well as mechanical, thermal and chemical stability within the operational temperature range of 800 – 1000 °C. Other potential electrolytes are indicatively, Scandia stabilized zirconia (ScSZ), Ceria based oxides (fluorite structure) either doped with Gd_2O_3 or Sm_2O_3 and the perovskite structures $La_{1-x}Sr_xGa_{1-y}Mg_yO_{2.85}$ (LSGM) fig. 1.16. Apart from YSZ, the rest of the candidates need to be further studied and developed, so as to prove their adequacy for SOEC electrolytes. Furthermore, even though YSZ is very well studied during the development of the solid oxide fuel cells, there are still research issues to be solved in the electrolysis mode and especially under long term operation.

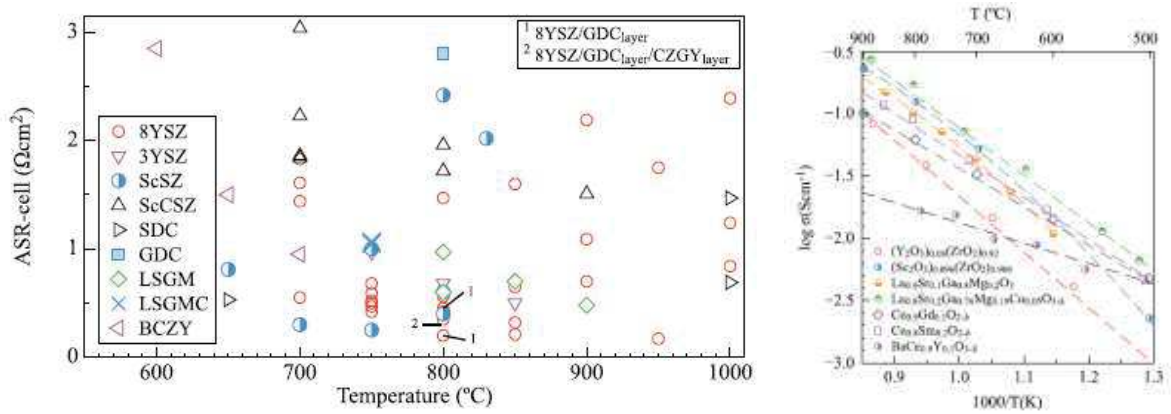

Figure 1.16. a) Area specific resistance vs. Temperature for different electrolyte materials: yttria-stabilized zirconia (8YSZ), yttria-partially-stabilized zirconia (3YSZ),scandia- stabilized zirconia(ScSZ),scandia-ceria-stabilized zirconia (ScCSZ), samaria-doped ceria (SDC), gadolinia-doped ceria (GDC), lanthanum strontium gadoliniumman- ganite (LSGM), lanthanum strontium gadolinium manganite cobaltite (LSGMC), yttria-doped bariumcerate-zirconate (BCZY), $Ce_{0.43}Zr_{0.43}Gd_{0.1}Y_{0.04}O_{2-\delta}$ (CZGY), b) Selected data on the ionic conductivity of electrolyte materials [21].

Oxygen/air electrodes for SOEC

The majority of studies are devoted to control the complex electrode morphologies through processing, or adding a secondary ion-conducting phase or by using a mixed ionic-electronic conductor (MIEC) to increase the reaction region[21]. However, the most used material is the lanthanum strontium manganite (LSM), which is the SoA oxygen/air electrode for SOFCs. LSM has a thermal expansion coefficient close to that of the YSZ electrolyte and this is an important stabilization parameter, which adds points to the mechanical integrity of the cell[17], [79]. Moreover, it exhibits low chemical interaction with YSZ, which prolongs the components` lifetime. LSM is an excellent electronic conductor (its electronic conductivity is ~200 S cm^{-1} at 800 C), but with a negligible oxygen ionic conductivity (e.g., 10^{-16} cm^2 s^{-1} at 700 C)[38]. Thus, in order to extend or improve the TPB size one approach is to create composites of LSM and electrolyte materials, or the usage of different mixed ion-electron conducting electrodes such as: lanthanum strontium ferrite (LSF), lanthanum strontium cobaltite (LSCo), lanthanum strontium copper ferrite (LSCuF) and lanthanum strontium cobalt ferrite (LSCoF), where the stoichiometry

of these materials plays a vital role in the electrochemical activity of the air electrode[17], [79], [105].

1.2.5. Preparation of SOC electrodes by infiltration method

Development of innovative electrode materials with excellent performance and stability is a main research goal for solid oxide electrolysis cells (SOECs) and solid oxide fuel cells (SOFCs). Either by modifying the state of-the-art Ni based anodes, or through exploring alternative metal cermet or perovskite based materials, wet impregnation/infiltration is shown to be one of the most effective approaches for both cell fabrication and performance optimization fig. 1.17 [38]. The optimization of traditional nickel based anodes by replacement of nickel by other inert metal or ceramic species, and some metal supported designs with impregnated catalyst are all presented and discussed, mainly focusing on the cell performance, redox and thermal stability, long-term reliability, carbon and sulfur tolerance of the anodes[38], [104], [106]–[114].

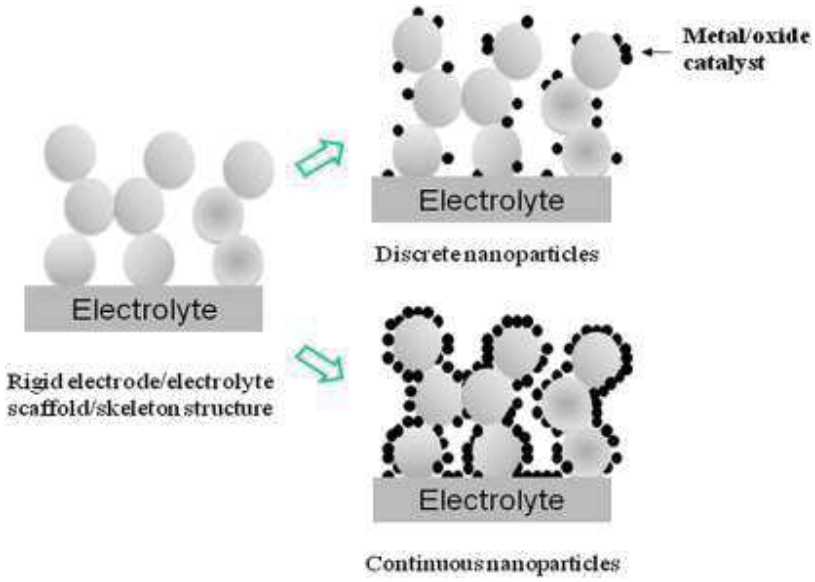

Figure 1.17. Scheme of the infiltrated nano-structured electrodes on pre-sintered porous electrode or electrolyte scaffold/ skeleton[38].

The idea is based on infiltrating the porous electrodes with precursor solutions after the sintering step and the formation of nanoparticles by simple heat treatment in air. The nanoparticles increase the triple phase boundary (TPB) length and catalytic activity of the electrode. In order to increase the mass load of the infiltration several loading steps are performed by micro pipette or

by sample immersion in vacuum. Data from various authors provide a wide range of mass loading depending on the infiltrated particles and the electrode composite. Fig. 1.18 shows schematically a typical synthesis route for the deposition of nano-sized particles into a pre-fired electrode or electrolyte scaffold or framework via infiltration of metal salt or nanoparticle suspension solutions. For example, wet infiltration of CeO_2 and Gd-doped CeO_2 (GDC) into pre-fired LSM cathode can be carried out by simply placing a drop of a $Ce(NO_3)_3$ or mixed $Gd(NO_3)_3$ and $Ce(NO_3)_3(Gd_{0.2}Ce_{0.8}(NO_3)x)$ solution on top of the coating which infiltrates the cathode layer by capillary force; the infiltration process is further facilitated under vacuum[38]. Then the infiltrated LSM is heated at 500-800 °C to decompose the metal salt solution, forming CeO_2 or GDC nanoparticle phase. The phase formation temperature of the catalytic phase (i.e, CeO_2 or GDC) is much lower than the processing temperature of the standard LSM (i.e., 1150 °C in this case). The significantly reduced phase formation temperature avoids the grain growth, resulting in the deposition of nano-sized GDC particles on the surface of grains of LSM scaffold.

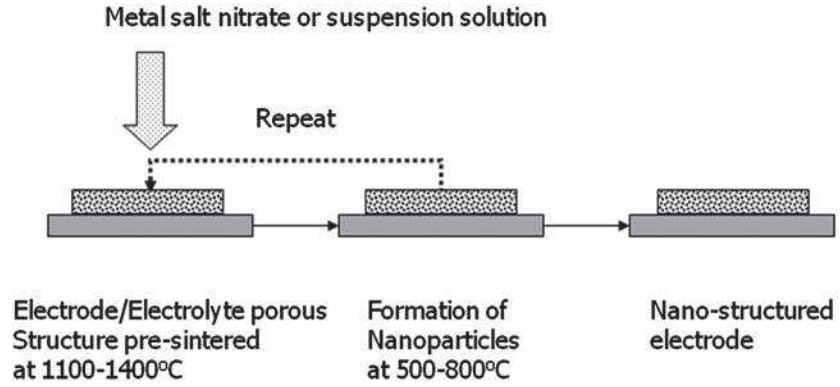

Figure 1.18. Typical process for the infiltration of metal salt nitrate solution or nanoparticle suspension into pre-sintered electrode or electrolyte porous structure[39].

Cu-based anodes were utilized for the direct oxidation of CH_4 in SOFC instead of Ni-based anodes[115]. Cu melting temperature is 1083 °C, significantly lower than 1453 °C for Ni. Consequently, Cu-based cermet anodes cannot be produced using the same methods applied for Ni-based cermet anodes. Gorte. et Vohs developed a method to impregnate $Cu(NO_3)_2$ solution into porous YSZ scaffold prepared on a dense YSZ electrolyte layer, followed by calcinations to decompose the nitrate and form the oxide[116]. As shown in fig. 1.19 both the dense electrolyte and the porous scaffold can be fabricated by conventional tape casting techniques. Other

components such as ceria, perovskite oxides and precious metal catalysts can be added via infiltration processes[39].

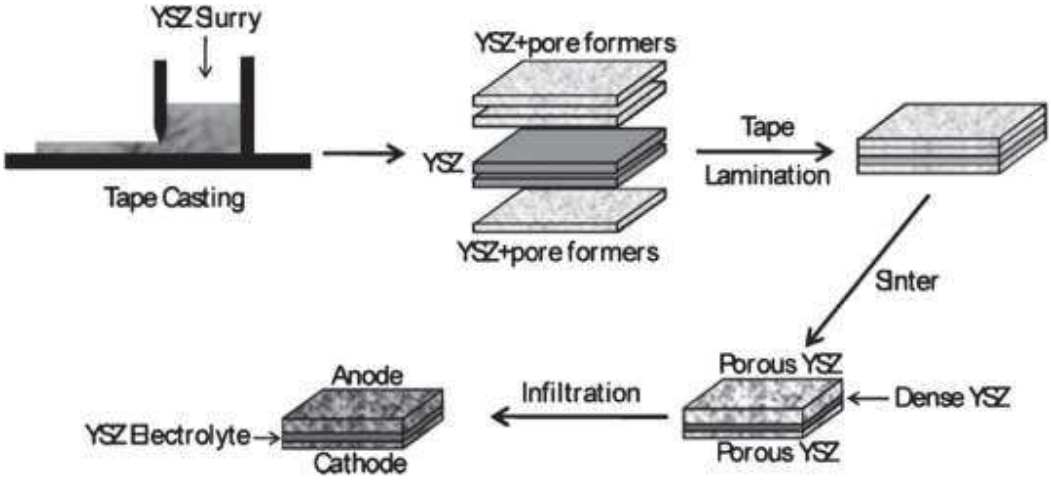

Figure 1.19. Diagram showing the steps used to fabricate an SOFC in which the electrodes are produced by infiltration of active components into a porous YSZ scaffold[40].

Yuri Choi et al. fabricated a novel cathode by infiltration method with a better wetability assisted using layer by layer (LbL) assembly process of polyelectrolytes. LbL assembly has been widely used as a versatile method for fabricating multilayer thin films onto solid surfaces with controlled structure and composition. Preparation of the electrode with LbL-assisted infiltration fig. 1.20 leads to a 6.5-fold reduction in the electrode fabrication time while providing uniform and small formation of $Pr_{0.7}Sr_{0.3}CoO_{3-\delta}$ (PSC) particles on the electrode. By this method the surface area increased by 24.5% which resulted in increasing of the number of active sites of the prepared electrode and exhibits superior electrochemical performance (up to 36.1%) while preserving the electrical properties of the electrode. Because of its versatility and tenability, the LbL-assisted infiltration process may become a new route for fabrication of composite electrodes for other energy storage and conversion devices.

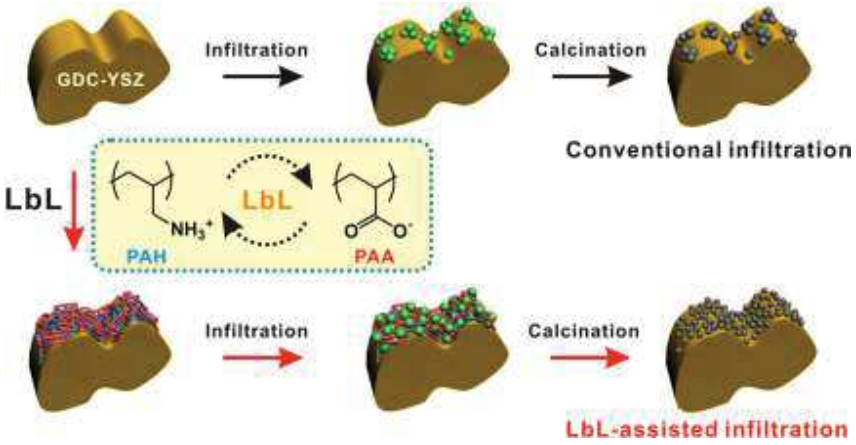

Figure 1.20. Schematic representation of (top) conventional infiltration method and (bottom) layer-by-layer (LbL) assembled polyelectrolyte multilayer-assisted infiltration for a SOFC electrode.

Inkjet printing is an infiltration method which utilizes less processing steps, without the necessity for employing vacuum, while at the same time one can achieve deep penetration of the ink into the thick anode supports with uniforms lateral delivery of the ink with nanolitre precision[107]. Mitchell Williams et al. reported that infiltration of CGO into a composite NiO/CGO symmetric cell infiltrated using 20 printing cycles of the propionic acid ink demonstrated a lower polarisation resistance fig. 1.21 than the reference cell without any infiltration. The smaller polarisation resistance arc for the infiltrated sample indicates that the infiltrated CGO nanoparticles effectively extend the triple phase boundary (TPB).

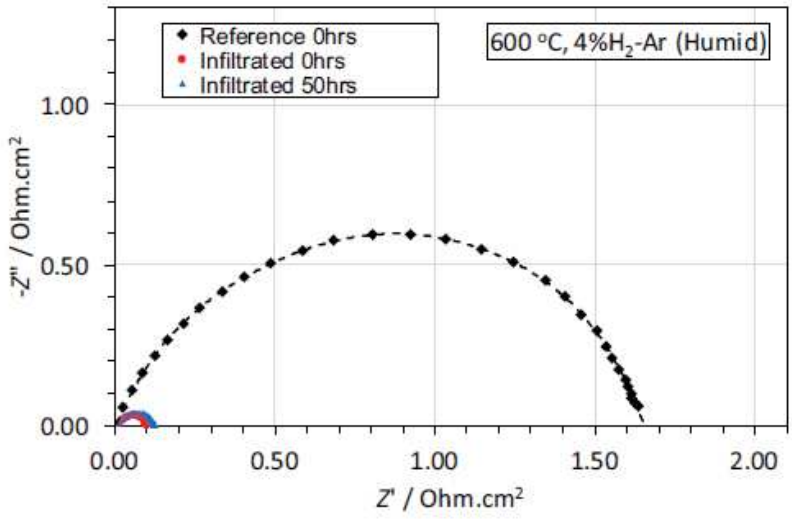

Figure 1.21. Nyquist plots for symmetric anode cells tested at 600 °C. The size of the arc indicates the magnitude of the polarisation losses. The infiltrated cell showed much lower polarisation losses than the reference both before and after 50 h aging.

In a conclusion, infiltrated electrodes show high long term durability under high temperature steam electrolysis compared with the conventional electrodes.

1.3. Operando Spectroscopic studies of SOEC

High temperature water electrolysis is a complex process, hence studying the reaction mechanism, the reaction kinetics, the redox stability, and the surface electrocataysis requires the utilization of high surface sensitive spectroscopic techniques such as surface enhanced Raman studies, FTIR, and X-ray Photoelectron and Near-edge X-ray Absorption Fine Structure Spectroscopies; which will be discussed in the next section.

1.3.1. Raman studies

The redox properties of both Ni/YSZ (Nickel Yttria Stabilized zirconia) and Ni/GDC or Ni/CGO (Nickel gadolinium doped ceria) composite cermets are of main importance for the operation of solid oxide electrochemical cells. Although these systems have been widely studied, a full comprehension of the reaction dynamics at the interface of these materials is lacking. Raman spectroscopy is an ideal tool for the in situ study of chemical processes occurring at active surfaces[41], [94], [117]–[127]. Specifically, in situ Raman spectroscopic monitoring of the redox cycle was used to investigate water dissociation on Ni/YSZ and Ni/GDC surfaces [41]. NiO reduction is a key issue for both SOEC and SOFC systems, where the reduction and oxidation (redox) tolerance of Ni-based electrodes is of important practical consideration. Such processes have been studied in detail for SOFC anodes, the results of which are directly applicable to SOECs.

Robert et al.[41] studied the redox process in pure GDC and NiO when exposed to wet and dry hydrogen and then compared them to the cermet behavior in order to understand the redox mechanism. As shown in fig. 1.22A in dry hydrogen, GDC reduces relatively rapidly via a series of intermediate phases, while NiO reduces via a single-step process. In wet reducing atmospheres however Fig. 1.22A, the oxidation state of pure GDC is initially stabilized due to the dissociation of water by reduced Ce(III) and subsequent incorporation of oxygen into the

structure. In the reduction process involving the composite cermet shown in Fig. 1.22B, the close proximity of the NiO improves the efficiency and speed of the composite reduction process. Although NiO is already incorporated into working cells, these observations suggest direct routes to further improve cell performance.

The reduction process is greatly enhanced due to the presence of NiO/Ni within the NiO-GDC cermets compared to the pure GDC. In humidified reducing atmospheres, the oxidation state of the pure GDC surface is strongly stabilized due to the dissociation of water by reduced Ce(III) followed by the subsequent incorporation of the released oxygen into the GDC. However, significant reduction of GDC within cermet composites subjected to humidified atmospheres was observed, although this is followed by the swift GDC re-oxidation due to later water dissociation and oxygen incorporation. NiO reduction is observed to proceed through a single step process that is unaffected by the water vapor content or the presence of GDC. This allowed the activation energy for the surface specific reduction of NiO to be extracted from the time-dependent Raman data obtained at the different temperatures investigated. This activation energy was found to be 35.9±4.6 $kJmol^{-1}$, which is consistent with previously reported values. The complexity of the interactions involved during surface reduction within operational systems as revealed here points to a number of strategies to optimize fuel cell performance[41].

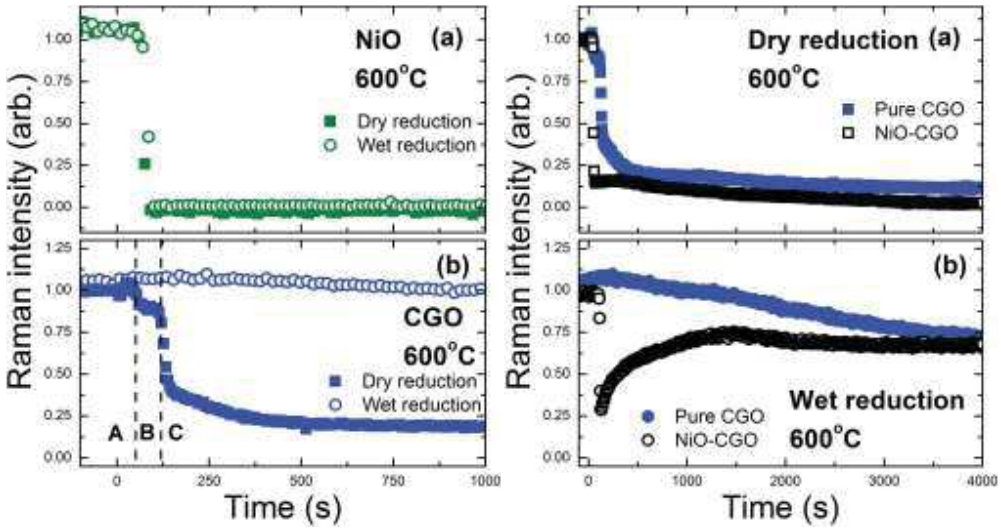

Figure 1.22. A) Normalized intensities of the a) NiO and b) CGO Raman peaks monitored as a function of time from pure NiO and CGO samples exposed to dry and wet 75% N_2:25% H_2 flowing at 100 cm^3 m^{-1} . The reduction of NiO is unchanged by the presence of water in the

reduction gas, while the CGO appears to be strongly stabilized B) Normalized intensities of the CGO peak monitored from pure and NiO-CGO composites under a) dry and b) wet 75% N_2:25% H_2 flowing at 100 cm^3 min^{-1} over long timescales. CGO within the cermet appears to reduce more rapidly, and without intermediate phases when exposed to dry H_2. It is also more strongly reduced. When exposed to wet H_2, the CGO within the composite is reduced relatively quickly before recovering on longer timescales, tending to the same oxidation state observed for pure CGO[41].

1.3.2. FTIR

Infrared absorption spectroscopy (IR) is one of the most powerful spectroscopic techniques available for the characterization of heterogeneous catalytic systems, while several variations of the technique exist to fit the requirements of different systems as shown in fig. 1.23 [42]. Electrochemical in-situ FTIR spectroscopy (in-situ FTIRS) can provide real-time information about the chemical nature of adsorbates and the solution species involved in electrochemical reactions, helping to elucidate the mechanism of complex electrocatalytic processes [120], [127]–[129]. Co-electrolysis of carbon dioxide requires detailed understanding of the complex reactions, transport processes and degradation mechanisms occurring during operation in SOEC. In order to fully understand and characterize co-electrolysis, in situ monitoring of the reactants, products and SOC is necessary[43]. Infrared absorption spectroscopy is particularly suited for this application because most molecular vibrational modes fall into the energy range of mid-infrared light (2.5–50 μm, 4000–200 cm^{-1}). However, operando FTIR studies in transmission mode are difficult and not representative of working conditions due to the requirement of transparent electrodes for cell polarization. An alternative approach is to use diffuse reflectance infrared Fourier transform spectroscopy (DRIFTS) as shown in fig. 1.24, another technique commonly employed in the catalysis community. The experimental configuration has the advantage of allowing the typical powder-basket arrangement to be replaced by a small solid oxide cell operated in a scenario very similar to most lab-scale electrochemical tests. DRIFTS is ideal for in situ monitoring of co-electrolysis as both gaseous and adsorbed CO and CO_2 species can be detected, however up to now it is very rarely used for this purpose.

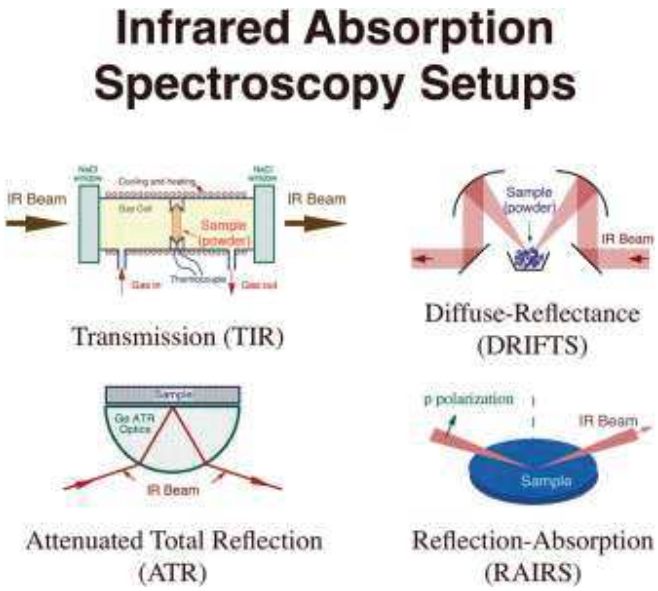

Figure 1.23. Common setups used for the characterization of catalytic samples using infrared absorption spectroscopy. Top, left: transmission (TIR) mode, where the IR beam is directed through a self-sustained sample placed inside the catalytic reactor and collected after exiting for analysis. Top, right: diffuse reflectance (DRIFTS) mode, where powder samples are radiated by a focused IR beam and the scattered light collected using a high-area parabolic mirror. Bottom, left: attenuated total reflection (ATR) mode, where the sample is placed on the outside of the flat surface of the prism used to direct the beam. Bottom, right: reflection–absorption (RAIRS) mode, where the beam is bounced from a flat reflective surface before collection[42].

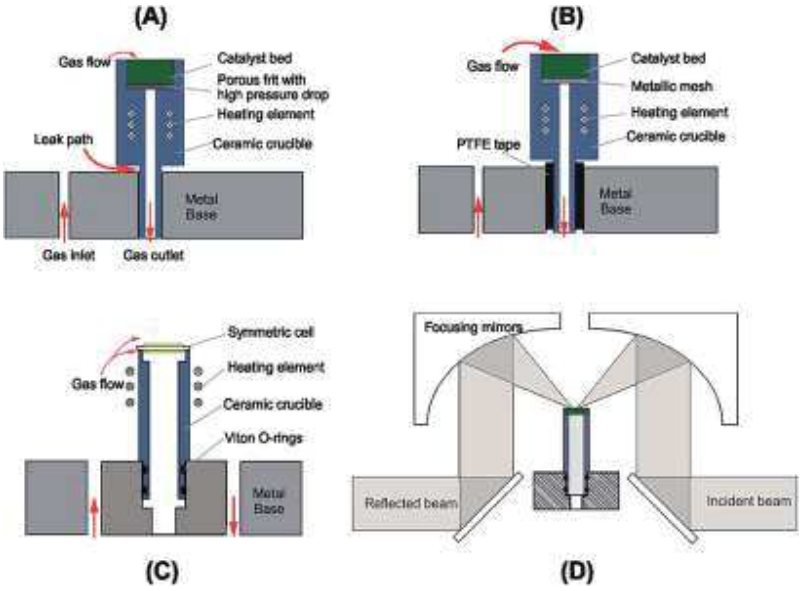

Figure 1.24. Schematic drawing the evolution of the base unit design and the optical path through the DRIFTS apparatus. (A) As purchased Spectra-Tech configuration. (B) Modification to reduce gas leak in the chamber. (C) SOC operation configuration. (D) Full schematic view of DRIFTS rig showing mirror assembly and beam path[43].

There are very few FTIR studies to examine SOECs and most focus mainly on SOFCs operation. Murai et al.[130] used IR emission spectroscopy to study the oxygen electrode material in SOCs, and simplified the experiment by using symmetric Pt/YSZ/Pt cells to study the oxygen reduction reaction. It was found that the electrode microstructure and silica contamination caused significant variation in both electrochemical performance and spectroscopic response. In general, very few operando IR studies exist to examine the fuel electrode in detail, with very few exceptions like the work of Kirtley et al[131].

1.3.3. X-ray Photoelectron and Near-edge X-ray Absorption Fine Structure Spectroscopies

X-ray photoelectron spectroscopy (XPS) is a surface-sensitive quantitative spectroscopic technique that measures the elemental composition and the chemical state of the outer (1-10) nm of a solid surface[132]. As shown in fig. 1.25 when the sample surface is irradiated with X-ray photons of energy hν, these photons interact with the electrons of the sample atoms and consequently photoelectrons are emitted with specific kinetic energy (KE) E_{kin}; which depends on their binding energy (BE) E_{bin} and the work function φ of the sample (which in the calculations is replaced by the work function of the analyzer) [132] as shown in (eq.18). X-ray photoelectron spectra are displayed as plots of the number of photoelectrons (intensity) as a function of their binding energy or, alternatively, their kinetic energy fig. 1.25. Based on these spectra both qualitative and quantitative information of the surface can be provided.

$$E_{kin} = h\nu - E_{bin} - \varphi \quad \text{(Eq.18)}$$

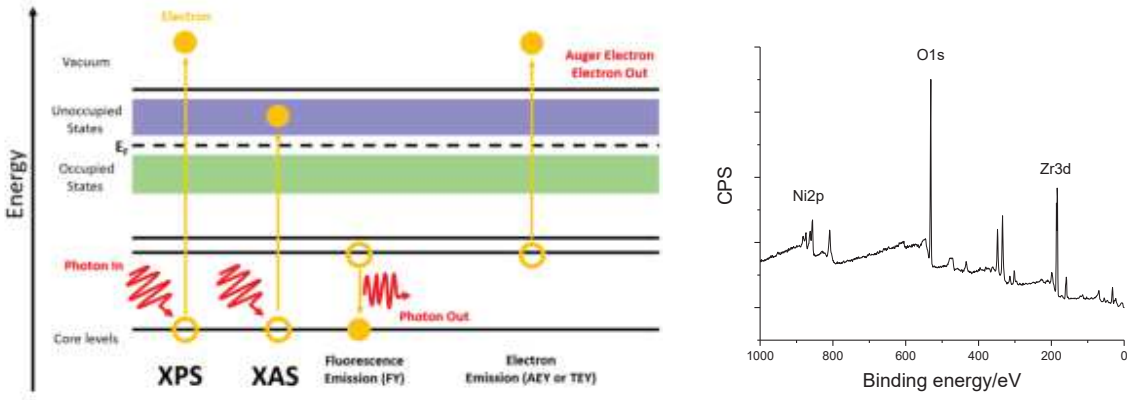

Figure 1.25. Schematic of the processes occurring during photoemission and absorption spectroscopies[44]. Survey spectrum for Ni-YSZ cathode electrode after heating under 0.5 mbar O_2 to remove carbon.

Near edge X-ray absorption fine structure (NEXAFS) determines the valance state and local-symmetry of an element and it is not only element specific but also sensitive to its local coordination environment [45]. NEXAFS should not be confused with the so called extended X-ray absorption fine structure (EXAFS) method, which is a technique that provides local structural information of the absorbing element by measuring X-ray absorption in the energy region corresponding to excitation of core electrons of the element[133]. The NEXAFS spectrum exhibits strong and distinctive features in the energy region just below and up to about 30 eV above the absorption edge[134], [135]. When both of these techniques are combined the method is usually called as X-ray absorption fine structure (XAFS) and can provide a complete picture of electronic structure of a system. One should note that for EXAFS and XAFS hard X-rays are used (so mainly the K-edge is studied), while for the NEXAFS spectra shown in this work we excited the Ni L and Ce M edges by using soft X-rays. The reason of high surface sensitivity of NEXAFS technique is the relatively low kinetic energies of the electrons and the corresponding mean free path in the matter, similar to XPS. The surface sensitivity of this method can be further enhanced by recording electrons with particular kinetic energy, typically Auger electrons. As an example, the analysis of the O K edge spectra (NEXAFS) in combination with theoretical calculations of various Co-Ce compounds is given. This analysis can provide information aboutthe oxygen sites of different binding configuration and environments[136].Fig. 1.26 shows the absorption spectra at the oxygen (O) K-edge for Co doped CeO_2 nanoparticles along with the

reference spectrum of Ce_2O_3. Three main features marked as $a_1(4f^0)$, $b_1(5d\text{-}e_g$, and $c_1(5d\text{-}t_{2g})$ can be seen at 530.0, 532.7 and 537.0 eV for pure and Co doped CeO_2 nanoparticles, and broader and less intensive features were also observed near 543.0 eV. Consequently, by comparing the O K-edge spectra of Co doped CeO_2 with CeO_2 and Ce_2O_3 , it is observed that the spectral features of doped samples resemble with those of CeO_2, which reflects that most of the Ce ions are in +4 state[45].

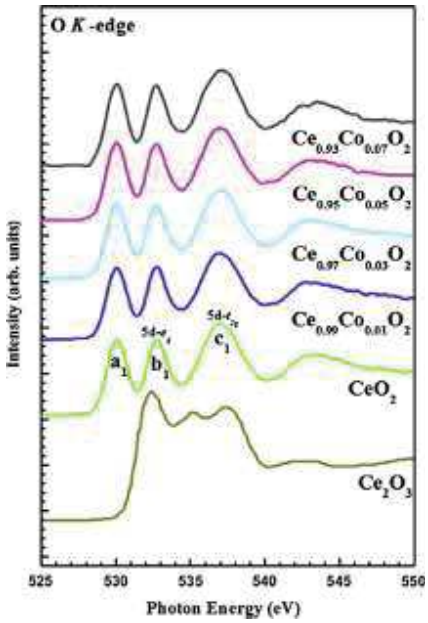

Figure 1.26. O K-edge spectra of $Ce_{1-x}Co_xO_2(0 \leq X \leq 0.07)$ nanoparticles along with reference spectrum of Ce_2O_3[45].

Current studies in solid oxide fuel/electrolysis cells (SOFC/SOEC) are mainly focused on Ni-cermets based electrodes and perovskite-type electrode materials such as $La_{0.6}Sr_{0.4}CoO_{3-\delta}$(LSC), $La_{0.6}Sr_{0.4}FeO_{3-\delta}$(LSF), and $SrTi_{0.7}Fe_{0.3}O_{3-\delta}$ (STF).The chemical environment of surface ions is different from the bulk and therefore ions of an oxide may exhibit modified chemical surface states (e.g., different oxidation number or neighboring atoms). Still those that do not necessarily contribute to the electrochemical surface reaction have to be distinguished from the reacting or catalyzing species. While the bulk defect chemistry of many mixed conducting oxides is quite well understood, little is known about the surface chemistry and reaction mechanisms of oxygen exchange on polarized mixed conducting electrodes[46], [52], [137], [138]. This knowledge may help to develop more effective strategies for electrode optimization and to establish a firm basis

of electrode reactions in solid state electrochemistry. In-situ techniques are of high relevance in addressing these topics[16], [131], [139]–[142]. For a mechanistic interpretation of oxygen exchange kinetics also the effect of electrochemical polarization and atmosphere on the binding energy and concentration of surface species needs to be investigated. Since in situ XPS (typically called Near ambient pressure XPS, NAP-XPS) and NEXAFS are key methods used in this thesis a mini review of their previous application over SOEC electrodes is given below.

Application of NAP-XPS and NEXAFS in studies of perovskite electrodes

Fleig et al.[46] investigated the response of surface species of (LSC), (LSF), and (STF) peroveskite-type electrode under different gases atmospheres. XPS spectra measured on LSC, STF, and LSF under polarization in 0.5 mbar of O_2 are shown in Fig. 1.27. Except for the Co 2p peak, all signals show significant energy shifts. The applied bias causes a very subtle change in the Co 2p satellite features between 785 and 790 eV, which can be used as an indication for the oxidation state of cobalt. Additionally, there is a very weak effect of polarization on the chemical states of the Fe 2p peaks, indicating no chemical changes. The different response of LSC compared to STF and LSF is most probably related to its metal-like electronic structure and the resulting fundamentally different relation between oxygen nonstoichiometry, Fermi level and oxygen partial pressure in the two electrodes.

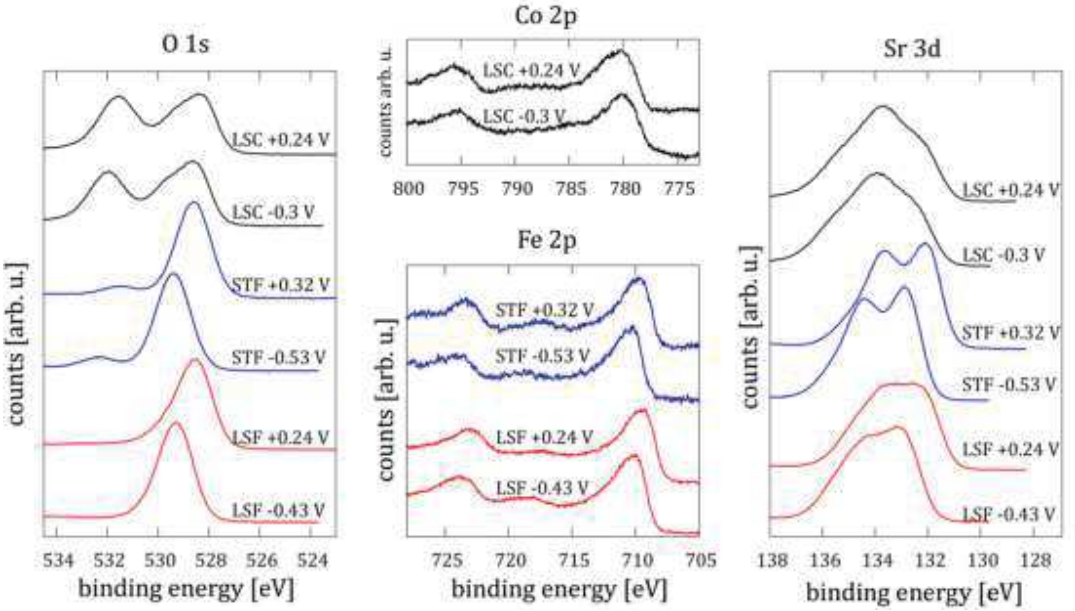

Figure 1.27. O 1s, Fe 2p, Co 2p, and Sr 3d core level XPS spectra of LSC (black), STF (blue), and LSF (red) thin films under polarization (indicated voltage)[46].

Under polarization in 0.5 mbar of H_2/H_2O atmosphere, Fe shows significant chemical changes: at open-circuit voltage, the satellite structure indicates mixed Fe^{2+}/Fe^{3+} valence near the surface. Anodic bias increases the amount of Fe^{3+} and for both LSF and STF no Fe^{2+} satellite features are present when $\eta \geq +280$ mV (fig. 1.28a,b). On the other hand, cathodic bias increases the amount of $Fe^{2+}$and even leads to the formation of Fe^0. The formation of metallic iron is accompanied by a strong decrease of the total iron signal intensity (fig. 1.28a, b), and a distinct increase of the water splitting activity, as seen by the strongly asymmetric current−voltage characteristics (fig. 1.28e). There the formation and re-oxidation of metallic iron is highly reversible. It occurs at overpotential of −20mV and the Fe^0 peak vanishes at open circuit potential. Also lowering the chemical potential of oxygen in the atmosphere by increasing the hydrogen content leads to formation of Fe^0 (lowest spectra in fig. 1.28b, d). Despite equal polarization, the electrode current is smaller which is due to the presence of metallic Fe (open circles in fig. 1.28e). This can be interpreted as additional evidence that the strong nonlinearity of the current−voltage characteristics is indeed related to the presence of Fe^0 on the surface.

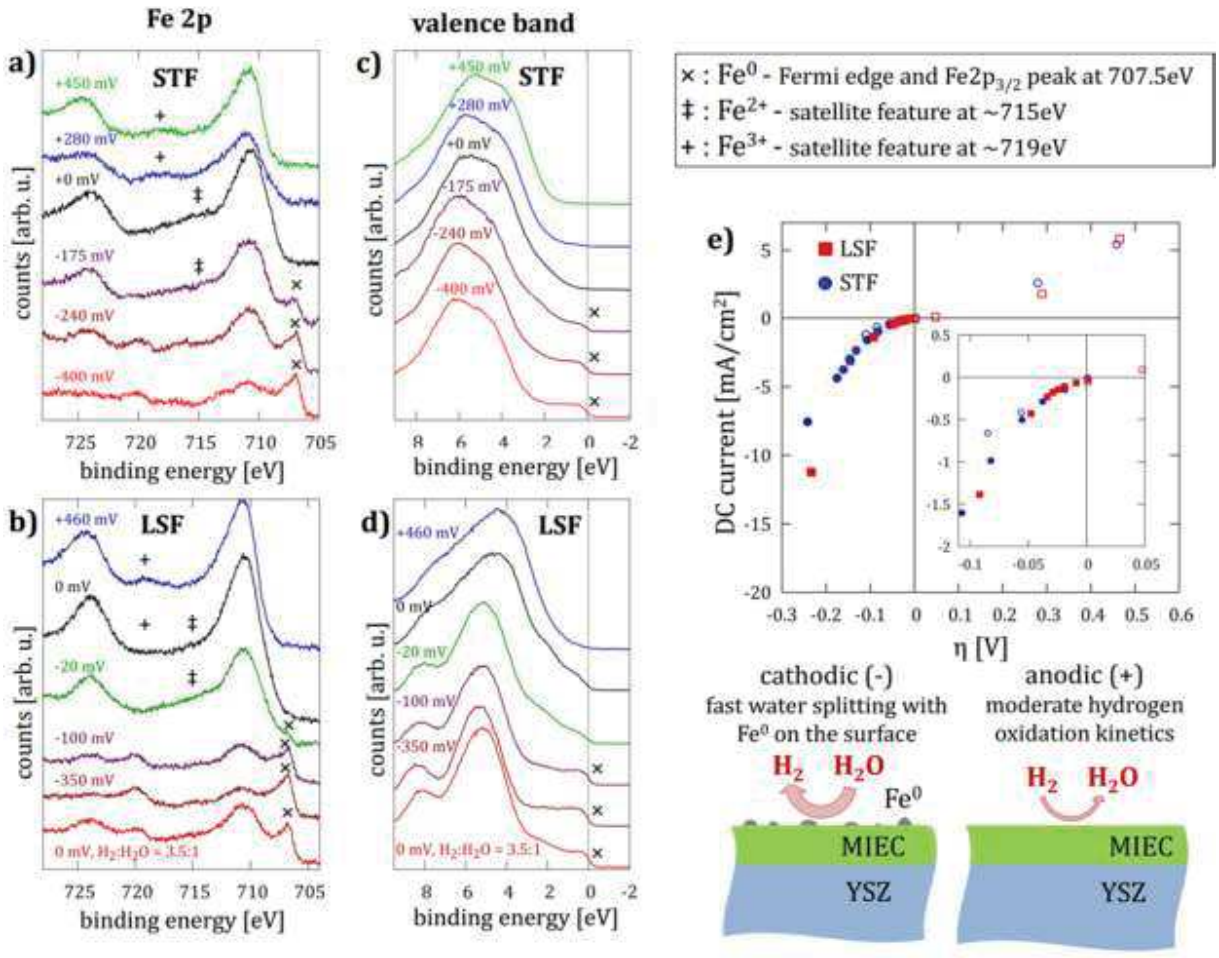

Figure 1.28. Valence band and Fe 2p XPS spectra of STF (a, c) and LSF (b, d) polarized by different overpotentials in H_2/H_2O atmosphere. Each spectrum is plotted with the same scale. The applied overpotentials are indicated for each spectrum.(e) DC-characteristics of LSF (red squares) and STF (blue circles)[46].

Klötzer et al.[47] investigated the surface chemistry and water splitting kinetics of the perovskite-type mixed conductor $La_{0.6}Sr_{0.4}FeO_{3-d}$(LSF) under electrochemical polarization in humid H_2 atmospheres by NAP-XPS. The measured I-V curves showed in fig. 1.29 for LSF working electrode. Three selected Fe2p spectra, corresponding to three different polarization states, reveal that a metallic iron species already evolves at relatively low cathodic overpotentials. Upon formation of this Fe^0 species, the electrochemical water splitting activity of the LSF surface strongly increased, leading to a highly asymmetric current–voltage curve, which does not follow an exponential function (for example, the Butler–Volmer equation) with

electrochemically meaningful parameters. This indicates a mechanistic change of the reaction kinetics at the LSF surface. The cathodically formed Fe^0 was quickly re-oxidized to mixed Fe^{2+}/Fe^{3+} valence after removing the polarization (within the time between two simultaneous XPS/impedance measurements of about 200 to 600 s). Accordingly, the IV curve was highly reversible.

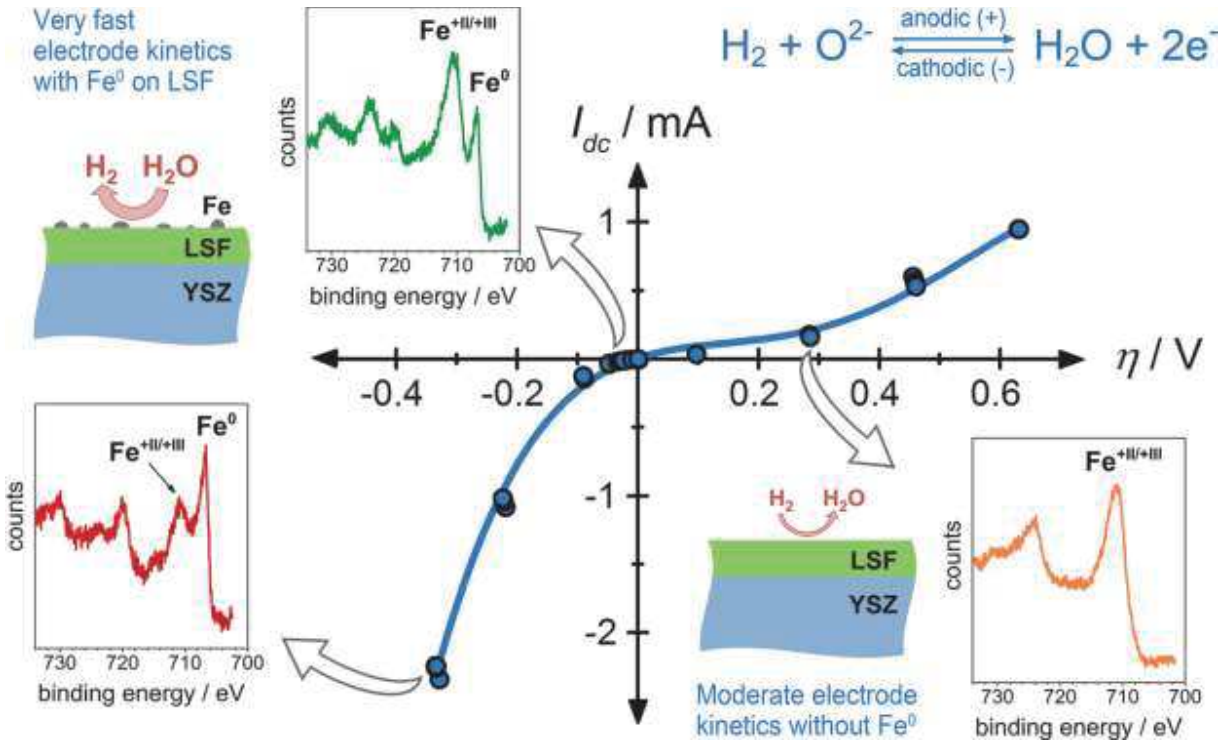

Figure 1.29. Current–overpotential curve (I_{dc} vs.) of LSF in a humid reducing atmosphere (0.25 mbar H_2+0.25 mbar H_2O).The reaction proceeding on the surface of the LSF working electrode is given on the top right. For selected points of the curve (indicated by arrows), the Fe2p XPS spectra are shown as insets. The sketches indicate the situation for the LSF surface and the resulting reactivity, respectively[47].

Zafeiratos et coworkers [137] compared the surface reactivity of the two most commonly used types of SOC electrodes, (Ni/YSZ) cermet and $La_{0.75}Sr_{0.25}Cr_{0.9}Fe_{0.1}O_3$ perovskite at intermediate temperature and at gas-phase environments relevant for both SOC modes. In situ synchrotron-based NAP-XPS and NEXAFS experiments, assisted by theoretical spectral simulations and combined with microscopy and electrochemical measurements, showed that the surface of both electrode types readjusts fast to the reactive gas atmosphere and their surface composition is

notably modified. In the case of Ni/YSZ, this is followed by evident changes in the oxidation state of nickel, while for $La_{0.75}Sr_{0.25}Cr_{0.9}Fe_{0.1}O_3$, a fine adjustment of the Cr valence and strong Sr segregation is observed. An important difference between the two electrodes is their capacity to maintain adsorbed hydroxyl groups on their surface, which is expected to be critical for the electrocatalytic properties of the materials.

Application of NAP-XPS and NEXAFS in studies of Ni-based cermet electrodes

El Gabaly et al.[48], [143]–[146] studied the local electrical potentials in Ni/YSZ/Pt solid-oxide electrochemical cell in 150 mTorr H_2O + 150 mTorr H_2 at about 700 °C using operando NAP-XPS. The overpotentials at the Ni/YSZ interface and YSZ/Pt interface were measured from the kinetic energy shifts of the Zr XPS peak with cell bias. During the SOEC operation, the Pt, Ni, and YSZ surfaces underwent no chemical changes, as revealed through the XPS spectra. Therefore, the peak shifts with cell bias have no contributions from chemical shifts[146]. The same group also studied the oxidation of Ni electrodes in 300 mTorr of water and 15 mTorr of hydrogen (20 : 1 ratio) atmosphere at 700 °C, as it is one of the leading cause of degradation by NAP-XPS [48]. Three different stages of Ni oxidation in the model SOFC were investigated. The cell was positively biased in order to perform electrochemical oxidation. When V_{bias}<0.4V the Ni surface remains metallic during hydrogen oxidation, when V_{bias}> 0.4 V, the Ni at the Ni/YSZ interface undergoes a phase transition to NiO, and finally when V_{bias}> 1.0 V, the surface of the Ni electrode totally oxidizes. The Ni $2p_{3/2}$ peaks were deconvoluted into components as shown in fig. 1.30 pointing to an almost completely oxidized Ni electrode. It was concluded that NiOOH is the only oxide phase coexisting with the metallic Ni phase. More specifically, the electrode is 9 ± 2% Ni metal and 91 ± 2% NiOOH.

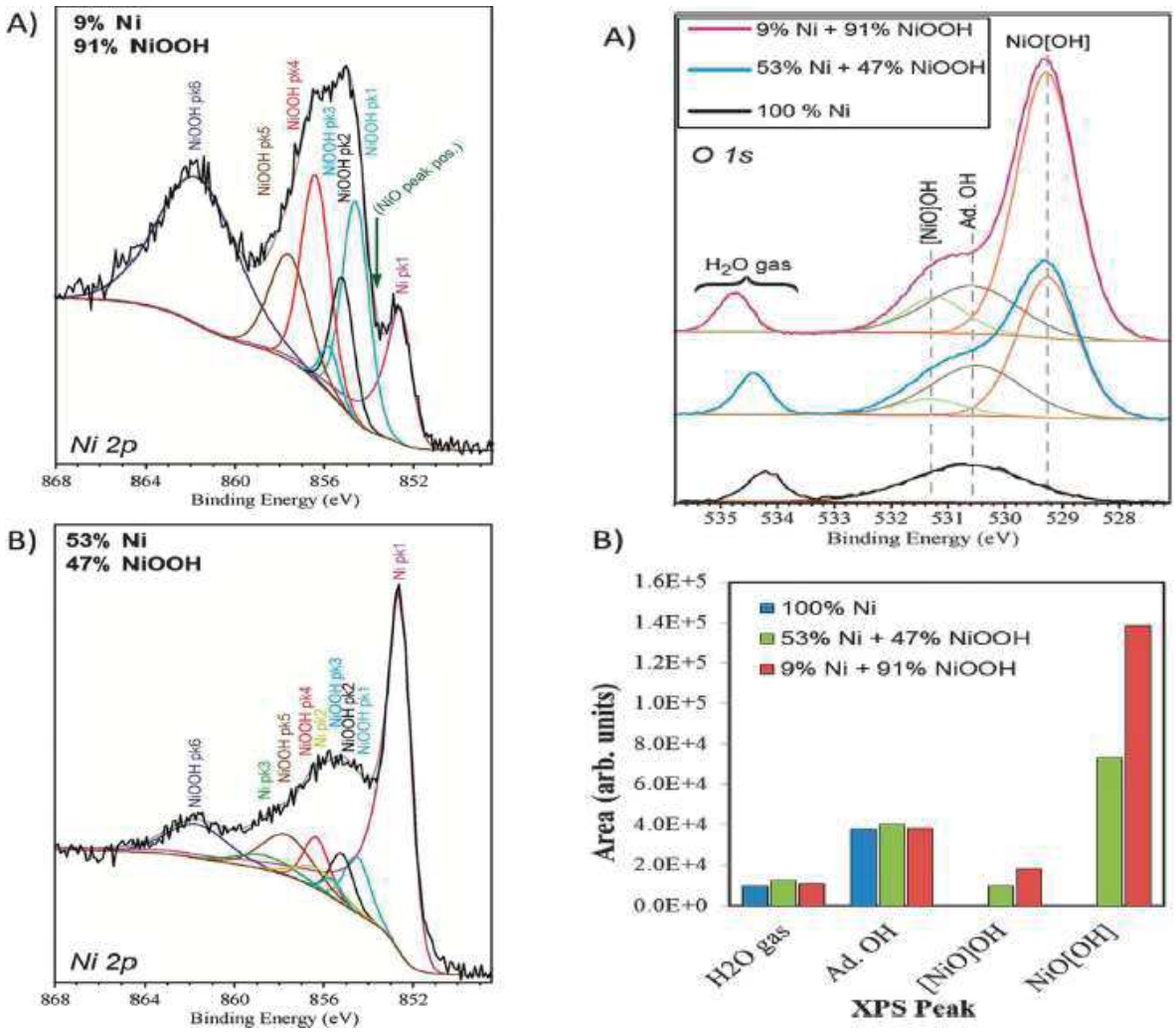

Figure 1.30. (*left*) Operando Ni $2p_{3/2}$ XPS spectra and fitted synthetic deconvolutions of very oxidized (A) and partially oxidized (B) Ni electrodes. Of the three peaks of metallic Ni only the main metallic peak (Ni pk1) could be resolved in (A)[48]. (*right*) Operando O 1s XPS spectra acquired from Ni electrode at three different oxidation conditions: no oxidation (black), partially oxidized (blue), and very oxidized (magenta). [NiO]OH and NiO[OH] represent the oxygen components present in NiOOH and do not appear in the metallic Ni. (B) Bar chart comparing the areas of the synthetic peaks shown in (A)[48].

Additional information comes from the O 1s XPS peak during Ni oxidation. Fig. 1.30 shows the O 1s spectra corresponding to the three different conditions for which Ni 2p spectra were presented as partially and nearly completely oxidized. The bottom spectrum was taken concurrent to the Ni metal at zero bias and characterizes the oxygen species, while the peak at

530.5 eV results from adsorbed hydroxyl groups. The peak at 534 to 535 eV is from the gas-phase water over the electrode. The surfaces of both semi oxidized and totally oxidized Ni (fig. 1.30) show two additional peaks: the lattice hydroxide component at 531.3 eV (labeled [NiO]OH) and the lattice O^{2-} component at 529.3 eV (labeled NiO[OH]). These two peaks correspond to the two differently bonded oxygen species existing in NiOOH. In contrast, the peaks at 529.3 and 531.3 eV appear and completely disappear reversibly with oxidation/reduction.

Eichhorn et al.[7], [49], [147] studied the mechanism of electrocatalytic water splitting ($H_2O + 2e^- \rightarrow H_2 + O^{2-}$) and electro oxidation of hydrogen ($H_2 + O^{2-} \rightarrow H_2O + 2e^-$) at 700 °C in 0.5 Torr of H_2/H_2O on a CeO_{2-x}/YSZ/Pt solid oxide electrochemical cell using NAP-XPS. The measurements were taken when the cell was negatively biased (hydrogen electro-oxidation on ceria and water electrolysis at Pt), positively biased and at OCP. The electrochemically active regions on ceria are defined by large surface potential drop and shift in the equilibrium Ce^{3+}/Ce^{4+} ratios. In the inactive regions of the ceria electrode, the absence of a net current leaves the ceria redox states and hydroxyl adsorbate concentrations in their equilibrium conditions regardless of the applied potential. At +1.2 V applied bias, the OH^-/O^{2-} concentration ratio shows no change in the active region relative to the equilibrium conditions at OCV. However, the large increase of surface Ce^{3+} ions in the active region (fig. 1.31) significantly reduces the magnitude of the dipole moment between the surface OH^- adsorbate and the electrode. The buildup of Ce^{3+} ions and associated surface vacancies reduces the Ce−OH bond polarization relative to the Ce^{4+} dominated surface. At −1.2 V applied bias (H_2electro-oxidation on ceria), the Ce^{3+}/Ce^{4+} ceria surface ratios slightly change (fig. 1.37a) and a small but significant increase in the OH^- adsorbate concentration in the active region with an accompanying decrease in surface O^{2-} concentration is observed.

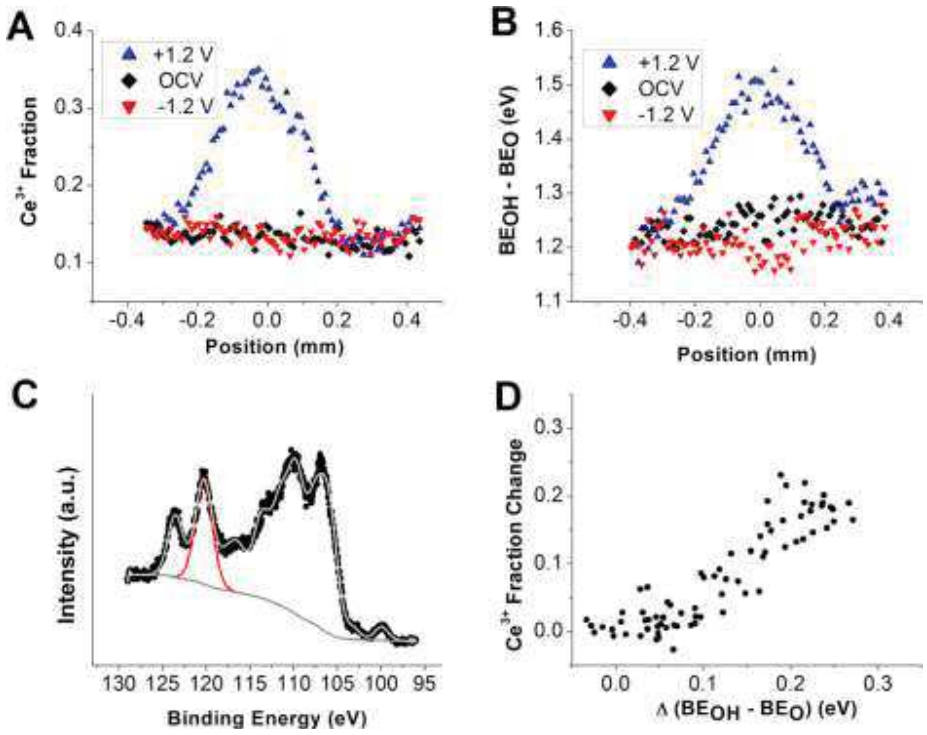

Figure 1.31. (A) Spatially resolved cerium redox changes (Ce^{3+} fraction) calculated from fitted Ce 4d spectra under OCV and ±1.2 V applied biases. (B) Spatially resolved binding energy separations (i.e., surface potential steps) between surface adsorbates (OH^-) and solid surface (O^{2-}) derived from O 1s spectra under OCV and ±1.2 V applied biases. (C) Example of Ce 4d peak fitting. (D) Correlation between Ce^{3+} fraction changes and surface potential step changes under +1.2 V applied bias versus OCV. The Ce^{3+} positions were corrected for a 50 μm experimental shift associated with using different beam energies in different XPS measurements[49].

Ce^{3+} and OH^- are both surface intermediates in the ceria catalyzed electro-oxidation of H_2 and H_2O electrolysis processes. Shifts in their concentrations provide insight into rate-limiting surface processes. At −1.2 V, the accumulation of OH^- adsorbates in the active region indicates that OH^- consumption is rate-limiting. At +1.2 V, the OH^-maintains its equilibrium concentration while the Ce^{3+} concentration increases significantly. The buildup of surface Ce^{3+} and the lack of changes in OH^-/O^{2-} concentration ratio are being a rate limiting process. As a result, the first step in water electrolysis ($H_2O + Ce^{3+} \rightarrow Ce^{4+} + OH^- + H^{\bullet}$) and the last step in

hydrogen electro-oxidation ($Ce^{4+} + OH^{-} + H^{\bullet} \rightarrow H_2O + Ce^{3+}$) are proposed by the authors as the rate-limiting steps on the ceria-based SOC electrocatalysts[49].

As NiGDC cathodes improve the performance of SOECs devices as compared to that of Ni-yttria stabilized zirconia (Ni-YSZ) electrodes, Zafeiratos et coworkers [1], [50], [148] studied the surface state of nickel/gadolinium-doped ceria (Ni-GDC) under O_2, H_2, H_2O environments, and under water electrolysis conditions at intermediate temperature. Fig. 1.32a& b-left spectra show the Ce 3d-Ni 2p NAP-XPS peaks of Ni-GDC at 500 °C and 700° C after about 20 min in 0.2 mbar O_2. Reference spectra of CeO_2 and NiO compounds recorded under identical conditions were used for comparison. The Ce 3d spectrum of CeO_2 reference powder (spectrum at the bottom of fig. 1.31a-left spectra), has three pairs of spin-orbit doublets and the characteristic intense peak at ~917 eV, in full consistence with previous reports for Ce^{4+}. The Ni 2p reference peak is centered at 855.5 eV and is accompanied by a satellite peak shifted by 6.2 eV at higher binding energies, indicating NiO formation. The enhanced Ni 2p peak intensity at 500 °C as compared to 700 °C suggests that lower temperature favors the presence of nickel at the surface. Due to the higher analysis depth of NEXAFS in TEY mode as compared to NAP-XPS (4 or 5 nm instead of 1.7 nm), NEXAFS results can be used to conclude if oxidation is also propagated in deeper layers or if it is restricted at the outer surface. The NEXAFS spectra confirm the NAP-XPS results and indicate that the oxidation propagates at least in the outer 4 nm. The relative intensity of NiO NEXAFS peak as compared to that of CeO_2 is enhanced at 500°C, similar to the observations in NAP-XPS results. Overall, the spectroscopic results show that NiGDC cermet surface is readily oxidized in O_2 without evident differences in the two examined temperatures.

The oxidized Ni-GDC was exposed afterwards to 0.2 mbar H_2 at the same two temperatures. Ni 2p peak shifts to 852.6 eV while the intensity of the accompanied satellite peak decreases considerably, demonstrating reduction of NiO to metallic Ni as shown in fig. 1.32a& b-Right spectra. The Ce 3d region is also markedly modified as compared to the O_2 environment. Notably, the intensity of the peak at ~917 eV, characteristic for Ce^{4+}, decreases and new peaks at ~905 eV and 886.4 eV appear due to Ce^{3+} formation. Additionally, at 700 °C ceria is transformed to Ce^{3+}, while at 500 °C the Ce 3d spectrum contains about 25% unreduced Ce^{4+}.The NAP-XPS results are fully supported by the NEXAFS spectra shown in fig. 1.32b-(Right spectra). The Ce M-edge at 700 °C is in good agreement with Ce^{3+} while at 500 °C the Ce

M-edge is a superimposition of the Ce^{4+} and Ce^{3+} spectral features. Finally, the Ni L-edge is the same at both temperatures and corresponds to metallic nickel.

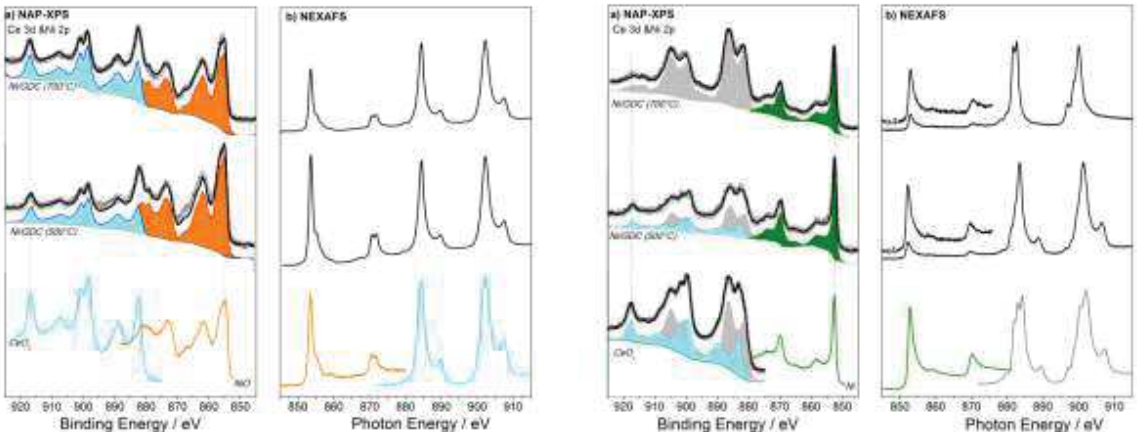

Figure 1.32. Left spectra (a) Ce 3d-Ni 2p (hν=1065 eV) NAP-XPS spectra (b) Ni $L_{3,2}$-and Ce $M_{5,4}$-edges NEXAFS spectra. The measurement conditions were 0.2 mbar O_2at 700 °C (top) and 500 °C (middle). The measured Ce 3d&Ni2p spectrum (open symbols) is well fitted (black solid line) by a linear combination of the reference CeO_2 and NiO spectra shown at the bottom of the figure and measured under similar acquisition conditions over standard powder samples. **Right spectra** (a) Ce 3d-Ni 2p (hν=1065 eV) NAP-XPS spectra (b) Ni $L_{3,2}$-and Ce $M_{5,4}$-edges NEXAFS spectra. The Ni $L_{3,2}$ edge is magnified 4 times. The measurement conditions were 0.2 mbar H_2at 700 °C (top) and 500 °C (middle). The measured Ce3d&Ni2p spectrum (open symbols) is well fitted (black solid line) by a linear combination of the reference $CeO_{1.5}$ and metallic Ni spectra shown at the bottom of the figure and measured under similar acquisition conditions over standard powder samples[50].

When Ni-GDC is exposed to water vapour, the adjustment of the surface oxidation state to the gas environment was found to be much slower than under H_2, which is kinetically rapid[1], [50], [137], [148]. In fig. 1.33 the Ce 3d and Ni $2p_{3/2}$ spectra of Ni-GDC pre-treated under H_2 (fig. 1.33a) or O_2 (fig. 1.33b) and consequently exposed to 0.2 mbar of H_2O vapour at 700 °C are shown. When pre-reduced Ni-GDC is exposed to steam (fig. 1.33a), an additional Ni $2p_{3/2}$ peak appears at the high BE side, due to oxidized nickel. From the shape of the Ni 2p peak it is evident that after about two hours in steam only a small amount of nickel (ca. 10 %) remains at the metallic state. After about 2 hours in the steam the Ce 3d spectrum corresponds to the overlap

of CeO_2 and $CeO_{1.5}$ reference spectra suggesting coexistence of these two states. Oxidation of reduced ceria ($CeO_{1.5}$) surface by water molecules has been proposed to take place via the interaction of H_2O with oxygen vacancies. In the case of the pre-oxidized Ni-GDC (fig. 1.33b), exposure to steam modifies the Ce 3d spectrum, while the Ni $2p_{3/2}$ peak is practically unaffected. The intensity increase of the Ce 3d peak components at ca. 886 and 904 eV is associated to the Ce^{3+} state. This means that GDC can be partly reduced by steam under the employed conditions. This was confirmed by stepwise annealing Ni-GDC in UHV conditions ($<1x10^{-7}$ mbar) at temperatures up to 600 °C. From these experiments it becomes evident that it is possible to decompose NiO even from 400 °C, while GDC remains fully oxidized up to the maximum annealing temperature. Therefore it is clear that ceria surface reduction in steam is not a thermal effect.

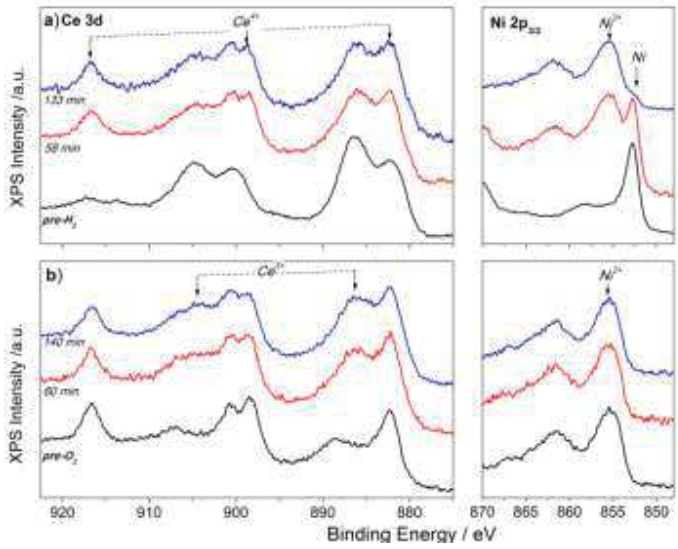

Figure 1.33.(a) Ce 3d and Ni $2p_{3/2}$ (hv=1065 eV) NAP-XPS spectra of the Ni-GDC electrode recorded at 700 °C at various H_2O exposure periods a) electrode pre-treated in H_2, (b) electrode pre-treated in O_2[50].

The electrochemical response and NAP-XPS results of the pre-reduced Ni-GDC electrode upon step polarization in 100% H_2O are shown in fig. 1.34 [1]. The current density increases monotonically with the cell bias as shown in fig. 1.34a but lower currents were measured in the downward cycle as compared to those at upward cycle, with an overall current density loss of about 5% (star-point in fig. 1.34a), after about 8 h of repeating the same measurements.

Operando NAP-XPS results show that the ceria oxidation state is not modified under bias. On the contrary, NiO undergoes partial reduction starting at -0.8 V, where the current density is approximately 30 mA/cm^2. The partial reduction of NiO is enhanced at -1 V, while upon further bias to -1.3 V it is fully reduced and subsequently remains to the metallic state even when the potential is stepped backwards. The reduction of NiO upon bias is not abrupt but progressive, as indicated by the modifications in the Ni 2p spectrum recorded at different time intervals at -1 V. Figure 1.40b shows that above -1 V nickel is metallic, while at -1 V and below, nickel is partly oxidized but the cell seems not to be deactivated. On the other hand, fig. 1.34c shows that the electrocatalytic performance is influenced by the modifications of the electrode surface morphology, i.e. nickel coarsening, which are reflected here by the changes in the Ni 2p and Ce 3d peak area ratio (Ni/Ce AR). It was found that the higher the Ni/Ce AR, the higher the cell current at constant voltage, regardless of the nickel oxidation state (e.g. at -1 V) as in fig. 1.34c. This explains the systematically lower current observed in the downward potential cycle as compared to the upward. Reduction of nickel at high potentials provokes lower Ni/Ce ARs and deteriorates the cathode performance, probably by decreasing the TPB length. As shown in fig. 1.34b, when the cell is operating at high voltages (>-1 V) nickel oxide is transformed to metallic nickel. In this case, introduction of H_2 has no effect on the nickel surface oxidation state, but still affects the oxidation state of ceria[1].

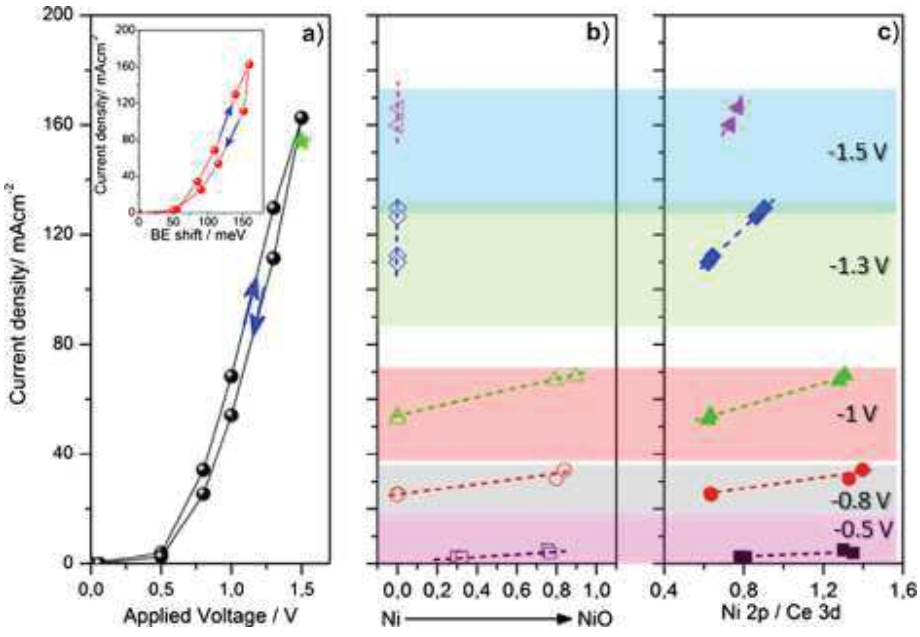

Figure 1.34. (a) I–V polarization curves for Ni/GDC electrode under H_2O feed recorded in potential step-up and down cycles. The green star represents the cell current measured in H_2O after 8 h of operation. The current density for various applied potentials as a function of: (b) NiO_x valence and c) Ni/Ce AR measured by APXPS. The color zones represent the applied potentials. Prior to the potential application the sample was pretreated in H_2 and remained at O.C. in the feed gas for about 30 min. The voltage was applied directly between the working (Ni/GDC) and the counter (Pt) electrodes[1].

Ce 3d and Ni $2p_{3/2}$ spectra were recorded using 2 photon energies as shown in fig. 1.35. The contribution from $CeO_{1.5}$ and metallic Ni spectra features are clearly enhanced in the more surface sensitive measurement mode (i.d.=1.5 nm) indicating that NiO and CeO_2 are located in the deeper layers and the surface is dominated by Ni and $CeO_{1.5}$ in a core-shell like structure. Metallic Ni shell over NiO has been reported only for electrochemical reduction of NiO, while for chemical reduction the inverse scheme with a NiO shell over Ni is typically observed [1]. The chemical reduction usually proceeds via diffusion of Ni cations into the subsurface, always leaving a NiO shell on the surface. On the other hand, it is suggested that electrochemical reduction takes place by an outward diffusion of O anions, resulting in the formation of a Ni-shell with a gradually increased thickness[1]. Fig. 1.35c shows the ratio of the overall Ni 2p to Ce 3d peaks (Ni/Ce) and that of the metallic Ni and $CeO_{1.5}$ component in the Ce 3d spectrum (Ni^0/Ce^{3+}) for two information depths (i.ds.) and for various cell conditions. The Ni/Ce AR decreases in more reducing gas phase atmospheres, while it is systematically higher at the 1.5 nm compared to 3 nm analysis depth. Ni/Ce AR is higher in the surface sensitive mode, especially when nickel is (partially) oxidized, which is a strong evidence of NiO segregation over CeO_2. However, this difference fades away when nickel and ceria are further reduced e.g. in H_2. Furthermore, the Ni^0/Ce^{3+} partial ratio remains identical in the two depths independently of the atmosphere and application of the bias voltage (fig. 1.35c).

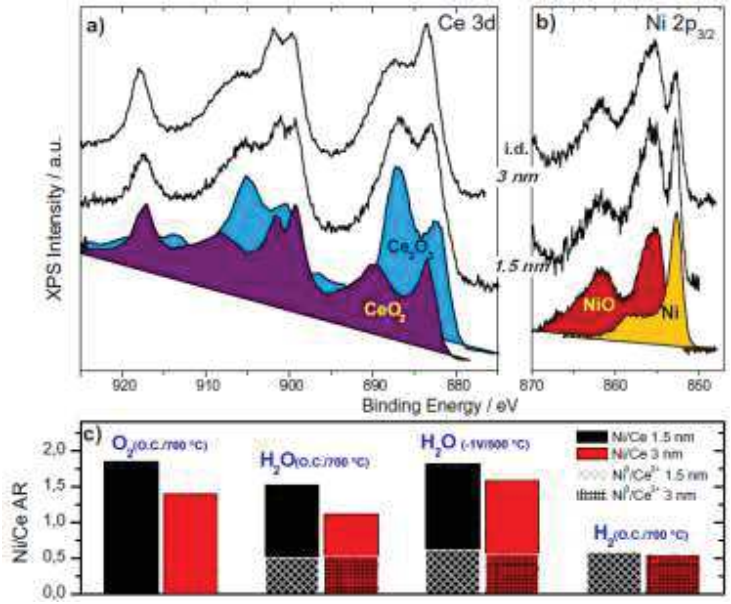

Figure 1.35. (a) Ce 3d and (b) Ni 2p3/2 APXPS spectra in two information depths (i.d.) under H_2O at 500 °C and -1 V bias. The reference spectra recorded on CeO_2, $CeO_{1.5}$, NiO and Ni are shown in the bottom of the graph. c) The Ni 2p to Ce 3d APXPS area ratio of the overall (Ni/Ce) peak and only the metallic Ni and $CeO_{1.5}$ components (Ni^0/Ce^{3+}) for the two i.d.s. The conditions where the spectra were recorded are indicated in the graph[1].

1.4. Structure and Objectives of PhD Thesis

The solid oxide electrolysis cells (SOEC) technology is attractive for storage and regeneration of renewable energy. A SOEC uses electricity to split, e.g. water in the form of steam, into H_2 and O_2. In this way, electrical energy is transformed into chemical energy with high efficiency due to the relatively high temperature operation (700-1000 °C). However, the deterioration of the electrodes during operation remains a critical issue which hinders the penetration of SOEC technology in the energy market. Ni-based cermets, especially Ni-YSZ, are composite materials composed of ceramic (cer) and nickel (met) and are currently the most widely used cathode electrodes of SOEC. This is mainly due to their low cost and high electrocatalytic activity. The role of Ni is to provide the electrocatalytic sites and electronic conductivity, while YSZ conducts oxygen ions into the electrolyte and secures the mechanical stability of the electrode. Since YSZ exhibits negligible electrocatalytic activity towards water dissociation, the electrochemical reactions mainly occur in the vicinity where Ni, YSZ and fuel gas are encountered. Therefore, replacing YSZ with a porous mixed ionic-electronic conductor (MIEC), which can also act as the

electrocatalyst, has been considered as a method to increase the reaction site density as compared to Ni-YSZ electrodes. Doped ceria (DC) is probably the most suitable MIEC material for such cause, since it combines good electronic and ionic conductivities with high electrochemical activity.

However, durability remains a major issue for reliable operation of SOEC systems. A variety of processes accountable for permanent performance degradation of SOECs has been identified based on post-mortem cell analysis. Besides, transient/reversible degradation processes are typically examined by indirect methods, like impedance spectroscopy. This is because the application of material characterization techniques during SOEC operational conditions is challenging. In the first part of my PhD, we provide a study of direct correlation between Ni-YSZ and Ni-GDC electrodes surface oxidation state and their performance during steam electrolysis using operando experimental evidences provided by near ambient pressure X-ray photoelectron and near edge X-ray absorption fine structure spectroscopies. We show that nickel surface oxidation may induce significant performance degradation over Ni-YSZ cathodes, while on the contrary has only minor effects on Ni-GDC. Remarkably, we found that in case of Ni-GDC electrodes, small modification of GDC oxidation state can have important impact on the electrolysis performance. The results highlight the crucial role of the cathode electrode surface oxidation state on the SOEC function and have potential implications for the design and operation strategies of more efficient and durable SOEC devices.

These results gave us the idea of impregnation of Ni-YSZ electrodes with ceria or metal/ceria solutions which has shown a quite promising enchantment of the electrochemical performance. One remaining challenge is keeping Ni and DC sites in close proximity by controlling the deposition process, so as to avoid segregation of the two materials during the high temperature operation and prevent loss of the electrochemical active area. In the second part of my PhD, we propose a novel and simple approach to develop SOEC devices by surface modification of standard Ni-YSZ electrodes using nickel-substituted ceria nanoparticles ($Ni_{0.1}Ce_{0.9}O_{2-x}$) as promoters. Near ambient pressure X-ray photoelectron (NAP-XPS) and absorption (XAS) spectroscopies were applied *in situ* in order to characterize the (*$NiCeO_x$ NPs*)-Ni/YSZ oxidation state and composition under cell operation and compare it with this of nickel/yttrium stabilized zirconium (Ni/YSZ).We found a significant improvement of the steam electrolysis performance

of Ni-YSZ electrodes after modification even at relatively low temperature and 100% steam. Maintenance of a significant population of Ce^{3+} and Ni^{3+} sites able to form on $Ni_{0.1}Ce_{0.9}O_{2-x}$ but not to conventional supported Ni/CeO_2, are identified as the main cause of the improved performance. The morphological changes of the electrode are examined by *ex-situ* scanning electron microscopy. We expect that the proposed concept to combine Ni and ceria sites in close proximity by forming nanoparticles is a key factor to optimize the efficiency and longevity of the cathode electrodes so as to develop SOEC devices with improved performance.

Chapter 2. Materials and Experimental Techniques

II. Chapter 2. Materials and Experimental Techniques

2.1. Materials used in this thesis

2.1.1. Cell fabrication

Prefabricated electrolyte supported half cells consisting of Ni-based cermet working electrodes

Conventional electrolyte supported electrochemical cells using Ni-based cermets (Ni/YSZ & Ni/GDC) and impregnated Ni/YSZ electrodes with Ni-substituted Ceria NanoParticles (NiCeOx NPs) as electrocatalytic promoters are studied in this work. The electrolyte in all the cells analyzed is 8YSZ which has a high mechanical stability. Synthesis and characterization of Nickel-doped ceria nanoparticles ($Ni_{0.1}Ce_{0.9}O_{2-x}$NPs) will be discussed in chapter 4. Part of the conventional half cells of NiO-YSZ (66:34 wt%) and NiO-GDC (65:35 wt%) working electrodes were synthesized by our project collaborator at CERTH (Thessaloniki, Greece) with the electrodes applied over 150 and 300 μm thickness YSZ electrolyte, respectively[137], [149]. In addition commercial cells from Kerafol GmbH, 8YSZ were also used. Both type of cermet electrodes were prepared via the deposition precipitation method and applied on 1 inch yttria-stabilized zirconia (YSZ) pellets using the screen printing technique (see fig. 2.1). The electrode catalysts loading is 8 mg cm^{-2}, while the electrode was directly deposited on the YSZ electrolyte without using a GDC protection layer, which is typical in commercial applications.

Preparation of platinum counter and reference electrodes

Platinum was chosen for as the reference and counter electrode due to its known performance stability in oxidizing and reducing environments[150]. The Pt counter electrode was painted using platinum paste (ESL, 542-DG) opposite to Ni-GDC or Ni-YSZ electrodes with similar symmetrical shape and surface area to them. The Pt reference electrode was on the same side as the counter electrode separated by a gap of about 3 mm as shown in fig. 2.1. The area ratio between counter and reference electrodes was approximately 5 to 1. A reference symmetric cell composed exclusively of Pt electrodes was also fabricated and tested in order to address possible effects of oxygen addition to the reaction kinetics. Electrochemical experiments were also performed on commercial prefabricated NiO-YSZ//YSZ and NiO-GDC//YSZ half cells (Kerafol

GmbH, both 150 μm YSZ) in a laboratory reactor[23] which could operate at conditions similar to those of the synchrotron experiments. The fabrication of Pt will be discussed further in detail.

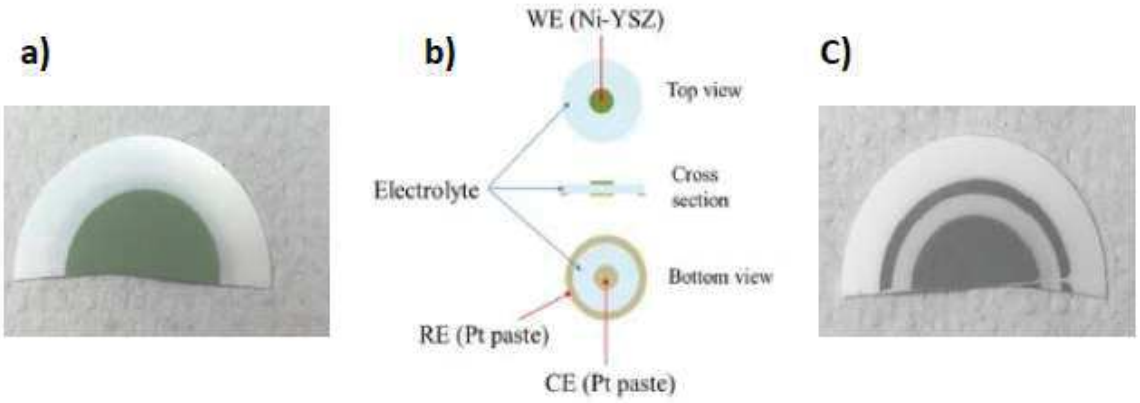

Figure 2.1. (a) Top view for the Ni-YSZ/YSZ/Pt cell for Ni-YSZ cathode electrode, (b) Schematic diagrams of cell configuration and setup, (c) Bottom view of the Countering& Reference electrodes Pt**.**

At the beginning of this PhD work I was encountered with strong delamination problems, especially of the Pt-electrodes, which resulted to increase in operation cell potentials consumption. Therefore, at the beginning of the PhD thesis a reliable Pt electrode fabrication method was established. The preparation of the platinum electrode is performed on several steps: a) Pretreatment of YSZ substrate prior to Platinum paste application by using an alumina (Al_2O_3) pneumatic sandblaster sputtering equipment in order to increase surface roughness. b) Pre-deposition of Platinum by Cleaning the YSZ surface, first by high pressure air to remove the residual alumina and then by ethanol to remove the organic contaminations. c)Several layers of Pt paste (a solution of platinum metal diluted by an organic compound) were deposited at the surface of the YSZ electrolyte. . Optimization of the thickness of the platinum layer was performed manually by using a brush (11810 of 1.3 mm * 8.0 mm L). Finally, the thermal treatment of the Platinum paste was done by two different baking procedures as shown in table.1, after drying at 80 °C for 30 minutes in both cases in order to remove the organic part of the paste.

Table2.1. The thermal treatment Procedures for Pt paste.

The Procedure	Fast procedure	Slow procedure
Drying step	125 °C: 12 min	400 °C: 2h with rate: 4.5°/min
Firing temperature	980 °C for 11 min	800°C25 min with rate: 2°/min
Rate	50°C / min for the 2 steps	50°C / min for the 2 steps

The topographical differences between the surfaces structure of Pt electrodes are shown in fig. 2.2 after firing at 980 °C and 800 °C. In the case of the fast procedure, platinum aggregates and fractures in smaller particles. These fractures might be due to the interaction of platinum with the electrolyte (YSZ) during the baking procedurebut are not due to the changes in the expansion coefficient, as for platinum the expansion coefficient is 8.8*1/K, very close to that of the electrolyte (YSZ, 10.5*1/K).

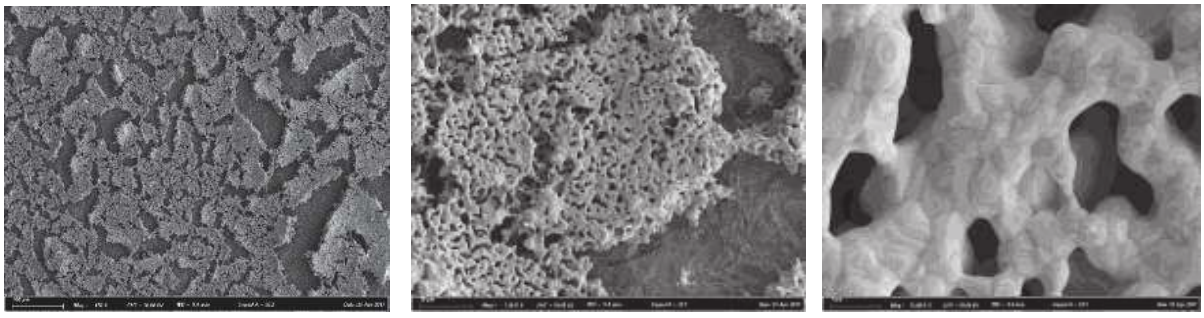

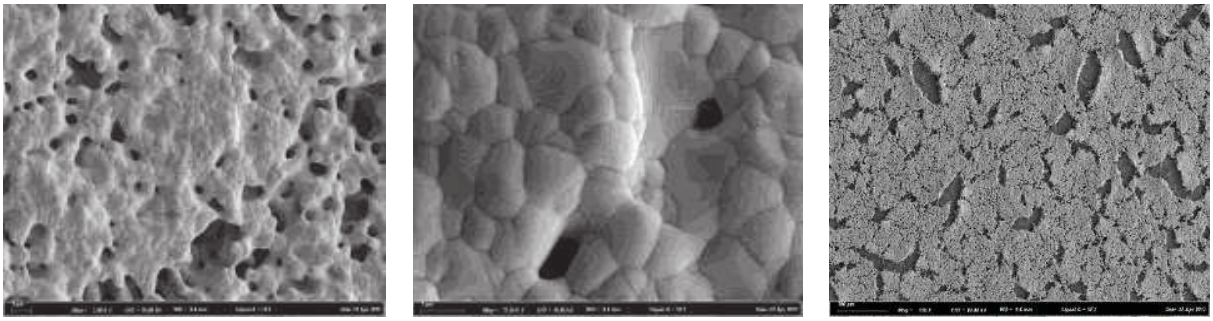

Figure 2.2. SEM micrograph for the Pt electrode after firing procedure, **(top)** prepared with the fast baking procedure (980 °C), these images illustrate high density of fractures. (**Bottom**) prepared with the slow baking procedure (800 °C). These images illustrate some fractures and aggregations much less than the above.

NAP-XPS spectra of the Pt working electrode under H_2, polarization in H_2O/H_2 mixture and O_2, were investigated to study the redox stability as shown in fig. 2.3. Pt 4f doublet peaks spectra were found at 71.4 and 74.7 eV due to metallic Pt (peaks due to platinum oxide are not detected). In addition, a component at around 76 eV due to Al2p overlapping with the Pt 4f peak exists in the spectra, that can be attributed to the presence of alumina residuals remaining after the surface roughening procedure. The peak area of the alumina contamination is not negligible (19.93% in the first spectrum). Al/Pt ratio at the two different analysis depth (0.651 at 225 eV and 1.05 at 510 eV) show that the percentage of Al at the surface is smaller than that at deeper layers. This implies that the Al contaminations is mainly located at the surface of the electrolyte (YSZ), and not at the surface of platinum, therefore it is not expected to influence the conductivity of the platinum electrode.

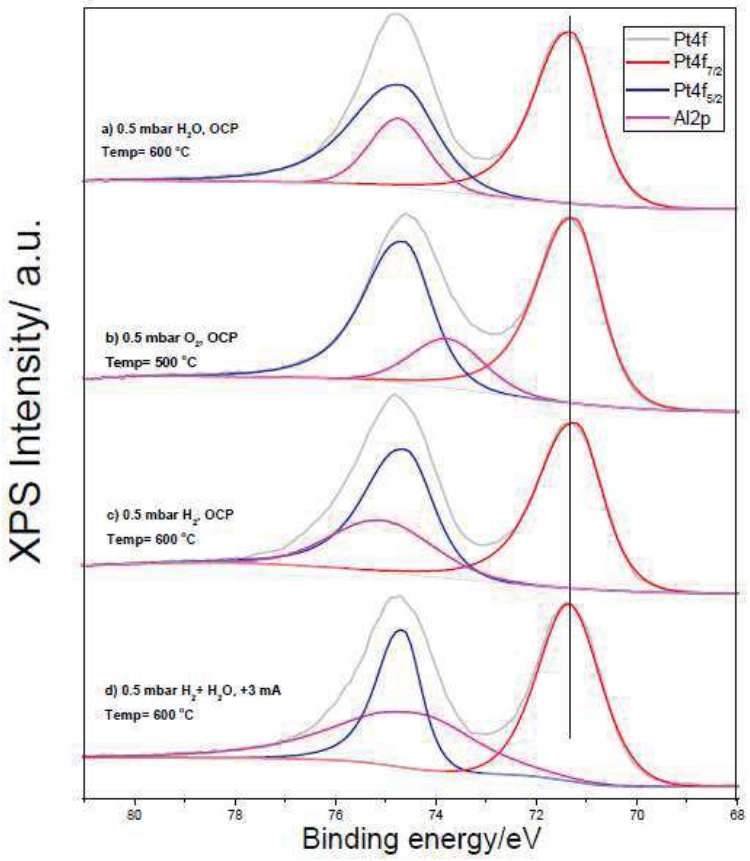

Figure 2.3. The NAP-XPS Pt4f spectra measured on the Pt countering electrode (hv =255 eV) in a) 0.5 mbar H_2O,b) 0.5 mbarO_2, c) 0.5 mbar H_2 and d) 0.5 mbar H_2/H_2O under +3mA, prepared with the slow baking procedure (800 °C).

2.1.2. Three electrode configuration electrochemical Cell

Electrochemical measurements such as EIS and IV can be made in different configurations, among which the most common ones are the so called two-, three- and four-electrode configurations (see fig. 2.3). In the simplest one (fig. 2.4a), the current is applied and the measurement is done using the same two electrodes, named the working electrode (WE) and the counter electrode (CE). In this case, of course, $Z(j\omega)$ includes contributions due to the sample interface at both electrodes. In order to reduce the influence of such interfaces, a third electrode, called reference electrode (RE), can be added, as shown in fig. 2.4b. In this case, the test signal is applied between the WE and the RE, while the current is measured at the CE. Since no current is drawn at the RE, the measured impedance includes only the contribution of the interface at the WE. Most of this PhD experimental work has been done in three electrode configuration. A

further electrode can be added in a four electrode configuration, (shown in fig. 2.4c), as it is often the case in galvanostatic EIS. The sine-wave test current is applied between (WE) and (CE), while the voltage is measured between the (added) working sensing electrode (WSE) and RE. Since no current is drawn at both WSE and RE, the measured impedance is independent of the electrode–sample interfaces. In practice, the use of a higher number of electrodes makes the measurements more complex but also more precise; thus, a trade-off is in order with the optimum solution depending on the constraint of any specific application.

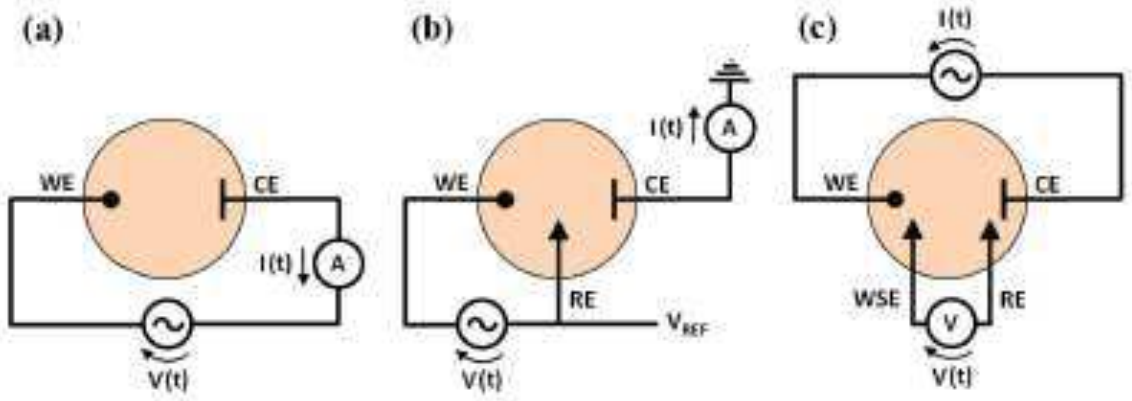

Figure 2.4. Measurement setup configurations used in EIS featuring (a) two electrodes, (b) three electrodes and (c) four electrodes[51].

2.2. ICPEES-based experimental setup for electrochemical and ex situ XPS characterization

The electrochemical performance has been studied firstly at ICPEES, in the surface analysis laboratory set-up, using a variable pressure reactor simulating the conditions of NAP-XPS experiments performed at synchrotron facilities. Polarization curves and electrochemical impedance spectroscopy (EIS) measurements were conducted by using a VersaSTAT 3 (AMETEK Scientific Instruments) potentiostat/galvanostat. The three-electrode configuration was mainly used, which allowed the measurement of the overpotential of the working electrode without the influence of the counter electrode. The overpotential was calculated from the DC set voltages by subtracting the OCP and after IR correction.

2.2.1. Laboratory setup description

a) Primary laboratory setup

The set-up has been previously constructed by V. Papaefthymiou and W. Doh at ICPEES (Strasbourg, France) for MEA tests under low humidity ambient conditions. It consists of a stainless steel cylindrical chamber equipped with a sample holder, oxygen-free liquid water reservoir, capacitance gauge CMR 392 and control unit RVC 300 (Pfeiffer Vacuum), vacuum pipeline valve PV25MK (Edwards) and a dual stage rotary vane vacuum pump 5 E2M5 (Edwards)[151]. The electrochemical cell is placed on the ceramic sample holder and is covered by three stainless steel plates from both sides. An Au grid is used as the current collector and placed between the MEA and covering plates from both electrode sides. The plates are connected through the corresponding wires to the potentiostat. The photos of the set-up and the sample holder are shown in fig. 2.5.

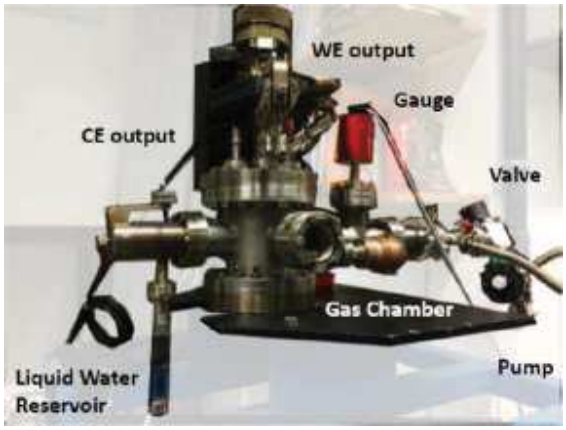

a)

b)

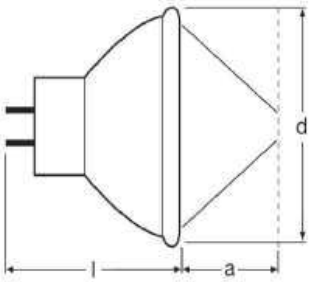

C)

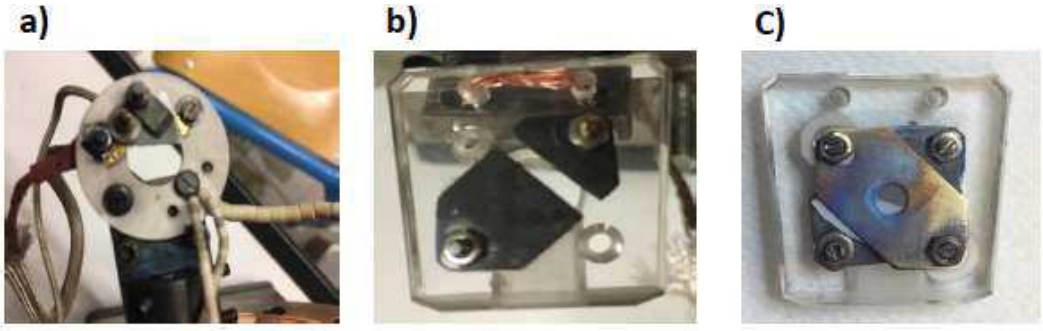

Figure 2.5. (top) Left panel: detailed photograph of the Laboratory set-up for the electrochemical tests of the cells under the gas-phase conditions[151]. Right panel: Laboratory set-up. (**middle**) a) The primary setup sample holder connected in the setup, b) sketch for the lamp showing the focal point, C) Infra-red lamp64635 HLX, Halogen lamps with reflector MR16; temperature at the focal point, approximately 1300 °C. (**bottom**) a) The three electrode configuration connection in primary setup sample holder containing the electrochemical cell, b) The bottom stainless steel current collector sample holder which is similar to synchrotron setup, c) The top stainless steel current collector sample holder used to fix the cell.

b) Advanced laboratory setup (Electrochemical test and XPS measurements separately)

As shown in fig. 2.6, the combined UHV/electrochemical setup used in this PhD work consists of four chambers: i) the main chamber, which operates under UHV conditions (10^{-9} Torr)[132] and includes a monochromatic Al - *K*α X-ray source [hν=1486.6 eV][152] and a dual anode X-ray gun, ii) the preparation chamber with a base pressure of 10^{-8} Torr, iii) a load lock chamber to insert the sample holder into the setup and finally iv) the variable pressure chamber for electrochemical and/or gas treatment experiments, which operates normally between 0.5 mbar and 23 mbar).

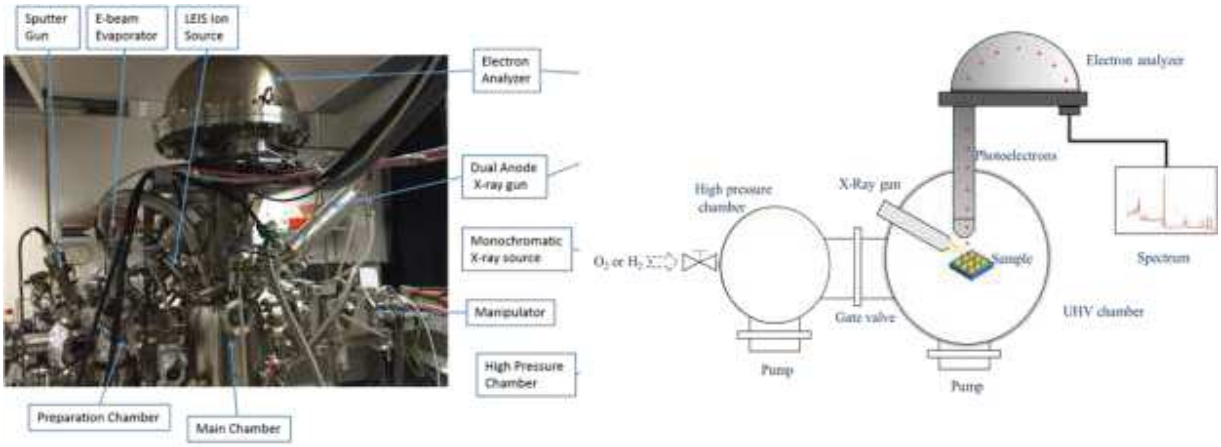

Figure 2.6. XPS laboratory setup and its Schematic drawing for the operation process at (ICPEES, France).

The electrochemical cells are mounted between two stainless steel clamps. The first is attached to the working electrode on the top and is pressing the counter electrode. The second is pressing the gold wire attached to the reference electrode from the bottom. The stainless steel clamps were also used as the current collectors and they were connected through two ball pressed screws with the potentiostat. Heating was performed from the BN-heater from Omnivac. Detailed photos of the E/C cell mounting and the sample holder are shown in fig. 2.7. The measurements were performed in a one atmosphere setup. The gas flow into the reaction cell was controlled by mass flow controllers while the gas phase was monitored by an online quadrupole mass spectrometer (QMS) as shown in fig. 2.7.

Figure 2.7. a) The sample holder inside the variable pressure chamber. b) Variable pressure chamber of the advanced Laboratory set-up for the electrochemical tests of the cells under the gas-phase conditions. c) The three electrode configuration connection setup sample holder containing the electrochemical cell. d) Mass flow controllers which control the gas flow into the reaction cell and quadrupole mass spectrometer (QMS) to monitor the gas phase.

2.2.2. In-situ Near-Ambient Pressure spectroscopy Setup

XPS is generally performed under vacuum conditions mainly to avoid the scattering of electrons by gas molecules above the sample. However, for thermodynamic and/or kinetic reasons, the catalyst's chemical state observed under vacuum reaction conditions is not necessarily the same as that of a catalyst under realistic operating pressures. Therefore, investigations of catalysts should ideally be performed under reaction conditions, i.e., in the presence of a gas or gas mixtures. Using differentially pumped chambers separated by small apertures, XPS can operate at pressures of up to 1 Torr, and with a differentially pumped lens system, the pressure limit has been raised to about 10 Torr as shown in fig. 2.8 [52], [153], [154]. The key to increase the pressure limit in NAP-XPS is to decrease the effective path length of the electrons through the high pressure region. This can be achieved by moving the sample closer to the aperture. However, because the pressure drops by several orders of magnitude across the aperture, there is a minimum distance at which the sample should be kept from the aperture to ensure homogeneous pressure conditions across the sample surface.

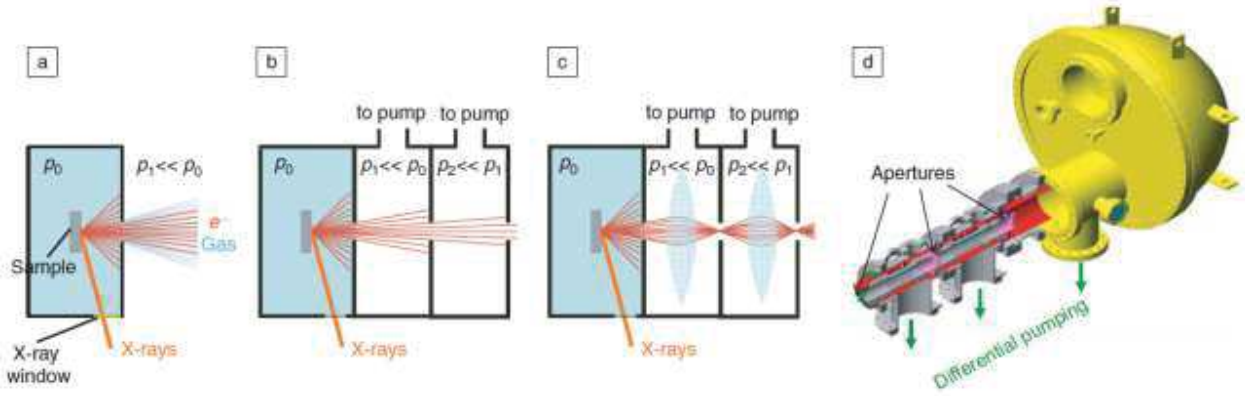

Figure 2.8. a) The principle of high-pressure x-ray photoelectron spectroscopy (HP-XPS). The sample is placed in a high-pressure chamber that is separated from the x-ray source by an x-ray–transparent window. Electrons and gas escape through a differentially pumped aperture. b) A

conventional HP-XPS setup. Several differential pumping stages are needed to keep the electron analyzer under vacuum when the pressure in the sample cell is close to 1 Torr or higher. There is a tradeoff between the pumping efficiency, given by aperture sizes and spacings, and the solid angle of transmission of electrons through the differential pumping stages. c) The principle of HP-XPS using a differentially pumped electrostatic lens system. The electrons are focused onto the apertures using electrostatic lenses in the differential pumping stages, which increases the efficiency of electron collection and allows for a reduction of the size of the apertures for improved differential pumping. d) Differentially pumped electrostatic lens system and hemispherical analyzer (Phoibos 150, Specs GmbH, Berlin) of the HP-XPS instruments at BESSY, taken from [52].

In-situ near ambient pressure XPS and NEXAFS measurements were done at the third generation synchrotron facilities, at HZB/BESSY II (Berlin, Germany). The unique properties of synchrotron radiation are wide-energy tunability, high brilliance and high photon flux[155], [156]. The in-situ measurements of Ni based cermets were performed at the ISISS (Innovative station for *in-situ* spectroscopy) beam line at the Inorganic Chemistry department of the FHI fig. 2.9. The configuration of the used set-up allowed recording both photoemission and absorption spectra at the gas-phase pressure up to few mbars. The Phoibos 150 electron analyzer (SPECS) is equipped with a 2D Delay Line detector from Surface Concept. The gases were introduced into the NAP-XPS chamber through the leak valves using the mass flow controllers. The composition of the ambient in the analyzing chamber was constantly monitored by an on-line quadrupole mass spectrometer (QMS, Prisma, Pfeiffer Vacuum, Inc., Germany). The QMS was used to continuously record the traces of H_2O, H_2 and O_2 during the measurements. For NEXAFS studies, the Auger electron yield was measured with the electron spectrometer. The total electron yield was collected via a Faraday cup via the first aperture of the differential pumping system with an applied accelerating voltage. For XPS measurements performed at ISISS beamline, pass energies of 50 eV were used. The inelastic mean free paths (IMFP) of the emitted electrons were estimated using QUASES-IMFP-TPP2M software for Ni/Ce 1.5 nm and Ni/Ce 3 nm. The analysis depth was calculated as three times the IMFP (ID=3λ). The depth-dependent measurements were carried out using photon energies 1065 eV and 1320 eV for Ce3d-Ni2p spectra (corresponding to 1.5, 3 nm of the analysis depth for Ni^0, Ce^{3+}).

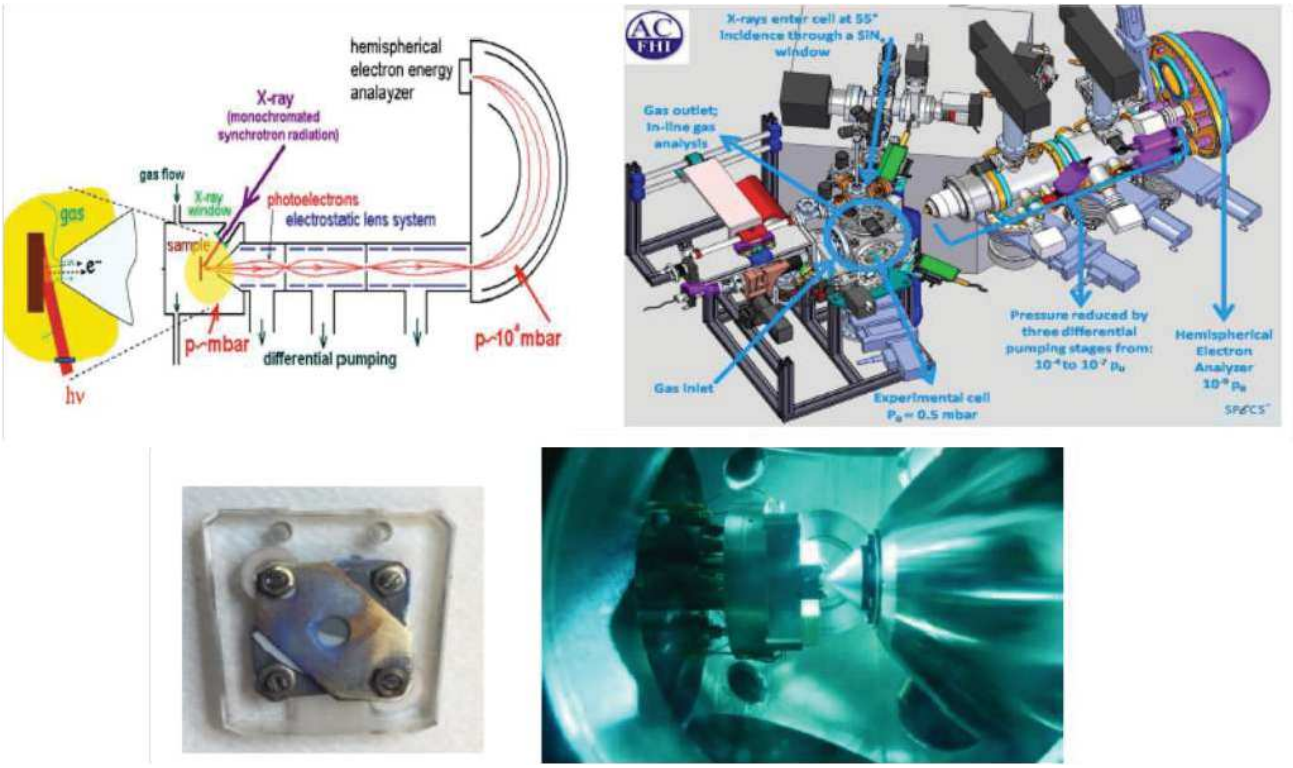

Figure 2.9. (**top**) Schematic diagram of the in-situ NAP-XPS set-up under the electrochemical gas-phase conditions, at the right side the detailed design of the NAP-XPS set-up in HZB/BESSY II (Berlin, Germany). (**bottom**) The sample holder in detail in mounted inside the NAP-XPS chamber.

For synchrotron based experiments the SOEC cells (schematically shown in fig. 2.10) were mounted between two stainless steel clamps, the one at the top with a 4 mm diameter slit and the other at the bottom was separated in two stainless steel plates for the reference and the counter electrodes respectively. The stainless steel clamps were also used as the current collectors and they were connected through two ball pressed screws with the potentiostat. Heating was performed from the rear side using an IR-laser, while the temperature was monitored at the center of the working electrode by a pyrometer. The measurements were performed in a one atmosphere setup[157]. The gas flow into the reaction cell was controlled by mass flow controllers while the gas phase was monitored by an online quadrupole mass spectrometer (QMS). Electrical potentials were applied between the working and the counter electrodes and the current flow was measured using a computer controlled VersaSTAT3-200[158]

potentiostat/galvanostat (Princeton Applied Research).The working electrode was grounded and the bias voltage was applied on the counter electrode.

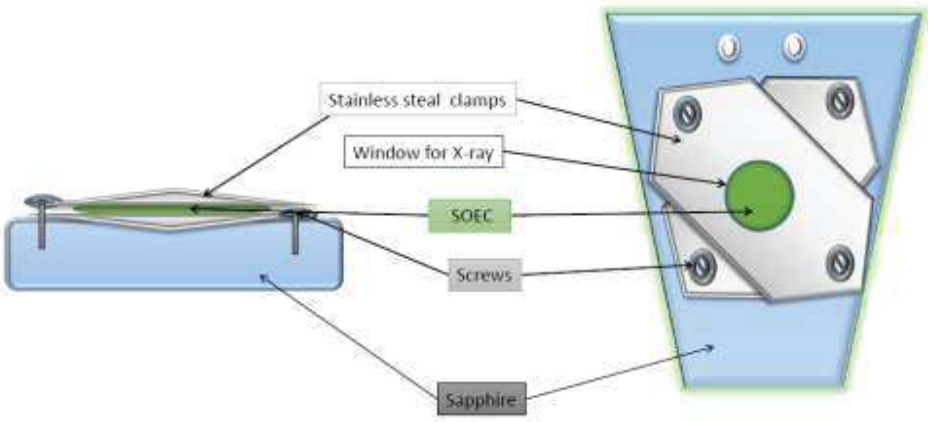

Figure 2.10. a) Sketch of the sample holder used to fix the SOEC in the NAP-XPS chamber[151].

2.2.3. Analyzed samples

Preliminary experiments were performed in ICPEES on Ni-based cermets cathode electrode for SOEC under different gases and under water electrolysis operation conditions. Also, synthesis and characterization of nickel-doped ceria nanoparticles $Ni_{0,1}Ce_{0,9}O_{2-x}$ were done in ICPEES before testing their influence on the electrochemical cells in synchrotron facilities. The in-situ investigation was performed firstly on Ni-based cermets under intermediate electrolysis condition:

i) NiGDC/YSZ/Pt electrochemical cell,

ii) NiYSZ/YSZ/Pt electrochemical cell (Chapter 3).

iii) Nickel-doped ceria nanoparticles $Ni_{0,1}Ce_{0,9}O_{2-x}$(Chapter 4).

iv) ImpregnatedNiCe@NiYSZ (Chapter5).

2.3. XPS data Analysis

This section demonstrates the procedure used for the fitting of Ni2p-Ce3d XP spectra and the electrochemical measurements (IV, EIS) normalization. For XPS data, the deconvolution was done using the CasaXPS software. The relative amount of NiO, Ni, CeO_2 and $CeO_{1.5}$ was

estimated by deconvolution of the overall Ni 2pand Ce3d spectra to individual components, using reference peaks of the pure phases.

2.3.1. XPS Spectra Analysis

The surface atomic ratios for the Ni-GDC and Ni-YSZ cathode electrodes and the Nickel-doped ceria nanoparticles were calculated based on the intensities of the XPS spectra using the following equation[155]:

$$\frac{A.r(a)}{A.r\ (b)} = \frac{I(a)/(Cs(a).f(a))}{I(b)/(Cs(b).f(b))} \qquad \text{(Eq.19)}$$

where $\frac{A.r(a)}{A.r\ (b)}$ is the atomic ratio of elements (a) and (b),

I– the intensities obtained from the XPS spectra for the corresponding element,

f– the energy dependent incident photon flux,

Cs– the photoelectric cross-section for the interested atomic orbital taken,

The intensity of incident photon flux as a function of their energy recorded at BESSY II is shown in (fig. 2.11).

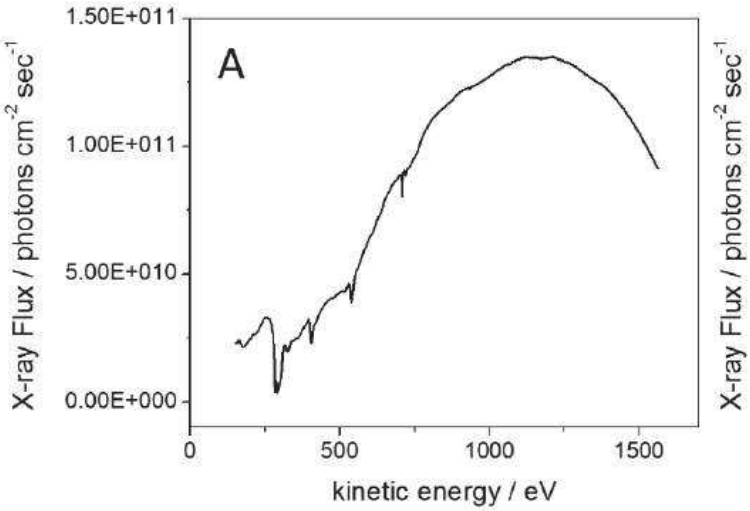

Figure 2.11. Incident photon flux vs kinetic energy recorded at ISISS.

The fitting procedure for Ni2p and Ce3d is quite complex due to the partial overlapping between Ni2p and Ce3d XPS spectra. Accordingly, reference peaks of the pure phases for (Ni, NiO, $CeO_{1.5}$ and CeO_2) were used to deconvolute the Ni2pCe3d spectra. Fig. 2.12 illustrates fitting in both Ni-YSZ and Ni-GDC electrodes after and during water electrolysis condition. XPS

measurements shown at the top of fig. 2.12 were performed ex-situ after the electrochemical measurements, while those at the bottom in-situ under polarization. The Ni 2p peak can be deconvoluted into two components; one sharp Ni $2p_{3/2}$ peak around 853 eV which corresponds to metallic Ni, and a broader Ni $2p_{3/2}$ feature at 856 eV associated to oxidized Ni as shown in fig. 2.12 [25], [50], [159]. In the case of Ni-GDC electrode the analysis of the Ce 3d spectrum during and after current application in 0.5 mbar H_2O shows that GDC contains contributions of both Ce^{3+} and Ce^{4+} cations. The Ce 3d spectrum is characterized by components at ca. 886 and 904 eV is associated to the Ce^{3+} state and the peak at 917 eV, which is associated toCe^{4+} state[1], [50], [64], [144].

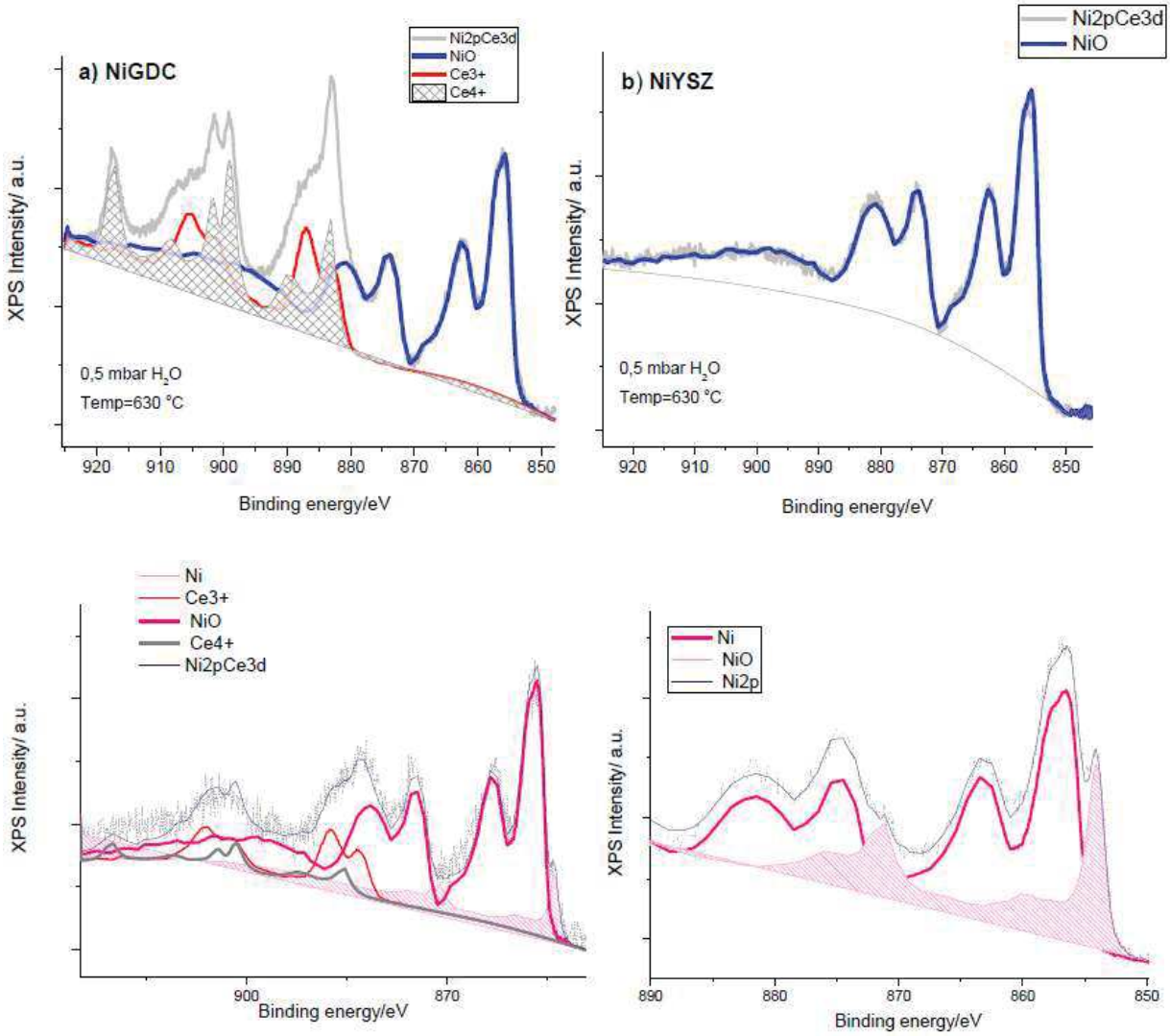

Figure 2.12. (top) Example of the peak fitting procedure used for the estimation of ceria and nickel stoichiometry a) NiGDC cathode electrode, b) NiYSZ cathode electrode for *ex-situ XPS* measurements after exposure to polarization under 0.5 mbar H_2O electrolysis condition at 630 °C. **(bottom)** Example of the peak fitting procedure used for the estimation of ceria and nickel stoichiometry, left) NiGDC cathode electrode, right) NiYSZ cathode electrode for *in-situ XPS* measurements under negative polarization in 0.5 mbar H_2O electrolysis condition at 630 °C.

2.4. Electrochemical testing techniques(EIS, Chronoamperometry, IV)

Electrochemical Impedance Spectroscopy (EIS)

Electrochemical impedance spectroscopy (EIS), in which a sinusoidal test voltage or current is applied to the sample under test to measure its impedance over a suitable frequency range, is a powerful technique to investigate the electrical properties of a large variety of materials. In practice, the measured impedance spectra, usually fitted with an equivalent electrical model, represent an electrical fingerprint of the sample providing an insight into its properties and behavior. EIS is essentially carried out as follows. In one of its two versions, the so-called "potentiostat EIS", a sine-wave voltage (eq.20) is applied to the sample under test and the induced current as shown in (eq.20) is measured. Then, the complex impedance is calculated as shown in (eq.22)[51].

$$V(t) = \bar{V} + \hat{V} \cdot \sin(\omega t) \quad \text{(Eq.20)}$$

$$I(t) = \bar{I} + \hat{I} \cdot \sin(\omega t + \varphi) \quad \text{(Eq.21)}$$

$$Z(j\omega) = \frac{V(j\omega)}{I(j\omega)} = \frac{\hat{V}}{\hat{I}} \cdot e^{-j\theta} = |Z| \cdot e^{j.Arg(z)} \quad \text{(Eq.22)}$$

$$= Re(z) + j \cdot Im(Z)$$

Here, $\hat{V}$and $\hat{I}$are the voltage and the current amplitude, respectively; $\bar{V}$ and $\bar{I}$ are the voltage and the direct current (DC) values; f is the signal frequency; $\omega = 2\pi f$ the angular frequency; φ the phase difference between V(t) and I(t); $V(j\omega)$ and $I(j\omega)$ the Steinmetz transforms of V(t) and I(t), respectively. In the other version of EIS, known as "galvanostat EIS", the sample is stimulated with a sine-wave current and the voltage drop is measured (of course, the impedance being still given by (eq.22). In most cases, the investigation by potentiostat EIS or galvanostat

EIS is equivalent and provides the same results. There are, however, application-specific conditions making one technique more suitable than the other.

The impedance $z(j\omega)$ is defined in the case of linear time invariant systems, exhibiting three conditions: (a) linearity, (b) stability and (c) causality. However, since electrochemical systems exhibit a typically non-linear behavior, to avoid excessive perturbations to the SUT (Sample under the test), small values of $\hat{V}$ (usually in the range 10 to 100 mV) are used to operate in a pseudo-linear region where $z(j\omega)$ does not depend on $\hat{V}$. The ohmic drop (given by the high frequency cut off in the impedance spectra measured at identical conditions), The Nyquist plots were fitted using the ZView2-Software, in order to identify the frequency response of the different involved phenomena.

Chronoamperometry

The chronoamperometry technique is very useful indication for the changing of the oxidation state of the electrode materials, and also it is very rabid to notice the degradation phenomena illustrated in the increasing of the voltage consumption. Most of the PhD *In-situ* NAP-XPS/NEXAFS measurements were performed under constant current applied between the working and counter electrodes. These measurements will be discussed in more detail in Chapters 3 and 5.

IV curves

Current-voltage curves were obtained under steam electrolysis conditions in various vapour pressure regimes (0.5, 10 and 23 mbar). Since the measurements were carried out in a three-electrode set-up, the resulted potential is defining the working electrode potential. Typically before I V measurements, the cells were treated with (50%H_2/50%H_2O) mixtures and then exposed to water vapours.The potential scale was then recalculated with IR correction in order to obtain the overpotential of the WE, and the current was recalculated with the area of each cell used.

2.4.1. I-V Curves and EIS Normalization for different cells

This section demonstrates the normalization procedure of the electrochemical measurements (both IV and EIS) used in most of the experiments presented in this PhD thesis. The followed

procedure is the same for Ni-GDC/YSZ/Pt or Ni-YSZ/YSZ/Pt electrochemical cells. The IV curves recorded in 3-elecrtode cells and the voltage (Vapp) was applied and measured in respect to the reference electrode of the cell. The overpotential η at the WE was obtained by subtracting the ohmic drop in the electrolyte (and the contact resistances and wires) from the applied voltage Vapp. using equation 23 [160].

$$\eta = -(\text{Vapp.} - \text{Rohm} * \text{IDC}) \qquad \text{(Eq.23)}$$

where Rohm represents the ohmic resistance (obtained from the high frequency intercept in impedance spectra, and IDC is the steady state DC (direct current) current flowing during polarization experiments. On the other side, the current density I in (mA/cm^2) is normalized by the surface area of the WE, given by:

$$I = \frac{\text{IDC}}{\text{WE surface area}} \qquad \text{(Eq.24)}$$

An example of converting the y-axis of an IV curve from the measured potential V to the overpotential at the working electrode η is given in fig. 2.13.

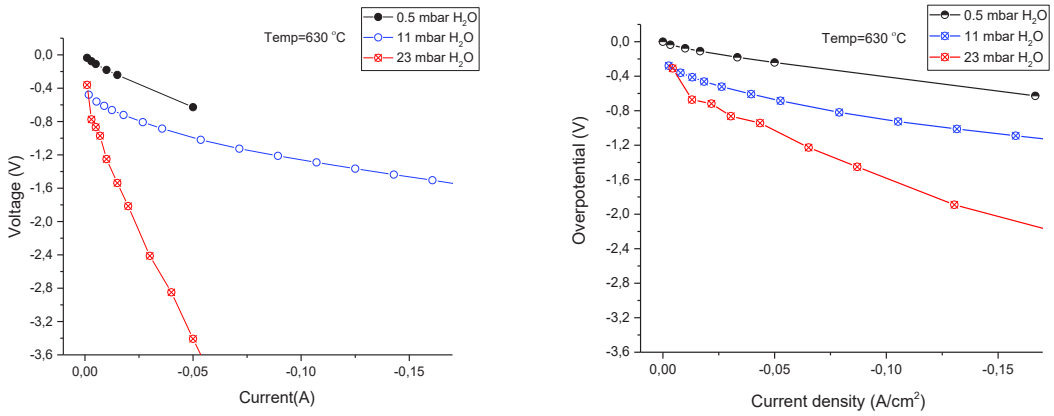

Figure 2.13. Left IV Curve: Before normalization, Right IV Curve: After normalization Current density-overpotential curves measured under steam electrolysis conditions at 630 °C in3 vapour pressure regimes (0.5, 10 and 23 mbar).

The normalization procedure for the Nyquist plot by galvanostatic EIS measurements was done by taking into account the surface area of the electrode. The simple formulas 25 and 26 were used to normalize the plots. A characteristic example is shown in fig. 2.14.

$$Zre(Ohm.cm2) = Zre * \text{WE surface area} \quad \text{(Eq.25)}$$

$$Zim(Ohm.cm2) = |Zim| * \text{WE surface area} \quad \text{(Eq.26)}$$

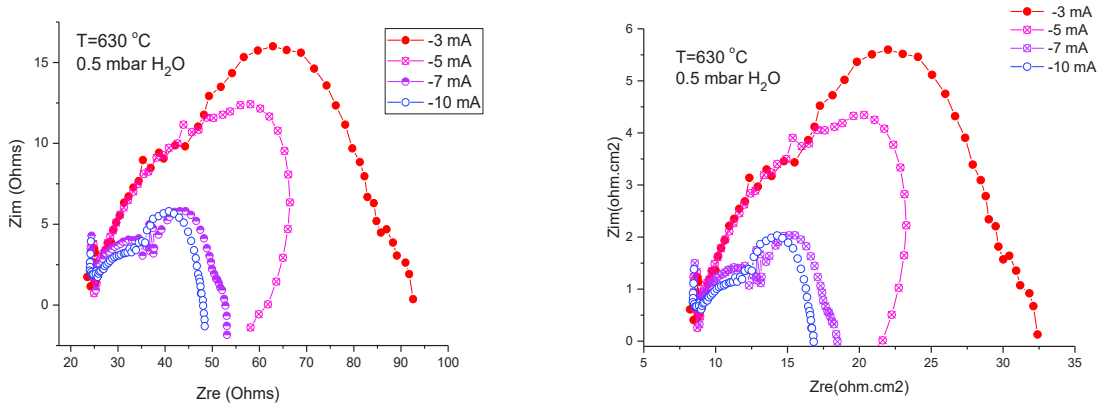

Figure 2.14. Left EIS: Before normalization, Right EIS: After normalization, Nyquist plot by galvanostat EIS obtained on Ni-YSZ cathode under 0.5 mbar water vapor and 630 °Cat different currents at the advanced laboratory setup (ICPEES, France).

2.5. Short technical description of the main Characterization techniques

Pristine and post-mortem electrochemical cells have been characterized in-situ and ex-situ using the methods included in this chapter.

2.5.1. X-ray Diffraction

The phase composition of the CeO_2/ NiO (10 mol%) powder sample and $Ni_{0.1}Ce_{0.9}O_{2-x}$drop casted sample were studied with X-ray powder diffraction (XRD) using a Bruker D8 Advance diffractometer with a Cu source.The program FullProf[161]was used for Le Bail refinements. The reference data were taken from the database of the International Centre for Diffraction Data (ICDD).

2.5.2. X-ray Photoelectron Spectroscopy

Primary experiments of the pristine and post-mortem electrochemical cells have been performed using XPS under UHV conditions (10^{-9} mbar). The apparatus is equipped with a VSW Class WA hemispherical electron analyzer (150 mm radius) and a monochromatic Al Ka X-ray source

(1486.6 eV). The analysis of the XP spectra will be discussed for each particular case in the next chapters.

2.5.3. Scanning Electron Microscopy

Combining scanning electron microscopy technique with the in-situ electrochemical NAPXPS results is a great tool for the interpretation of the morphological changes occuring to the electrode during the measurements. The SEM instrument used for my PhD studies is Zeiss Gemini SEM 500 with a lattice resolution of 1 nm. The measurements were done by Thierry Dintzer (ICPEES, France).Energy dispersive X-ray spectroscopy (EDXS) mapping was combined with the SEM images to resolve the different elements on the surface of the electrodes.

2.5.4. Scanning Transmission Electron Microscopy

Metal-substituted Ceria NanoParticles (NiCeOx NPs) were used in this workas electrocatalytic promoters for improving the working electrode electrochemical performance. The TEM analysis of $Ni_{0.1}Ce_{0.9}O_{2_x}$was carried out in the scanning mode (STEM) using bright field and annular dark field detectors on a JEOL 2100F working at 200 kV, equipped with a probe aberration corrector. The analysis was done at IPCMS (France).The sample powder was dispersed in a beaker containing ethanol solution and sonicated for 5 minutes inside an ultrasound bath. Then, a dropper (Pasteur pipette) was used to deposit one drop of the as prepared solution on a commercial copper grid covered with a holey carbon membrane destined to the TEM observation.

2.5.5. Raman Spectroscopy

Raman spectroscopy is sensitive to the modification of the local structure of the crystals and particularly to lattice defects. Raman spectra were acquired using a micro-Raman spectrometer (Horiba LabRam), with excitation wavelength of 532 nm. A 100xobjective was used to focus the excitation laser to an approximately 1mm spot with a laser power of less than 1 mW, to avoid heating and damage of the sample.

Chapter 3. Influence of surface state on the electrochemical performance of nickel-based cermet electrodes during steam electrolysis

III. Chapter 3. Influence of surface state on the electrochemical performance of nickel-based cermet electrodes during steam electrolysis

3.1. Introduction

Nickel-based cermet electrodes are the most widely adopted electrodes in solid oxide cell fabrication. Precisely, Ni, in combination with yttria-stabilized zirconia (YSZ) or gadolinium-doped ceria (GDC), forming Ni-YSZ or Ni-GDC cermets respectively, are used for SOECs cathode electrodes. Due to its low cost, high electron conductivity and thermal compatibility with other cell components, nickel mixed with yttria-stabilized zirconia (YSZ)[11] is the most commonly used SOEC cathode [86]. The role of Ni is mainly to provide the electrocatalytic sites and electronic conductivity, while YSZ conducts oxygen ions into the electrolyte and secures the mechanical stability of the electrode[77]. Since YSZ exhibits negligible electrocatalytic activity towards water dissociation, the electrochemical reactions mainly occur in the vicinity of Ni, YSZ and fuel gas (three-phase boundaries, 3PB).[77] Therefore replacement of YSZ with a porous mixed ionic-electronic conductor (MIEC) material, which can also act as the electrocatalyst, has been considered as a method to increase the reaction sites of the electrodes. Doped ceria (DC) is probably the most suitable MIEC material for this purpose, since it combines good electronic and ionic conductivities with high electrochemical activity.[162] The electrochemical reaction sites over DC are not limited in the 3PB with nickel but are extended to the entire DC surface. A major drawback of SOECs devices is the insufficient long term stability of their performance.[163] Changes of the chemical composition and the oxidation state of the cathode electrode have been also reported to induce deactivation.[164] Oxidation of nickel to NiO or $Ni(OH)_2$, may occur when the cell is operating under low H_2 production and high steam concentration conditions,[165] by air leaks in the fuel circulation system, or even after long term operation. Extended nickel oxidation or bulk NiO formation, has an evident macroscopic influence on the cell (e.g. micro cracks, coarsening etc.), due to the large Ni-NiO volume change.[166] Moreover, under mild oxidative conditions a NiO layer can be formed on top of the Ni phase affecting the cell performance.[164] This kind of degradation is usually reversible and the performance is improved upon reduction of nickel, challenging its detection by post-mortem cell analysis.[1] Much less is known about the chemical state of ceriain Ni-GDC electrodes, but since oxygen vacancies are considered as the electrochemically reactive sites, a mixed Ce^{3+}/Ce^{4+} oxidation state is usually assumed.[167] The electrochemical methods typically employed for in

situanalysis of SOECs, for example impedance spectroscopy measurements, cannot provide analytical evidence about the oxidation state of each electrode components, therefore the correlation between the SOEC performance and the electrode chemical state remains elusive[164], [168].

In situ near ambient pressure X-ray photoelectron and near edge absorption fine structure spectroscopies (NAPXPS and NEXAFS, respectively) were performed at ISISS beamline at BESSY synchrotron radiation facility at the Helmholtz- Zentrum-Berlin. Two types of electrolyte supported electrochemical cells, with different working, but identical counter and reference electrodes, were fabricated for this study. The NiO-YSZ (Fuel Cell Materials, 66:34 wt%, 8-mol.% Y_2O_3-*doped* ZrO_2) and NiO-GDC. Initial annealing of the cells in 0.5 mbar O_2 was used prior to spectroscopic measurements to eliminate residual carbon from the surface. After this procedure the C 1s signal was within the noise level during all experiments. Unless otherwise stated, the total pressure during the experiments was kept constant at 0.5 mbar. No significant electrostatic charging was observed under the employed temperature and pressure conditions. The average thickness of the NiO overlayer formed over the metallic nickel particles core was determined by the Ni 2p photoelectron peak intensity using the simplified formula described in reference [171].

Electrochemical experiments were also performed on commercial prefabricated NiO-YSZ//YSZ and NiO-GDC//YSZ half cells (Kerafol GmbH, both 150 μm YSZ) in a laboratory reactor[23] which could operate at conditions similar to those of the synchrotron experiments. The aim was twofold: first to confirm that the electrochemical response of the cells under the employed reaction conditions is a general characteristic of the cermet electrodes, and to perform EIS characterization of the cells without the time restrictions applied in synchrotron-based experiments. These experiments confirmed the reproducibility of the electrochemical performance, while the EIS spectra and the scanning electron microscopy (SEM) micrographs presented in this work were recorded using these cells. The surface morphology was inspected by SEM using a Zeiss GeminiSEM 500 microscope. Energy-dispersive X-ray spectroscopy (EDXS) mapping was combined with the SEM images to resolve the different elements on the surface of the electrodes.

In this work we provide a direct correlation between Ni-YSZ and Ni-GDC electrodes surface oxidation states and their performance during steam electrolysis using operando experimental evidence provided by near ambient pressure X-ray photoelectron and near edge X-ray absorption fine structure spectroscopy. We show that nickel surface oxidation may induce significant performance degradation in Ni-YSZ cathodes, while on the contrary it has minor effects in Ni-GDC. Remarkably, we found that in case of Ni-GDC electrodes, small modification of GDC oxidation state can have an important impact on the electrolysis performance. The results highlight the crucial role of the cathode electrode surface oxidation state on the SOEC functionality and have potential implications for the design and operation strategies of more efficient and durable SOEC devices.

This chapter is based on the published article: Basma Mewafy, Fotios Paloukis, Kalliopi M. Papazisi, Stella P. Balomenou, Wen Luo, Detre Teschner, Olivier Joubert, Annie Le Gal La Salle, Dimitris K. Niakolas and Spyridon Zafeiratos. Influence of surface state on the electrochemical performance of nickel-based cermet electrodes during steam electrolysis. ACS Applied Energy Materials **2019**, doi: *10.1921/acsaem.9b00779*.

3.2. Description of the *in situ* electrochemical experiments with O_2 introduction in the H_2O/H_2 feed

The degradation tests in the presence of O_2 were performed following a similar experimental routine for both cell types. The electrodes were initially reduced in H_2 at 640 °C and then the gas feed switched to 75% H_2O/25% H_2 and a constant current between the cathode and the anode at 640 °C (electrolysis conditions) was applied. Gradually and without changing the operation conditions otherwise, different amounts of O_2 (from 3% up to 17%) were introduced in the H_2O/H_2 mixture keeping the overall pressure constant at 0.5 mbar. The degradation of the cell was evaluated by measuring the potential change between working and reference electrodes. This potential is corrected for the ohmic drop (given by the high frequency cut off in the impedance spectra measured at identical conditions) and is presented as the overpotential. The Electrochemical Impedance Spectra (EIS) were measured in galvanostatic conditions (20 mA) with frequency range from 10 mHZ to to 100 KHz (for Ni-GDC electrode) or 500 KHz (for Ni-YSZ electrode) and a signal amplitude of 2 mA. The Nyquist plots were fitted using the ZView2-Software, in order to identify the frequency response of the different involved phenomena. To compare the cells with Ni-YSZ and Ni-GDC electrodes the % increase of the potential as compared to its initial values (before O_2 introduction) was calculated. Please note that prior to the introduction of O_2 the sample was left to the same conditions for about 1 h in order to stabilize the potential.

3.3. The effect of nickel oxidation on the cell performance

The reduction kinetics of nickel oxide (NiO) in H_2 are extremely fast, especially at high temperature, therefore NiO reduces to metal within few seconds in the H_2O/H_2 mixture.[1], [41], [169], [172] In order to investigate the effect of nickel oxidation during steam electrolysis, O_2 was co-introduced with H_2O/H_2 at constant current operation conditions. Nickel oxidation is expected to be homogeneous into the whole cermet volume, since at intermediate temperatures (<700 °C) the oxidation process is not limited by the O_2 gas diffusion[173]. Accordingly, the NAP-XPS spectra recorded on the surface of the cathode are also representative for the chemical state at the interface with YSZ electrolyte. Below we describe the experiments performed at two cells utilizing Ni-YSZ and Ni-GDC electrodes, respectively.

3.3.1. Ni-YSZ cathode: Surface composition and electrochemical behavior

Fig. 3.1a shows the evolution of the Ni-YSZ/YSZ/Pt cell overpotential and the QMS signal of m/e 32 (oxygen) as a function of time. A constant current of -100 mA/cm^2 was applied at the Ni-YSZ cathode while the 3/1 H_2O/H_2 mixture composition and the overall pressure were maintained throughout the experiment. Initially under H_2O/H_2 flow the overpotential is stabilized at ca. 0.9 V after a short transition period of about 15 min. The introduction of O_2 in the H_2O/H_2 feed induces significant cell deactivation as indicated by the gradual increase of the overpotential. A clear trend between the increase of O_2 partial pressure and the overpotential can be established, while the process is reversible and the potential recovers when O_2 is switched back to lower pressure (around 210 min in Fig. 3.1a). Characteristic Ni 2p NAP-XPS spectra collected at various stages of the experiment are shown in figure 1b. Based on earlier photoemission studies the Ni 2p peak can be deconvoluted into two components; one sharp Ni $2p_{3/2}$ peak around 853 eV which corresponds to metallic Ni, and a broader Ni $2p_{3/2}$ feature at 856 eV associated to oxidized Ni[50], [159], [174]. The spectrum recorded in H_2O/H_2, is exclusively due to metallic Ni, while upon co-feeding of O_2 the characteristic peak of oxidized Ni appears. The contribution of the NiO-related component to the overall Ni 2p spectrum increases with the O_2 partial pressure. Please note that the Ni $2p_{3/2}$ peak at 853 eV does not exhibit the distinctive shoulder at about 854.5 eV typically observed for stoichiometric NiO[175]. This fact suggests that the structural and electronic properties of oxidized Ni differ from those of bulk NiO material. However, for simplicity we will refer to the oxidized Ni as NiO.

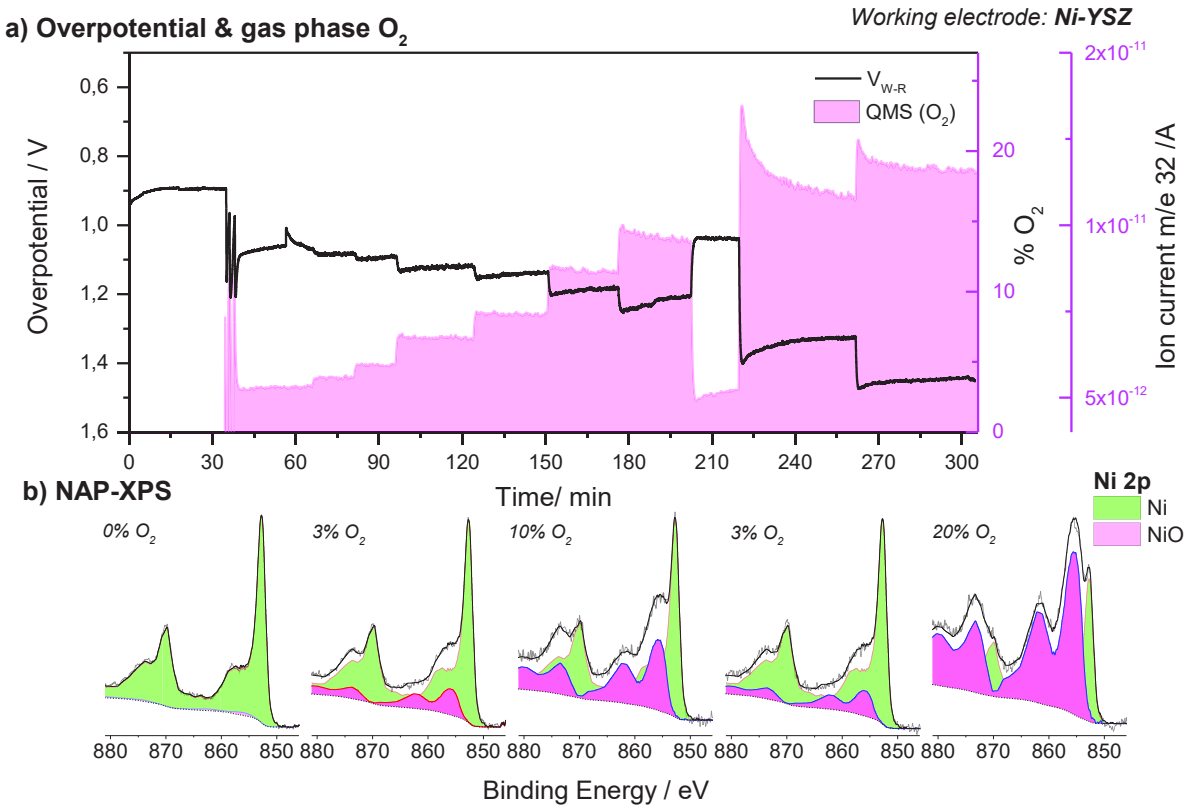

Figure 3.1. a) Time evolution of the Ni-YSZ cathode overpotential (*black line*) and the on line mass spectrometer signal of oxygen (*pink line*) measured at constant current of -100 mA/cm^2 while different concentrations of O_2 were introduced in the H_2O/H_2 feed. The temperature was kept constant at 640 °C. b) Ni 2p NAP-XPS spectra recorded during characteristic moments of the conditions appearing in a. Two Ni 2p components were used to fit the spectra corresponding to metallic Ni (green) and oxidized NiO (pink).

3.3.2. Ni-GDC cathode: Surface composition and electrochemical behavior

The influence of nickel oxidation on the Ni-GDC cathode performance was examined on a Ni-GDC/YSZ/Pt cell following a procedure similar to Ni-YSZ. The overpotential and m/e 32 QMS signal recorded at -100 mA/cm^2 and at various O_2 concentrations in the H_2O/H_2 mixture are shown in fig. 3.2a. Surprisingly, while the increase of the O_2 partial pressure in the H_2O/H_2 feed is manifested by the online QMS signal, the overpotential change is minor in comparison to the Ni-YSZ electrode. As shown by the real time NAP-XPS spectra in fig. 3.2b, the evolution of NiO component in the Ni 2p peak follows the O_2 partial pressure confirming that nickel is

gradually oxidized by gas phase O_2, similar to Ni-YSZ. Thus, surface NiO formation has a much inferior effect on the Ni-GDC cell overpotential as compared to Ni-YSZ cell.

Comparison of the Ni 2p spectra of the two electrodes fig. 3.1b and 3.2b shows that nickel oxidation starts at lower % O_2 for Ni-YSZ as compared to Ni-GDC. This divergence might be attributed to differences in the microstructure and/or the ability of nickel to chemisorb and dissociate oxygen species from the gas phase, which are known factors affecting nickel oxidation[176]–[178]. One can argue that the preparation and the pre-treatment of the two electrodes affect differently the nickel microstructure and surface sites and in turn, influence the oxidationkinetics. However, the observed differences are restricted at the initial oxidation stages, while at higher % O_2 nickel oxidation is similar for both electrodes.

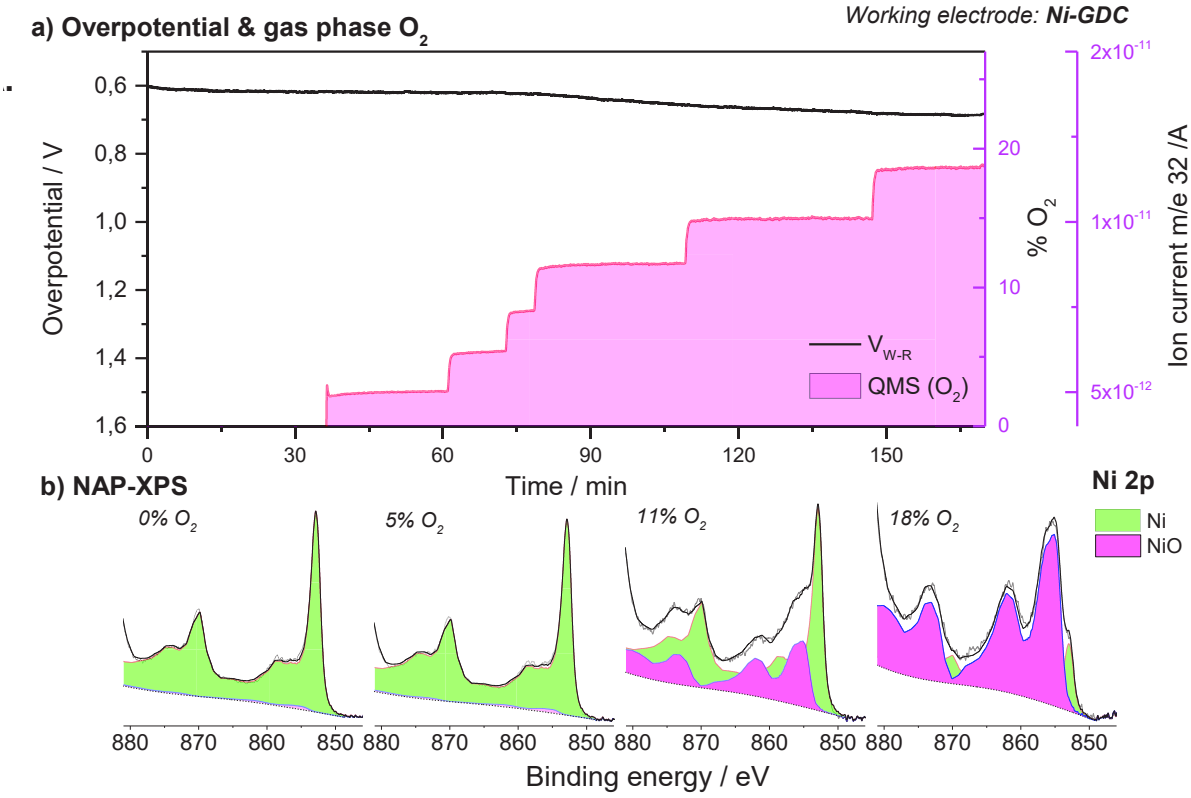

Figure 3.2. a) Time evolution of the Ni-GDC cathode overpotential (*black line*) and the *on line* mass spectrometer signal of oxygen (*pink line*) measured at constant current of -100 mA/cm^2 while different concentrations of O_2 were introduced in the H_2O/H_2 feed. The temperature was kept constant at 640 °C. b) Ni 2p NAP-XPS spectra recorded during characteristic moments of

the conditions appearing in a. Two Ni 2p components were used to fit the spectra corresponding to metallic Ni (green) and oxidized NiO (pink).

3.4. Stability of Pt electrodes: Surface composition and electrochemical behavior

In order to ensure the chemical stability of Pt electrodes in the presence of O_2, the Pt 4f spectra of the counter electrode under similar conditions were measured by NAP-XPS in a separate experiment as shown in fig. 3.3. These experiments show that Pt is metallic under all tested conditions and its oxidation state is not affected by the applied current or by gas phase O_2.

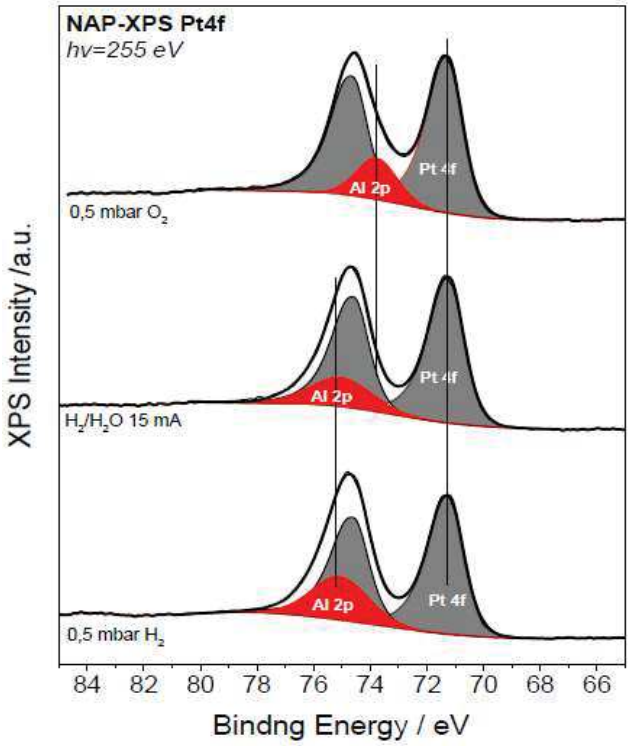

Figure 3.3. The NAP-XPS Pt 4f peak measured on the counter electrode of the Ni-YSZ/YSZ/Pt cell in 0.5 mbar (*from bottom to the top*) H_2 at 500 °C, H_2O/H_2 at 640 °C and application of +15 mA between Pt and Ni-YSZ electrodes, O_2 at 500 °C. The Pt 4f peak is identical in all cases and corresponds to that of the metallic Pt without any evident peak of PtO_x. The peak of Al 2p is due to traces of alumina visible through the pores of the Pt electrode. Alumina remained on the YSZ electrolyte after the sandblaster cleaning procedure and before application of the platinum paste.

Apart from the chemical stability of Pt we also tested the influence of O_2 addition on the electrochemical reaction kinetics, considering that O_2 is the product of oxygen ion oxidation at the anode and by introducing it in the feed we change the reaction equilibrium. For this purpose we prepared symmetric electrochemical cells where Ni-YSZ was replaced by a Pt electrode. Since, as shown in fig. 3.3, the Pt oxidation state is not influenced by the introduction of O_2 in the feed, this experiment can indicate a possible influence of the reaction kinetics on the overpotential on chemically stable electrodes. In fig. 3.4 we show that the addition of O_2 in the H_2O/H_2 feed does not have an evident effect on the measured overpotential when a symmetric Pt cell is used, and accordingly its effect on the electrochemical reaction kinetics should be neglected. Therefore, since O_2 addition has no measurable effects on the chemical state of Pt counter/reference electrodes and the reaction kinetics, the overpotential increase observed upon introduction of O_2 should be correlated to the distinct modifications observed on the cathode chemical state.

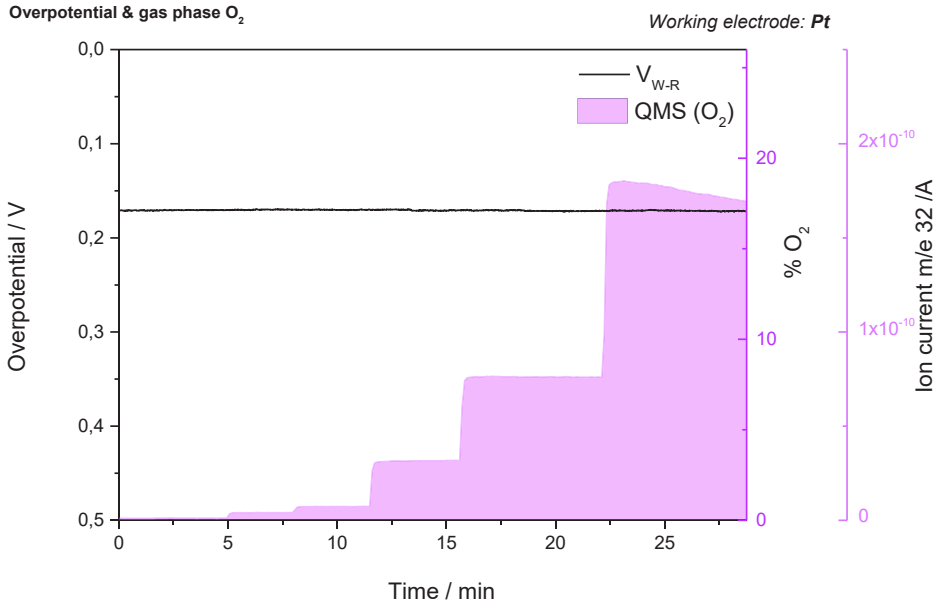

Figure 3.4. Time evolution of the Pt cathode overpotential (*black line*) and the on line mass spectrometer signal of oxygen (*pink line*) measured at constant current of 40 mA/cm^2 while different concentrations of O_2 were introduced in the H_2O/H_2 feed. The temperature was kept constant at 650 °C.

3.5. The effect of the oxidation state of the ceramic part on the cell performance

3.5.1. Zr 3d for Ni-YSZ ceramic part

Having shown that the surface oxidation state of nickel has divergent impact on Ni-YSZ and Ni-GDC electrodes, we explore now the effect of the chemical state of the ceramic part. In case of Ni-YSZ, the Zr 3d core level peak (fig. 3.5) is characteristic of doped YSZ[169], [179]. The spectrum shifts to higher binding energy under polarization as compared to open circuit, however the peak shape is not affected by the applied current or the presence of O_2. The observed binding energy shift is induced by changes of the overpotential across the Ni/YSZ electrochemical interface as has been demonstrated in previous photoemission studies.[146], [180] The stable Zr 3d peak shape is in agreement with reports suggesting that the chemical state of YSZ is not influenced by the applied current or the presence of O_2[169]. The high thermal and chemical stability of the YSZ surface, support the hypothesis that the performance of the cell with Ni-YSZ cathode is primarily related to the oxidation state of nickel.

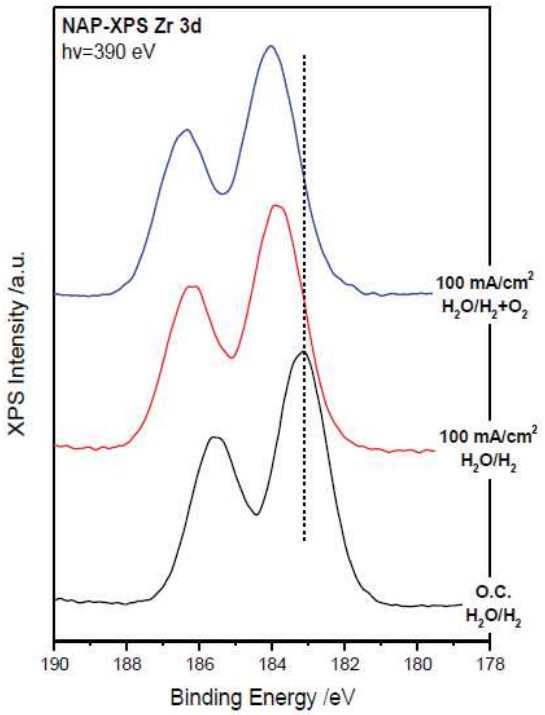

Figure 3.5. The NAP-XPS Zr 3d peak measured on the Ni-YSZ cathode electrode in 0.5 mbar H_2O/H_2 at 640 °C (*from bottom to the top*) at open circuit, application of 100 mA/cm^2 and application of 100 mA/cm^2 and co-feed of O_2.

3.5.2. Ce 3d for Ni-GDC ceramic part

In case of the Ni-GDC electrode the analysis of the Ce 3d spectrum prior to current application shows that GDC contains contributions of both Ce^{3+} and Ce^{4+} cations (fig. 3.6) in accordance with several previous reports of ceria in H_2O/H_2 mixture.[1], [50], [142], [181], [182] The ratio between Ce^{3+} and Ce^{4+} does not change appreciably with the applied current, yet upon O_2 introduction a small, but consistent, increase of the Ce^{4+} component is observed in the Ce 3d spectrum (fig. 3.6.) This can be clearly seen in the Ce M_5-edge NEXAFS spectrum shown in fig. 3.7. Although ceria oxidation state is much less influenced in the presence of O_2 as compared to nickel, according to previous findings its impact on the electrode activity might be substantial[7], [142], [148].

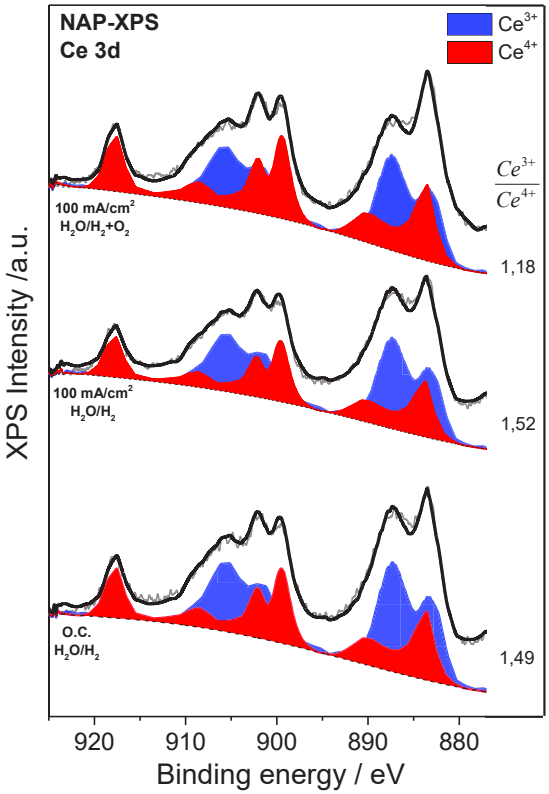

Figure 3.6. The NAP-XPS Ce 3d spectra measured on the Ni-GDC cathode electrode in 0.5 mbar H_2O/H_2 at 640 °C (*from bottom to the top*) at open circuit, application of -100 mA/cm^2 and application of -100 mA/cm^2 and co-feed of O_2. Two Ce 3d components were used to fit the spectra corresponding to Ce^{3+} (blue) and Ce^{4+} (red) oxidation states.

3.5.2.1. Ce M_5-edge NEXAFS spectrum of Ni-GDC electrode in H_2O/H_2 and $H_2O/H_2/O_2$ environments

The Ce M_5- edge NEXAFS lines (fig. 3.7) were used to detect slight modifications in the GDC oxidation state since NEXAFS spectra have a much higher signal to noise ratio as compared to NAP-XPS. In addition, due to the higher analysis depth of NEXAFS in TEY mode as compared to NAP-XPS (4 or 5 nm instead of ca. 2 nm), NEXAFS results can be used to conclude if oxidation is also propagated in deeper layers or if it is restricted exclusively at the outer surface. The Ce M_5- edge peaks recorded at 640 °C in galvanostatic mode (-100 mA/cm^2) before and during co-feed of O_2 in the H_2O/H_2 mixture show some marginal, but reproducible, differences. The curve obtained by subtraction of the spectra recorded in H_2O/H_2 from the one in $H_2O/H_2/O_2$ (indicated as Diff. in fig. 3.7) after proper intensity normalization, resembles very much to that of the standard CeO_2 sample (CeO_2 ref.). This observation suggests that by introducing O_2 in the H_2O/H_2 feed we increase the amount of the Ce^{4+} component in the Ce M_5- edge spectra. This observation implies partial oxidation of GDC in $H_2O/H_2/O_2$ in accordance with the NAP-XPS results shown in the main text.

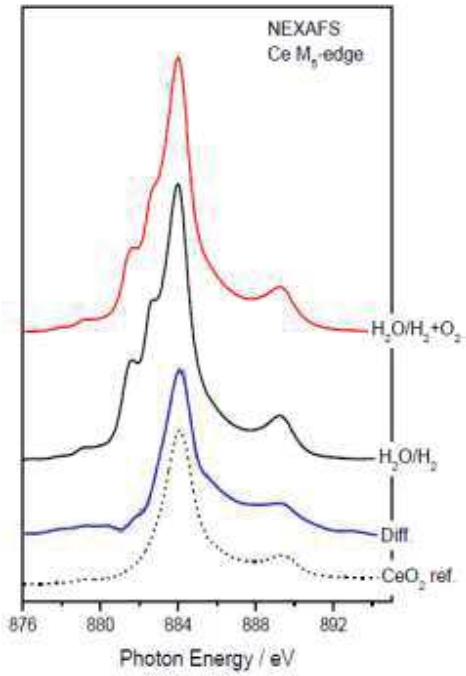

Figure 3.7. Ce M_5-edge NEXAFS spectra measured on the Ni-GDC electrode in 0.5 mbar H_2O/H_2 at 640 °C and at a current of -100 mA/cm^2 before and during co-feed of O_2. The

mathematical difference between the two curves is shown in blue line, while the reference spectrum of Ce_2O is included for comparison.

3.6. The effect of ceria oxidation state: Surface composition and electrochemical behavior

3.6.1. The effect of ceria oxidation state over reduced Ni-GDC electrode

The impact of the GDC oxidation state cannot be safely evaluated from the above presented results because the introduction of O_2 in the H_2O/H_2 mixture influences the chemical state of both nickel and GDC areas. In order to maintain nickel in a stable oxidation state while varying that of GDC, we take advantage of the much slower kinetics of ceria reduction in H_2O/H_2 mixture as compared to nickel oxide[50]. In particular, a pre-oxidized Ni-GDC electrode was exposed to H_2O/H_2 atmosphere and almost instantly an electrical current of -100 mA/cm^2 was applied while Ce 3d spectra were collected in short time periods (ca. every 10 min). Fig. 3.8a presents the evolution of the overpotential as a function of time recorded in this experiment. It is clear that within the first 40 min the overpotential decreased around 200 mV, while a plateau of about 750 mV was reached after 1 hour. The Ni $2p_{3/2}$ spectrum recorded in H_2O/H_2 mixture prior to current application shows a characteristic peak of metallic Ni (fig. 3.8b). This confirms that NiO which is formed during the pre-oxidation step is reduced almost instantly to the metallic state upon introduction of H_2O/H_2. On the other hand, the Ce 3d peak shape is modified (fig. 3.8b), which, according to the fitting process, is due to the relative increase of the Ce^{3+} species as shown in fig. 3.9. The noticeable agreement between the formation of Ce^{3+} and the improvement of the cell performance becomes evident in (fig. 3.8a), where the evolution of ceria oxidation state is compared with the cell overpotential.

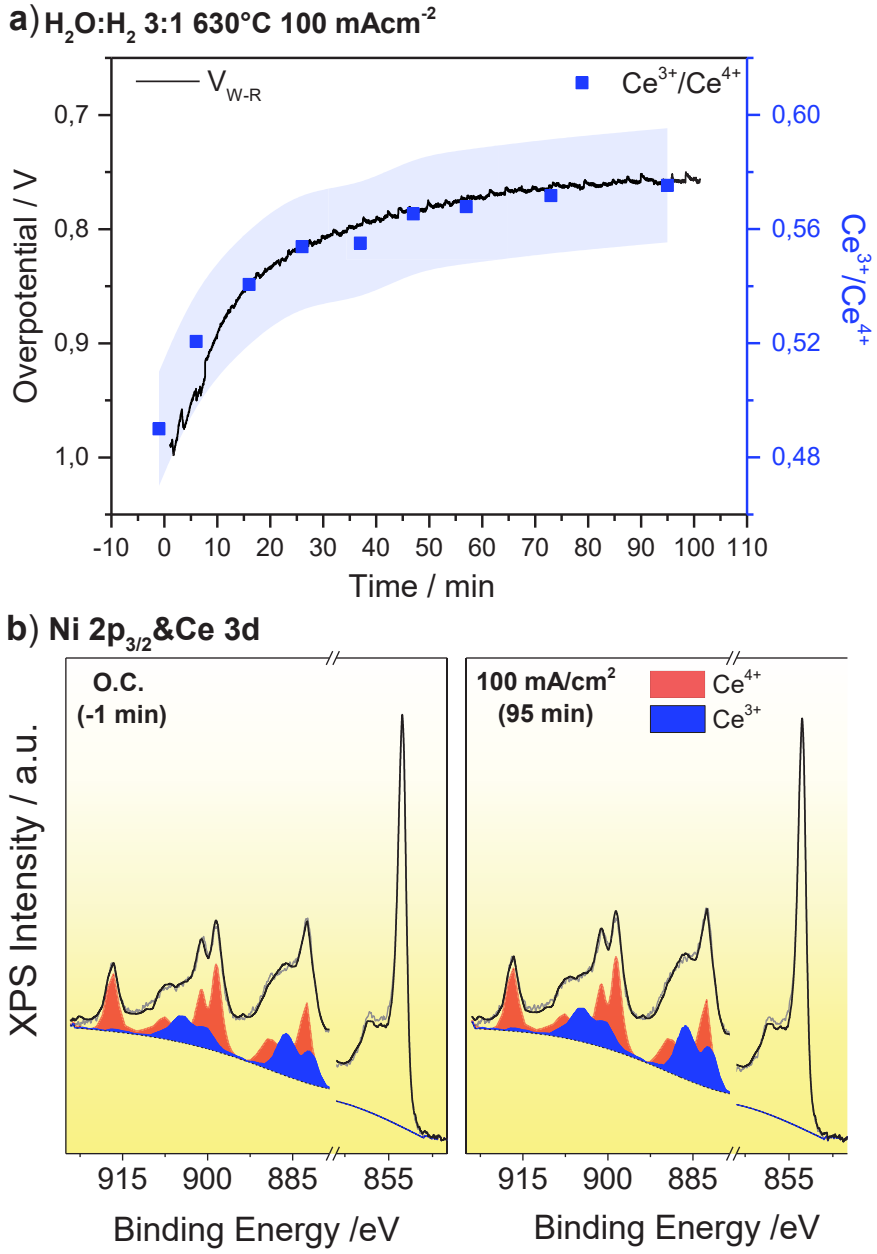

Figure 3.8. Reduction of Ni-GDC electrode a) Time evolution of the Ni-GDC/YSZ/Pt cell overpotential (*solid black line*), and the evolution of Ce^{3+}/Ce^{4+} components ratio (*blue points*) as derived by the analysis of the corresponding NAP-XPS Ce 3d spectra. Measurements were performed on pre-oxidized Ni-GDC cathodes in 3:1 H_2O/H_2 gas mixture at 640 °C and at constant current of -100 mA/cm^2. The blue color background represents the uncertainty in the calculation of the Ce^{3+}/Ce^{4+} ratio mainly related to the deconvolution procedure. b)

Characteristic $Ni2p_{3/2}$ and Ce 3d NAP-XPS spectra in H_2O/H_2 before and after current application. Two Ce 3d components were used to fit the spectra corresponding to Ce^{3+} (*blue*) and Ce^{4+} (*red*) oxidation states of ceria.

Fig. 3.9 below shows a comparison of the Ce 3d and Ni 2p NAP-XPS spectra recorded in H_2O/H_2 before the current application (O.C.) and after 95 min in electrolysis conditions. From the difference spectrum it becomes clear that the small modification in the spectrum form is related to the apearacne of extra Ce^{3+}species (reduction of GDC).

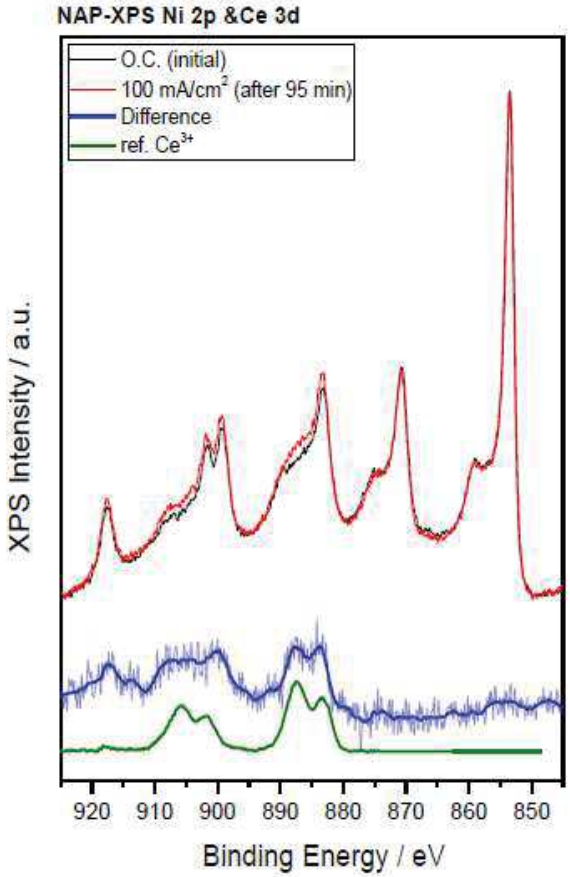

Figure 3.9. Ce 3d NAP-XPS spectra measured on the Ni-GDC cathode electrode in H_2O/H_2 before the current application (O.C.) and after 95 min in electrolysis conditions. The difference curve as well as the reference spectrum of $CeO_{1.5}$ is included for comparison.

3.6.2. The effect of ceria oxidation state over a morphologically stable Ni-GDC electrode

Despite the fact that in the above described dynamic experiment the oxidation state of Ni was constant, the Ni2p/Ce3d peak area ratio was decreasing with time, as shown in fig. 3.10 for the evolution of the Ni2p/Ce 3d peak areas ratio as a function of time for Ni-GDC under steam electrolysis conditions. This indicates losses of nickel surface area[1],[146][50], which can potentially influence the Ni-GDC electrode performance. The two primary factors contributing to the changes of the Ni2p/Ce3d peak area ratio are the modification in the volume of nickel and ceria particles and the mutual surface segregation between them, as described elsewhere[1], [148]. In order to stabilize the electrode morphology, the cell was annealed at 810 °C in H_2O/H_2 for about 6 hours. This treatment decreased the Ni/Ce ratio by about 40% (from 5.9 to 3.7), while it stabilizes the ratio during the following tests. High temperature pretreatment in H_2/H_2O induces also a significant reduction of GDC as evident by the increase of the Ce^{3+} to Ce^{4+} ratio from 0.57 to 1.54.

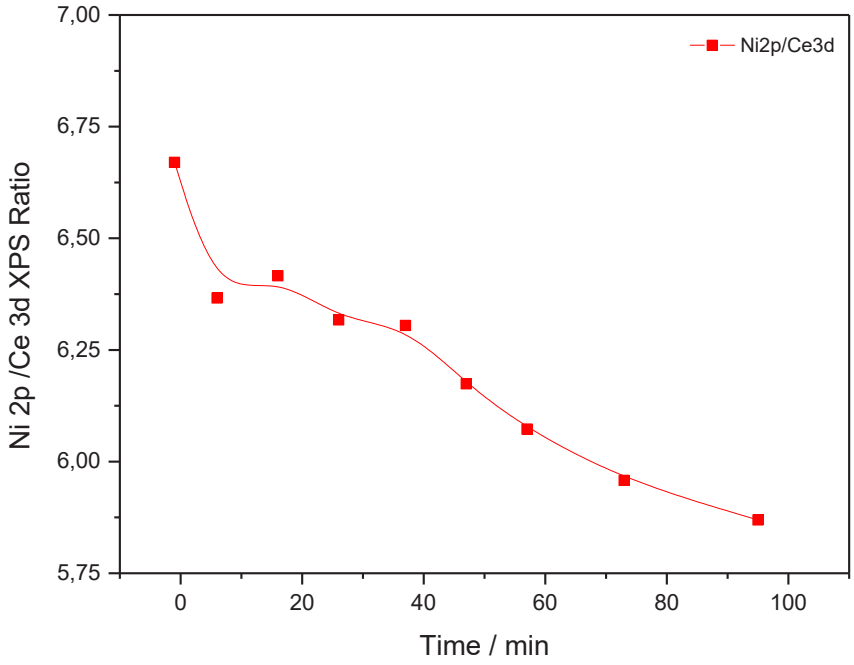

Figure 3.10. Time evolution of the Ni2p/Ce 3d peak area ratio derived by the analysis of the corresponding NAP-XPS spectra. Measurements were performed on preoxidized Ni-GDC cathode electrodes in 3:1 H_2O/H_2 gas mixture at 640 °C and at constant current of -100 mA/cm^2.

Fig. 3.11 correlates the ceria oxidation state and the cell overpotential for practically stable electrode morphology (as shown by the almost fixed Ni/Ce ratio). The different ceria oxidation states were obtained either by subjecting the sample in O_2 prior to the electrochemical reaction or by in situ transformation of GDC during electrochemical testing (the conditions of each measuring point are included in fig. 3.11 and explained in table. 3.1). In all cases the cell was measured under identical electrolysis conditions (in H_2O/H_2 mixture at -100 mA/cm^2). In this way we were able to monitor the effect of ceria oxidation state over a morphologically stable Ni-GDC electrode. A monotonic inverse correlation of the ceria oxidation state with the overpotential is observed with a significantly higher Ce^{3+}/Ce^{4+} ratio (more reduced ceria) to be favorable to lower electrolysis overpotentials.

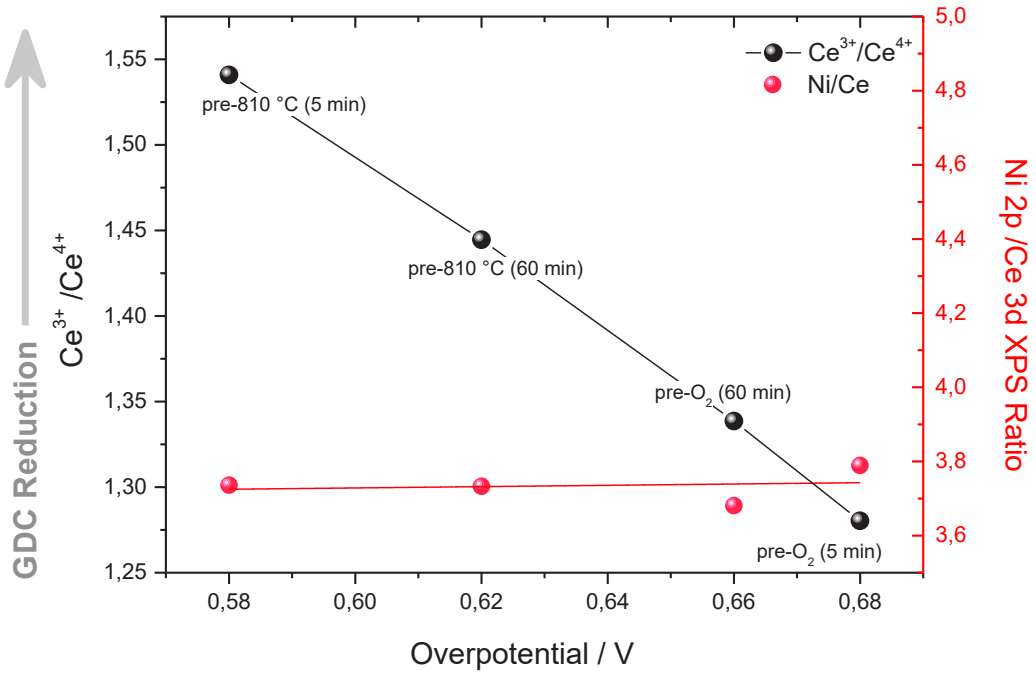

Figure 3.11. Correlation of GDC oxidation state as expressed by the Ce^{3+}/Ce^{4+} ratio and the corresponding Ni 2p/Ce 3d peak area ratio obtained by the analysis of Ce 3d NAP XPS peak as a function of the overpotential. The measurements were performed on Ni-GDC cathodes in 3:1 H_2O/H_2 gas mixture at 640 °C and at constant -100 mA/cm^2 current after cell pre-treatment at the indicated conditions.

Table 3.1. Detailed description of the Ni-GDC electrode conditioning steps shown in fig. 3.11 of the main paper. Pretreatments were performed in the spectrometer chamber (*in situ*) under overall pressure of 0.5 mbar. The pretreatment steps are given with chronological order labeled as steps 1, 2 and 3.

<table>
<tr><th rowspan="2">Abbreviation</th><th colspan="3">Pretreatment Description</th></tr>
<tr><th>Step 1</th><th>Step 2</th><th>Step 3</th></tr>
<tr><td>pre-810°C (5 min)</td><td rowspan="4">H_2O/H_2 at 810 °C for 6 hours</td><td>-100 mA/cm^2 in 3:1 H_2O/H_2 at 640 °C for 5 min[1]</td><td></td></tr>
<tr><td>pre-810°C (60 min)</td><td>-100 mA/cm^2 in 3:1 H_2O/H_2 at 640 °C for 60 min[1]</td><td></td></tr>
<tr><td>pre-O_2 (5 min)</td><td rowspan="2">3:1:1 $H_2O/H_2/O_2$ at 640 °C for 30 min</td><td>-100 mA/cm^2 in 3:1 H_2O/H_2 at 640 °C for 5 min[1]</td></tr>
<tr><td>pre-O_2 (60 min)</td><td>-100 mA/cm^2 in 3:1 H_2O/H_2 at 640 °C for 60 min[1]</td></tr>
</table>

3.7. Morphology of the tested cells

The SEM micrographs recorded on the surface of the two electrodes after the oxidation tests are presented in fig. 3.12. Both electrode types show a typical cermet structure with high porosity and distinctive grains of nickel and ceramic phases, in the size range of 1 to 5 µm. The nickel and ceramic parts of the electrode are distinguished by the EDX analysis and can be seen in the higher magnification images. The nickel particles for both electrodes appear rough and also include some irregular-shaped pores on their surface. Although nickel particles look similar in both electrode types, the morphology of the ceramic parts differs. The YSZ areas (fig. 3.12a) do not contain pores but have clearly distinguished boundaries between the sintered YSZ grains. On

the other hand the GDC (fig. 3.12b) is evidently more porous as compared to YSZ, indicating that GDC areas of the electrode are composed by a network of smaller GDC particles.

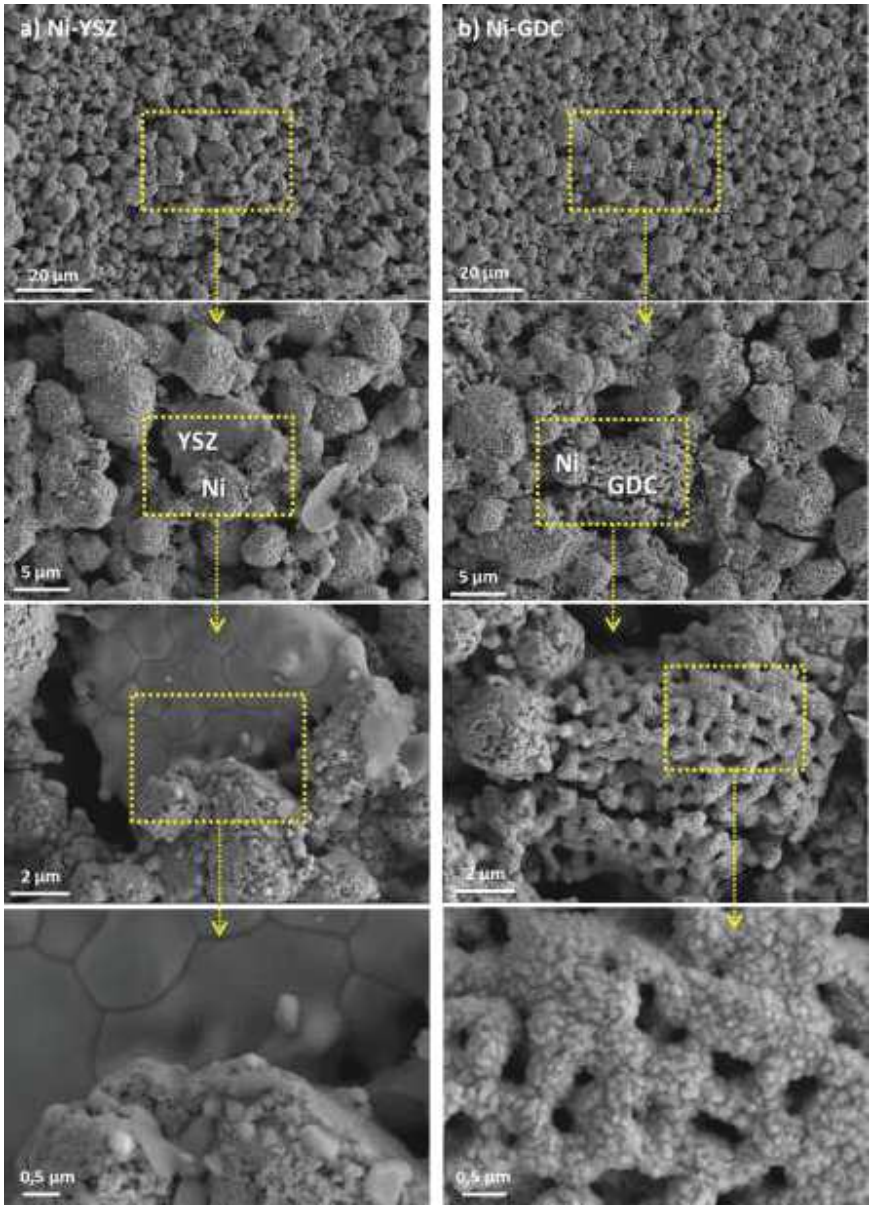

Figure 3.12. Characteristic SEM micrographs of the surface of a) Ni-YSZ and b) Ni-GDC cathode electrodes recorded after the oxidation tests.

The differences in the porosity allows one to argue that even if nickel and ceramic wt% composition is similar in the two electrodes, the surface area of GDC should be considerably higher than that of YSZ due to the porous morphology of the former. Consequently, higher

population of electrochemically active sites are expected for Ni-GDC as compared to the Ni-YSZ electrode. Likely, this might justify lower overpotential of Ni-GDC cell as compared to Ni-YSZ for the same current densities in fig. 3.1 and fig. 3.2. Nevertheless, comparison of the SEM images of Ni-YSZ and Ni-GDC spent electrodes reveal no discernible morphological differences, at least in the nickel areas. Accordingly, the differences in the electrochemical response of the two electrodes observed upon nickel oxidation cannot be justified by analogous differences in the surface structure, leaving the changes of the surface oxidation state as the most plausible explanation of the electrochemical performance.

3.8. Comparison of Ni-YSZ and Ni-GDC electrochemical performance

Comparison of fig. 3.1 and 3.2 suggests that Ni-YSZ and Ni-GDC electrodes respond differently to surface NiO formation. The effect of nickel oxidation on the overpotential of the two electrodes is directly compared in fig. 3.13a, showing the % increase of the overpotential as a function of the nickel oxidation state and the average NiO film thickness. The latter was calculated by the analysis of the Ni 2p spectra recorded in the course of the experiment.[171] A monotonic increase of the overpotential with nickel oxidation is observed for both electrodes, but in case of Ni-YSZ the overpotential increase is considerably higher. This is a quite substantial difference which indicates that the role of nickel during water electrolysis might vary in the two cermet electrodes.

Electrochemical impedance spectroscopy (EIS) is often used in order to distinguish the contribution of different cell components or processes to the total electrode impedance. The EIS spectra of Ni-YSZ and Ni-GDC electrodes measured in H_2O/H_2 (3/1) and $H_2O/H_2/O_2$ (3/1/1) feeds are compared in the Nyquist plots given in fig. 3.13b and c, respectively. The Nyquist plots of both electrodes consist of two main semi circles. The depressed high frequencies arc is attributed to the electrolyte (YSZ) bulk impedance and can be quantified by a simple fit to a resistor in parallel with a constant phase element (CPE), while the low frequency arc corresponds to processes taking part at the electrodes, typical for low temperature cell operation[183]. It can be seen that the EIS spectra of Ni-YSZ and Ni-GDC electrode cells in H_2O/H_2 are different, while they also respond differently when 20% of O_2 is added into the H_2O/H_2 flow. In order to get insights into these differences the Nyquist plots are fitted using convenient equivalent electrical circuits. In particular for the Ni-YSZ cell, a $(R_{HF}//CPE_{HF}) + (R_{BF}//CPE_{BF})$ circuit is

suitable for modelling, whereas for Ni-GDC cell, better fitting was obtained with a $(R_{HF}//CPE_{HF})+(R_{MF1}//CPE_{MF1})+(R_{MF2}//CPE_{MF2})+(R_{BF}//CPE_{BF})$ circuit (the equivalent circuits used for each cell are shown above the corresponding Nyquist plots in fig. 3.13.

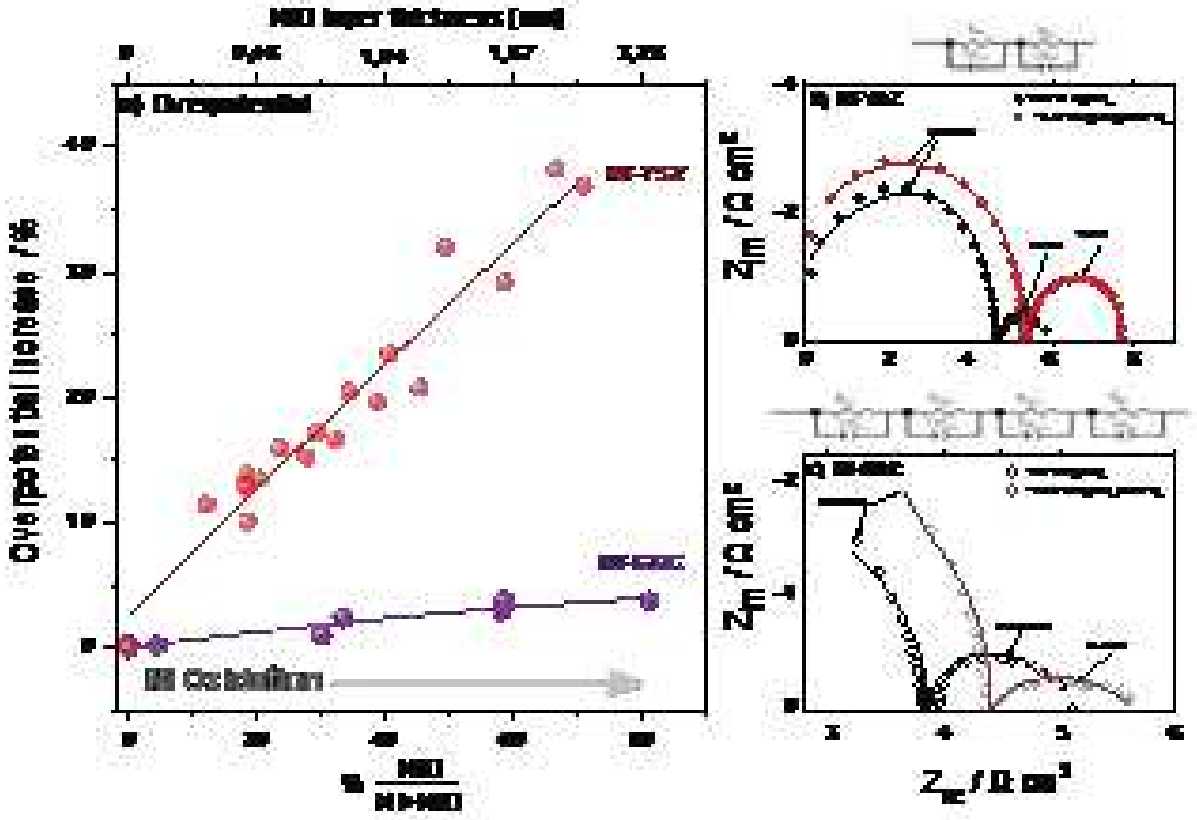

Figure 3.13. a) Comparison of the % overpotential increase of cells with Ni-YSZ and Ni-GDC cathode electrodes as a function of the relative amount of NiO and the average NiO film thickness (derived by the analysis of the corresponding NAP-XPS Ni 2p spectra recorded using 1320 eV photon energy). Measurements were performed at 640 °C and at constant current of -100 mA/cm^2 while different concentrations of O_2 were introduced in the H_2O/H_2 feed. Impedance spectra presented in Nyquist form, obtained under constant applied current of -100 mA cm^{-2} at 640 °C in H_2O/H_2*(3/1)* and $H_2O/H_2/O_2$*(3/1/1)* at total pressure of 0.5 mbar from two electrochemical cells with b) Ni-YSZ and c) Ni-GDC working electrodes. The equivalent circuits used for the fitting of impedance data are shown above of each graph. Measured data are given by symbols, whereas fit results are shown by lines. In both cells Pt counter and reference electrodes with identical geometry were used.

It should be noted that the equivalent circuit was not used for an accurate determination of each capacitance or resistance value, but mainly aims to separate the different contributions in the total resistance of the two samples (i.e. the different rate-determining steps) and identify them from their associated capacitance range. The impedance formula of a Constant Phase Element (*CPE)* is $1/Q(j\omega)^n$, with an associated real capacity part calculated from the formula $(RC)^n=RQ$[184]. The resistance and capacity values of the corresponding fitting are collected in Table 5. For the four diagrams, the high frequencies semi-circle is related to a capacity value of 10^{-7} F cm^{-2}, i.e. slightly higher than that typically observed for pure GDC or YSZ electrolytes[185]. This suggests that the corresponding phenomena are linked to the bulk impedance of the electrolyte and also to transfer reactions occurring near the electrode/electrolyte interface[89], [185]–[188]. The latter assertion was confirmed by additional EIS measurements done at different temperatures, which show a regular increase of the corresponding resistance when the temperature increases, as it is typically observed for thermally activated phenomena. In all cases the capacity value of the low frequency semi-circle (C_{BF}) ranges between 1.1 F cm^{-2} and 5.5 F cm^{-2} implying that the associated process is due to mass transfer phenomena occurring at the external side of the electrode. This attribution is in accordance with conclusions established by other authors[89], [143], [189]–[191]and was also confirmed by supplementary experiments which show the dependency of the latter phenomenon on the oxygen concentration.

Table3.2. Comparison of resistance and capacity values determined from the fit of impedance diagrams of Figures 3.13b and c. The range values within the difference between the simulated and experimental resistance values are also given.

	$R_{HF}\cdot S$ (Ωcm^2)	C_{HF}/S ($F\ cm^{-2}$)	$R_{MF1}\cdot S$ ($\Omega\ cm^2$)	C_{MF1}/S ($F\ cm^{-2}$)	$R_{MF2}\cdot S$ ($\Omega\ cm^2$)	C_{MF2}/S ($F\ cm^{-2}$)	$R_{BF}\cdot S$ ($\Omega\ cm^2$)	C_{BF}/S ($F\ cm^{-2}$)
Ni-YSZ 0.9V H_2O/H_2	4.6 ± 0.2	$2.1\ 10^{-7}$	-	-	-	-	1.30 ± 0.05	1.1
Ni-YSZ 1.46V H_2O/H_2 + 20% O_2	5.4 ± 0.2	$2.2\ 10^{-7}$	-	-	-	-	2.4 ± 0.1	3.4
Ni-GDC 0.6V H_2O/H_2	3.8 ± 0.2	$2.8\ 10^{-7}$	0.04±0.01	0.09	0.03±0.01	0.22	1.30± 0.05	5.5
Ni-GDC 0.77V H_2O/H_2 + 20% O_2	4.4± 0. 1	$2.4\ 10^{-7}$	0.28±0.02	0.09	0.70±0.02	0.18	0.4 ± 0.05	3.0

In the absence of oxygen, the two RHF values obtained for the Ni-YSZ and Ni-GDC cells are not the same, in agreement with the differences in charge transfer reactions involving GDC and YSZ. On the contrary the RBF values are identical, suggesting that RBF depends mainly on the reaction (e.g. adsorption of H_2O onto Ni sites) and not on the electrode type. The medium frequency features, associated to the RMF1 and RMF2 resistances and appearing only in the case of the Ni-GDC electrode, are assigned to polarization processes specific of the porous GDC electrode and its ability to compensate change in oxygen stoichiometry[89], [192]. It can be seen that when 20% of O_2 is added to the H_2O/H_2 flow, the RHF increases by 0.8 and 0.6 Ω cm2 for

Ni-YSZ and Ni-GDC electrodes respectively. This confirms that this resistance is not only due to YSZ or GDC conductivity, which should not be affected by Ni oxidation, but also contains the charge transfer contribution through the Ni areas. In addition, introduction of O_2 increases the RBF of Ni-YSZ by 1.1 Ω cm^2, whereas for Ni-GDC the (RMF1+RMF2+RBF) remains practically stable, suggesting that for the Ni-GDC electrode surface NiO formation does not hinder the external adsorption phenomena. Nevertheless, other processes linked to RMF1 and RMF2 resistances are slightly affected, probably due to Ce^{4+} formation as suggested by the Ce 3d spectra analysis. This result signifies that in the case of GDC, contrary to what was observed for YSZ, surface NiO formation does not influence the global mass transfer reaction kinetics which remains the rate-limiting process. Since apart of the cathode electrode, both cells have the same configuration, it is reasonable to assume that the surface oxidation state of nickel affects the electrical conduction of both cermet electrodes, but is not a crucial factor of the electrocatalytic activity of Ni-GDC, probably due to a compensation brought by the charge change in the Ce^{4+}/Ce^{3+} couple.

3.9. Comparison of the electrocatalytic activity of Ni-YSZ and Ni-GDC during steam electrolysis

The above described results suggest that the cathode surface chemical state is a crucial element of the SOEC electrochemical performance during steam electrolysis. The key processes taking place during steam electrolysis over the two cermet electrodes under reduced and partially oxidized conditions are schematically illustrated in fig. 3.14. Nickel oxidation is a known cause of cell deactivation, due to the lower NiO electrical conductivity and mechanical problems caused by volume expansion, but the specific effect of nickel *surface oxidation* on the *nm*-scale is revealed here for the first time. Previous H_2 electroxidation studies over GDC-based electrodes proposed that the reaction is predominately taking place at the ceria/gas 2PB and in a much lesser extent on the oxide/metal/gas 3PB[162]. GDC, as a MIEC material, is able to conduct *both oxygen ions and electrons*. As a result, the electrocatalytically active reaction sites will be extended to the entire GDC/gas interface. However, as mentioned above, the performance of the cell is not only a factor of the electrocatalytic activity, but also of the electrical losses of the cell, which are reflected to the electrical conductance. Here we provide direct evidence that a few nm thick layer of NiO over metallic Ni particles of the Ni-GDC cermet has a small, but not negligible, effect on the electrical performance. This is consistent with the higher electronic

conductivity of metallic nickel as compared to ceria, which is suppressed upon nickel oxidation influencing the cathode conductance.

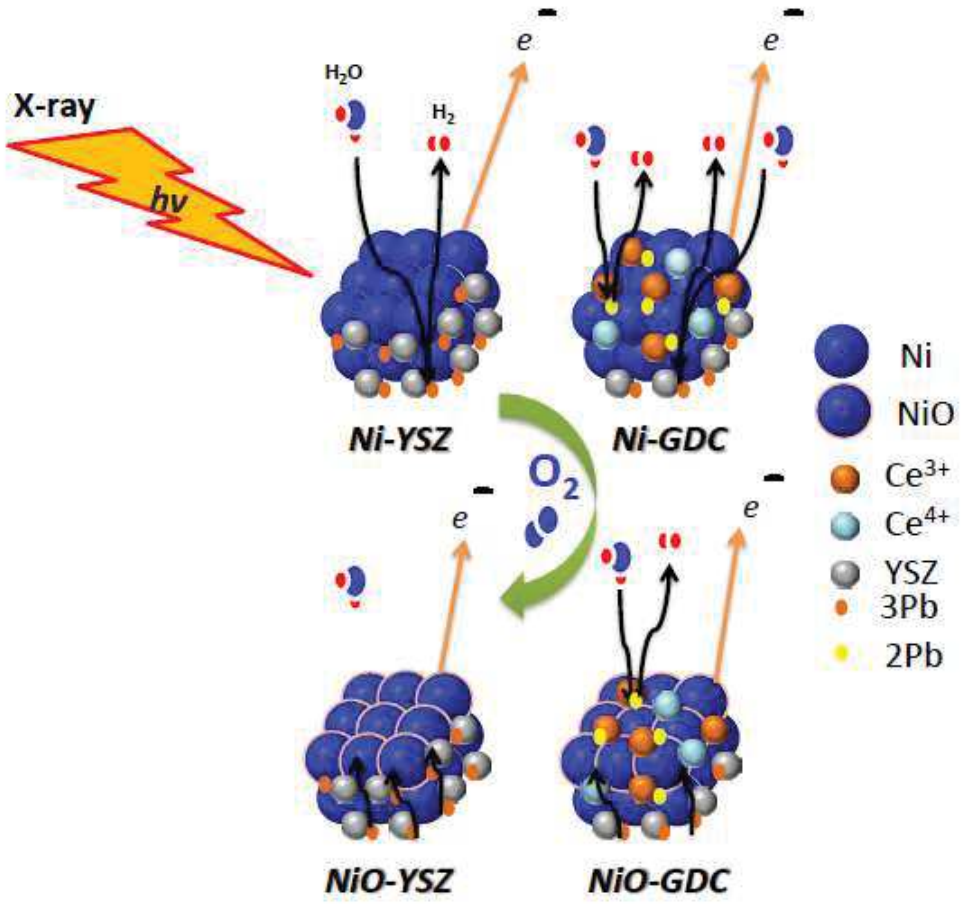

Figure 3.14. Simplified schematic illustration of steam electrolysis pathways over Ni/YSZ and Ni/GDC electrode surfaces in a) reduced and b) partially oxidized states. The specific sites that electrochemical reaction takes place are not shown in this figure.

Another remarkable result is that small changes of ceria surface oxidation state in the GDC parts may notably influence the cell overpotential. Despite the fact that previous studies have shown that ceria is maintained in a mixed Ce^{3+}/Ce^{4+} state during electrolysis conditions,[1], [7] this is the first time that the GDC valence state is directly correlated to the electrolysis performance of Ni-GDC. In particular, we found that reduced surface Ce^{3+}sites are beneficial for the cell performance. This result is not yet fully understood but it is most probably related to the increase of the concentration of oxygen vacancies and polarons (Ce^{3+}) accompanying the reduction of

GDC, which act as new electrochemical reaction sites promoting the activity of the electrode,[193] balancing the negative effect of the Ni oxidation.

The positive effect of Ce^{3+} can be also anticipated based on our previous findings on methane electroxidation over Ni-GDC,[148] which demonstrated that reduced surface ceria sites (Ce^{3+}) are optimal for high fuel cell currents. Therefore, it seems likely that reduction of GDC is a critical general characteristic related with the performance of GDC electrodes. Of course, one has to keep in mind that the valence state is determined by the reaction conditions (mixture composition, temperature and cell current),[7], [50] which will define the oxidation state of GDC under reaction equilibrium. However, our results propose that the enhancement of the GDC reducibility might be an efficient strategy to improve the performance of Ni-GDC based SOEC cells.

The reducibility of both doped and un-doped ceria might be enhanced by controlling the characteristics of the sample [194], [195] and ref. therein. In particular the number and type of defects, the population of the grain boundaries and the particle size, are known factors influencing the reduction of cerium oxide[194]–[196]. In case of doped ceria literature reports are not conclusive regarding the effect of dopant type and concentration in the ceria reducibility. For example, some studies concluded that doping will markedly increase the reducibility of ceria as compared to the pure phase,[197] while others found that dopants either do not affect ,or even hinder, the reducibility of ceria.[198], [199] Nevertheless in an eventual attempt to produce electrodes with enhanced ceria reducibility one should also take into account the fact that reduction of ceria in the bulk will increase its electronic conductivity inducing unwanted leakage current, which if present decreases the overall cell efficiency. Therefore, in an ideal case the surface of ceria electrode should be able to reduce easily to Ce^{3+} to enhance electrocatalytic activity, while in the bulk the GDC composition should remain unafected so as to maintain the mechanical and electrical properties of GDC.

3.10. Conclusions of Chapter 3

The relationship between the cell performance and the cathode surface oxidation state for Ni-YSZ and Ni-GDC cermet electrodes during steam electrolysis was analyzed. A few nm thick NiO layer on Ni-YSZ electrode was found to increase significantly the overpotential for electrolysis reaction, but in the case of Ni-GDC its effect was minor. The surface of YSZ at the

Ni-YSZ cermet was chemically stable under all conditions, whereas that of GDC was modified both by the pre-treatment and by the electrochemical operation itself. Strong evidences are provided about the influence of the GDC surface oxidation state to the cathode overpotential during electrolysis and in particular, improvement of the performance with the degree of GDC surface reduction. Overall, throughout this study we demonstrated that small, reversible modifications on the outer few nm of the cathode electrodes might have a major influence on the cell electrochemical performance during steam electrolysis.

Chapter 4. Synthesis and characterization of nickel-doped ceria nanoparticles with improved surface reducibility

IV. Chapter 4. Synthesis and characterization of nickel-doped ceria nanoparticles with improved surface reducibility

4.1. Introduction

As we illustrated in the previous chapter, there is a strong evidence for the influence of the GDC surface oxidation state to the cathode overpotential during electrolysis and in particular improvement of the performance with the degree of GDC surface reduction. This motivates us to think of how to improve the Ni-YSZ cathode electrode and at the same time to reserve the mechanical stability that is given by YSZ ceramic part. In this chapter we will present our study for the synthesis and characterization of nickel-doped ceria nanoparticles compared to conventional supported Ni/CeO_2, and in chapter 5 we will discuss its influence on the electrochemical performance for the impregnated NiCe@NiYSZ cathode electrode and ceria surface reducibility.

Nickel-doped ceria nanoparticles ($Ni_{0.1}Ce_{0.9}O_{2-x}$ NPs) were fabricated from Schiff-base complexes and characterized by various microscopic and spectroscopic methods. Clear evidence is provided for incorporation of nickel ions in the ceria lattice in the form of Ni^{3+} species which is considered as the hole trapped state of Ni^{2+}. The $Ni_{0.1}Ce_{0.9}O_{2-x}$ NPs exhibit enhanced reducibility in H_2 as compared to conventional ceria-supported Ni particles, while in O_2 the dopant nickel cations are oxidized at higher valence than the supported ones. Cerium (IV) oxide, also known as ceria (CeO_2), is largely exploited in catalysis and electrocatalysis,[194] for example, as a constituent of three-way automotive catalysts[200]. The unique catalytic properties of ceria have been connected to the facile and reversible exchange between Ce^{4+} and Ce^{3+} oxidation states which allows fast uptake and release of oxygen under oxidizing and reducing conditions, respectively. Although oxidation of Ce^{3+} ions is kinetically fast, the reduction of Ce^{4+} is generally sluggish, therefore great effort has been devoted to promote ceria reducibility[201] either by modifying the size and the morphology of the crystals or by partial substitution of cerium by metal ions[202], [203]. The latter has been also exploited as a strategy to produce catalysts containing metal ions atomically dispersed on the oxide support, usually referred to as single-atom catalysts[204], [205]. A prerequisite for the synthesis of metal-substituted ceria particles is the formation of a homogenous solid solution between the metal and ceria. Conventional catalyst synthesis methods, e.g. co-precipitation, are not capable of that and

typically lead to the formation of segregated metal/ceria agglomerates[206]. Therefore, realizing the homogeneous dispersion of metal into the ceria lattice is a critical challenge in the effort to synthesize novel single atom catalysts and there are only few available methods for that.

Recently W. L. Wang et al.,[207] proposed a synthesis route that involves a solution of the two metal salts which react in a continuous reactor in the presence of supercritical water (374 °C and 23 MPa). Alternatively, S. McIntosh and coworkers, demonstrated that Cu-doped ceria nanoparticles can be synthesized at room temperature in aqueous solution using a modified base precipitation method[208]. These methods do not involve organic compounds and so, they do not require a cleaning step after preparation. On the downside, the absence of an organic protective layer constitutes the particles potentially vulnerable to aggregation and agglomeration. In an alternative synthesis method put forward by Elias et al.[209], a solution-based pyrolysis route is followed to produce phase pure, monodisperse $M_{0.1}Ce_{0.9}O_{2-x}$ (M: Ni, Co, Au) nanoparticles.

To ensure close association of cerium and transition metal ions during their nucleation and growth, heterobimetallic Schiff base complexes were used as inorganic precursors. By this method the nanoparticles are surrounded by an oleylamine protective layer, which allows obtaining narrow size distributions of relatively small particles (ca. 3 nm). However, the synthesis is relatively complex since it requires 3 consecutive steps. In this work we modulated/simplified the previously proposed method[209] to prepare nickel-doped ceria NPs from Schiff base metal complexes obtained in one step, without pre-synthesis of the salpn (N,N0-bis(salicylidene)-1,3-diaminopropane) ligand molecule. The structure and composition of the produced NPs were verified by various methods, including XPS, HR-TEM, Raman and XRD, while their surface reducibility is compared to conventional supported Ni/CeO_2 using in situ structural and surface sensitive techniques.

This chapter is based on the published article: Wassila Derafa, Fotios Paloukis, Basma Mewafy**,**Walid Baaziz, Ovidiu Ersen, Corinne Petit, Gwenaël Corbel and Spyridon Zafeiratos "Synthesis and characterization of nickel-doped ceria nanoparticles with improved surface reducibility". RSC Adv., 2018, 8, 40712, DOI: 10.1039/c8ra07995a

4.2. Materials and methods

$Ni_{0.1}Ce_{0.9}O_{2-x}$ nanoparticles (NiCeNPs) were synthesized by mixing the heterobimetallic Schiff base complexes precursors in oleylamine and reflux at 180 °C under Ar (see Fig. 4.1). The Schiff base complexes were prepared directly, without using a Schiff base ligand as in ref. [209]. For characterization, the NiCe NPs were dispersed in hexane solution and drop casted on various inert supports (polycrystalline gold foil, silicon wafer and fused quartz glass) and the solvent was allowed to evaporate at room temperature, leaving a layer of nanoparticles grafted on the support. A reference 10%Ni/CeO_2sample (Ni/CeO_2) was prepared by the co-precipitation synthesis route. Detailed description of the synthesis and the characterization methods is given below.

4.2.1. Synthesis of $Ni_{0.1}Ce_{0.9}O_{2-x}$ nanoparticles

The synthesis of $Ni_{0.1}Ce_{0.9}O_{2-x}$ nanoparticles in close to that described by J.S. Elias and al.[209] but took place in 2 steps instead of 4 steps. Ce(III)L complex and Ce(III)Ni(II)-L binuclear complex have been prepared on one step separately. The bidentate Schiff-base complex was synthesized by the published method [[200], [209]] based on click chemistry. After mixing both Schiff-base complexes in the ratio 8/1 according to the desired compound the $Ni_{0.1}Ce_{0.9}O_{2-x}$ nanoparticles have been obtained by pyrolysis of the mixture.

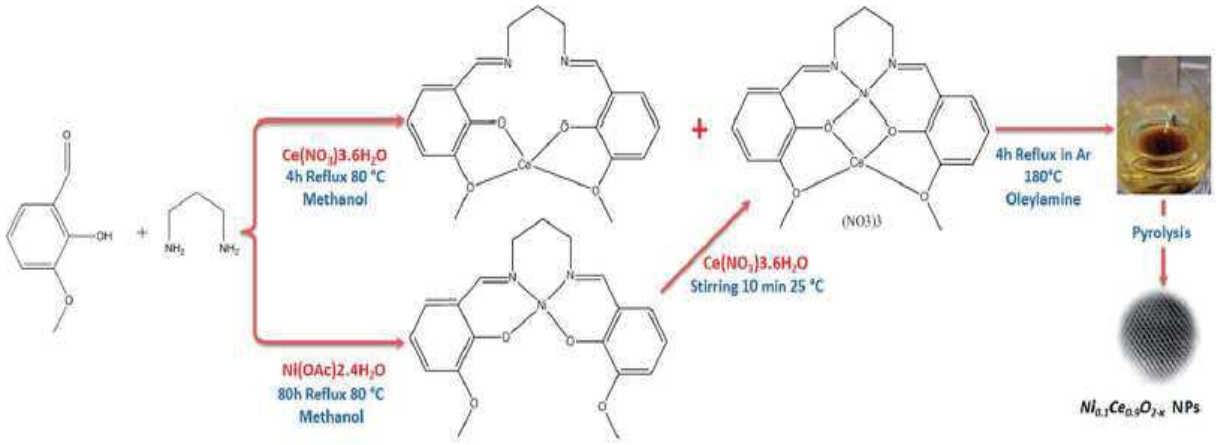

Figure 4.1. Schematic illustration of the preparation of the $Ni_{0.1}Ce_{0.9}O_{2-x}$nanoparticles.

4.2.1.1. Preparation of Ce(III)-L complex

In a solution of 20 ml of methanol we added two equivalents of 2-hydroxy-3-methoxybenzaldehyde (0.30 g, 2 mmol), an equivalent of 1,3-diaminopropane (0.07 g, 1 mmol) and an equivalent of cerium (III) nitrate hexahydrate Ce (NO_3) 2.6 H_2O (0.406 g, 1 mmol), giving an yellow precipitate immediately, according to (fig. 4.2). The yellow suspension was stirred at reflux for 4 hours before cooling to room temperature. The crude product was filtered through a frit, washed with cold EtOH (3 x 20 mL) and dried under vacuum to give Ce(III)-L complex as a yellow powder with a yield of one step synthesis of 94%; purity is controlled by TLC plate and Rf = 11% eluent (CH_2Cl_2 / EtOH).

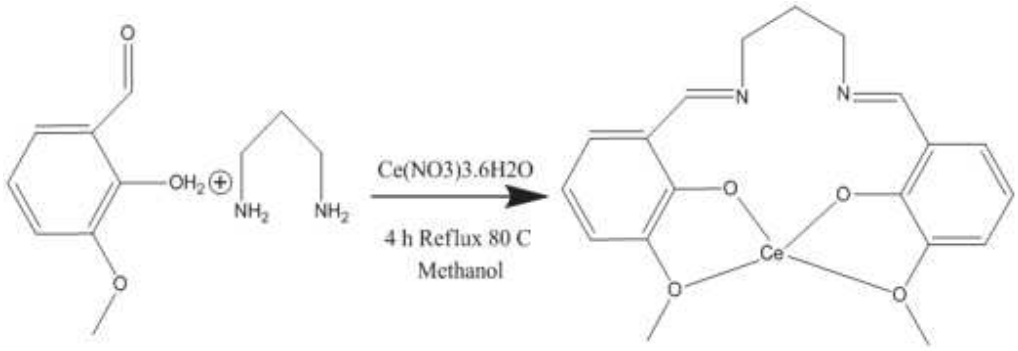

Figure 4.2. Synthesis step of Ce^{III}-(N,N'-bis (3-methoxysalicylidene)-propylene-1,3-diamine).

4.2.1.2. Preparation of Ce(III)Ni (II)-L binuclear complex:

In a three-necked flask we put a mixture of two equivalent of 2-hydroxy-3-methoxybenzaldehyde (4 g , 26.31 mmol), an equivalent of 1,3-diaminopropane (1.05 g, 15 mmol) and an equivalent of Nickel(II) tetrahydrate Ni $(OCOCH_3)_2$. $4H_2O$ (3.33 g, 13.5 mmol) in a solution of 50 ml of methanol. The green solution was refluxed at 80 °C for 9 h and after cooling down at room temperature an equivalent of cerium(III) nitrate hexahydrate Ce $(NO_3)_2$. $6H_2O$ (5.48 g 13.5 mmol) dissolved in 5 ml of methanol was added to the solution. Consequently the mixture was stirred for 10 minutes and then allowed to crystallize at room temperature, according to fig. 4.3. After reducing the volume of the solution to 20 ml yellow-green crystals were obtained, filtered and washed by (3 * 20 ml) of methanol. The yield of the synthesis of the Ce(III)Ni(II)-L binuclear complex is 57%, its purity is controlled by TLC plate and the Rf = 20% eluent (CH_2Cl_2 / EtOH 8.5 / 1.5).

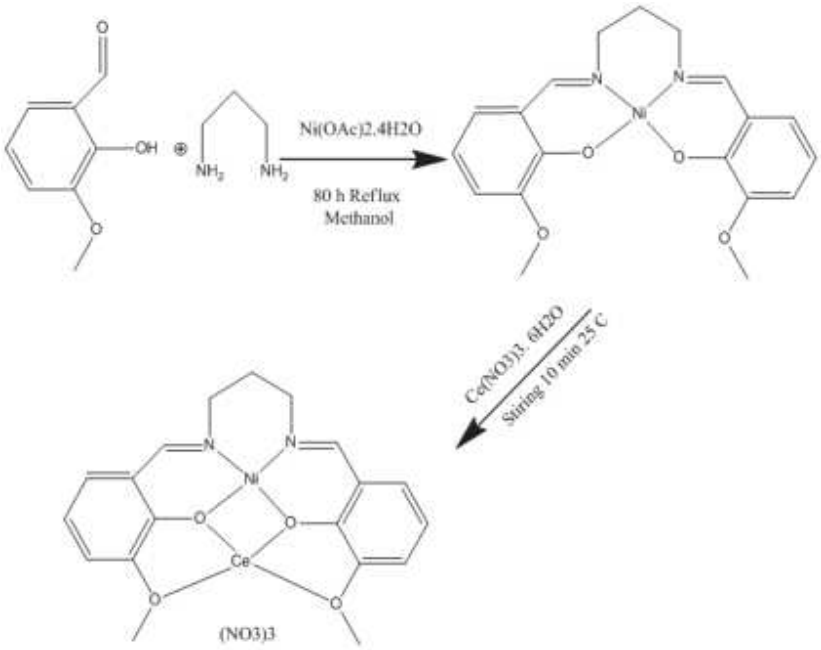

Figure 4.3. Synthesis step of Ni^{II}-Ce^{III} (N,N'-bis(3-methoxysalicylidene)-propylene-1,3-diamine).

4.2.1.3. Preparation of $Ni_{0.1}Ce_{0.9}O_{2-X}$ nanoparticles[1,2] :

The $Ni_{0.1}Ce_{0.9}O_{2-X}$ nanoparticles were prepared by a mixture of (0.092 g, 0.173 mmol) of Ce (III)-L and Ni (II) Ce (III)-L (0.440 g, 0.547 mmol) in 40 ml of oleylamine. The mixture was refluxed at 180 °C under argon for 4 hours, and the remaining dark brown product was isolated by centrifugation. The brown solutions were divided into fractions of 3.5 mL and flocculated with ethanol (30 mL each). Consequently the brown flocculent was isolated by centrifugation (4000 rpm for 20 min) and redispersed in hexane (5 mL fractions). Bulk precipitates were removed by centrifugation (3000 rpm for 3 min) and subsequent decanting of these solutions. This process was repeated two times to give brown hexanes solutions of $Ni_{0.1}Ce_{0.9}O_{2-x}$. After drop casting on a support the $Ni_{0.1}Ce_{0.9}O_{2-X}$ nanoparticles were calcined at 400°C in air for 1 hour to remove the protective organic cap layer.

4.2.2. Synthesis of 10% Ni/CeO_2 using the co-precipitation method

The 10% Ni-CeO_2 reference material was prepared by the co-precipitation method using metal nitrates. In particular, an aqueous solution containing the required amounts of Nickel(II) nitrate hexahydrate [$Ni(NO_3)_2 \cdot 3H_2O$] (Sigma-Aldrich) and Cerium(III) nitrate hexahydrate

[$Ce(NO_3)_3 \cdot 6H_2O$ (Sigma-Aldrich)] with their concentration of 0.1N each, were simultaneously precipitated using an aqueous solution containing 0.25 N KOH. The pH was maintained between 9.5 and 10 during the process. The co-precipitated mass was thoroughly washed, filtered and dried at 90 °C for 12 h in air followed by calcination in furnace.

4.3. Characterization methods

4.3.1. XPS analysis

The XPS analysis chamber is equipped with VSW Class WA hemispherical electron analyzer (150 mm radius) and a monochromatic Al Kα X-ray source (1486.6 eV). Oxidation/reduction treatments were carried out in a flow-through variable-pressure reactor attached to the UHV setup (0.6 L volume). Each oxidation/reduction step lasted 30 min at constant temperature and gas pressure. The pressure of the gas (H_2 or O_2) treatment was 7 mbar. Subsequently to the gas treatment, the sample was cooled to room temperature in gas and the reactor was evacuated to 5 × 10^{-8} mbar. Then the sample was transferred in vacuum into the analysis chamber for XPS characterization.

4.3.2. XRD Analysis

The XRD spectra were recorded at 25°C intervals between 25 and 400°C (heating rate of 10°C/min, temperature stabilization for 20 min, cooling rate of 60°C/min) by using a XRK 900 Anton Paar reactor chamber attached to a PANalytical θ/θ Bragg-Brentano Empyrean diffractometer ($CuK\alpha_{1+2}$ radiations) equipped with the PIXcel^{1D} detector. The sample was deposited on the sieve (pore size ∅ 0.2mm) of the open sample holder cup, made of glass ceramic Macor, thus allowing gas to flow through and eventually reacting with the sample. For the CeO_2/NiO (10mol%) powder sample, the diffractogram was collected at each temperature in the [20°-130°] scattering angle range with a 0.0131° step for a total acquisition time of 220 min. For the $Ni_{0.1}Ce_{0.9}O_{2-x}$ drop casted sample, the diffractogram was collected at each temperature in the [20°-65°] scattering angle range with a 0.0131° step for a total acquisition time of 155 min. The program FullProf [210]was used for Le Bail refinements.

4.3.3. Raman Analysis

Raman spectra were acquired using a micro-Raman spectrometer (Horiba LabRam), with excitation wavelength of 532 nm. A 100× objective was used to focus the excitation laser to an

approximately 1 μm spot with a laser power of less than 1 mW to avoid heating and damage of the sample.

4.3.4. Microscopy

The surface morphology was inspected by SEM using a Zeiss GeminiSEM 500 microscope. Energy-dispersive X-ray spectroscopy (EDXS) mapping was combined with the SEM images to resolve the different elements on the surface of the electrodes. The TEM analysis of $Ni_{0.1}Ce_{0.9}O_{2-x}$ was carried out on a JEOL 2100F working at 200 kV accelerated voltage, equipped with a probe corrector for spherical aberrations, and a point-to-point resolution of 0.2 nm. The sample was dispersed by ultrasounds in an ethanol solution for 5 minutes and a drop of the solution was deposited on a copper covered with a holey carbon membrane for observation.

4.4. Surface Composition for $Ni_{0.1}Ce_{0.9}O_{2-x}$ nanoparticles

The X-ray diffraction (XRD) patterns of NiCe NPs before and after calcination are shown in fig. 4.4a. Both patterns are characteristic of fluorite-type CeO_2 phase without extra peaks originating from Ni-containing phase. The absence of Ni diffraction peaks indicates the successful introduction of the entire amount of Ni ions in the ceria lattice and the absence of segregated nickel[211].The cubic unit cell parameter is slightly increasing after calcination from 5.421(1) °A to 5.424(1) °A in good agreement with the parameter determined by Elias et al. for ceria NPs (a Ceria z 5.42 °A)[209]. The unit cell parameter for the NiCe NPs is larger than the one typically reported for undoped bulk CeO_2 grains (5.411 °A)[212]. At first sight, this may appear to oppose the fact that nickel ion is smaller in size than Ce^{4+},[213] however the lattice expansion can be explained by the creation of extrinsic oxygen vacancies through the aliovalent substitution of Ce^{4+} with Ni^{n+}.

Raman spectroscopy is sensitive to the modification of the local structure of the ceria crystal and particularly to lattice defects[117]. Fig. 4.4b shows the baseline corrected Raman spectra of fresh and calcined NiCe NPs. The main Raman band at 458 cm^{-1} corresponds to the triply degenerate F_{2g} mode of fluorite-type ceria structure and it can be considered as the symmetric stretching mode of oxygen atoms around cerium ions. Two additional features are observed at about 545 and 620 cm^{-1} which according to previous studies are induced by defects in the ceria structure[117], [126]. The lower-wave number band at 545 cm^{-1} is attributed to defect sites that include an O^{2-} vacancy (extrinsic vacancy), while the higher-wave number band at 620 cm^{-1} is

induced by the presence of Ce^{3+} or Ni^{3+} ions[117], [120], [124], [126].The peak at 225 cm^{-1} is the transverse optical (TO) phonon mode, which becomes Raman active due to the disorder induced by doping in CeO_2[124]. Comparison of the Raman spectra before and after calcination in fig. 4.4b shows that fresh NiCe particles contain a great number of defect sites which, to a large extent, remain also after calcination at 400 °C. Since the amount of extrinsic oxygen vacancies is directly related to the oxidation state of nickel ions, this indicates the stability of nickel oxidation state during calcination.

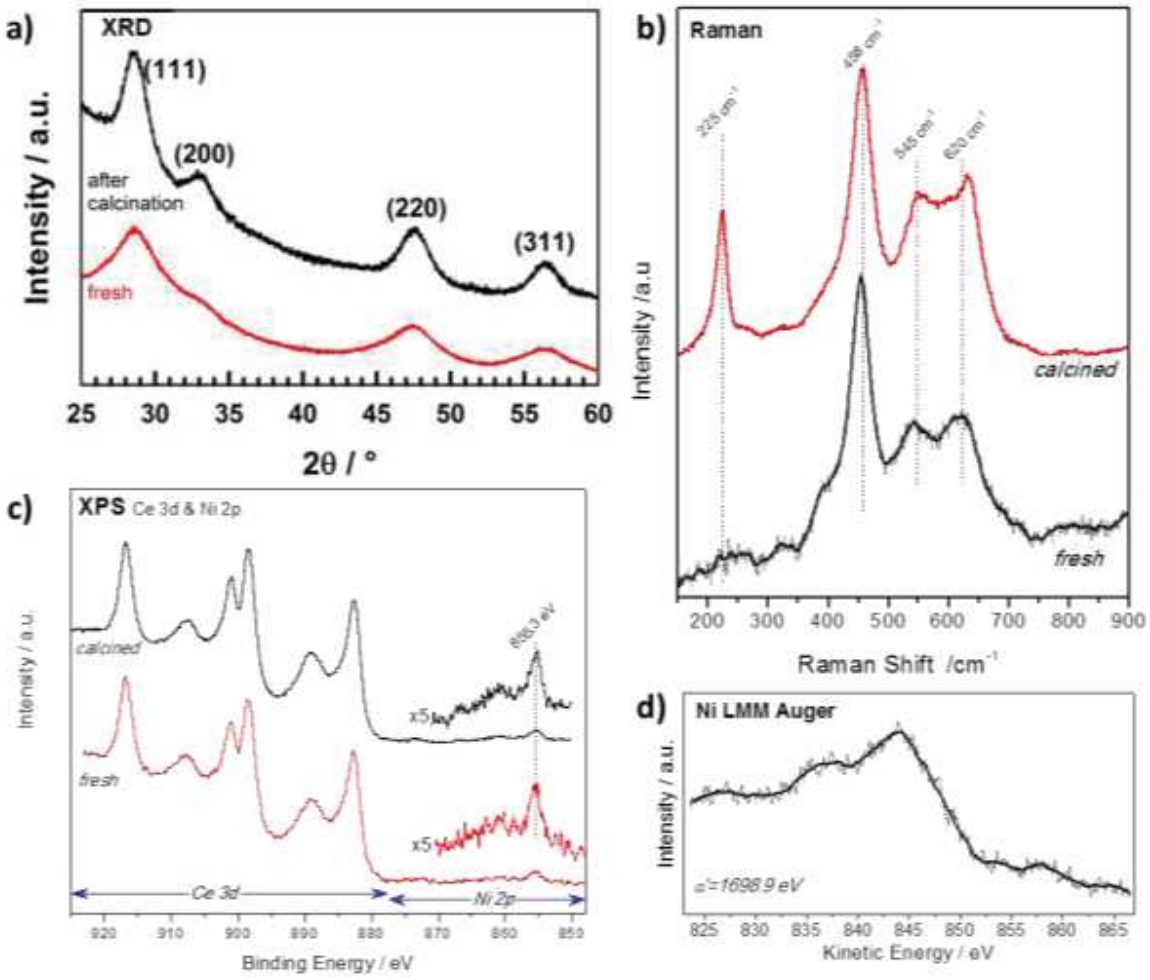

Figure 4.4. (a) XRD patterns b) Raman spectra and c) XPS spectra d) Auger spectrum of $Ni_{0.1}Ce_{0.9}O_{2-x}$ particles as synthesized (red) and after calcination at 400 °C in O_2 (black).

XPS can be used to confirm the oxidation state of Ce and Ni ions as well as their surface arrangement[148]. In fig. 4.4c the Ce 3d and Ni 2p spectra before and after calcinations of NiCe NPs are presented. The Ce 3d photoelectron peak contains several multiple splitting features including the intense peak at 916.8 eV which is characteristic for Ce^{4+} ions [148]. The Ni $2p_{3/2}$ line is composed by a main peak at 855.3±0.1 eV and a satellite feature at higher binding energies with relative intensity about 25 ±5% of the main Ni $2p_{3/2}$ peak. The binding energy (BE) position and the peak shape do not correspond to nickel oxides or hydroxides reported in relevant literature[24], [174], [214], [215]. Similarly, the Ni LMM Auger peak shape and the so called modified Auger parameter (α') at 1698.9 eV shown in fig. 4.4d, differ from previously published results of oxidized nickel compounds [214]. These findings suggest that the chemical environment around Ni cations varies from the known bulk nickel oxides (e.g. NiO). On the other hand, previous studies of Ni^{3+} species formed after potassium interaction with NiO [216], [217] exhibit similar Ni $2p_{3/2}$ peak characteristics with the one found here, which is a strong evidence that in the case of NiCe NPs, nickel is mainly in the Ni^{3+} state. More conclusive results about the oxidation state of nickel will be provided after comparison with supported nickel oxide particles in the next section. The Ni:Ce atomic stoichiometry calculated by XPS is found 12:88 ± 2%, close to the expected stoichiometry of $Ni_{0.1}Ce_{0.9}O_{2-x}$ particles (10:90). This stoichiometry remains constant after calcinations, which indicates the stability of the NPs during this process and excludes surface segregation phenomena. Overall XRD, Raman and XPS analysis of the NiCe NPs provides solid evidence for the formation of Ni doped-ceria particles with the expected stoichiometry and high stability to the calcination procedure.

The SEM micrograph of the NiCe NPs applied by drop casting on a SiO_2/Si substrate is shown in (fig. 4.5a). The texture of the fresh film is not homogenous and consists of flat areas interrupted by parts where the texture is porous. After calcinations at 400 °C and removal of the capping oleylamine layer, the NPs have the tendency to agglomerate and form a flat and homogenous film on both SiO_2/Si and Au foil substrates as shown in fig. 4.5b and 4.5c. Apparently, the flat nature of the NiCe NPs film demonstrates the tendency of the solution to wet the support and form layers instead of agglomerated particles. Based on the quantitative analysis of the SEM images using EDX the Ni atomic ratio was found 11.0 ±1.5%, which is in good agreement with both XPS findings and the nominal Ni loading.

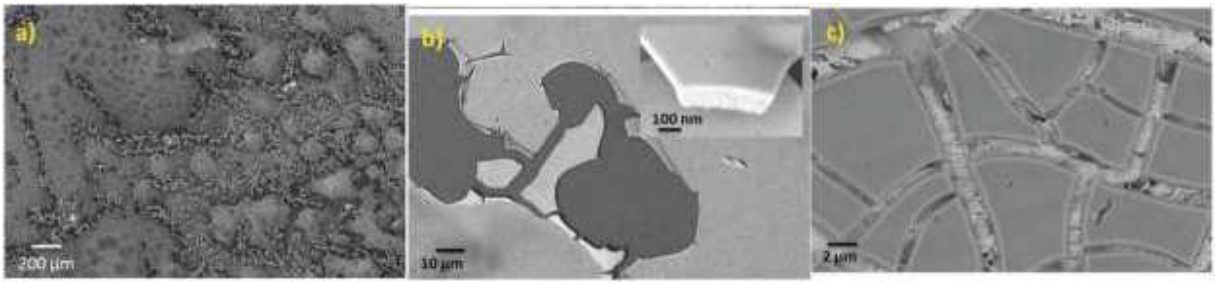

Figure. 4.5. SEM images of a $Ni_{0.1}Ce_{0.9}O_{2-x}$ layer (a) fresh after drop casting the solution on a SiO_2/Si wafer (b) after calcination at 400 °C on a SiO_2/Si wafer and (c) after calcination at 400 °C on a Au polycrystalline foil.

The HR-TEM image (fig. 4.6a) after calcination shows aggregated NiCe NPs with a mean diameter of about 4 nm, similar to previous work[209]. Typical high resolution STEM images (fig. 4.6b and 4.6c) show the high crystallinity of the calcined NiCe NPs and reveal that the crystallites are formed in truncated octahedral crystal habits. The corresponding Fast Fourier Transform (FFT) patterns (fig. 4.6d) suggest that the {111} and {100} are the mainly exposed facets of the NPs.

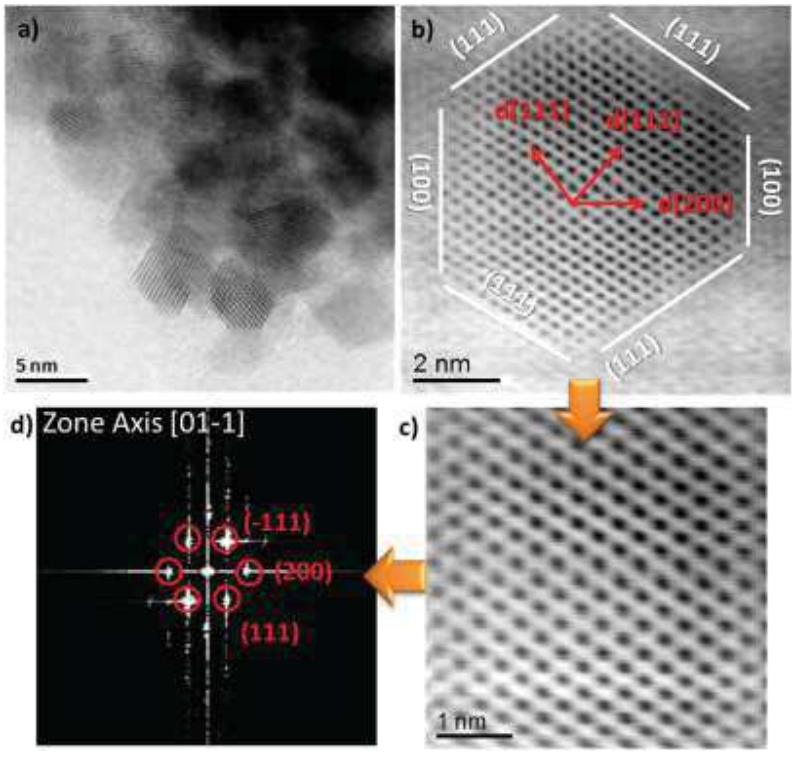

Figure. 4.6. High resolution bright field STEM image and the corresponding FFT diffraction pattern of $Ni_{0.1}Ce_{0.9}O_{2-x}$ formed after calcination at 400 °C.

4.5. Investigation of the redox properties of $Ni_{0.1}Ce_{0.9}O_{2-x}$nanoparticles

The redox stability of NiCe NPs is investigated next, in comparison with supported Ni/CeO_2 of the same nominal composition. Generally in catalytic studies temperature programmed methods (TP) are employed to examine the redox properties. However such methods are not suitable for NiCe NPs, since they require a relatively high solid sample loading, which bypasses the capacity of the synthesis method and needs scale up. Furthermore, TP methods present some drawbacks mostly related to the overlapping of the peak profiles and the difficulty to identify with certainty surface and bulk processes. Alternatively, analytical methods can be used to provide direct information about the oxidation state during, or after redox treatments[218], [219]. Although this is a more elaborate approach, it is preferential for the purpose of this study, since it can be specific on the surface redox properties providing that surface sensitive methods are used.

4.5.1. In situ XRD analysis during redox cycles

The thermal stability of the two samples was determined by XRD under either $96\%N_2$-$4\%O_2$ or $96\%N_2$-$4\%H_2$ atmosphere at different temperatures along the profiles displayed in fig. 4.7.

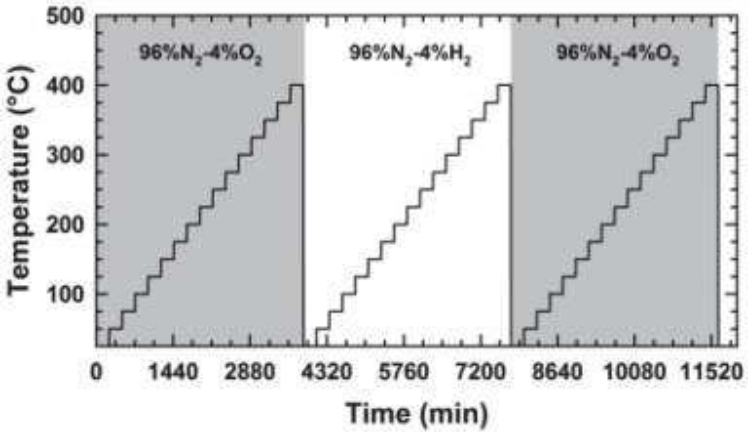

Figure 4.7. Temperature profiles.

Temperature-controlled X-ray diffractograms were collected. For the CeO_2/NiO (10mol%) powder sample, the diffractogram was collected at each temperature in the [20°-130°] scattering angle range with a 0.0131° step for a total acquisition time of 220 min. For $Ni_{0.1}Ce_{0.9}O_{2-x}$ drop casted sample, the diffractogram was collected at each temperature in the [20°-65°] scattering angle range with a 0.0131° step for a total acquisition time of 155 min.

4.5.1.1. $Ni_{0.1}Ce_{0.9}O_{2-x}$ drop-casted on quartz substrate

The raw drop casted sample does not contain any secondary phase. Whatever the annealing temperature under diluted oxygen, the diffraction pattern remains similar to that of a ceria type compound. It suggests that a partial substitution of cerium by nickel occurs. When the sample is annealed under diluted hydrogen, no appearance of nickel metal as secondary phase is observed, whatever the annealing temperature. The sample is then stable in reducing atmosphere up to 400°C. The diffraction patterns of the sample recorded under diluted hydrogen are similar to those recorded under diluted oxygen. Indeed, after being annealed at 400°C either under 96%N_2-4%O_2 or 96%N_2-4%H_2 atmosphere, the cubic unit cell parameter of ceria at room temperature did not change as shown in table 4.1. The program FullProf was used for Le Bail refinements. The cubic unit cell parameter of the sample is in agreement with the parameter determined by Elias *et al.* ($a_{Ceria} \approx 5.42$ Å in[22]).

4.5.1.2. Powder Ni/CeO_2 (10mol%)

Raw powder Ni/CeO_2 (10mol%) contains NiO as secondary phase, as is evident by the (200) peak at around 43.3° in 2theta in agreement with the JCPDS card n° 01-071-1179. When this powder is annealed under diluted hydrogen, a reduction of NiO into Ni starts at 275°C (appearance of the (111) peak at around 44.5° in 2theta in agreement with the JCPDS card n° 00-004-0850). At 300°C, Ni is the only secondary phase present in the sample. When this powder is now re-annealed under diluted oxygen after being reduced, the diffraction lines assigned to Ni start decreasing in intensity at around 275°C. A diffuse peak at around 43.3° in 2theta assigned to NiO, appears only above 300°C. At 400°C, the oxidation is not complete and a large amount of Ni remains present. After being annealed at 400°C either under 96%N_2-4%O_2 or 96%N_2-4%H_2 atmosphere, the cubic unit cell parameter of ceria at room temperature did not change (table 4.1). The program FullProf was used for Le Bail refinements. Ceria remains stable in diluted hydrogen in the temperature range 25-400°C.

Table 4.2. Cell parameters of the $Ni_{0.1}Ce_{0.9}O_{2-x}$ NPs (left) and 10%Ni/CeO_2 as defined by in situ XRD.

Sample	a_{Ceria} (Å) at 25°C, after annealing at 400°C, under 96%N_2-4%O_2	a_{Ceria} (Å) at 25°C, after annealing at 400°C, under 96%N_2-4%H_2
CeO_2/NiO (10 mol%)	5.4103(1)	5.4109(1)
$Ni_{0.1}Ce_{0.9}O_{2-x}$	5.421(1)	5.424(1)

The in situ temperature controlled XRD experiments obtained during consecutive reduction and oxidation (redox) cycles of pre-calcined NiCe NPs and Ni/CeO_2 are compared in (fig. 4.8). The diffraction patterns of NiCe are similar to those of pure CeO_2 cubic structure and remain almost identical in both H_2 and O_2 atmospheres for all annealing temperatures (fig. 4.8). Notably, there is no appearance of diffraction peaks related to Ni or NiO. The calculated cubic unit cell parameter of NiCe NPs remains practically constant in both atmospheres (table 4.1). Therefore, within the XRD detection limits, the NiCe NPs are stable during the redox treatment in terms of dispersion and nature of the presented phases, in good agreement with previous ex situ XRD reports[220]. The average apparent size of the NiCe crystallites determined at room temperature (by refinement after removing the instrumental line broadening) was 20(2) °A, and 37(4) °A after calcination at 400 °C in O_2 and H_2, respectively, which is in good agreement with the HR-TEM results. The results show that the NPs can be reduced, inducing a large amount of oxygen vacancies while keeping their structure practically stable. In contrast to NiCe NPs, in the XRD pattern of Ni/CeO_2, in addition to the CeO_2 diffraction, Ni-related peaks are detected (fig. 4.8). In particular, the calcined Ni/CeO_2 contains a large (200) Bragg peak at around 43.3° in 2q assigned to NiO. When annealed in H_2, a complete reduction of NiO into Ni occurs at 300 °C (appearance of the (111) peak at around 44.5° in 2q assigned to Ni in fig. 4.7). In a consecutive reoxidation cycle, a large amount of metallic Ni remains present even after annealing in O_2 at 400 °C, indicating that the reoxidation is partial fig. 4.8. The diffraction peaks related to CeO_2 and

accordingly the cubic unit cell parameters of Ni/CeO_2 sample remain practically stable during both redox treatments (table 4.1).

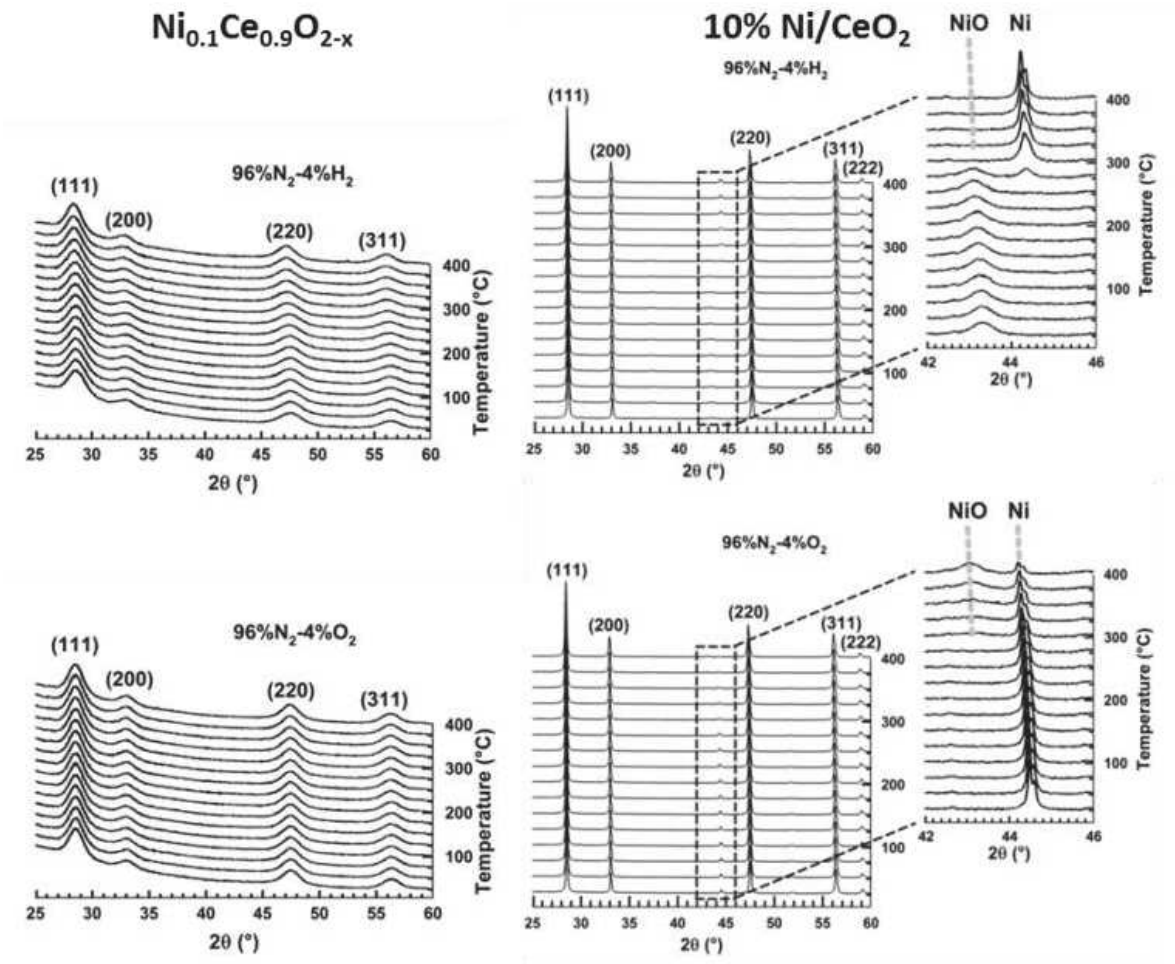

Figure 4.8. In situ XRD patterns of $Ni_{0.1}Ce_{0.9}O_{2-x}$ NPs (left) and 10%Ni/CeO_2 (middle) upon treatment up to 400 °C in O_2 and H_2 atmospheres. Whatever the samples, all Bragg peaks are singly indexed on to the CeO_2-like fluorite cubic sub cell. An enlarged view of the 42-46 degrees region is also given at the right or the figure.

4.5.2. Ex situ XPS analysis

The XPS analysis performed under gas and temperature conditions similar to XRD is informative of the stability in the near surface region. The Ce 3d and Ni 2p spectra of the NiCe NPs and Ni/CeO_2 after H_2 and O_2 treatments at two characteristic temperatures are shown in fig. 4.9. Comparison of the relative Ni 2p to Ce 3d peak intensities between the two samples shows

that in case of Ni/CeO_2 the intensity of Ni 2p peak is enhanced as compared to the NiCe NPs. In particular, the atomic ratio of Ni increases to 35 ± 2 from about 12 ± 2 at $Ni_{0.1}Ce_{0.9}O_{2-x}$ in case of Ni/CeO_2, which seems surprising since both samples have the same nominal Ni loading. This is rationalized by taking into account the differences in the morphology of the two samples. The co-precipitation forms Ni particles dispersed on the ceria surface,[221] while Ni in the case of NiCe NPs is inserted into ceria lattice. Given that XPS is surface sensitive, Ni particles dispersed over ceria support (Ni/CeO_2) is expected to have an enhanced Ni atomic ratio in XPS, as compared to Ni atoms inserted into the fluorite lattice of ceria (NiCe NPs).

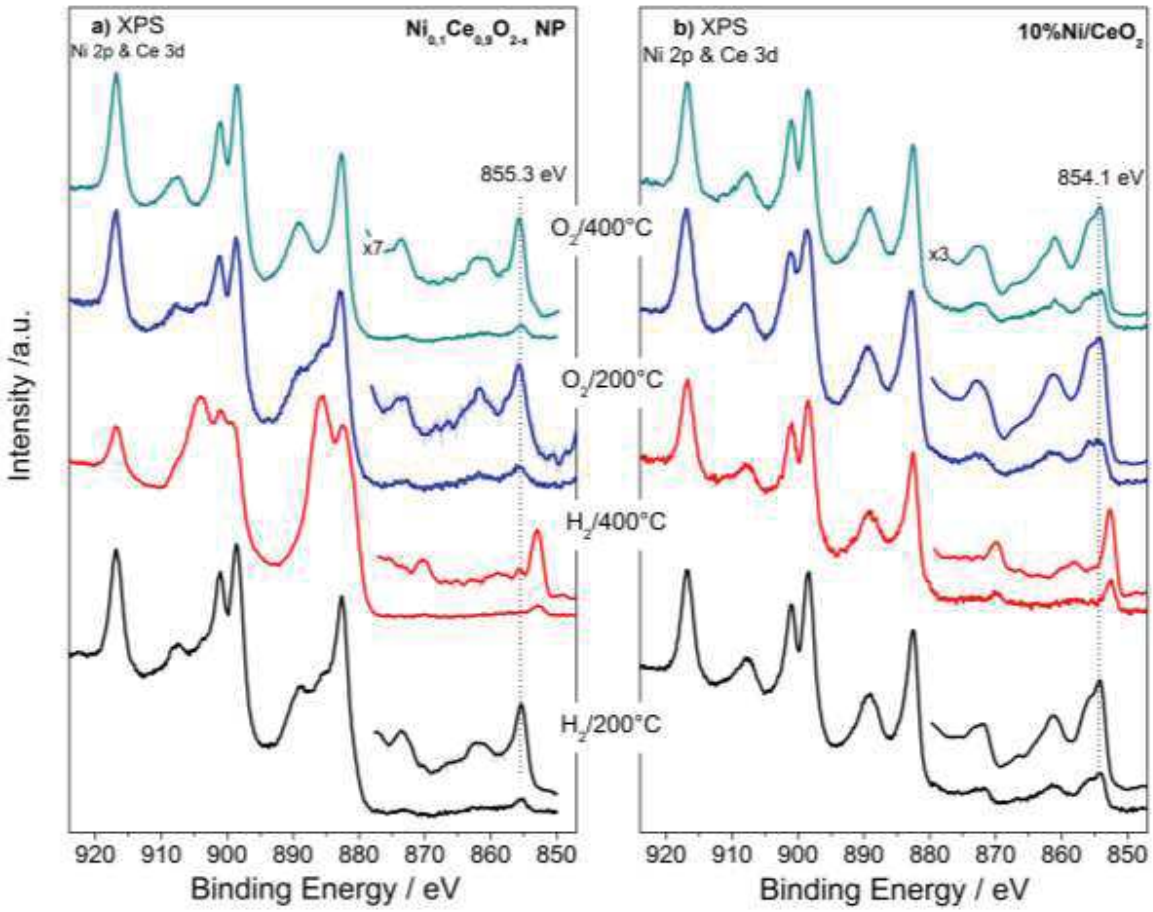

Figure 4.9. Ni 2p and Ce 3d XPS specta of $Ni_{0.1}Ce_{0.9}O_{2-x}$ NPs (a) and 10%Ni/CeO_2 (b) upon treatment up to 400 °C in O_2 and H_2 atmospheres.

Apart of the differences in the peak area ratio, the two samples exhibit clear differences also in the peak shape (fig. 4.10). As discussed above, in O_2 and low temperature H_2 the Ni $2p_{3/2}$ peak of NiCe NPs is likely due to Ni^{3+} species. In case of Ni/CeO_2, the main Ni $2p_{3/2}$ peak at 854.1 eV is accompanied by a prominent shoulder around 855.3 eV and an intense satellite feature (50 ±5% of the main Ni $2p_{3/2}$ peak height) shifted by 6.9 eV of the main peak (fig. 4.10a), typical characteristics of the Ni 2p spectrum for bulk NiO[24], [174], [214], [215]. These differences confirm that in the case of NiCe NPs nickel is mainly in the Ni^{3+} state, while for Ni/CeO_2 it is oxidized to NiO (Ni^{2+} valence) and reveal a fundamental chemical modification of nickel imbedded in the ceria lattice as compared to supported nickel particles. The oxidation state of nickel remains unchanged up to 200 °C in H_2, while at 400 °C in H_2 Ni $2p_{3/2}$ shifts at 852.7 eV and the satellite peak intensity drops considerably. This is a clear indication of reduction of nickel to the metallic state for both samples and completes the XRD observations shown above.

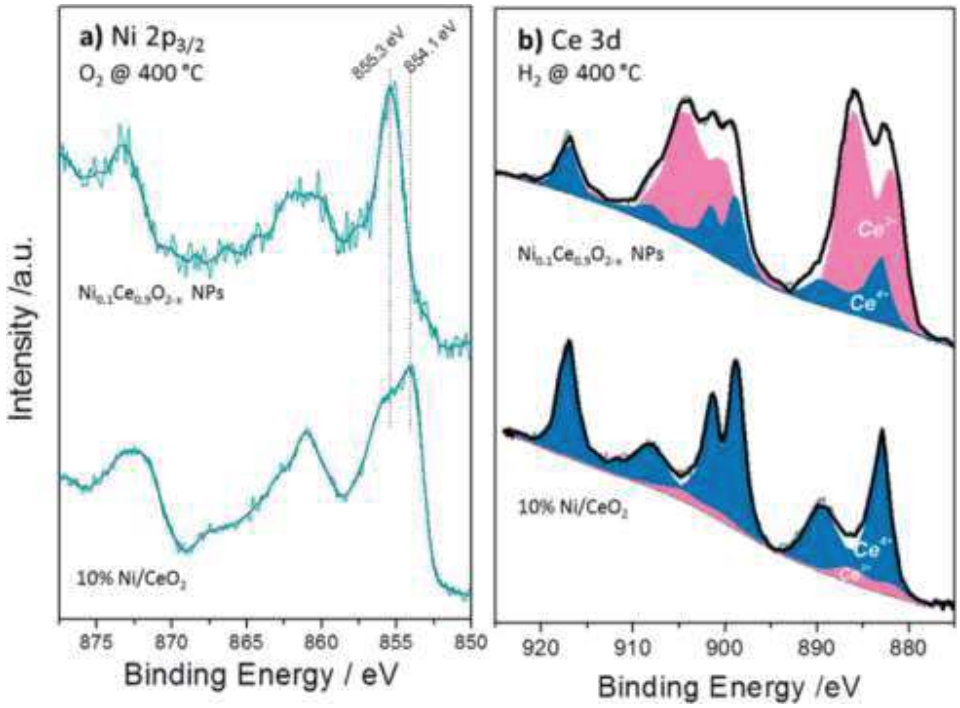

Figure 4.10. (a) Comparison of the Ni $2p_{3/2}$ spectra between 10% Ni/CeO_2 and NiCe NPs samples recorded after calcination at 400 °C (b) deconvolution procedure of two characteristic Ce 3d XPS spectra using Ce^{4+} and Ce^{3+} line shapes derived from reference samples recorded under identical reduction conditions (400 °C in H_2).

The Ce 3d spectra of the two samples differ considerably after H_2 and O_2 treatments. The % Ce^{3+} species obtained after deconvolution of Ce 3d peak in Ce^{3+} and Ce^{4+} components (fig. 4.10b) are given in table. 4.2. From this table it is clear that under identical H_2 treatment conditions the amount of $Ce3^{+}$ species for NiCe NPs is up to 7 times higher as compared to Ni/CeO_2. The ceria stoichiometry is $CeO_{1.63}$ in case of NiCe NPs, as calculated by the % Ce^{3+} at 400 °C in H_2. Such a composition adopts a Bixbyite type C–Ce_2O^{3+d} structure, which has a cubic superstructure (a ≈11.11 °A), originating from the ordering of oxygen vacancies along the [111] direction of the fluorite type structure. The calculated XRD pattern of C–$Ce_2O_{3+\delta}$ contains several superstructure peaks of low intensity at 2Θ 19.5°, 34.2°,37.9° and 41.4°, in addition to intense peaks at 2Θ 27.8°, 32.2°,46.2°similar to those observed for CeO_2. However the detection of the small superstructure peaks characteristic of the C–$Ce_2O_{3+\delta}$ phase in the XRD pattern of NiCe NPs (fig. 4.4), is impossible due to a broadening of all Bragg peaks induced by the small size of coherent diffraction domains (37(4) °A).

Doped-ceria nanoparticles have been studied for a number of applications including catalytic CO oxidation[208], [209] and electrocatalytic CO_2 reduction, [222] showing an excellent performance as compared to standard supported catalysts. The reducibility of ceria, i.e. the facile transformation of Ce cations from Ce^{4+} to Ce^{3+}, is a crucial property for the catalytic applications, since it is related to the ability of the material to release and uptake O atoms during reactions[223]. The present findings show that the reducibility of ceria is enhanced when Ni is doped into the lattice, as compared to Ni deposited over ceria supports. The enhanced reducibility of NiCe NPs can be used to design improved catalysts when enhanced ceria reducibility is required. For example, facile ceria reduction is known to promote heterogeneous catalytic reactions following the Mars–van-Krevelen reaction mechanism[224], [225].

Table 4.2. The % concentration of Ce^{3+} species at different gas treatments as derived by the analysis of the Ce 3d XPS spectra.

Conditions	% Ce^{3+}	
	$Ni_{0.1}Ce_{0.9}O_{2-x}$	$10\%Ni/CeO_2$
calcined	0	0
200 °C in H_2	27	5
400 °C in H_2	74	10
200 °C in O_2	31	10
400 °C in O_2	0	0

Apart of the apparent influence on the ceria reducibility, the synthetic strategy reported here has an additional advantage which is related to the fact that the NiCe NPs are solved in hexane solution. This solvent has a high viscosity (0.30 mPas@25 °C) which allows facile access of the solution containing NiCe NPs via capillary forces into the channels of porous supports as compared to NPs in aqueous media. High viscosity can find direct application for the use of this material in the preparation of solid oxide cell electrodes (SOCE). In recent years there is an increased interest to fabricate SOCE by direct infiltration of the electrode material on a porous electrolyte scaffold[40], [114], [226], [227]. Typically, ceria is deposited from nitrate solutions which have much lower viscosity than hexane, often resulting in a non-uniform in depth distribution of ceria into the pores of the scaffold. The application of doped ceria nanoparticles prepared by the method described in this work for the development of highly efficient SOCE, will be explored in future studies. We expect that the enhanced reducibility of ceria which was evident in this study, in combination with the facile application of the nanoparticles into the channels of the scaffold, based on the high viscosity of hexane solutions, is a promising combination which can contribute to the development of more robust and active solid oxide electrodes for fuel cell and electrolysis applications.

4.6. Conclusions of Chapter 4

In summary, $Ni_{0.1}Ce_{0.9}O_{2-x}$ nanoparticles with mean diameter of about 4 nm were synthesized from heterobimetallic Schiff base complexes precursors using a two-step process. The as prepared particles are dispersed in hexane solution and later drop casted onto planar supports for characterization. A variety of analytical methods including XPS, XRD, Raman, STEM, and SEM were applied to ascertain the structure, morphology and chemical state of the nanoparticles before and after calcination at 400 °C. Among other things, the results illustrated the presence of trivalent Ni^{3+} ions and a considerably high amount of defect sites into the ceria particles. The reduction/oxidation of the $Ni_{0.1}Ce_{0.9}O_{2-x}$nanoparticles in H_2/ O_2 ambients respectively, was studied by XPS and in situ XRD. For comparison ceria-supported nickel particles prepared by standard co-precipitation method, were examined under the same conditions. Notably, the surface reducibility of ceria is enhanced when Ni is doped into the ceria lattice, as compared to ceria acting just as the Ni support. Considering that the reducibility of ceria determines to a large extent the facility of this material to store and release oxygen, the $Ni_{0.1}Ce_{0.9}O_{2-x}$ nanoparticles prepared by this method can be potentially exploited in a variety of technological fields such as heterogeneous catalysis and solid oxide electrochemical cells.

Chapter 5: Nickel-doped ceria nanoparticles as promoters of Ni-YSZ electrodes of Solid Oxide Electrolysis Cells

V. Chapter 5: Nickel-doped ceria nanoparticles as promoters of Ni-YSZ electrodes of Solid Oxide Electrolysis Cells

5.1. Introduction

As discussed in chapter 3, there is a monotonic correlation of the ceria oxidation state with the overpotential drop for cells with Ni-GDC cathode electrodes under steam electrolysis conditions. Additionally, in chapter 4 we have shown that the reducibility of ceria for $Ni_{0.1}Ce_{0.9}O_{2-x}$ nanoparticles (NiCe NPs) determines to a large extent the facility of this material to store and release oxygen under oxidizing and reducing conditions, respectively. Combining the high mechanical stability of Ni-YSZ with the enhanced capacity of $Ni_{0.1}Ce_{0.9}O_{2-x}$ NPs to exchange fast its oxidation state could be a promising approach for SOECs development.

There are two general approaches to develop electrodes for solid oxide electrochemical cells. One is to synthesize new electrode materials (e.g., typically cermets or perovskite type) with improved properties and apply them on the electrolyte by using traditional fabrication process (i.e. screen printing). [82], [228], [229] An alternative approach is to develop new methodologies for fabricating electrodes over electrolytes, trying to optimize the performance and stability of already existing state-of-the-art SOEC materials [39], [40], [226], [229], [230]. An effective fabrication method which has attached a lot of attention is to utilize the electrolyte material as a porous electrode scaffold and infiltrate directly into it electrochemically active and electronically conductive components. [39], [40], [226], [230], [231] It is needless to say that the first approach has much lower technology readiness level (TRL), since even if highly electrochemically active materials are found, they should also respect other requirements before being integrated to SOEC cells. For example electrode materials should not react with other parts of the cell, like electrolyte and interconnect materials, while they should have compatible thermal expansion coefficients and be able to maintain certain porosity. The second approach possesses many advantages, since it can be directly integrated to the existing SOEC technology.

To promote water dissociation and hydrogen production of GDC-based electrocatalysts one has to optimize the number of the electrocatalytic active sites. Theoretical investigations proposed that this can be done by increasing the population of ceria oxygen vacancies as well as the interfacing of ceria and Ni areas at the electrode [232]–[234]. However building GDC-based cermets with these characteristics that can also withstand at high SOEC operation temperatures

remains a difficult task. In addition, substitution of YSZ with GDC in SOEC electrodes faces several technical difficulties including the poor mechanical strength of GDC as compared to YSZ and the ease of GDC reduction which increases the electronic conductivity of the electrode and eventually might lead to short-circuits problems in the cell. Since electrochemical reactions take place at surfaces, incorporating GDC on the surface of conventional Ni-YSZ electrodes could be an effective method to improve the electrochemical performance, with minor impact on the thermal and mechanical stability of the cell. Impregnation of Ni-YSZ electrodes with ceria or metal/ceria solutions has been shown a quite promising enhancement of the electrochemical performance [106], [170], [235], [236]. The impregnation method is a popular approach for the preparation of well-dispersed catalysts through low-temperature decomposition, and has been used to improve redox stability due to structural advantages. One remaining challenge though is to control the deposition process so as to keep Ni and GDC sites in close proximity and avoid segregation of the two materials during the high temperature reaction conditions, which will cause loss of the electrochemical active area.

Recently, Simona et al.[231] reported about a stable SOEC cell performance by infiltration of Ni-YSZ conventional electrode with $Ce_{0.8}Gd_{0.2}O_{2-\delta}$ (CGO) nanoparticles. The loading of 125 mg CGO per 1 cm^3 Ni-YSZ backbone; reduced the cell voltage degradation rate from 699 mV kh^{-1} for the bare Ni-YSZ electrode to 66 mV kh^{-1} for the infiltrated electrode at 800 °C and -1.25 A cm^{-2}. On the other hand, after introducing the CGO nanoparticles, the microstructure and chemical composition of both electrodes showed that the steam reduction mechanism was changed and the degradation was due to different mechanisms compared to the parent electrode.

Hussain et al. and Yurkiv et al. investigated Ni-ceria-impregnated $SrTiO_3$-based anodes for low temperature SOFCs[112], [237], [238]. Futamura et al. [236] developed zirconia-based electrolyte-supported SOFCs Ni-impregnated anodes with dispersed Ni catalyst nanoparticles on conducting oxide LST-GDC backbones, that exhibit lower anode non-ohmic overvoltage and improved I-V performance. Moreover, the co-impregnation of Ni catalysts and GDC nanoparticles further improves the electrochemical characteristics due to a decrease in anode ohmic (IR) loss and non-ohmic overvoltage. This anode shows comparable I-V performance to

conventional anodes for typical humidified hydrogen fuels and is a promising redox-stable alternative for application at high fuel utilization.

In this chapter we propose a novel strategy to increase the performance and stability of SOEC cells by surface modification of standard Ni-YSZ electrodes using nickel-substituted ceria nanoparticles ($Ni_{0.1}Ce_{0.9}O_{2-x}$) as promoters. This approach provides highly reducible ceria and abundant Ni/ceria interface sites combined together into a single material. Moreover, due to their small size the NPs can be easily incorporated on standard Ni-YSZ electrodes (acting as a back-bone) with minimal fingerprint to the overall cell characteristics. We show that $Ni_{0.1}Ce_{0.9}O_{2-x}$ NPs have very distinct electronic and redox properties as compared to conventional ceria-supported Ni particles. Notably, we demonstrate that modification of Ni-YSZ electrodes with $Ni_{0.1}Ce_{0.9}O_{2-x}$ NPs results to superior performance for low temperature water electrolysis as compared to unmodified electrodes.

5.2. Experimental part

Electrolyte-supported NiYSZ//YSZ//Pt SOEC cells with a Pt reference electrode were prepared and used to evaluate the effect of NiCe NPs on the performance of Ni-YSZ electrodes during water electrolysis. The Ni-YSZ working electrode (WE) was fabricated using a typical preparation procedure for solid oxide button cells [239]. Platinum was used for counter (CE) and reference (RE) electrodes due to its high performance stability [170] in order to minimize discrepancies in the cell performance related to the CE.

5.2.1. Fabrication of $Ni_{0.1}Ce_{0.9}O_{2-x}$ modified Ni-YSZ cells

The Ni-YSZ working electrode (WE) was fabricated by our collaborators in Centre for Research and Technology-Hellas (CERTH, Thessaloniki-Greece) using a commercial NiO-YSZ cermet powder (Fuel Cell Materials, 66% by weight NiO, 34% by weight $(Y_2O_3)_{0.08}(ZrO_2)_{0.92}$) which was formed as ink (solid content 70 %wt.) and applied by means of screen printing (STV, mesh 40 μm) on an Yttria-Stabilized-Zirconia (YSZ) pellet (Kerafol, 8YSZ) with a thickness of 150 μm. The half cells were calcined in air at 1350 °C for 3 h. The mean Ni-YSZ electrode thickness was about 40-50 μm as estimated by cross-sectional SEM images. For the preparation of CE, platinum paste (Pt ink 5542-DG, ESL) was painted symmetrically opposite of the WE and was separated by about 3 mm from the RE painted at the same side as described before in chapter 2.

After painting the Pt electrodes the cell was left to dry for about 1 hour at 100°C and then fired in air at 980 °C for 10 min.

The Ni-YSZ electrode was used as a scaffold and was impregnated with $Ni_{0.1}Ce_{0.9}O_{2-x}$ – containing hexane solution. The solution was dropped onto the Ni-YSZ scaffold using a 10 μL micropipette. Different loadings of $Ni_{0.1}Ce_{0.9}O_{2-x}$ –containing hexane solution were tested, namely from 100 to 500 μL/cm^2. Using NPs diluted in a hexane solution is beneficial for the infiltration process because of the low surface tension (18.4 mN/m) at room temperature, which should help to wet the pores of the Ni-YSZ electrode better than other solvents, i.e. water (71.97 mN/m). In addition hexane is a liquid with low viscosity which can easily penetrate the pores of the electrode during infiltration.

After the impregnation and prior to the electrochemical tests the electrode was fired for 1 hour in 7 mbar O_2 at 400 °C to remove the organic residuals and consequently underwent reduction in 7 mbar H_2 at 450 °C. The fabrication process of the $Ni_{0.1}Ce_{0.9}O_{2-x}$ modified Ni-YSZ electrode is graphically summarized in fig. 5.1. Electrochemical experiments, before and after modification with the NiCe NPs, were performed at the same cells (specimens) to assure that the performance won't be influenced by possible differences in the cell fabrication. The improvement of the Ni-YSZ electrode performance after NiCe NPs modification was confirmed by 4 repeated electrochemical tests using each time different Ni-YSZ cells.

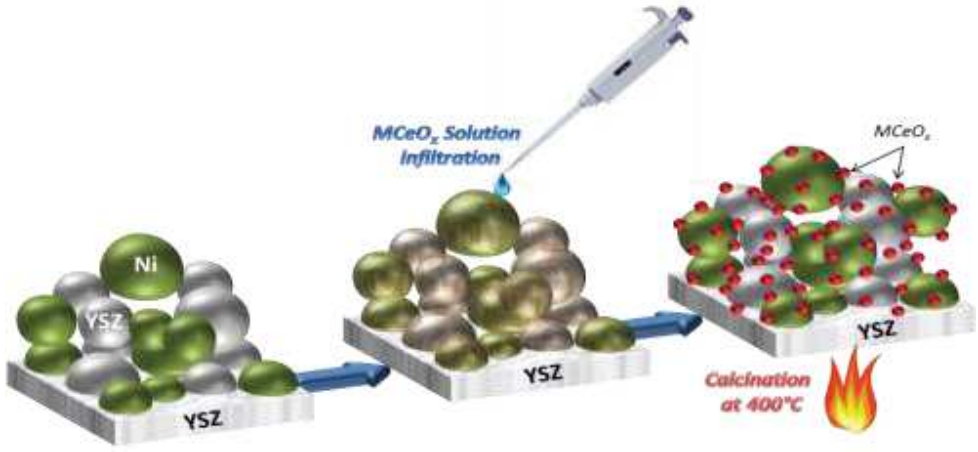

Figure 5.1. Schematics of the $Ni_{0.1}Ce_{0.9}O_{2-x}$ modified Ni-YSZ sample preparation.

5.2.2. Characterization Methods

The X-ray photoelectron spectroscopy (XPS) measurements were carried out in an UHV setup (base pressure 1×10^{-9} mbar) [240] described in chapter 2. Each oxidation/reduction step lasted 30 min at constant temperature and gas (H_2 or O_2) pressure of 7 mbar. Subsequently to the gas treatment, the sample was cooled to room temperature in gas and the reactor was evacuated to 5×10^{-8} mbar. Then the sample was transferred in vacuum into the analysis chamber for XPS characterization. Characterization of SOEC cell electrodes was performed with the sample heated at 220 °C where it was found that the conductivity was sufficient to avoid electrostatic charging problems during XPS measurements. Raman spectra were acquired at room temperature and atmospheric conditions using a micro-Raman spectrometer (Horiba LabRam), with excitation wavelength of 532 nm. A 100× objective was used to focus the excitation laser to an approximately 1 μm spot with a laser power of less than 1 mW to avoid heating and damage of the sample. The morphology of the cells before and after modification was investigated by a JEOL JSM-6700F scanning electron microscope.

5.2.3. Electrochemical measurments

SOEC cells with geometric surface areas between 0.2 and 0.4 cm^2 were mounted on a ceramic heater using gold wires at the back side as contacts for the CE and RE. Stainless steel clamps attached on the top of the cell were used as current collectors for the WE. The temperature was measured by a K-type thermocouple mounted directly at the side of the heater and the gas flow into the reaction cell was controlled by mass flow controllers. In order to provide insights of the electrode function the experiments were performed in a specially designed reactor described in chapter 2 [219] which allowed surface characterization of the WE after electrochemical testing without prior exposure to air. The particularity of this setup is that can operate at various pressures (from 10^{-3} mbar up to 1 bar) and that both sides of the cell are exposed in the same gas/vapour environment. Polarization curves and electrochemical impedance spectroscopy (EIS) measurements were conducted by using a VersaSTAT 3 (AMETEK Scientific Instruments) potentiostat/galvanostat. The three-electrode configuration allowed the measurement of the overpotential of the working electrode without the influence of the counter electrode. The overpotential was calculated from the DC set voltages by subtracting the OCP and the IR_{el}. The overpotential includes the ohmic drop in the electrolyte and the contact wires. Steam electrolysis

was tested at 100% H_2O atmosphere (without reducing agent in the feed) in 3 vapour pressure regimes (0.5 to 23 mbar). The cell operated at relatively low temperature (650±5 °C), since at this temperature range the oxidation of nickel parts of the Ni-YSZ cermet is less extended. As compared to the higher temperature operation of SOECs (>850 °C), where the use of H_2 co-feed is typically required in order to avoid Ni oxidation, low temperature operation offers the possibility to use 100% steam feed. Potentially such operation conditions are desired in order to simplify the design of the stacks and improve the mechanical stability of SOEC cells.

5.3. Result and discussion

5.3.1. Effect of water vapour pressure over Ni-YSZ cathode electrode overpotential

Since a big effort of this thesis is devoted to combine electrochemical measurements with in situ spectroscopy, the cell was exposed to relatively low steam partial pressures. In order to be able to compare these data with realistic SOEC cell operational conditions, we describe in this paragraph how the steam partial pressure influences the cell performance. Current-voltage (i-V) curves shown in fig. 5.2, were obtained in steam electrolysis conditions under 3 different vapour pressure regimes. In particular, the i-V curves were recorded at 100% H_2O atmosphere (without reducing agent in the feed) and in 0.5, 11 and 23 mbar total water vapour pressure (the water was directly evaporated in the reactor from a reservoir without the use of an inert carrier gas). Comparison of the 3 curves clearly illustrates that for the same current densities, higher water vapour pressures are correlated to higher overpotentials. This effect can be understood by the effect of water vapour pressure to the oxidation state of nickel. One can argue that as the water vapour pressure increases, nickel oxidation is enhanced, therefore the cell is deactivated. That is probably the reason why in the low pressure conditions used in NAP-XPS experiments the cell operates without severe deactivation while real testing conditions require the use of H_2/H_2O mixed atmosphere.

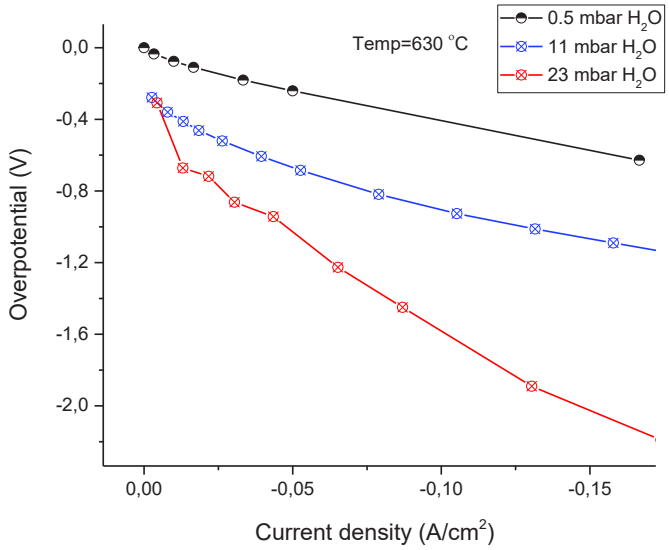

Figure 5.2. Current density-overpotential curves measured under steam electrolysis conditions at 630 °C in3 vapour pressure regimes (0.5, 10 and 23 mbar).

5.3.2. Water electrolysis over $Ni_{0.1}Ce_{0.9}O_{2-x}$ modified Ni-YSZ electrodes

Having shown in chapter 4 that $Ni_{0.1}Ce_{0.9}O_{2-x}$ NPs are relatively stable and prompt to the formation of oxygen vacancies, in this paragraph we explore its influence on the electrochemical activity of Ni-YSZ electrodes during steam electrolysis. In order to do so, the $Ni_{0.1}Ce_{0.9}O_{2-x}$ solution was directly drop-casted on the WE (Ni-YSZ) of a preformed Ni-YSZ/YSZ/Pt cell and subjected to oxidation and reduction pretreatments as described in the experimental part. The surface oxidation state of both electrodes after the last pretreatment step (7 mbar H_2) and before the water electrolysis test is verified by the XPS results shown in fig. 5.3. For brevity hereafter the $Ni_{0.1}Ce_{0.9}O_{2-x}$ modified Ni-YSZ/YSZ/Pt is abbreviated as NiCe@NiYSZ. For comparison, the performance of the Ni-YSZ/YSZ/Pt cell prior to modification was also evaluated under identical conditions (here after abbreviated as Ni-YSZ). As can been seen in fig. 5.3 after the H_2 pretreatment both electrodes contain metallic nickel on their surface, while after NiCe modification a clearly distinguishable signal due to the Ce 3d peak appears in the spectrum. What is interesting to note is that the shape of the Ce 3d peak indicates that the majority of ceria is in the reduced Ce^{3+} state. This supports the idea presented above that NiCe nanoparticles are

facile to reduce and can be easily transformed to the 3+ valence, which should be beneficial for water electrolysis.

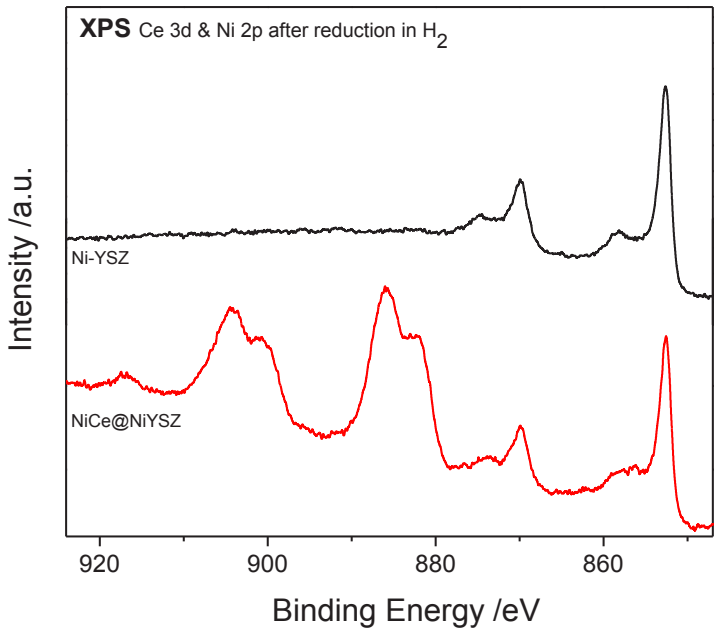

Figure 5.3. Ce 3d and Ni 2p spectra of the recorded over Ni-YSZ and 570NiCe@NIYSZ electrodes after reduction in 7 mbar H_2 at 400 °C.

Redox stability under cathodic polarization in steam

Before measuring the i-V curves from conventional Ni-YSZ and 570NiCe@NiYSZ impregnated electrodes, both cells were set under cathodic polarization of -10 mA/cm^2 in 0.5 mbar H_2O for 35 minutes. In fig. 5.4 the evolution of the cell potential as a function of time at constant current density is shown. It is evident that after modification of the NiYSZ electrode with NiCe NPs the potential of the cell drops significantly from -0.74 V to -0.28 V. Notably the impregnated cell not only shows significantly lower initial potentials but also is gradually improving with time. On the contrary, the potential of the cells with conventional Ni-YSZ cathodes was steadily increasing with time.

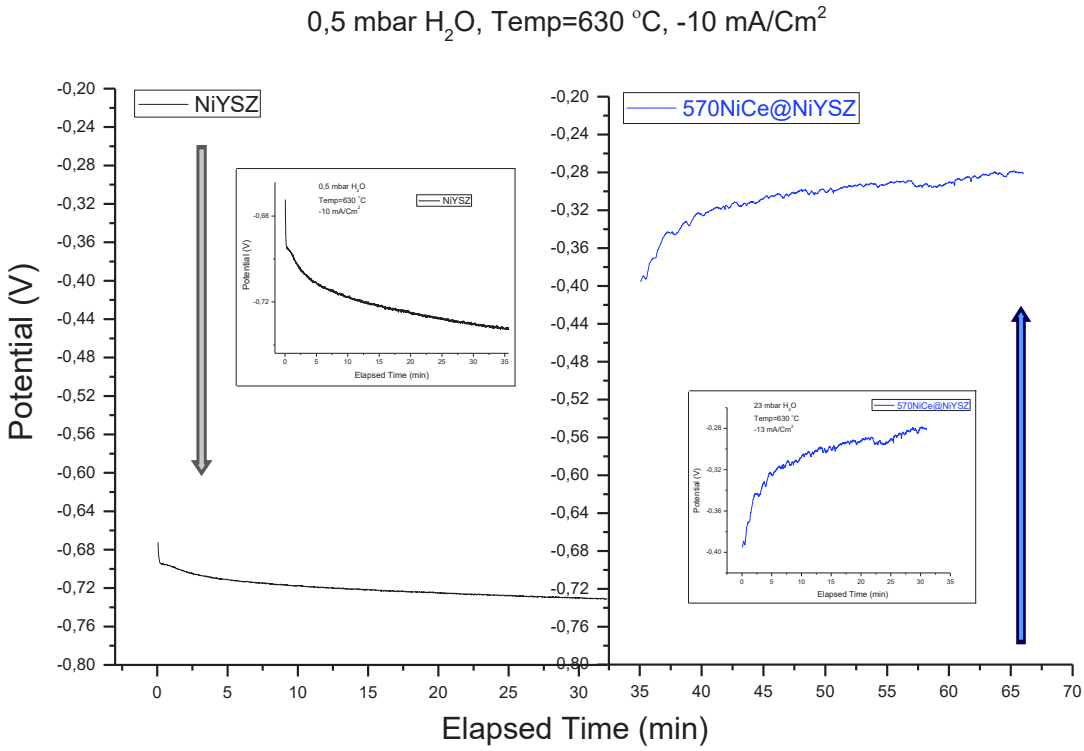

Figure 5.4. Time evolution of Ni-YSZ cathode electrode overpotential (*black line*) and 570NiCe@Ni-YSZ (*blue line*) measured at constant current of -10 mA/cm^2 at 630°C in 0.5 mbar of 100% H_2O.

The polarization curves under H_2O electrolysis conditions recorded on cells with Ni-YSZ cathodes before and after the addition of NiCe NPs at two operation pressures are shown in fig. 5.5a. In this graph only one characteristic NiCe NPs loading is shown, while later in this chapter we will illustrate the effect of different NiCe NPs loadings on the cell performance. It is clear that in both tested pressure regimes the polarization performance of Ni-YSZ is improved after impregnation with NiCe NPs. In particular, at 0.5 mbar after the addition of 570 µL/cm^2 of NiCe NPs solution the total overpotential, including activation, ohmic and concentration losses, drops up to 1 V, while at 23 mbar (which corresponds to about 77% relative humidity) the drop is even higher.

The impedance data were measured on two similar cells (Ni-YSZ/YSZ/Pt) but with different YSZ electrlolyte thicknesses. The first cell with electrolyte thickness of 300 µm was tested under

0.5 mbar H_2O at galvanostatic mode of -10 mA/cm^2 (fig. 5.5b) while the second cell with electrolyte thickness of 150 μm was tested under 23 mbar H_2O at galvanostatic mode of -30 mA/cm^2 (fig. 5.5c). From these results the total Ohmic resistance R_{el} can be found by reading the real axis value at the high frequency intercept. The diameter of the semicircle is equal to the polarization resistance, R_p which is related to the kinetics of the reactions and the diffusion of water both towards and away from the electrode. As can been seen, the polarization resistance decreases after NiCe addition in both pressure regimes. The ohmic resistance does not change considerably at the low pressure experiment while at higher pressure there is significant improvement of R_{el} in the case of NiCe addition (fig. 5.5c). This confirms the interpretation given above regarding the oxidative effect of water vapors on nickel especially at the higher pressure regime.

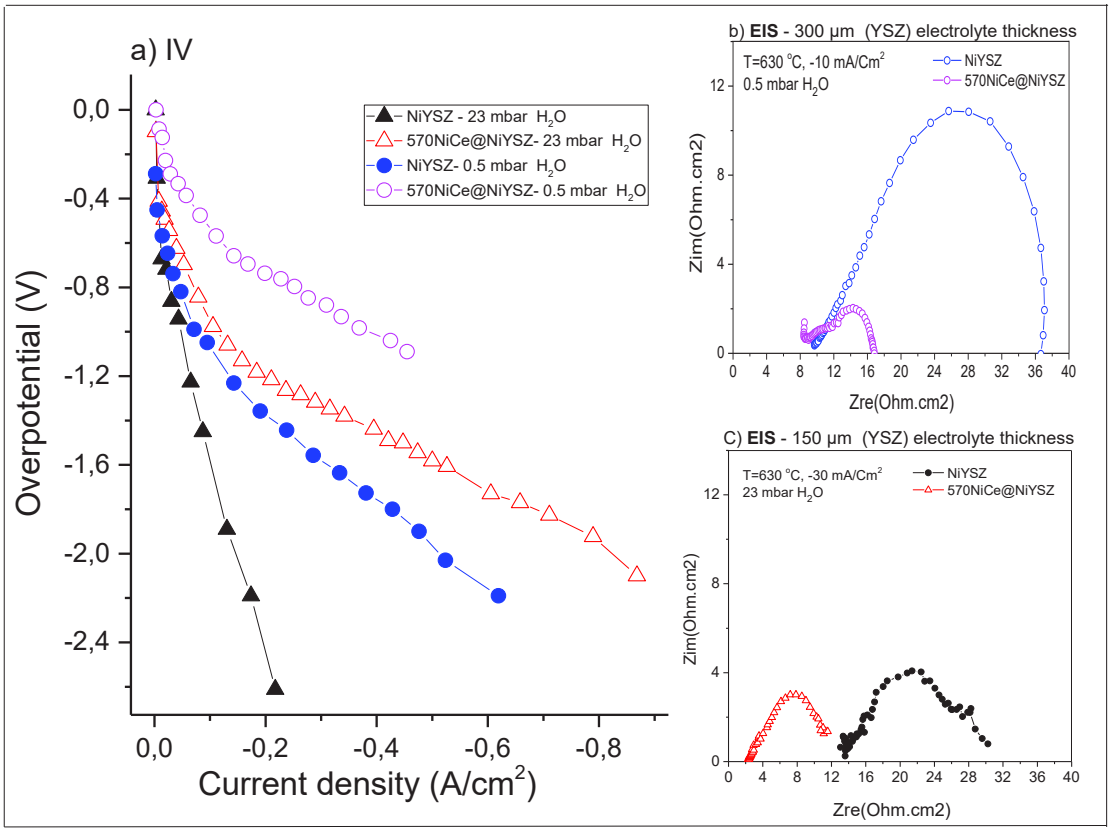

Figure 5.5. a) Current-overpotential curves measured under steam electrolysis conditions over Ni-YSZ and 570NiCe@NiYSZ electrodes during stem electrolysis at 630°C in 0.5 mbar and 23 mbar of 100% H_2O. Impedance spectra presented in Nyquist form, b) obtained under constant

applied current of -10 mA cm^{-2} at 0.5 mbar H_2O, C) obtained under constant applied current of -30 mA cm^{-2} at 23 mbar H_2O, both over Ni-YSZ and 570NiCe@NiYSZ electrodes at 630 °C.

The analysis of the Ni $2p_{3/2}$ and Ce 3d spectra recorded from the two electrodes after electrochemical reaction is presented in Figure 5.6. In the case of the 570NiCe@NiYSZ electrode, the deconvolution of Ce 3d spectra, performed after subtraction of the contribution of the overlapping Ni $2p_{3/2}$ component in Figure 5.6a, reveals coexistence of both Ce^{3+} and Ce^{4+} states. Please note that prior to the electrochemical tests the electrodes were reduced to metallic Ni and 100% Ce^{3+} in H_2 (*see* fig. 5.3). Thus pre-reduced NiCe NPs undergo oxidation under electrolysis conditions; however oxidation is only partial, since a significant portion of Ce^{3+} ions still remains. This is in accordance with previous studies on Nickel gadolinia-doped ceria (NiGDC) cermet electrodes which showed that a mixed Ce^{4+}/Ce^{3+} oxidation state is maintained in thermodynamic equilibrium with steam [50].

The analysis of the Ni $2p_{3/2}$ spectra is complicated due to the overlapping between photoemission and intense satellite peaks. As indicated in Figure 5.6b, four characteristic features can be distinguished in the Ni $2p_{3/2}$ spectra measured after steam electrolysis. The main peak at 854.1 eV and the distinct peak feature at 852.5 eV are typically assigned to oxidized Ni^{2+} and metallic Ni^0 [174] respectively, as discussed also above. The other two peak features at 855.7 (*sat.1*) and 861.0 eV (*sat.2*) are satellite features induced by complex final state photoemission phenomena taking place in oxidized nickel. All examined electrodes contain a metallic Ni^0 peak, suggesting that under the employed electrolysis conditions nickel is not fully oxidized. This can explain the electrochemical measurements which show that even in 100% H_2O the electrode has certain conductivity. Close examination of the Ni^{2+} and sat.1 peaks reveals that in the case of the 570NiCe@NiYSZ electrode the intensity of sat.1 peak is notably enhanced as compared to the NiYSZ samples. Since this peak shape does not correspond to any of the oxidized nickel species reported so far, we attempted to reproduce this feature by adding a small component with the characteristics of Ni 2p spectra found on $Ni_{0.1}Ce_{0.9}O_{2-x}$ NPs (see chapter 4). Indeed, as shown by the blue curve in figure 5.6b, about 10% of the Ni 2p signal of 570NiCe@NiYSZ electrode comes from Ni^{3+} species originating from NiCe NPs. This observation not only indicates that a significant population of these "doped" nickel species are present on the surface during electrolysis, but also shows that the oxidation state of nickel as Ni^{3+} in the $Ni_{0.1}Ce_{0.9}O_{2-x}$ particles

is stable during the electrochemical reaction (since the Ni 2p spectra also remain identical with those of the material prior to the doping).

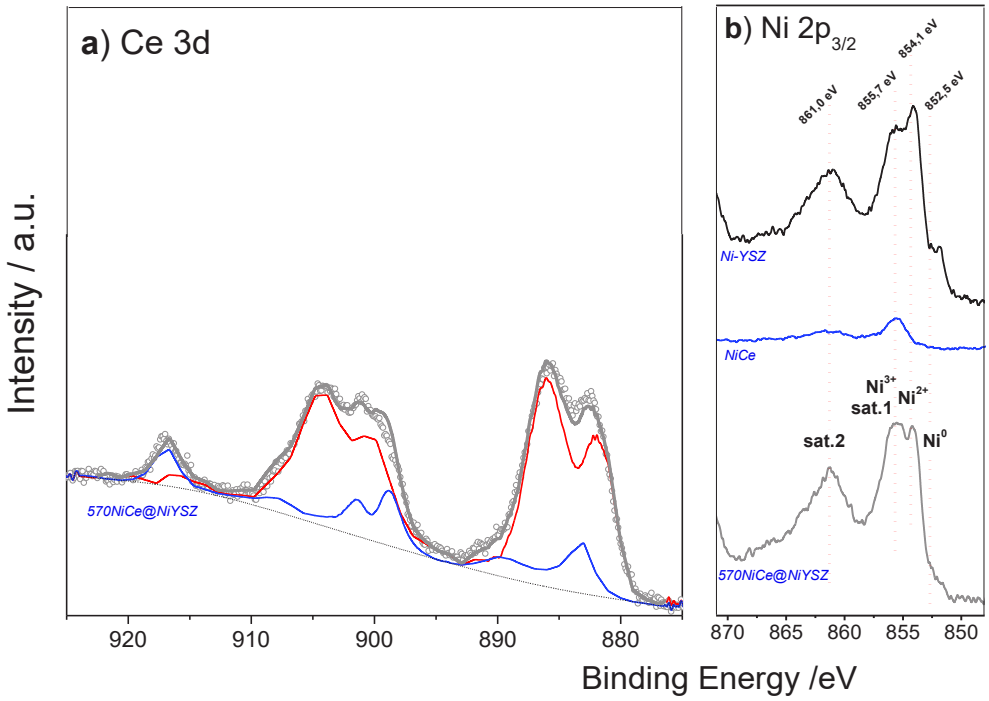

Figure 5.6. a) Ce 3d XPS spectra of 570NiCe@NiYSZ electrodes measured after steam electrolysis. The Ni $2p_{1/2}$ contribution has been properly subtracted and the spectra are deconvoluted using reference peaks measured on pure Ce^{3+} and Ce^{4+} ceria states b) Ni $2p_{3/2}$ XPS spectra measured on NiYSZ and NiCe@NiYSZ electrodes. The reference peak measured on $Ni_{0.1}Ce_{0.9}O_{2-x}$ NPs is included for comparison.

Surface morphology of $Ni_{0.1}Ce_{0.9}O_{2-x}$ modified Ni-YSZ electrodes

The surface morphology of the NiYSZ and 570NiCe@NiYSZ electrodes after electrolysis is analyzed by SEM (fig. 5.7). In both cases the electrodes are composed of well-mixed Ni and YSZ areas, which produce a very clear contrast in the SEM images. The YSZ areas are smooth for both electrodes, while Ni areas have a rough surface texture, which is quite distinct before and after modification. In particular for the Ni-YSZ electrode the Ni areas appear porous, while after doping there are no evident pores. In the high magnification images of the 570NiCe@NiYSZ electrode Ni and YSZ areas are covered with small nanoparticles with sizes in the range of 10-20 nm. The EDS profile from these areas show only peaks related to Ni and

YSZ, however the corresponding XPS analysis shown above confirms a clear signal of ceria species (see fig. 5.5), allowing to connect these particles with agglomerated $Ni_{0.1}Ce_{0.9}O_{2-x}$ NPs. Keeping in mind the very different surface sensitivity of the two methods, it is quite reasonable that small particles decorating the surface of the electrodes do not have a strong EDS signal in contrast to XPS.

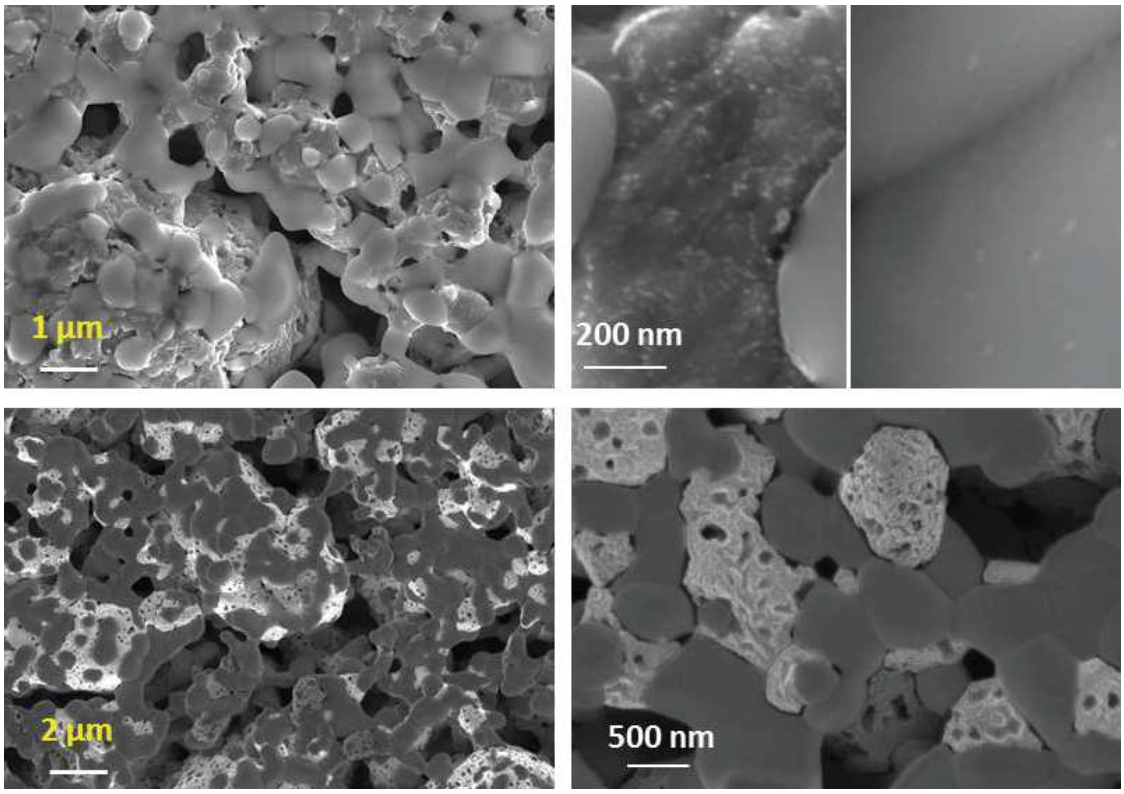

Figure 5.7. SEM micrographs of the Ni-YSZ electrodes before and after addition of $Ni_{0.1}Ce_{0.9}O_{2-x}$ NPs measured after water electrolysis conditions (at 650◦°C in 0.5 mbar of 100% H_2O).

The analysis of the Raman spectrum recorded on the 570NiCe@NiYSZ electrode after electrolysis is complicated because the Raman peaks related to ceria and YSZ are overlapping as shown in fig. 5.8. However the Raman spectrum remains similar to that of the original NiCe (see fig. 4.4) with a potential reduction of the features related to defect ceria sites. The cross sectional SEM images of the electrode shown in the same figure suggest that NiCe modification did not induce any noticeable macroscopic changes in the electrode porosity, validating the method of using NPs for the modification since they have a negligible influence of the electrode microscturcture.

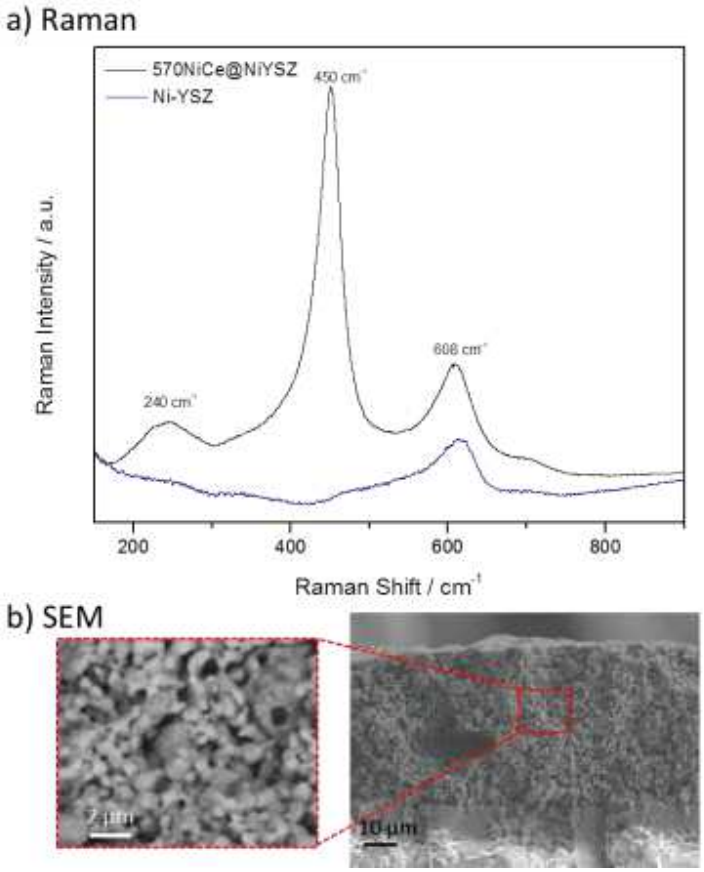

Figure 5.8. a) Raman spectra of the 570NiCe@NiYSZ and Ni-YSZ electrodes recorded after electrolysis experiment. b) Cross sectional SEM micrographs of the 570NiCe@NiYSZ electrode after electrolysis experiment**.**

5.3.3. Optimization of $Ni_{0.1}Ce_{0.9}O_{2-x}$ loading of the modified Ni-YSZ electrodes

In the previous section it was shown that impregnation with Ni-doped ceria nanoparticles allows introducing a high population of easily reducible and highly interfaced Ni-ceria sites on the surface of Ni-YSZ with negligible fingerprint to the overall cell morphology or electrode porosity. Electrochemical characterization under low temperature water electrolysis conditions showed that the modified Ni-YSZ electrodes are significantly improved and in particular the polarization losses are much lower as compared to the conventional (parent) unmodified cell. In addition after modification the Ni-YSZ electrodes maintain their activity even at highly oxidative electrolysis conditions, without the need of introducing a reducing agent (e.g. H_2). Ex-situ surface characterization suggested that the enhancement of the performance is related to a

significant population of Ce^{3+} and Ni^{3+} surface sites maintained on the Ni-YSZ surface during electrolysis. Consequently, it is very important to investigate the effect of different loadings of the NiCe NPs and also optimize all the factors that could influence the electrochemical measurements combined with the surface characterization. In the next section, we will discuss ex-situ and in-situ NAP-XPS results for the impregnated samples with different loadings of NiCe NPs under steam electrolysis conditions.

The effect of NiCe NPs loading over NiYSZ electrode electrochemical performance

The population of Ce^{3+} and Ni^{3+} surface sites originated from Ni-doped ceria nanoparticles helps to improve the electrochemical performance of the Ni-YSZ electrode as discussed above. In order to understand more precisely the influence of these created electrocatalytic sites, the Ni/YSZ electrodes were modified using increasingly higher loading of NiCe NPs and consequently the electrochemical performance of the cell was compared under identical steam electrolysis conditions. In particular 100, 200, 300, 400 and 500 μL/cm^2 of the $Ni_{0.1}Ce_{0.9}O_{2-x}$ containing hexane solution was impregnated on the same Ni-YSZ electrode. After each impregnation step, the electrode was subjected to oxidation-reduction pre-treatments as discussed above to remove the organic part. After each NiCe NPs loading i-V and EIS measurements were performed under 0.5 mbar H_2O and 630 °C. These measurements are presented in fig. 5.9.

The i-V curves illustrate that the overpotential consumption of the conventional Ni-YSZ electrode before the impregnation is higher as compared to that measured after the impregnation with different NPs loadings. Pease note that a higher cell voltage at the same current densities means that a larger input of power is needed to split water and generate the same amount of hydrogen. At low current densities the overpotential of 100NiCe@Ni-YSZ is already lower than that on conventional Ni-YSZ (at -0.1 A/cm^2= -0,821 V and -1,045 V respectively). At higher 200NiCe@Ni-YSZ loading the cell performance is improved even more substantially (ca. -0,4 V at -0.1 A/cm^2), while at even higher loading, the cell overpotential remains practically stable. One can calculate that for 100NiCe@Ni-YSZ, the overpotential decreased by 21% as compared to the Ni-YSZ before impregnation while for the 200-500NiCe@Ni-YSZ loadings, the decrease ranges from 62 to 66 %. At higher current densities (at -0.6 A/cm^2) the effect of the NiCe NPs modification is even more evident with almost 24.6% decrease for the 100NiCe@Ni-YSZ (from

-2,19 V for Ni-YSZ the overpotential drops to -1,65 V) and almost 45% decrease for the 200-500NiCe@NiYSZ. One interesting point to note is that all these measurements were performed on the same cell intermittent for 50h and exposed every time to oxidation reduction before steam electrolysis, therefore the effect of NiCe NPs also competes the expected degradation of the cell after this relatively long testing period.

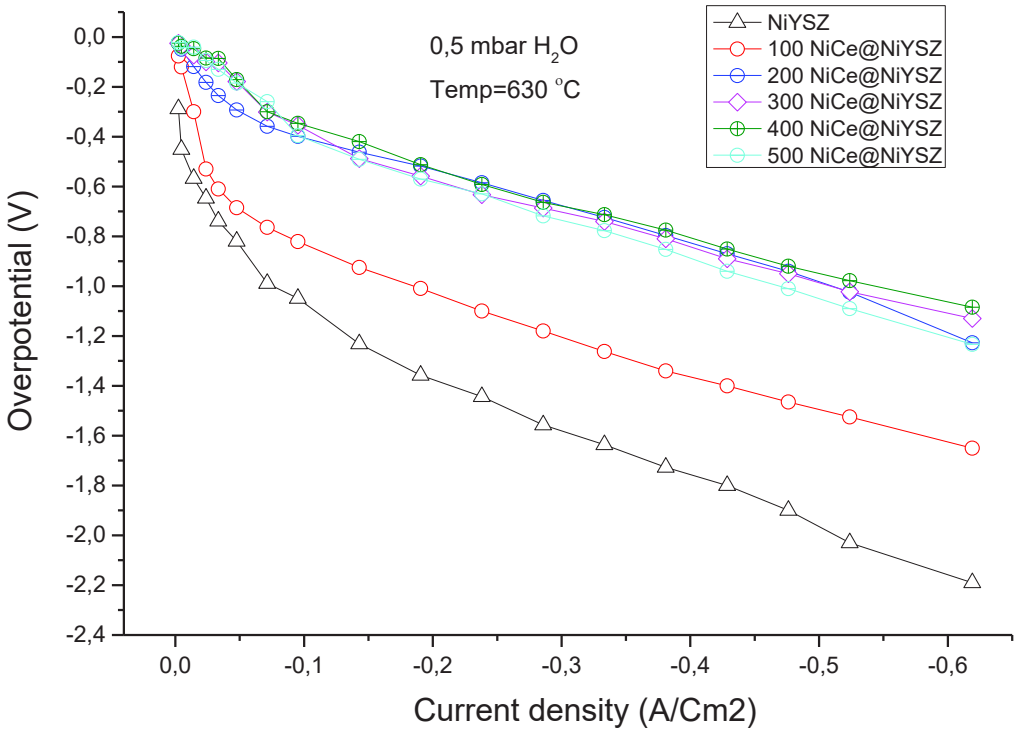

Figure 5.9. a) Current-overpotential curves measured under steam electrolysis conditions over Ni-YSZ conventional electrode and 100NiCe@NiYSZ, 200NiCe@NiYSZ, 300NiCe@NiYSZ, 400NiCe@NiYSZ and 500NiCe@NiYSZ impregnated electrodes (from bottom to top) during steam electrolysis at 630°C in 0.5 mbar of 100% H_2O.

The effect of hexane solution over NiYSZ electrode electrochemical performance

The oxidation/reduction treatment process on the impregnated Ni-YSZ electrode is a necessary step to remove the organic part around of the NPs and also the possible remainings of the hexane solvent itself. As discussed above in order to do this the cell is subject to a redox cycle (up to 400 °C). In order to clearly demonstrate the effect of NiCe NPs it is important to estimate the effect

of this redox procedure on the cell performance. In order to do so we perform a "placebo" experiment where the NiYSZ electrodes were impregnated in pure hexane (which does not contain any NiCe NPs) and subjected to the same redox treatment.

In fig. 5.10, the i-V curves illustrate that the overpotential of the conventional Ni-YSZ electrode after the "placebo" impregnation increases as compared to its initial state. In particular the degradation (as manifested by the i-V curves) is increasing when the loading of hexane solvent increases from 100 to 200 μL/cm^2 as is revealed from the IV slope and the higher overpotential consumption values in fig. 5.10.

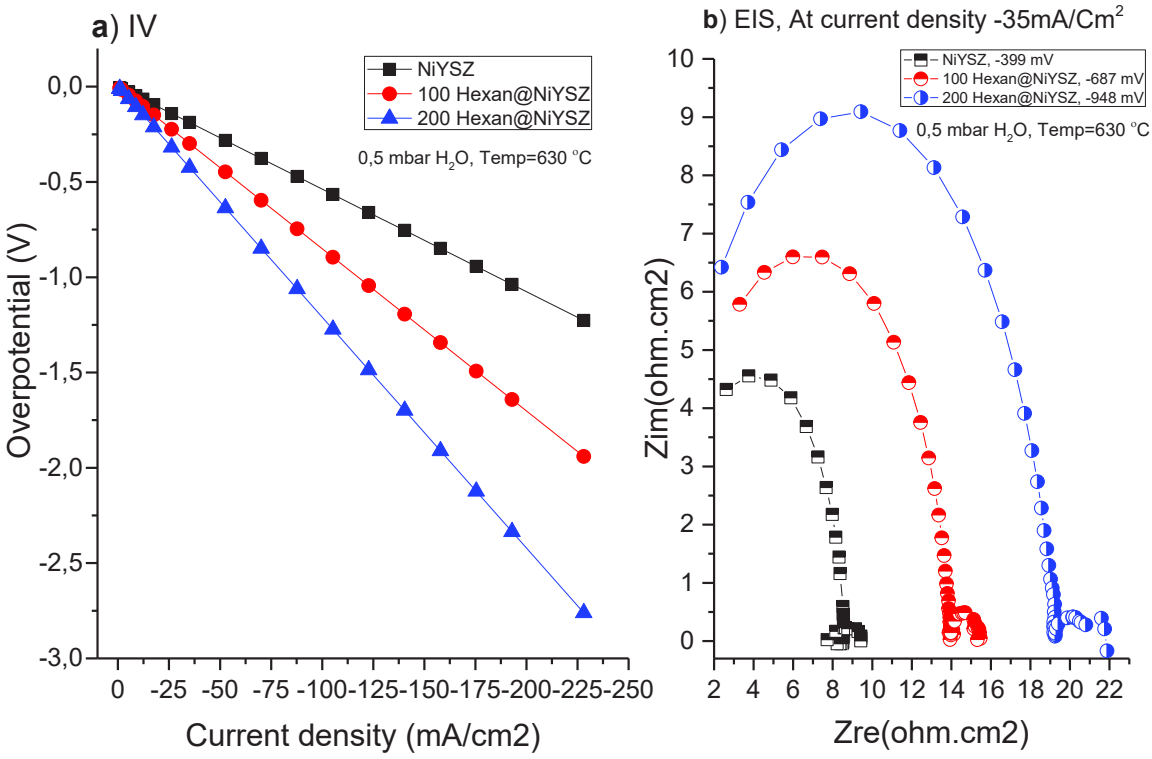

Figure 5.10 a) Current-overpotential curves measured under steam electrolysis conditions over Ni-YSZ conventional electrode, 100Hexane@NiYSZ and 200Hexane@NiYSZ impregnated electrodes (from bottom to top) during steam electrolysis at 630°C in 0.5 mbar of 100% H_2O. b) Impedance spectra presented in Nyquist form, obtained under constant current density of -35 mA/cm^2, the EIS are measured for Ni-YSZ conventional electrode, 100Hexane@NiYSZ and

200Hexane@NiYSZ impregnated electrodes during stem electrolysis at 630°C in 0.5 mbar of 100% H_2O.

The EIS recorded at -35 mA/cm^2 reveal that the observed differences in the cell voltage between the Ni-YSZ electrode before and after the "placebo" impregnation is correlated with an increase of both R_{el} and R_P contributions, as shown in table 5.1. Ex-situ XPS measurements on 200hexane@Ni-YSZ shown in fig. 5.12 (please look at the following paragraphs) reveals that nickel is totally oxidized after exposing to the oxidation/reduction treatment followed by the steam electrolysis test, which is in a good agreement to previous results[48], [50], [148].

Table5.1. Comparison of the ohmic and polarization resistances values determined from the impedance diagrams of fig. 5.11 over Ni-YSZ conventional electrode, 100Hexane@NiYSZ and 200Hexane@NiYSZ impregnated electrodes.

Loading of NPs ($\mu L/cm^2$)	-35 mA/cm^2	
	Ohmic Resistance (R_{el}) ($\Omega.cm^2$)	**Polarization Resistance(R_p) ($\Omega.cm^2$)**
Ni-YSZ	**8.5 ± 0.1**	**0.9 ± 0.1**
100Hexane@Ni-YSZ	**13.9 ± 0.1**	**2 ± 0.1**
200Hexane@Ni-YSZ	**19.2 ± 0.1**	**2.6 ± 0.1**

5.4. The effect of ceria oxidation state: Surface composition and electrochemical behavior

The challenge of Ni-YSZ impregnation with NiCe NPs is to combine the thermal and mechanical stability of NiYSZ and the high electrochemical electronic activity of GDC. By this way we optimize the number of the electrocatalytic active sites by manipulating their population though the amount of loading, without changing the macroscopic properties of the electrode. To ensure the efficiency of impregnated NiCe@Ni-YSZ electrodes; their performance was compared with cells with conventional Ni-GDC cathode electrodes. In fig. 5.11 we compare the i-V curves of cells with NiGDC electrodes, with these of cells with modified and unmodified NiYSZ

electrodes. For these tests it was decided to use pure steam atmospheres and relatively low temperature (630 C). As can be seen in fig. 5.11 the cell with the unmodified NiYSZ electrode operates at much higher overpotentials as compared to the other electrodes. The cell with NiGDC works at lower overpotentials than NiYSZ but the cell with 500NiCe@NiYSZ shows the better electrochemical performance among the 3 tested electrodes. The difference is small at low currents but it turns to become important at higher current densities. This implies that the modified NiYSZ cells do not only provide potentially better mechanical stability than NiGDC but can also combine this with enhanced electrochemical performance.

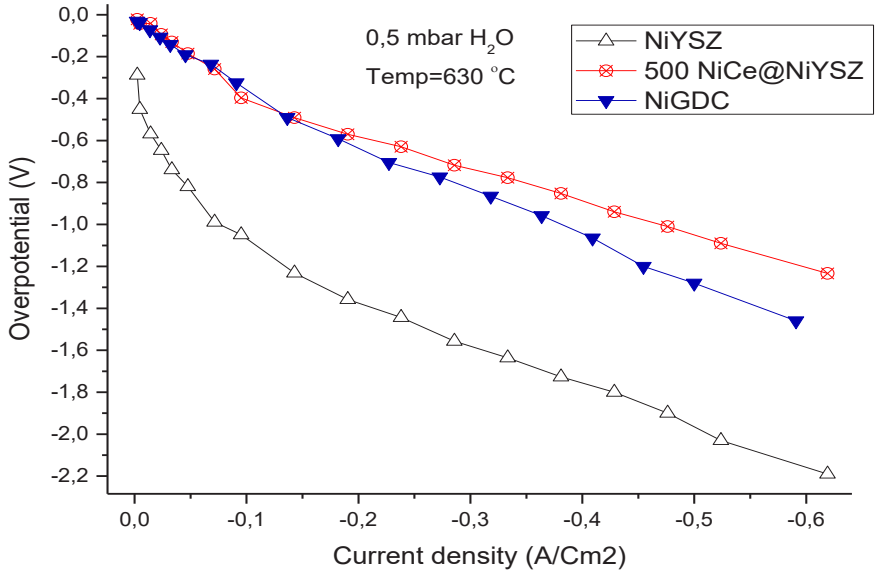

Figure 5.11. a) Current-overpotential curves measured under steam electrolysis conditions over Ni-GDC and Ni-YSZ conventional electrodes and 500NiCe@NiYSZ impregnated electrodes (from bottom to top) during steam electrolysis at 630°C in 0.5 mbar of 100% H_2O.

Ex-situ XPS measurements on both electrodes of 500NiCe@Ni-YSZ and Ni-GDC after the steam electrolysis tests are shown in fig. 5.12. These measurements reveal mainly the composition of the cell surface without being very informative about its chemical state, especially for nickel since it is known that it is easy to oxidize in air. According to previous findings although ceria oxidation state in oxidative atmosphere (steam) is much less influenced as compared to nickel, its impact on the electrode electrochemical performance is substantial [7],

[142], [148]. Nickel is totally oxidized as Ni^{2+} after the steam electrolysis tests for all electrodes as shown in fig. 5.13. As mentioned above one cannot safely assign this oxidation to the operation conditions, since part of it might be also due to atmosphere exposure after the reaction. Although the chemical state of ceria is in a mixed $Ce^{3+/}Ce^{4+}$ oxidation state for both electrodes, the doped ceria in NiCe@Ni-YSZ electrode is relatively more reduced (contains higher contribution of Ce^{3+} species) as compared to NiGDC. Comparison of the $Ce^{3+/}Ce^{4+}$ of the corresponding Ce3d spectra (fig. 5.12) shows a $Ce^{3+/}Ce^{4+}$ ratio of 1,24 in the case of 500NiCe@Ni-YSZ as compared to 0,81 for the Ni-GDC electrode. Although it is not clear how much the oxidation state of ceria was affected by the air exposure, these findings confirm what is presented in chapter 4 regarding the high reducibility of NiCe NPs as compared to bulk GDC. Also, they are in a good agreement with the results in chapter 3 connecting the formation of Ce^{3+} and the improvement of the cell performance, as shown by the cell overpotential.

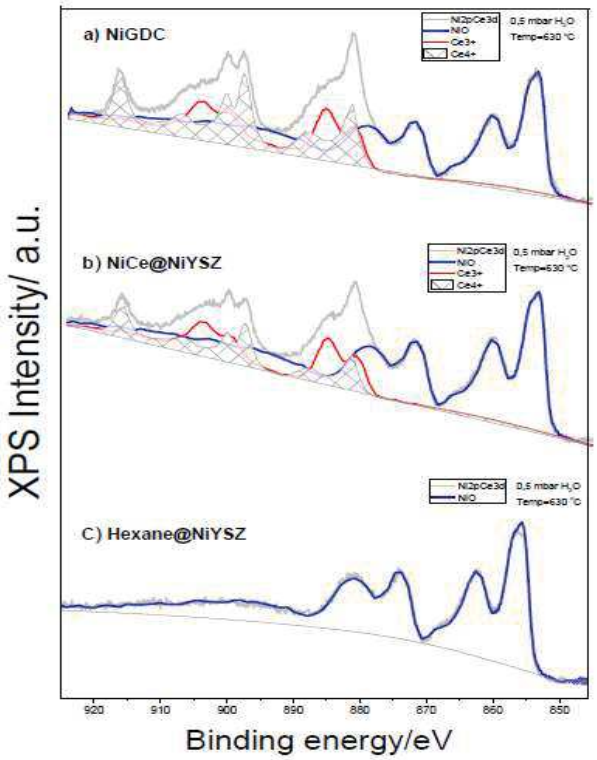

Figure 5.12. a) Characteristic $Ni2p_{3/2}$ and Ce 3d XPS spectra after exposing to steam electrolysis in 0.5 mbar H_2O at 630°C for Ni-GDC electrode, b) 500NiCe@NiYSZ and C)

200Hexane@NiYSZ. Two Ce 3d components were used to fit the spectra corresponding to Ce^{3+} (*red*) and Ce^{4+} (*grey*) oxidation states of ceria and NiO (blue) for Ni 2p.

5.5. Comparison of Ni-YSZ, Ni-GDC and NiCe@Ni-YSZ electrochemical performance in the presence of O_2

In chapter 3 we presented experiments where O_2 was deliberately introduced in the H_2O/H_2 feed in order to investigate the effect of the surface oxidation on the electrochemical performance of Ni-GDC and Ni-YSZ electrodes (please refer to fig. 3.13a). In this paragraph we follow the same approach in order to explore the resistance in O_2 of the Ni-YSZ electrode after impregnation with Ni-doped ceria nanoparticles. Fig. 5.13 shows the % increase of the overpotential as a function of the nickel oxidation state and the average NiO film thickness for the three electrodes (the data for cells with NiYSZ and NiGDC electrodes are reproduced from fig. 3.13 for comparison). Even if the $Ni_{0.1}Ce_{0.9}O_{2-x}$ NPs loading of the NiYSZ modified electrode is relatively low (20 μL/cm^2) its degradation upon introduction of O_2 is significantly lower as compared to the parent (unmodified) electrode. However, the degradation is higher as compared to the cells with the NiGDC cathode electrodes. This is probably the effect of the relatively lower amount of NiCe NPs, since in figure 5.9 it was shown that the best loading for an optimum modification is at least 10 times higher.

In addition to that, the evolution of the % overpotential in the case of the 20NiCe@Ni-YSZ is not linear like in the other two electrodes, but develops into two step points. In particular at the initial step of nickel oxidation (NiO/Ni+NiO ≈15) there is a sudden increase of the overpotential, similar to that observed at the NiYSZ electrode. However, upon further nickel oxidation the increase of the overpotential is very mild, like the one observed in the case of the NiGDC electrode. The EIS spectra of 20NiCe@Ni-YSZ measured in H_2O/H_2 (3/1) and $H_2O/H_2/O_2$ (3/1/1) feeds are shown together with those of Ni-YSZ and Ni-GDC electrodes in the right part of fig. 5.13. The EIS shown in fig. 5.13b&c were recorded at -100 mA/cm^2 and reveal that the observed differences in the cell voltage between the Ni-YSZ electrode before the impregnation and after each loading for the impregnated Ni-YSZ electrode come from the R_{el} and R_P contributions. As it is explained in chapter 3, the high frequencies semi-circle is related to the bulk impedance of the electrolyte and also to transfer reactions occurring near the electrode/electrolyte interface[89], [185]–[188]. The low frequency semi-circle is related to mass transfer phenomena occurring at the external side of the electrode[89], [143], [189]–[191] For

the conventional Ni-YSZ electrode, the EIS high frequency and low frequency contributions are shown in fig. 5.11, the Rel = 4.6 ± 0.2 Ω.cm^2 and R_p=1.30 ± 0.05Ω.cm^2 as shown in table 3.2. When the electrode was impregnated with 20NiCE@Ni-YSZ, the high frequency contribution decreased to R_{el}= 3.8 ± 0.05 Ω.cm^2 and the low frequency contribution to R_p=1.2 ± 0.05 Ω.cm^2. When 20% O_2 was introduced in the fuel feed, both the high frequency and low frequency contributions are: Rel = 5.4 ± 0.2 Ω.cm^2 & R_p= 2.4 ± 0.1Ω.cm^2 and Rels = 4.5 ± 0.2 Ω.cm^2 & R_p= 2.2 ± 0.1Ω.cm^2 for Ni-YSZ and 20NiCe@Ni-YSZ respectively.

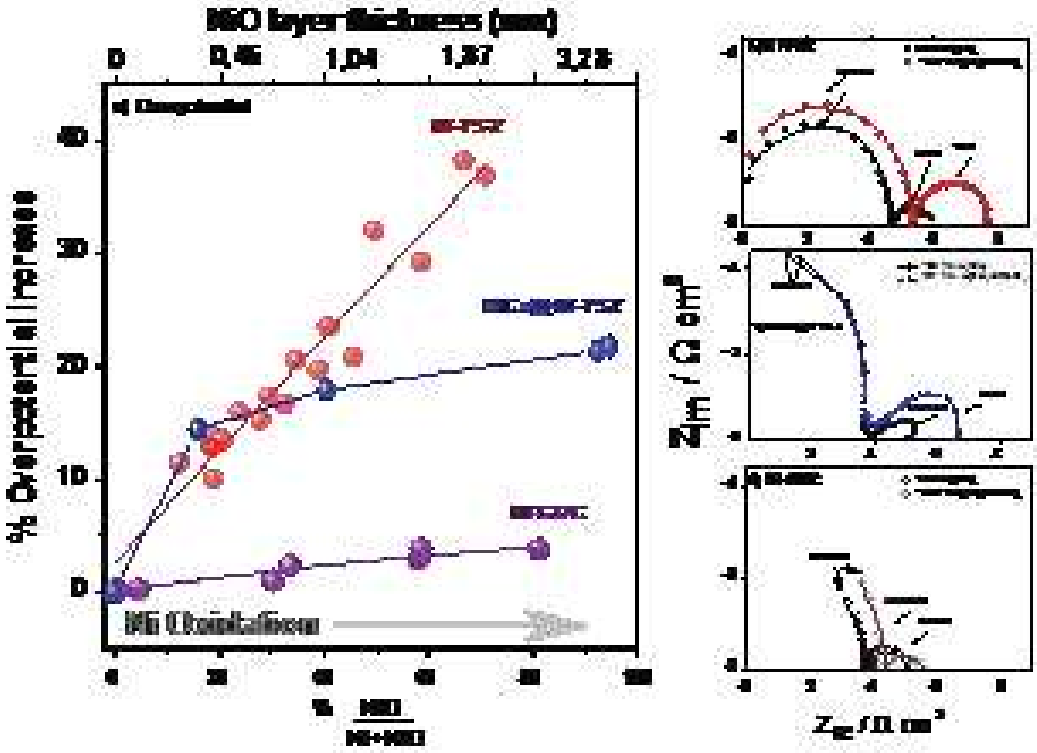

Figure 5.13. Comparison of the % overpotential increase of cells with Ni-YSZ and Ni-GDC and 20NiCe@Ni-YSZ cathode electrodes as a function of the relative amount of NiO and the average NiO film thickness (derived by the analysis of the corresponding NAP-XPS Ni 2p spectra recorded using 1320 eV photon energy). Measurements were performed at 640 °C and at constant current of -100 mA/cm^2 while different concentrations of O_2 were introduced in the H_2O/H_2 feed. Impedance spectra presented in Nyquist form, obtained under constant applied current of -100 mA cm^{-2} at 640 °C in H_2O/H_2*(3/1)* and $H_2O/H_2/O_2$*(3/1/1)* at total pressure of 0.5

mbar from two electrochemical cells with a) Ni-YSZ, b) 20NiCe@Ni-YSZ and c) Ni-GDC working electrodes.

The evolution of the Ni 2p and Ce 3d spectra recorded in situ under constant current and in various O_2 concentrations in the feed are shown in figure 5.14a. The evolution of ceria and nickel oxidation states obtained after the deconvolution of the photoelectron peaks is shown in figure 5.14b. It is obvious that the oxidation of nickel is followed by a parallel oxidation of ceria parts of the NiCe NPs. This shows that ceria sites of NPs are facile to oxidize by O_2, which can partly explain the higher rate of deactivation on this electrode as compared to NiGDC.

This experiment shows that even if nickel oxidation partly deactivates the cell, a very small quantity of Ni-doped ceria nanoparticles on the NiYSZ surface could increase the resistance of the electrode in O_2 environments, being beneficial for the electrochemical performance. As the reaction sites is not only taking place at the oxide/metal/gas 3PB but also at the ceria/gas 2PB, the surface of the modified electrodes contains ceria that can be reduced easily to Ce^{3+} enhancing in this way the electrocatalytic activity. At the same time at these mild oxidation conditions the bulk of the electrode remains reduced allowing a reasonable cell operation performance.

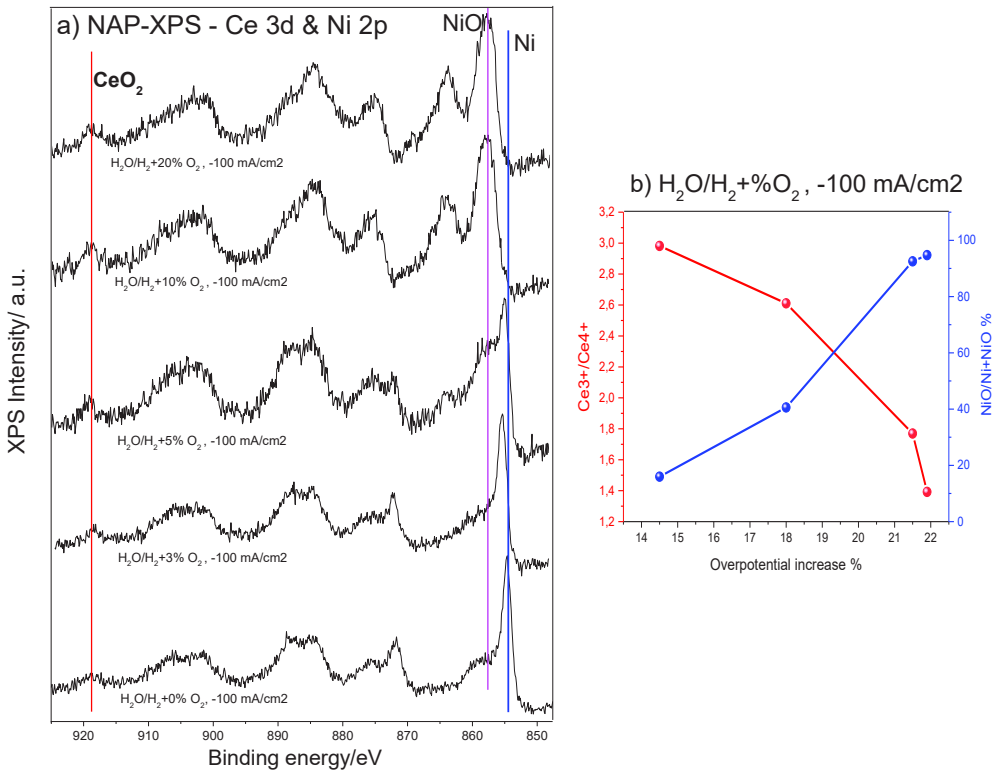

Figure 5.14. The NAP-XPS Ce 3d Ni 2p spectra measured on the 20NiCe@Ni-YSZ cathode electrode in 0.5 mbar H_2O/H_2 at 640 °C under -100 mA/cm^2 and co-feed of O_2 (*from bottom to the top*). b) The evolution of Ce^{3+}/Ce^{4+} components ratio as derived by the analysis of the corresponding NAP-XPS Ce 3d spectra.

5.6. Conclusions of Chapter 5

This work presents a simple and efficient method to increase the electrochemical performance of standard Ni-YSZ cermet electrodes for solid oxide electrolysis cells, by impregnation with Ni-doped ceria nanoparticles. The proposed method allows introducing a high population of easily reducible and highly interfaced Ni-ceria sites on the surface of Ni-YSZ with negligible fingerprint to the overall cell morphology, mechanical properties or electrode porosity. Electrochemical characterization under low temperature water electrolysis conditions showed that the modified Ni-YSZ electrodes are significantly improved and in particular the polarization losses are much lower as compared to the original (parent) unmodified cell. In addition after modification the Ni-YSZ electrodes maintain their activity even at highly oxidative electrolysis conditions, without the need of introducing a reducing agent (e.g. H_2). Surface characterization

suggested that the enhancement of the performance is related to a significant population of Ce^{3+} and Ni^{3+} surface sites maintained on the Ni-YSZ surface during electrolysis.

General conclusions and perspectives

The objective of this thesis is to study the Ni-based cermet electrodes performance during operation under intermediate temperature steam electrolysis, focusing on the comprehension of the particular effect of the electrode surface state. Based on the detailed physicochemical understanding gained in the first part of the work, a rational strategy for improvement of the cell performance and durability is envisaged and tested at the end of this thesis.

A leading cause of degradation in Ni-based cermet electrodes is nickel oxidation, which could be a result of air leakage in the fuel circulation system or long operation under high steam concentration conditions. Based on well-known phenomena, such as the low electrical conductance of nickel oxide and the mechanical problems caused by its volume expansion during oxidation, the detrimental effect of extended/bulk oxidation in the cell performance is well understood. However, this thesis focuses on the effect of the limited surface oxidation of the nickel areas, which are much less studied and less recognized as a cause of deactivation.

In-situ and Ex-situ experiments on Ni-GDC and Ni-YSZ electrodes were performed under different water vapour pressures, reduction and oxidation environments and different polarization at ISISS beamline in HZB/BESSY II and ICPEES laboratory setup.

In chapter 3, we showed that the surface chemical state of the Ni-based cermets cathode electrodes is a crucial element on their electrochemical performance during steam electrolysis. Specifically, the effect of nickel surface oxidation on the nm-scale of both Ni-GDC and Ni-YSZ electrodes is revealed. Comparative electrochemical measurements and in-situ NAP-XPS results show that a few nm thick NiO layer on Ni-YSZ electrode was responsible of the significant overpotential increase during the electrolysis reaction, but in case of Ni-GDC its effect was minor. The YSZ ceramic part of Ni-YSZ cermet was chemically stable under all conditions of this study, whereas for Ni-GDC cermet the GDC was modified both by the pre-treatment and by the electrochemical operation itself. The improvement of the performance of the Ni-GDC cathode electrode was found to be due to the slight increase of the Ce^{3+}/Ce^{4+} ratio. When Ni is oxidized the electrochemical reaction sites are blocked in case of Ni-YSZ, but for Ni-GDC the

(Ce^{3+}) electrochemical reaction sites balance the negative effect of the Ni oxidation and promote the activity of the electrode.

These findings allowed us to propose the idea of doping the Ni-YSZ electrode surface with NiCe NPs taking into account that the doped ceria nanoparticles should be able to reduce easily to Ce^{3+} so as to enhance the electrocatalytic activity. Also, the doping process should not influence the composition of the bulk in order to maintain the mechanical stability of the electrode.

In chapter 4, the fabrication and characterization of Nickel-doped ceria nanoparticles and conventional ceria-supported Ni particles (10% Ni-CeO_2) are discussed. The synthesis of $Ni_{0.1}Ce_{0.9}O_{2-x}$ nanoparticles is close to that described by J.S. Elias and al.[209] but took place in 2 steps instead of 4. On the other side, the 10% Ni-CeO_2 reference material was prepared by the co-precipitation method using metal nitrates. For $Ni_{0.1}Ce_{0.9}O_{2-x}$ nanoparticles the XRD shows the absence of Ni diffraction peaks which indicates the successful introduction of the entire amount of Ni ions in the ceria lattice and the absence of segregated nickel. Raman spectra show a band at 620 cm^{-1} which is induced by the presence of Ce^{3+} or Ni^{3+} ions. XPS confirms that nickel is mainly in the Ni^{3+} state and Ni:Ce atomic stoichiometry is found 12:88 ± 2%, close to the expected stoichiometry of $Ni_{0.1}Ce_{0.9}O_{2-x}$ particles (10:90). All these findings give clear evidence for incorporation of the nickel ions in the ceria lattice in the form of Ni^{3+} species, which is considered as the hole trapped state of Ni^{2+}.

The redox stability of NiCe NPs and 10% Ni-CeO_2 reference material are investigated by in situ temperature controlled XRD and XPS. The XRD results show that the NiCe NPs are stable during the redox treatment but the Ni/CeO_2 is not. Under identical H_2 treatment conditions the amount of $Ce3^{+}$species calculated from the deconvolution of the Ce3d spectra for NiCe NPs is up to 7 times higher as compared to Ni/CeO_2. These findings show that the reducibility of ceria is enhanced when Ni is doped into the lattice, at least as compared to Ni deposited directly onto ceria supports.

In chapter 5, the effect of $Ni_{0.1}Ce_{0.9}O_{2-x}$ NPs doping into the Ni-YSZ electrode electrochemical performance under different water vapour pressures and different environments was studied. The polarization curves of the Ni-YSZ electrode before and after the addition of NiCe NPs are evidences for the improvements of the cell, as the overpotential consumption decreases after

impregnation. The loaded 570 μL/cm^2 NiCe NPs@Ni-YSZ electrode showed significant decrease of the overpotential under 0.5 and 23 mbar H_2O. The XPS results measured after steam electrolysis revealed the coexistence of both Ce^{3+} and Ce^{4+} states. These findings indicated that the population of Ce^{3+}partially hinders the degradation of Ni- cermets.

The effect of the nanoparticles loading on the NiYSZ electrode was examined in order to optimize the proposed process. Different loadings were prepared by impregnation of 100, 200, 300,400 and 500 μL/cm^2 of the $Ni_{0.1}Ce_{0.9}O_{2-x}$ NPs on the same Ni-YSZ electrode. All cells were measured under 0.5 mbar H_2O and 630 °C. Comparison of the results obtained by ex-situ XPS with the i-V curves of the conventional Ni-GDC, Ni-YSZ and impregnated Ni-YSZ electrodes revealed that the best electrochemical performance for the 500NiCe@Ni-YSZ is due to the higher $Ce^{3+/}Ce^{4+}$ ratio as compared to GDC-containing cermets. Additionally, in-situ NAP-XPS measurements were performed under the same percentage of Ni oxidation for Ni-GDC, Ni-YSZ and 20NiCe@Ni-YSZ, showing the % increase of the overpotential as a function of the nickel oxidation state. Even if we are aware that the tested loading is relatively low, it shows better performance, especially at high O_2 concentrations, as compared to the conventional Ni-YSZ electrode.

In this work, in-situ NAP-XPS on the Ni-based cermets cathode electrodes was performed under intermediate temperature and low water vapour pressure. One can propose that in the future these electrodes should be tested under real operation conditions in order to explore the commercial interest of the proposed method. Application of NiCe NPs could be extended to different kind of SOEC electrode materials. For example, perovskite based cathode electrodes are very promising but their activity is still limited as compared to cermet electrodes. Therefore impregnation of these electrodes with the NiCe NPs synthesized in this work might be a simple way to increase their electrocatalytic activity. Finally, as we showed here, Ni oxidation is a strong reason for the cell deactivation, especially when hydrogen is not co-fed with the steam fuel. Since removing H2 from the cell feed will considerably simplify the engineering of electrolysis stacks, in the future nickel should be replaced from the cermet electrodes with alternative materials that might be more resistant to oxidative environments, with a reasonable amount of electrochemical active sites.

References:

[1] V. Papaefthimiou *et al.*, "Operando observation of nickel/ceria electrode surfaces during intermediate temperature steam electrolysis," *J. Catal.*, vol. 352, pp. 305–313, 2017.

[2] L. Gradisher, B. Dutcher, and M. Fan, "Catalytic hydrogen production from fossil fuels via the water gas shift reaction," *Appl. Energy*, vol. 139, pp. 335–349, 2015.

[3] C. C. Cormos, "Hydrogen production from fossil fuels with carbon capture and storage based on chemical looping systems," *Int. J. Hydrogen Energy*, vol. 36, no. 10, pp. 5960–5971, 2011.

[4] T. Kåberger, "Progress of renewable electricity replacing fossil fuels," *Glob. Energy Interconnect.*, vol. 1, no. 1, pp. 48–52, 2018.

[5] I. Dincer and C. Acar, "Review and evaluation of hydrogen production methods for better sustainability," *Int. J. Hydrogen Energy*, vol. 40, no. 34, 2014.

[6] J. P. Stempien, Q. Sun, and S. H. Chan, "Solid Oxide Electrolyzer Cell Modeling: A Review," *Open Access J. J. Power Technol.*, vol. 93, no. 4, pp. 216–246, 2013.

[7] C. Zhang *et al.*, "Measuring fundamental properties in operating solid oxide electrochemical cells by using in situ X-ray photoelectron spectroscopy," *Nat. Mater.*, vol. 9, no. 11, pp. 944–949, 2010.

[8] T. Ishihara, N. Jirathiwathanakul, and H. Zhong, "Intermediate temperature solid oxide electrolysis cell using LaGaO 3 based perovskite electrolyte," *Energy Environ. Sci.*, vol. 3, no. 5, pp. 665–672, 2010.

[9] E. C. Shin *et al.*, "Polarization mechanism of high temperature electrolysis in a Ni-YSZ/YSZ/LSM solid oxide cell by parametric impedance analysis," *Solid State Ionics*, vol. 232, pp. 80–96, 2013.

[10] D. Todd, M. Schwager, and W. Mérida, "Thermodynamics of high-temperature, high-pressure water electrolysis," *J. Power Sources*, vol. 269, pp. 424–429, 2014.

[11] S. D. Ebbesen, S. H. Jensen, A. Hauch, and M. B. Mogensen, "High temperature electrolysis in alkaline cells, solid proton conducting cells, and solid oxide cells," *Chemical Reviews*, vol. 114, no. 21. pp. 10697–10734, 2014.

[12] L. Bi, S. Boulfrad, and E. Traversa, "Steam electrolysis by solid oxide electrolysis cells (SOECs) with proton-conducting oxides," *Chem. Soc. Rev.*, vol. 43, no. 24, pp. 8255–8270, 2014.

[13] G. Schiller, A. Ansar, M. Lang, and O. Patz, "High temperature water electrolysis using metal supported solid oxide electrolyser cells (SOEC)," *J. Appl. Electrochem.*, vol. 39, no. 2, pp. 293–301, 2009.

[14] A. Brisse, J. Schefold, and M. Zahid, "High temperature water electrolysis in solid oxide cells," *Int. J. Hydrogen Energy*, vol. 33, no. 20, pp. 5375–5382, 2008.

[15] J. Schefold, A. Brisse, and M. Zahid, “Electronic Conduction of Yttria-Stabilized Zirconia Electrolyte in Solid Oxide Cells Operated in High Temperature Water Electrolysis,” *J. Electrochem. Soc.*, vol. 156, no. 8, p. B897, 2009.

[16] M. Hävecker *et al.*, “Enhancing Electrochemical Water-Splitting Kinetics by Polarization-Driven Formation of Near-Surface Iron(0): An In Situ XPS Study on Perovskite-Type Electrodes,” *Angew. Chemie Int. Ed.*, vol. 54, no. 9, pp. 2628–2632, 2014.

[17] M. A. Laguna-Bercero, “Recent advances in high temperature electrolysis using solid oxide fuel cells: A review,” *J. Power Sources*, vol. 203, pp. 4–16, 2012.

[18] A. Nechache, M. Cassir, and A. Ringuedé, “Solid oxide electrolysis cell analysis by means of electrochemical impedance spectroscopy: A review,” *Journal of Power Sources*. 2014.

[19] X. K. Gu and E. Nikolla, “Fundamental Insights into High-Temperature Water Electrolysis Using Ni-Based Electrocatalysts,” *J. Phys. Chem. C*, vol. 119, no. 48, 2015.

[20] Y. Zheng *et al.*, “A review of high temperature co-electrolysis of H $_2$ O and CO $_2$ to produce sustainable fuels using solid oxide electrolysis cells (SOECs): advanced materials and technology,” *Chem. Soc. Rev.*, vol. 46, no. 5, pp. 1427–1463, 2017.

[21] S. Y. Gómez and D. Hotza, “Current developments in reversible solid oxide fuel cells,” *Renew. Sustain. Energy Rev.*, vol. 61, pp. 155–174, 2016.

[22] J. S. Elias, M. Risch, L. Giordano, A. N. Mansour, and Y. Shao-Horn, “Structure, bonding, and catalytic activity of monodisperse, transition-metal-substituted CeO<inf>2</inf> nanoparticles,” *J. Am. Chem. Soc.*, vol. 136, no. 49, 2014.

[23] W. Derafa *et al.*, “Synthesis and characterization of nickel-doped ceria nanoparticles with improved surface reducibility,” *RSC Adv.*, vol. 8, no. 71, pp. 40712–40719, 2018.

[24] V. V. Kaichev *et al.*, “Reversible Bulk Oxidation of Ni Foil during Oscillatory Catalytic Oxidation of Propane: A Novel Type of Spatiotemporal Self-Organization,” *Phys. Rev. Lett.*, vol. 119, no. 2, pp. 1–5, 2017.

[25] B. P. Payne, M. C. Biesinger, and N. S. McIntyre, “The study of polycrystalline nickel metal oxidation by water vapour,” *J. Electron Spectros. Relat. Phenomena*, vol. 175, no. 1–3, pp. 55–65, 2009.

[26] M. C. Biesinger, L. W. M. Lau, A. R. Gerson, and R. S. C. Smart, “The role of the Auger parameter in XPS studies of nickel metal, halides and oxides,” *Phys. Chem. Chem. Phys.*, vol. 14, no. 7, pp. 2434–2442, 2012.

[27] A. Gerson, M. C. Biesinger, R. S. C. Smart, B. P. Payne, and L. W. M. Lau, “X-ray photoelectron spectroscopic chemical state quantification of mixed nickel metal, oxide and hydroxide systems,” *Surf. Interface Anal.*, vol. 41, no. 4, pp. 324–332, 2009.

[28] BP Energy, “2018 BP Energy Outlook 2018 BP Energy Outlook,” *2018 BP Energy Outlook*, p. 125, 2018.

[29] M. Carmo and D. L. Fritz, “A comprehensive review on PEM water electrolysis,” vol. 8, no. 1, 2013.

[30] J. Wang and Y. Yin, “Fermentative hydrogen production using various biomass-based materials as feedstock,” *Renew. Sustain. Energy Rev.*, vol. 92, no. March, pp. 284–306, 2018.

[31] R. Łukajtis *et al.*, “Hydrogen production from biomass using dark fermentation,” *Renew. Sustain. Energy Rev.*, vol. 91, no. March, pp. 665–694, 2018.

[32] S. E. Hosseini and M. A. Wahid, “Hydrogen production from renewable and sustainable energy resources: Promising green energy carrier for clean development,” *Renew. Sustain. Energy Rev.*, vol. 57, pp. 850–866, 2016.

[33] H. K. Ju, S. Badwal, and S. Giddey, “A comprehensive review of carbon and hydrocarbon assisted water electrolysis for hydrogen production,” *Appl. Energy*, vol. 231, no. May, pp. 502–533, 2018.

[34] P. Millet, *Fundamentals of Water Electrolysis*. 2015.

[35] E. Lay-Grindler *et al.*, “Degradation study by 3D reconstruction of a nickel-yttria stabilized zirconia cathode after high temperature steam electrolysis operation,” *J. Power Sources*, vol. 269, 2014.

[36] W. Donitz and E. Erdle, “High-temperature electrolysis of water vapor--status of development a n d perspectives for application,” vol. 10, no. 5, pp. 291–295, 1985.

[37] A. Hauch, S. D. Ebbesen, S. H. Jensen, and M. Mogensen, “Solid Oxide Electrolysis Cells: Microstructure and Degradation of the Ni/Yttria-Stabilized Zirconia Electrode,” *J. Electrochem. Soc.*, vol. 155, no. 11, p. B1184, 2008.

[38] S. P. Jiang, “Nanoscale and nano-structured electrodes of solid oxide fuel cells by infiltration: Advances and challenges,” *Int. J. Hydrogen Energy*, vol. 37, no. 1, pp. 449–470, 2012.

[39] S. P. Jiang, “Nanoscale and nano-structured electrodes of solid oxide fuel cells by infiltration: Advances and challenges,” *Int. J. Hydrogen Energy*, vol. 37, no. 1, pp. 449–470, 2012.

[40] J. M. Vohs and R. J. Gorte, “High-performance SOFC cathodes prepared by infiltration,” *Adv. Mater.*, vol. 21, no. 9, pp. 943–956, 2009.

[41] R. C. Maher, P. R. Shearing, E. Brightman, D. J. L. Brett, N. P. Brandon, and L. F. Cohen, “Reduction dynamics of doped ceria, nickel oxide, and cermet composites probed using in Situ Raman spectroscopy,” *Adv. Sci.*, vol. 3, no. 1, pp. 1–8, 2015.

[42] F. Zaera, “New advances in the use of infrared absorption spectroscopy for the characterization of heterogeneous catalytic reactions,” *Chem. Soc. Rev.*, vol. 43, no. 22, pp. 7624–7663, 2014.

[43] D. J. Cumming *et al.*, “Development of a diffuse reflectance infrared fourier transform spectroscopy (DRIFTS) cell for the in situ analysis of co-electrolysis in a solid oxide cell,” *Faraday Discuss.*, vol. 182, pp. 97–111, 2015.

[44] V. Pfeifer, “PhD Thesis: Identification of reactive oxygen species in iridium-based OER catalysts by in situ photoemission and absorption spectroscopy,” p. 162, 2017.

[45] S. Kumar, S. Gautam, T. K. Song, K. H. Chae, K. W. Jang, and S. S. Kim, “Electronic structure study of Co doped CeO2nanoparticles using X-ray absorption fine structure spectroscopy,” *J. Alloys Compd.*, vol. 611, pp. 329–334, 2014.

[46] A. Nenning *et al.*, “Ambient pressure XPS study of mixed conducting perovskite-type SOFC cathode and anode materials under well-defined electrochemical polarization,” *J. Phys. Chem. C*, vol. 120, no. 3, pp. 1461–1471, 2016.

[47] A. K. Opitz *et al.*, “Enhancing electrochemical water-splitting kinetics by polarization-driven formation of near-surface iron(0): An in situ XPS study on perovskite-type electrodes,” *Angew. Chemie - Int. Ed.*, vol. 54, no. 9, pp. 2628–2632, 2015.

[48] F. El Gabaly, K. F. McCarty, H. Bluhm, and A. H. McDaniel, “Oxidation stages of Ni electrodes in solid oxide fuel cell environments,” *Phys. Chem. Chem. Phys.*, vol. 15, no. 21, p. 8334, 2013.

[49] C. Zhang *et al.*, “Mechanistic Studies of Water Electrolysis and Hydrogen Electro-Oxidation on High Temperature Ceria-Based Solid Oxide Electrochemical Cells,” *J. Am. Ceram. Soc.*, vol. 135, p. 11572, 2013.

[50] V. Papaefthimiou, D. K. Niakolas, F. Paloukis, T. Dintzer, and S. Zafeiratos, “Is Steam an Oxidant or a Reductant for Nickel/Doped-Ceria Cermets?,” *ChemPhysChem*, vol. 18, no. 1, 2017.

[51] M. Grossi, B. Riccò, M. Grossi, B. Riccò, M. Grossi, and B. Riccò, “Electrical impedance spectroscopy (EIS) for biological analysis and food characterization : a review To cite this version : HAL Id : hal-01579247 Electrical impedance spectroscopy (EIS) for biological analysis and food characterization : a review,” pp. 303–325, 2017.

[52] H. Bluhm, M. Hävecker, A. Knop-gericke, M. Kiskinova, R. Schlögl, and M. Salmeron, “I n Situ X-Ray Photoelectron Studies of Gas – Solid Interfaces at Near- Ambient Conditions,” vol. 32, no. December, pp. 1022–1030, 2007.

[53] J. Chi and H. Yu, “Water electrolysis based on renewable energy for hydrogen production,” *Cuihua Xuebao/Chinese J. Catal.*, vol. 39, no. 3, pp. 390–394, 2018.

[54] Graboski M.S. and McCormick R.L., “Combustion of fat and vegetable oil derived fuels in diesel engines,” *Prog. Energy Combust. Sci.*, vol. 24, no. 2, pp. 125–164, 1998.

[55] J. E. Zajic, N. Kosaric, and J. D. Brosseau, “Microbial production of hydrogen,” *Adv. Biochem. Eng. Vol. 9*, pp. 57–109, 2006.

[56] A. Nechache, M. Cassir, and A. Ringuedé, “Solid oxide electrolysis cell analysis by

means of electrochemical impedance spectroscopy: A review," *Journal of Power Sources*, vol. 258. 2014.

[57] M. Martı and R. Guerrero, "Updated hydrogen production costs and parities for conventional and renewable technologies," vol. 35, pp. 3929–3936, 2010.

[58] J. Durville, J. Gazeau, J. N. Ing, J. Cueugniet, L. Ing, and M. Septembre, "Filière hydrogène-énergie," 2015.

[59] N. Salhi, A. Boulahouache, C. Petit, A. Kiennemann, and C. Rabia, "Steam reforming of methane to syngas over NiAl2O4 spinel catalysts," *Int. J. Hydrogen Energy*, vol. 36, no. 17, pp. 11433–11439, 2011.

[60] D. C. Elliott and L. J. Sealock, "Aqueous Catalyst Systems for the Water-Gas Shift Reaction. 1. Comparative Catalyst Studies," *Ind. Eng. Chem. Prod. Res. Dev.*, vol. 22, no. 3, pp. 426–431, 1983.

[61] Gardiner, "Reactivity of coal gasification with steam and CO2," vol. 77, no. 15, pp. 1831–1839, 2000.

[62] U. K. Ts, "Microstructural studies of the copper promoted iron oxide/chromia water-gas shift catalyst," pp. 12–14, 2002.

[63] C. Ratnasamy, J. P. Wagner, C. Ratnasamy, and J. P. Wagner, "Water Gas Shift Catalysis Water Gas Shift Catalysis," vol. 4940, 2009.

[64] T. Tabakova, "Effect of additives on the WGS activity of combustion synthesized CuO / CeO 2 catalysts," vol. 8, pp. 101–106, 2007.

[65] K. Show, Y. Yan, M. Ling, G. Ye, T. Li, and D. Lee, "Bioresource Technology Hydrogen production from algal biomass – Advances , challenges and prospects," *Bioresour. Technol.*, vol. 257, no. February, pp. 290–300, 2018.

[66] K. Urbaniec and R. R. Bakker, "Biomass residues as raw material for dark hydrogen fermentation - A review," *Int. J. Hydrogen Energy*, vol. 40, no. 9, pp. 3648–3658, 2015.

[67] S. K. S. Patel, J. K. Lee, and V. C. Kalia, "Dark-Fermentative Biological Hydrogen Production from Mixed Biowastes Using Defined Mixed Cultures," *Indian J. Microbiol.*, vol. 57, no. 2, pp. 171–176, 2017.

[68] F. Monlau, A. Barakat, E. Trably, C. Dumas, J. P. Steyer, and H. Carrère, "Lignocellulosic materials into biohydrogen and biomethane: Impact of structural features and pretreatment," *Crit. Rev. Environ. Sci. Technol.*, vol. 43, no. 3, pp. 260–322, 2013.

[69] M. J. Taherzadeh and K. Karimi, *Pretreatment of lignocellulosic wastes to improve ethanol and biogas production: A review*, vol. 9, no. 9. 2008.

[70] S. Haghighi Mood *et al.*, "Lignocellulosic biomass to bioethanol, a comprehensive review with a focus on pretreatment," *Renew. Sustain. Energy Rev.*, vol. 27, pp. 77–93, 2013.

[71] D. Scamman and M. Newborough, "Using surplus nuclear power for hydrogen mobility

and power-to-gas in France," *Int. J. Hydrogen Energy*, vol. 41, no. 24, pp. 10080–10089, 2016.

[72] P. H. Floch, S. Gabriel, C. Mansilla, and F. Werkoff, "On the production of hydrogen via alkaline electrolysis during off-peak periods," *Int. J. Hydrogen Energy*, vol. 32, no. 18, pp. 4641–4647, 2007.

[73] S. Bennoua, A. Le Duigou, M. M. Quéméré, and S. Dautremont, "Role of hydrogen in resolving electricity grid issues," *Int. J. Hydrogen Energy*, vol. 40, no. 23, pp. 7231–7245, 2015.

[74] C. Cany, C. Mansilla, P. da Costa, and G. Mathonnière, "Adapting the French nuclear fleet to integrate variable renewable energies via the production of hydrogen: Towards massive production of low carbon hydrogen?," *Int. J. Hydrogen Energy*, vol. 42, no. 19, pp. 13339–13356, 2017.

[75] T. S. Generation and W. Photoelectrolysis, *Light , Water , Hydrogen*. .

[76] I. Dincer and C. Acar, "Review and evaluation of hydrogen production methods for better sustainability," *Int. J. Hydrogen Energy*, vol. 40, no. 34, pp. 11094–11111, 2014.

[77] X. K. Gu and E. Nikolla, "Fundamental Insights into High-Temperature Water Electrolysis Using Ni-Based Electrocatalysts," *J. Phys. Chem. C*, vol. 119, no. 48, pp. 26980–26988, 2015.

[78] P. Millet and S. Grigoriev, "Water Electrolysis Technologies," *Renew. Hydrog. Technol. Prod. Purification, Storage, Appl. Saf.*, pp. 19–41, 2013.

[79] P. Moc and A. Brisse, "A review and comprehensive analysis of degradation mechanisms of solid oxide electrolysis cells," vol. 8, 2013.

[80] C. Graves, S. D. Ebbesen, M. Mogensen, and K. S. Lackner, "Sustainable hydrocarbon fuels by recycling CO 2 and H 2 O with renewable or nuclear energy," vol. 15, pp. 1–23, 2011.

[81] J. Pawel, O. Lian, Q. Sun, and S. Hwa, "Energy and exergy analysis of Solid Oxide Electrolyser Cell (SOEC) working as a CO 2 mitigation device," vol. 7, pp. 0–9, 2012.

[82] F. S. da Silva and T. M. de Souza, "Novel materials for solid oxide fuel cell technologies: A literature review," *Int. J. Hydrogen Energy*, vol. 42, no. 41, pp. 26020–26036, 2017.

[83] M. Chen, J. V. T. Høgh, J. U. Nielsen, J. J. Bentzen, S. D. Ebbesen, and P. V. Hendriksen, "High temperature co-electrolysis of steam and CO2 in an SOC stack: Performance and durability," *Fuel Cells*, vol. 13, no. 4, pp. 638–645, 2013.

[84] A. Hauch, K. Brodersen, M. Chen, and M. B. Mogensen, "Ni/YSZ electrodes structures optimized for increased electrolysis performance and durability," *Solid State Ionics*, 2016.

[85] J. Mougin *et al.*, "Enhanced performance and durability of a high temperature steam electrolysis stack," *Fuel Cells*, vol. 13, no. 4, pp. 623–630, 2013.

[86] E. Lay-Grindler *et al.*, “Degradation study by 3D reconstruction of a nickel-yttria stabilized zirconia cathode after high temperature steam electrolysis operation,” *J. Power Sources*, vol. 269, pp. 927–936, 2014.

[87] M. Riegraf, A. Zekri, M. Knipper, R. Costa, G. Schiller, and K. A. Friedrich, “Sulfur poisoning of Ni/Gadolinium-doped ceria anodes: A long-term study outlining stable solid oxide fuel cell operation,” *J. Power Sources*, vol. 380, no. January, pp. 26–36, 2018.

[88] A. Hauch, S. D. Ebbesen, S. H. Jensen, and M. Mogensen, “Solid Oxide Electrolysis Cells: Microstructure and Degradation of the Ni/Yttria-Stabilized Zirconia Electrode,” *J. Electrochem. Soc.*, vol. 155, no. 11, p. B1184, 2008.

[89] M. Kusnezoff, N. Trofimenko, M. Müller, and A. Michaelis, “Influence of electrode design and contacting layers on performance of electrolyte supported SOFC/SOEC single cells,” *Materials (Basel).*, vol. 9, no. 11, 2016.

[90] M. S. Sohal, J. E. O’Brien, C. M. Stoots, V. I. Sharma, B. Yildiz, and A. Virkar, “Degradation Issues in Solid Oxide Cells During High Temperature Electrolysis,” *J. Fuel Cell Sci. Technol.*, vol. 9, no. 1, p. 011017, 2011.

[91] E. Lay-Grindler *et al.*, “Degradation study by 3D reconstruction of a nickel-yttria stabilized zirconia cathode after high temperature steam electrolysis operation,” *J. Power Sources*, vol. 269, pp. 927–936, 2014.

[92] P. S. Forms, “Horizon 2020 Call : H2020-JTI-FCH-2014-1 Type of action : FCH2-RIA Proposal number : 671481 Proposal acronym : SElySOs,” 2020.

[93] S. J. Kim, K. J. Kim, and G. M. Choi, “A novel solid oxide electrolysis cell (SOEC) to separate anodic from cathodic polarization under high electrolysis current,” *Int. J. Hydrogen Energy*, vol. 40, no. 30, pp. 9032–9038, 2015.

[94] K. S. Blinn and M. Liu, “BaZr0.9Yb0.1O3-δ-modified bi-electrode supported solid oxide fuel cells with enhanced coking and sulfur tolerance,” *J. Power Sources*, vol. 243, pp. 24–28, 2013.

[95] S. Y. Gómez and D. Hotza, “Current developments in reversible solid oxide fuel cells,” *Renew. Sustain. Energy Rev.*, vol. 61, pp. 155–174, 2016.

[96] J. C. Ruiz-Morales, J. Canales-Vázquez, J. Peña-Martínez, D. M. López, and P. Núñez, “On the simultaneous use of La0.75Sr0.25Cr0.5Mn0.5O3-δ as both anode and cathode material with improved microstructure in solid oxide fuel cells,” *Electrochim. Acta*, vol. 52, no. 1, pp. 278–284, 2006.

[97] X. Yang and J. T. S. Irvine, “(La0.75Sr0.25)0.95Mn0.5Cr 0.5O3 as the cathode of solid oxide electrolysis cells for high temperature hydrogen production from steam,” *J. Mater. Chem.*, vol. 18, no. 20, pp. 2349–2354, 2008.

[98] E. Lay, G. Gauthier, and L. Dessemond, “Preliminary studies of the new Ce-doped La/Sr chromo-manganite series as potential SOFC anode or SOEC cathode materials,” *Solid State Ionics*, vol. 189, no. 1, pp. 91–99, 2011.

[99] Y. Gan *et al.*, "Composite cathode La0.4Sr0.4TiO3−δ–Ce0.8Sm0.2O2−δ impregnated with Ni for high-temperature steam electrolysis," *J. Power Sources*, vol. 245, pp. 245–255, 2013.

[100] G. Meng *et al.*, "Effect of phytic acid on the microstructure and corrosion resistance of Ni coating," *Electrochim. Acta*, vol. 55, no. 20, pp. 5990–5995, 2010.

[101] W. Qi *et al.*, "Reversibly in-situ anchoring copper nanocatalyst in perovskite titanate cathode for direct high-temperature steam electrolysis," *Int. J. Hydrogen Energy*, vol. 39, no. 11, pp. 5485–5496, 2014.

[102] S. Xu, S. Chen, M. Li, K. Xie, Y. Wang, and Y. Wu, "Composite cathode based on Fe-loaded LSCM for steam electrolysis in an oxide-ion-conducting solid oxide electrolyser," *J. Power Sources*, vol. 239, pp. 332–340, 2013.

[103] Y. Song *et al.*, "Pure CO2 electrolysis over an Ni/YSZ cathode in a solid oxide electrolysis cell," *J. Mater. Chem. A*, vol. 6, no. 28, pp. 13661–13667, 2018.

[104] Z. Liu, B. Liu, D. Ding, M. Liu, F. Chen, and C. Xia, "Review Fabrication and modification of solid oxide fuel cell anodes via wet impregnation/infiltration technique," *J. Power Sources*, vol. 237, pp. 243–259, 2013.

[105] L. Blum, L. G. J. B. De Haart, J. Malzbender, N. H. Menzler, J. Remmel, and R. Steinberger-wilckens, "Recent results in Jülich solid oxide fuel cell technology development," vol. 241, pp. 477–485, 2013.

[106] A. R. Hanifi, M. A. Laguna-Bercero, T. H. Etsell, and P. Sarkar, "The effect of electrode infiltration on the performance of tubular solid oxide fuel cells under electrolysis and fuel cell modes," *Int. J. Hydrogen Energy*, vol. 39, no. 15, pp. 8002–8008, 2014.

[107] T. B. Mitchell-Williams *et al.*, "Infiltration of commercially available, anode supported SOFC's via inkjet printing," *Mater. Renew. Sustain. Energy*, vol. 6, no. 2, pp. 1–9, 2017.

[108] Y. Choi, S. Choi, H. Y. Jeong, M. Liu, B. S. Kim, and G. Kim, "Highly efficient layer-by-layer-assisted infiltration for high-performance and cost-effective fabrication of nanoelectrodes," *ACS Appl. Mater. Interfaces*, vol. 6, no. 20, pp. 17352–17357, 2014.

[109] H. Fan, Y. Zhang, and M. Han, "Infiltration of La0·6Sr0·4FeO3-δ nanoparticles into YSZ scaffold for solid oxide fuel cell and solid oxide electrolysis cell," *J. Alloys Compd.*, vol. 723, pp. 620–626, 2017.

[110] D. J. Cumming, A. R. Thompson, and R. H. Rothman, "Nickel Impregnated Cerium-Doped Strontium Titanate Fuel Electrode: Direct Carbon Dioxide Electrolysis and Co-Electrolysis," *J. Electrochem. Soc.*, vol. 163, no. 11, pp. F3057–F3061, 2016.

[111] D. Ding, X. Li, S. Y. Lai, K. Gerdes, and M. Liu, "Enhancing SOFC cathode performance by surface modification through infiltration," *Energy Environ. Sci.*, vol. 7, no. 2, p. 552, 2014.

[112] A. M. Hussain, J. V. T. Hogh, W. Zhang, and N. Bonanos, "Efficient ceramic anodes

infiltrated with binary and ternary electrocatalysts for SOFCs operating at low temperatures," *J. Power Sources*, vol. 216, pp. 308–313, 2012.

[113] M. Lomberg, E. Ruiz-Trejo, G. Offer, and N. P. Brandon, "Characterization of Ni-Infiltrated GDC Electrodes for Solid Oxide Cell Applications," *J. Electrochem. Soc.*, vol. 161, no. 9, pp. F899–F905, 2014.

[114] X. Lou, Z. Liu, S. Wang, Y. Xiu, C. P. Wong, and M. Liu, "Controlling the morphology and uniformity of a catalyst-infiltrated cathode for solid oxide fuel cells by tuning wetting property," *J. Power Sources*, vol. 195, no. 2, pp. 419–424, 2010.

[115] S. Park, "Direct Oxidation of Hydrocarbons in a Solid Oxide Fuel Cell: I. Methane Oxidation," *J. Electrochem. Soc.*, vol. 146, no. 10, p. 3603, 2002.

[116] S. Park, R. J. Gorte, and J. M. Vohs, "Tape Cast Solid-Oxide Fuel Cells for the Direct Oxidation of Hydrocarbons," *J. Electrochem. Soc.*, vol. 148, no. 5, p. A443, 2002.

[117] T. Taniguchi *et al.*, "Identifying defects in ceria-based nanocrystals by UV resonance Raman spectroscopy," *J. Phys. Chem. C*, vol. 113, no. 46, pp. 19789–19793, 2009.

[118] N. Mironova-Ulmane, A. Kuzmin, I. Steins, J. Grabis, I. Sildos, and M. Pärs, "Raman scattering in nanosized nickel oxide NiO," *J. Phys. Conf. Ser.*, vol. 93, no. 1, 2007.

[119] Z. Cheng and M. Liu, "Characterization of sulfur poisoning of Ni-YSZ anodes for solid oxide fuel cells using in situ Raman microspectroscopy," *Solid State Ionics*, vol. 178, no. 13–14, pp. 925–935, 2007.

[120] M. Li, U. Tumuluri, Z. Wu, and S. Dai, "Effect of dopants on the adsorption of carbon dioxide on ceria surfaces," *ChemSusChem*, vol. 8, no. 21, pp. 3651–3660, 2015.

[121] B. Xu, Q. Zhang, S. Yuan, M. Zhang, and T. Ohno, "Synthesis and photocatalytic performance of yttrium-doped CeO2with a porous broom-like hierarchical structure," *Appl. Catal. B Environ.*, vol. 183, pp. 361–370, 2016.

[122] A. Younis, D. Chu, Y. V. Kaneti, and S. Li, "Tuning the surface oxygen concentration of {111} surrounded ceria nanocrystals for enhanced photocatalytic activities," *Nanoscale*, vol. 8, no. 1, pp. 378–387, 2016.

[123] L. De Los Santos Valladares *et al.*, "Characterization of Ni thin films following thermal oxidation in air," *J. Vac. Sci. Technol. B, Nanotechnol. Microelectron. Mater. Process. Meas. Phenom.*, vol. 32, no. 5, p. 051808, 2014.

[124] B. Paul, K. Kumar, A. Chowdhury, and A. Roy, "Appearance of Fröhlich-like phonon mode and defect dynamics in La3+-doped ceria," *J. Appl. Phys.*, vol. 122, no. 13, 2017.

[125] R. Murugan, G. Vijayaprasath, T. Mahalingam, and G. Ravi, "Room temperature ferromagnetism of Ni doped cerium oxide single crystalline thin Films deposited by using rf magnetron sputtering," *Mater. Lett.*, vol. 162, pp. 71–74, 2016.

[126] C. A. Chagas, E. F. de Souza, R. L. Manfro, S. M. Landi, M. M. V. M. Souza, and M.

Schmal, “Copper as promoter of the NiO-CeO2catalyst in the preferential CO oxidation,” *Appl. Catal. B Environ.*, vol. 182, pp. 257–265, 2016.

[127] C. Thiabdokmai, A. Tangtrakarn, S. Promsuy, P. Ngiewlay, and C. Mongkolkachit, “Templateless synthesis and characterization of hollow gadolinium doped cerium oxide nanofibers by electrospinning,” *Adv. Mater. Sci. Eng.*, vol. 2014, 2014.

[128] J. Y. Ye, Y. X. Jiang, T. Sheng, and S. G. Sun, “In-situ FTIR spectroscopic studies of electrocatalytic reactions and processes,” *Nano Energy*, vol. 29, no. June 2016, pp. 414–427, 2016.

[129] S. Gopalakrishnan *et al.*, “Unravelling the structure and reactivity of supported Ni particles in Ni-CeZrO2catalysts,” *Appl. Catal. B Environ.*, vol. 138–139, pp. 353–361, 2013.

[130] T. Murai *et al.*, “Application of FT-IR for in situ investigation of high temperature electrode reactions,” *Solid State Ionics*, vol. 176, no. 31–34, pp. 2399–2403, 2005.

[131] J. D. Kirtley, D. A. Steinhurst, J. C. Owrutsky, M. B. Pomfret, and R. A. Walker, “In situ optical studies of methane and simulated biogas oxidation on high temperature solid oxide fuel cell anodes,” *Phys. Chem. Chem. Phys.*, vol. 16, no. 1, pp. 227–236, 2014.

[132] M. K. Kenjiro Oura, Victor G. Lifshits, Alexandar A. Saranin, Andrey V. Zotos, *An introduction-Surface Science*. .

[133] J. Stöhr, “NEXAFS Spectroscopy,” vol. 25, no. 0, p. 6221, 1992.

[134] U. St. HAEHNER, G.; Chem. Soc. Rev. 35 (2006) 12, 1244-1255; Sch. Chem. and U. E. Andrews, St. Andrews, Fife KY16 9ST, “Near Edge X-Ray Absorption Fine Structure Spectroscopy as a Tool to Probe Electronic and Structural Properties of Thin Organic Films and Liquids,” vol. 35, no. 2006, p. 2007, 2007.

[135] A. E. Russell and A. Rose, “X-ray Absorption Spectroscopy of Low Temperature Fuel Cell Catalysts,” *Chem. Rev.*, vol. 104, no. 10, pp. 4613–4636, 2004.

[136] M. Hävecker *et al.*, “Methodology for the structural characterisation of VxOy species supported on silica under reaction conditions by means of in situ O K-edge X-ray absorption spectroscopy,” *Phys. Status Solidi Basic Res.*, vol. 246, no. 7, pp. 1459–1469, 2009.

[137] F. Paloukis *et al.*, “Insights into the Surface Reactivity of Cermet and Perovskite Electrodes in Oxidizing, Reducing, and Humid Environments,” *ACS Appl. Mater. Interfaces*, vol. 9, no. 30, 2017.

[138] Z. Liu *et al.*, “Ambient pressure XPS and IRRAS investigation of ethanol steam reforming on Ni–CeO $_2$ (111) catalysts: an in situ study of C–C and O–H bond scission,” *Phys. Chem. Chem. Phys.*, vol. 18, no. 25, pp. 16621–16628, 2016.

[139] X. Shang, B. Dong, Y. M. Chai, and C. G. Liu, “In-situ electrochemical activation designed hybrid electrocatalysts for water electrolysis,” *Sci. Bull.*, vol. 63, no. 13, pp.

853–876, 2018.

[140] K. A. Stoerzinger, W. T. Hong, E. J. Crumlin, H. Bluhm, and Y. Shao-Horn, “Insights into Electrochemical Reactions from Ambient Pressure Photoelectron Spectroscopy,” *Acc. Chem. Res.*, vol. 48, no. 11, pp. 2976–2983, 2015.

[141] W. H. Doh, V. Papaefthimiou, T. Dintzer, V. Dupuis, and S. Zafeiratos, “Synchrotron radiation X-ray photoelectron spectroscopy as a tool to resolve the dimensions of spherical core/shell nanoparticles,” *J. Phys. Chem. C*, vol. 118, no. 46, 2014.

[142] C. Zhang *et al.*, “Mechanistic studies of water electrolysis and hydrogen electro-oxidation on high temperature ceria-based solid oxide electrochemical cells,” *J. Am. Chem. Soc.*, vol. 135, no. 31, pp. 11572–11579, 2013.

[143] Z. A. Feng, F. El Gabaly, X. Ye, Z. X. Shen, and W. C. Chueh, “Fast vacancy-mediated oxygen ion incorporation across the ceria-gas electrochemical interface,” *Nat. Commun.*, vol. 5, 2014.

[144] W. C. Chueh *et al.*, “Highly Enhanced Concentration and Stability of Reactive Ce $^{3+}$ on Doped CeO $_2$ Surface Revealed In Operando,” *Chem. Mater.*, vol. 24, no. 10, pp. 1876–1882, 2012.

[145] C. B. Gopal, F. El Gabaly, A. H. Mcdaniel, and W. C. Chueh, “Origin and Tunability of Unusually Large Surface Capacitance in Doped Cerium Oxide Studied by Ambient-Pressure X-Ray Photoelectron Spectroscopy,” pp. 4692–4697, 2016.

[146] F. El Gabaly *et al.*, “Measuring individual overpotentials in an operating solid-oxide electrochemical cell,” pp. 12138–12145, 2010.

[147] C. Zhang *et al.*, “Multi-element Activity Mapping and Potential Mapping in Solid Oxide Electrochemical Cells through the use of operando XPS Multi-element Activity Mapping and Potential Mapping in Solid Oxide Electrochemical Cells through the use of operando XPS Chemical Sc,” 2012.

[148] V. Papaefthimiou *et al.*, “On the active surface state of nickel-ceria solid oxide fuel cell anodes during methane electrooxidation,” *Adv. Energy Mater.*, vol. 3, no. 6, pp. 762–769, 2013.

[149] D. K. Niakolas, J. P. Ouweltjes, G. Rietveld, V. Dracopoulos, and S. G. Neophytides, “Au-doped Ni/GDC as a new anode for SOFCs operating under rich CH 4 internal steam reforming,” *Int. J. Hydrogen Energy*, vol. 35, no. 15, pp. 7898–7904, 2010.

[150] P. Kim-Lohsoontorn, Y. M. Kim, N. Laosiripojana, and J. Bae, “Gadolinium doped ceria-impregnated nickel-yttria stabilised zirconia cathode for solid oxide electrolysis cell,” *Int. J. Hydrogen Energy*, vol. 36, no. 16, pp. 9420–9427, 2011.

[151] V. Saveleva, “Investigation of the anodes of PEM water electrolyzers by operando synchrotron-based photoemission spectroscopy,” 2018.

[152] P. Van der Heide, “Xps instrumentation 3.1,” *X-Ray Photoelectron Spectrosc. An Introd.*

to Princ. Pract., no. c, pp. 27–60, 2012.

[153] G. L. Andersen, "Lawrence Berkeley National Laboratory," *Lawrence Berkeley Natl. Lab.*, pp. 0–45, 2010.

[154] N. Winograd and S. W. Gaarenstroom, "X Ray Photoelectron Spectroscopy Handbook.Pdf," *Phys. Methods Mod. Chem. Anal.*, vol. 2, pp. 115–169, 1980.

[155] J. W. John F. Watts, *An Introduction to Surface Analysis by XPS and AES, Wiley,2003*. .

[156] A. Knop-Gericke *et al.*, "Chapter 4 X-Ray Photoelectron Spectroscopy for Investigation of Heterogeneous Catalytic Processes," *Adv. Catal.*, vol. 52, pp. 213–272, Jan. 2009.

[157] M. S. Schmidt, K. Vels Hansen, K. Norrman, and M. Mogensen, "Three-phase-boundary dynamics at the Ni/ScYSZ interface," *Solid State Ionics*, 2009.

[158] H. Manual, "VersaSTAT 3."

[159] S. Zafeiratos and S. Kennou, "The interaction of oxygen with ultrathin Ni deposits on yttria-stabilized ZrO2(1 0 0)," *Surf. Sci.*, vol. 482–485, no. PART 1, pp. 266–271, 2001.

[160] A. K. Opitz *et al.*, "Surface Chemistry of Perovskite-Type Electrodes during High Temperature CO2 Electrolysis Investigated by Operando Photoelectron Spectroscopy," *ACS Appl. Mater. Interfaces*, vol. 9, no. 41, pp. 35847–35860, 2017.

[161] H. F. Poulsen, "Neutron Powder Diffraction," vol. 25, no. 2, pp. 2254–2261, 1989.

[162] W. C. Chueh, Y. Hao, W. Jung, and S. M. Haile, "High electrochemical activity of the oxide phase in model ceria-Pt and ceria-Ni composite anodes," *Nat. Mater.*, vol. 11, no. 2, pp. 155–161, 2012.

[163] K. Chen and S. P. Jiang, "Review—Materials Degradation of Solid Oxide Electrolysis Cells," *J. Electrochem. Soc.*, vol. 163, no. 11, pp. F3070–F3083, Jun. 2016.

[164] M. S. Schmidt, K. Vels Hansen, K. Norrman, and M. Mogensen, "Three-phase-boundary dynamics at the Ni/ScYSZ interface," *Solid State Ionics*, vol. 180, no. 4–5, pp. 431–438, 2009.

[165] S. Futamura *et al.*, "Alternative Ni-Impregnated Mixed Ionic-Electronic Conducting Anode for SOFC Operation at High Fuel Utilization," *J. Electrochem. Soc.*, 2017.

[166] M. Pihlatie, T. Ramos, and A. Kaiser, "Testing and improving the redox stability of Ni-based solid oxide fuel cells," vol. 193, pp. 322–330, 2009.

[167] M. Shishkin and T. Ziegler, "the three-phase boundary of solid oxide fuel cell anodes by density functional theory : a critical overview," no. 2, 2014.

[168] J. Schefold, A. Brisse, and H. Poepke, "ScienceDirect 23 , 000 h steam electrolysis with an electrolyte supported solid oxide cell," pp. 1–12, 2017.

[169] F. Paloukis *et al.*, "Insights into the Surface Reactivity of Cermet and Perovskite

Electrodes in Oxidizing, Reducing, and Humid Environments," *ACS Appl. Mater. Interfaces*, vol. 9, no. 30, pp. 25265–25277, 2017.

[170] P. Kim-Lohsoontorn, Y. M. Kim, N. Laosiripojana, and J. Bae, "Gadolinium doped ceria-impregnated nickel-yttria stabilised zirconia cathode for solid oxide electrolysis cell," *Int. J. Hydrogen Energy*, vol. 36, no. 16, pp. 9420–9427, 2011.

[171] C. J. Powell and A. Jablonski, "Journal of Electron Spectroscopy and Progress in quantitative surface analysis by X-ray photoelectron spectroscopy : Current status and perspectives," *J. Electron Spectros. Relat. Phenomena*, vol. 178–179, pp. 331–346, 2010.

[172] K. V. Hansen, T. Jacobsen, and K. Thyden, "In situ surface reduction of a NiO-YSZ-alumina composite using scanning probe microscopy," no. 1, 2014.

[173] J. Laurencin, V. Roche, C. Jaboutian, I. Kieffer, J. Mougin, and M. C. Steil, "Ni-8YSZ cermet re-oxidation of anode supported solid oxide fuel cell : From kinetics measurements to mechanical damage prediction," *Int. J. Hydrogen Energy*, vol. 37, no. 17, pp. 12557–12573, 2012.

[174] B. P. Payne, M. C. Biesinger, and N. S. McIntyre, "The study of polycrystalline nickel metal oxidation by water vapour," *J. Electron Spectros. Relat. Phenomena*, vol. 175, no. 1–3, pp. 55–65, 2009.

[175] M. A. Peck and M. A. Langell, "Comparison of Nanoscaled and Bulk NiO Structural and Environmental Characteristics by XRD, XAFS, and XPS."

[176] B. P. Payne, A. P. Grosvenor, M. C. Biesinger, B. A. Kobe, and N. S. Mcintyre, "Structure and growth of oxides on polycrystalline nickel surfaces," no. April, pp. 582–592, 2007.

[177] A. Cornish, T. Eralp, A. Shavorskiy, R. A. Bennett, and G. Held, "Oxidation of polycrystalline Ni studied by spectromicroscopy : Phase separation in the early stages of crystallite growth (a) (b)," pp. 6–9, 2010.

[178] "Influence of argon ion bombardment on the oxidation of nickel surfaces," vol. 369, pp. 217–230, 1996.

[179] F. Paloukis *et al.*, "In situ X-ray photoelectron spectroscopy study of complex oxides under gas and vacuum environments," *Appl. Surf. Sci.*, vol. 423, pp. 1176–1181, 2017.

[180] S. Ladas, "Origin of Non-Faradaic Electrochemical Modification of Catalytic Activity," pp. 8845–8848, 1993.

[181] E. Ioannidou, C. Neofytidis, L. Sygellou, and D. K. Niakolas, "Au-doped Ni/GDC as an Improved Cathode Electrocatalyst for H 2 O Electrolysis in SOECs," *Appl. Catal. B Environ.*, vol. 236, pp. 253–264, Nov. 2018.

[182] G. Nurk, K. Kooser, S. Urpelainen, T. Käämbre, and U. Joost, "Near ambient pressure X-ray photoelectron - and impedance spectroscopy study of NiO - Ce 0 . 9 Gd 0 . 1 O 2- δ anode reduction using a novel dual-chamber spectroelectrochemical cell," *J. Power*

Sources, vol. 378, no. October 2017, pp. 589–596, 2018.

[183] A. K. Opitz *et al.*, "The Chemical Evolution of the - La 0 . 6 Sr 0 . 4 CoO 3 − δ Surface Under SOFC Operating Conditions and Its Implications for Electrochemical Oxygen Exchange Activity," *Top. Catal.*, vol. 0, no. 0, p. 0, 2018.

[184] J. Macdonald, *Impedance spectroscopy: emphasizing solid materials and systems Editors Wiley-Interscience Publication*. Wiley, 1987.

[185] C. Lenser and N. H. Menzler, "Impedance characterization of supported oxygen ion conducting electrolytes," *Solid State Ionics*, vol. 334, no. October 2018, pp. 70–81, 2019.

[186] M. Riegraf, V. Yurkiv, R. Costa, G. Schiller, and K. A. Friedrich, "Evaluation of the Effect of Sulfur on the Performance of Nickel/Gadolinium-Doped Ceria Based Solid Oxide Fuel Cell Anodes," *ChemSusChem*, vol. 10, no. 3, pp. 587–599, Feb. 2017.

[187] L. Zhang, S. Ping, H. Quan, X. Chen, J. Ma, and X. Chao, "A comparative study of H 2 S poisoning on electrode behavior of Ni / YSZ and Ni / GDC anodes of solid oxide fuel cells," *Int. J. Hydrogen Energy*, vol. 35, no. 22, pp. 12359–12368, 2010.

[188] S. P. Jiang and S. P. S. Badwalab, "Hydrogen Oxidation at the Nickel and Platinum Electrodes on Yttria-Tetragonal Zirconia Electrolyte," vol. 144, no. 11, pp. 3777–3784, 1997.

[189] D. A. Harrington, "The rate-determining step in electrochemical impedance spectroscopy," *J. Electroanal. Chem.*, vol. 737, pp. 30–36, 2015.

[190] L.-P. Sun, H. Zhao, Q. Li, L.-H. Huo, J.-P. Viricelle, and C. Pijolat, "Study of oxygen reduction mechanism on Ag modified Sm1.8Ce0.2CuO4 cathode for solid oxide fuel cell," *Int. J. Hydrogen Energy*, vol. 38, no. 32, pp. 14060–14066, Oct. 2013.

[191] S. Primdahl and M. Mogensen, "Gas Diffusion Impedance in Characterization of Solid Oxide Fuel Cell Anodes," vol. 146, no. 8, pp. 2827–2833, 1999.

[192] A. K. Opitz, M. Brandner, V. A. Rojek-w, and M. Bram, "A novel Ni / ceria-based anode for metal-supported solid oxide fuel cells," vol. 328, 2016.

[193] C. Graves, C. Chatzichristodoulou, and M. B. Mogensen, "Kinetics of CO/CO $_2$ and H $_2$ /H $_2$ O reactions at Ni-based and ceria-based solid-oxide-cell electrodes," *Faraday Discuss.*, vol. 182, pp. 75–95, 2015.

[194] T. Montini, M. Melchionna, M. Monai, and P. Fornasiero, "Fundamentals and Catalytic Applications of CeO2 -Based Materials," *Chem. Rev.*, vol. 116, no. 10, pp. 5987–6041, May 2016.

[195] M. Mogensen, N. M. Sammes, and G. A. Tompsett, "Physical , chemical and electrochemical properties of pure and doped ceria," vol. 129, pp. 63–94, 2000.

[196] I. I. Soykal, H. Sohn, D. Singh, T. Miller, and U. S. Ozkan, "Reduction Characteristics of Ceria under Ethanol Steam Reforming Conditions : E ff ect of the Particle Size," 2014.

[197] J. Vecchietti *et al.*, “Surface Reduction Mechanism of Cerium–Gallium Mixed Oxides with Enhanced Redox Properties,” *J. Phys. Chem. C*, vol. 117, no. 17, pp. 8822–8831, May 2013.

[198] A. K. Lucid, P. R. L. Keating, J. P. Allen, and G. W. Watson, “Structure and Reducibility of CeO2 Doped with Trivalent Cations,” *J. Phys. Chem. C*, vol. 120, no. 41, pp. 23430–23440, Oct. 2016.

[199] W. Zaj and J. Molenda, “Properties of doped ceria solid electrolytes in reducing atmospheres,” vol. 192, pp. 163–167, 2011.

[200] J. Wang, H. Chen, Z. Hu, M. Yao, and Y. Li, “A review on the Pd-based three-way catalyst,” *Catal. Rev. - Sci. Eng.*, vol. 57, no. 1, pp. 79–144, 2015.

[201] L. Xiangwen, Z. Kebin, W. Lei, W. Baoyi, and L. Yadong, “Oxygen vacancy clusters promoting reducibility and activity of ceria nanorods,” *J. Am. Chem. Soc.*, vol. 131, no. 9, pp. 3140–3141, 2009.

[202] Y. Ma *et al.*, “Regulating the surface of nanoceria and its applications in heterogeneous catalysis,” *Surf. Sci. Rep.*, vol. 73, no. 1, pp. 1–36, 2018.

[203] A. Trovarelli, J. Llorca, and A. Catalysis, “Ceria Catalysts at Nanoscale: How Do Crystal Shapes Shape Catalysis? Ceria Catalysts at Nanoscale: How Do Crystal Shapes Shape Catalysis? ACS Paragon Plus Environment,” *ACS Catal.*, vol. 7, pp. 4716–4735, 2017.

[204] X. Yang, A. Wang, B. Qiao, and J. U. N. Li, “Single-Atom Catalysts : A New Frontier,” vol. 46, no. 8, 2013.

[205] M. Flytzani-Stephanopoulos and B. C. Gates, “Atomically Dispersed Supported Metal Catalysts,” *Annu. Rev. Chem. Biomol. Eng.*, vol. 3, no. 1, pp. 545–574, 2012.

[206] S. Mahammadunnisa, P. Manoj Kumar Reddy, N. Lingaiah, and C. Subrahmanyam, “NiO/Ce $_{1-x}$ Ni $_{x}$ O $_{2-\delta}$ as an alternative to noble metal catalysts for CO oxidation,” *Catal. Sci. Technol.*, vol. 3, no. 3, pp. 730–736, 2013.

[207] W. L. Wang *et al.*, “Organic-free synthesis and ortho-reaction of monodisperse Ni incorporated CeO2 nanocatalysts,” *J. Mater. Chem. A*, vol. 6, no. 3, pp. 866–870, 2018.

[208] C. D. Curran, L. Lu, C. J. Kiely, and S. McIntosh, “Ambient temperature aqueous synthesis of ultrasmall copper doped ceria nanocrystals for the water gas shift and carbon monoxide oxidation reactions,” *J. Mater. Chem. A*, vol. 6, no. 1, pp. 244–255, 2017.

[209] J. S. Elias, M. Risch, L. Giordano, A. N. Mansour, and Y. Shao-Horn, “Structure, bonding, and catalytic activity of monodisperse, transition-metal-substituted CeO2 nanoparticles,” *J. Am. Chem. Soc.*, vol. 136, no. 49, 2014.

[210] R. Tellgren, “Neutron Powder Diffraction in Sweden.,” *Phys. B*, vol. 26 A, pp. 55–69, 1985.

[211] Z. Weng *et al.*, “Metal/Oxide Interface Nanostructures Generated by Surface Segregation

for Electrocatalysis," *Nano Lett.*, vol. 15, no. 11, pp. 7704–7710, 2015.

[212] G. Zhou *et al.*, "High activity of Ce1-xNixO2-y for H 2 production through ethanol steam reforming: Tuning catalytic performance through metal-oxide interactions," *Angew. Chemie - Int. Ed.*, vol. 49, no. 50, pp. 9680–9684, 2010.

[213] B. Y. R. D. Shannon, M. H, N. H. Baur, O. H. Gibbs, M. Eu, and V. Cu, "Revised Effective Ionic Radii and Systematic Studies of Interatomie Distances in Halides and Chaleogenides Central Research and Development Department , Experimental Station , E . L Du Pont de Nemours The effective ionic radii of Shannon & Prewitt [Acta ," 1976.

[214] M. C. Biesinger, L. W. M. Lau, A. R. Gerson, and R. S. C. Smart, "The role of the Auger parameter in XPS studies of nickel metal, halides and oxides," *Phys. Chem. Chem. Phys.*, vol. 14, no. 7, p. 2434, 2012.

[215] M. C. Biesinger, B. P. Payne, L. W. M. Lau, A. Gerson, and R. S. C. Smart, "X-ray photoelectron spectroscopic chemical state Quantification of mixed nickel metal, oxide and hydroxide systems," *Surf. Interface Anal.*, vol. 41, no. 4, pp. 324–332, 2009.

[216] A. F. Carley, S. D. Jackson, J. N. O. Shea, and M. W. Roberts, "The formation and characterisation of Ni 3 + — an X-ray photoelectron spectroscopic investigation of potassium-doped Ni (110)– O," vol. 440, 1999.

[217] A. F. Carley, S. D. Jackson, J. N. Oïshea, M. W. Roberts, and A. No, "Oxidation states at alkali-metal-doped Ni (110) – O surfaces," no. 110, 2001.

[218] H. Sohn *et al.*, "Ethanol Steam Reforming Conditions : AP-XPS and XANES Studies Effect of Cobalt on Reduction Characteristics of Ceria under Ethanol Steam Reforming Conditions : AP-XPS and XANES Studies," 2016.

[219] W. Luo *et al.*, "Design and fabrication of highly reducible PtCo particles supported on graphene-coated ZnO," 2017.

[220] W. Qi *et al.*, "RSC Advances situ grown nickel nanocatalyst for direct high- temperature carbon dioxide electrolysis †," *RSC Adv.*, vol. 4, pp. 40494–40504, 2014.

[221] B. Nematollahi, M. Rezaei, and M. Khajenoori, "Combined dry reforming and partial oxidation of methane to synthesis gas on noble metal catalysts," *Int. J. Hydrogen Energy*, vol. 36, no. 4, pp. 2969–2978, 2011.

[222] T. Chen *et al.*, "Structure Evolution of Co-CoO Interface for Higher Alcohol Synthesis from Syngas over Co / CeO Catalysts Structure Evolution of Co-CoO x Interface for Higher Alcohol Synthesis from Syngas over Co / CeO 2 Catalysts," 2018.

[223] W. Zou *et al.*, "Engineering the NiO/CeO $_2$ interface to enhance the catalytic performance for CO oxidation," *RSC Adv.*, vol. 5, no. 119, pp. 98335–98343, 2015.

[224] S. Boghosian, "Ceria Nanoparticles Shape Effects on the Structural Defects and Surface Chemistry: Implications in CO oxidation by Cu/CeO2 oxides," no. 2010, 2018.

[225] I. Y. Kaplin *et al.*, “Sawdust as an effective biotemplate for the synthesis of Ce0.8Zr0.2O2 and CuO-Ce0.8Zr0.2O2 catalysts for total CO oxidation,” *RSC Adv.*, vol. 7, no. 81, pp. 51359–51372, 2017.

[226] P. Boldrin *et al.*, “Nanoparticle scaffolds for syngas-fed solid oxide fuel cells,” *J. Mater. Chem. A*, vol. 3, no. 6, pp. 3011–3018, 2015.

[227] A. Chrzan, S. Ovtar, P. Jasinski, M. Chen, and A. Hauch, “High performance LaNi1-xCoxO3-Δ(x = 0.4 to 0.7) infiltrated oxygen electrodes for reversible solid oxide cells,” *J. Power Sources*, vol. 353, pp. 67–76, 2017.

[228] “Recent advances in high temperature electrolysis using solid oxide fuel cells : A review,” *J. Power Sources*, vol. 203, pp. 4–16, 2012.

[229] J. T. S. Irvine, D. Neagu, M. C. Verbraeken, C. Chatzichristodoulou, C. Graves, and M. B. Mogensen, “Evolution of the electrochemical interface in high-temperature fuel cells and electrolysers,” *Nat. Energy*, vol. 1, no. 1, 2016.

[230] T. Wu, B. Yu, W. Zhang, J. Chen, and S. Zhao, “Fabrication of a high-performance nano-structured $Ln_{1-x}Sr_xMO_{3-\delta}$ (Ln = La, Sm; M = Mn, Co, Fe) SOC electrode through infiltration,” *RSC Adv.*, vol. 6, no. 72, pp. 68379–68387, 2016.

[231] A. ManSimona Ovtar,† Xiaofeng Tong, Janet J. Bentzen, Karl T. S. Thydén, Søren Bredmose Simonsen and Ming Chen*uscript, “Boosting performance and durability of Ni/YSZ cathode for hydrogen production at high current densities via decoration with nano-sized electrocatalysts,” 2019.

[232] Z. Weng *et al.*, “Metal/Oxide Interface Nanostructures Generated by Surface Segregation for Electrocatalysis,” *Nano Lett.*, vol. 15, no. 11, pp. 7704–7710, 2015.

[233] H. A. Hansen and C. Wolverton, “Kinetics and Thermodynamics of H_2O Dissociation on Reduced CeO_2 (111),” *J. Phys. Chem. C*, vol. 118, no. 47, pp. 27402–27414, 2014.

[234] Z.-K. Han and Y. Gao, “Water Adsorption and Dissociation on Ceria-Supported Single-Atom Catalysts: A First-Principles DFT+U Investigation,” *Chem. - A Eur. J.*, vol. 22, no. 6, pp. 2092–2099, Feb. 2016.

[235] Y. Chen, J. Bunch, C. Jin, C. Yang, and F. Chen, “Performance enhancement of Ni-YSZ electrode by impregnation of Mo 0.1Ce 0.9O 2+??,” *J. Power Sources*, vol. 204, pp. 40–45, 2012.

[236] S. Futamura *et al.*, “Alternative Ni-Impregnated Mixed Ionic-Electronic Conducting Anode for SOFC Operation at High Fuel Utilization,” *J. Electrochem. Soc.*, vol. 164, no. 10, 2017.

[237] A. Mohammed Hussain, J. V. T. Høgh, T. Jacobsen, and N. Bonanos, “Nickel-ceria infiltrated Nb-doped SrTiO3 for low temperature SOFC anodes and analysis on gas diffusion impedance,” *Int. J. Hydrogen Energy*, vol. 37, no. 5, pp. 4309–4318, 2012.

[238] V. Yurkiv *et al.*, “Evaluation of the Influence of Nickel Addition on LST-CGO Based

Solid Oxide Fuel Cell Anodes Performance," *ECS Trans.*, vol. 68, no. 1, pp. 1517–1526, 2015.

[239] F. M. Sapountzi, S. Brosda, K. M. Papazisi, S. P. Balomenou, and D. Tsiplakides, "Electrochemical performance of La0.75Sr0.25Cr0.9M0.1O3 perovskites as SOFC anodes in CO/CO2 mixtures," *J. Appl. Electrochem.*, vol. 42, no. 9, pp. 727–735, 2012.

[240] W. Luo and S. Zafeiratos, "Tuning Morphology and Redox Properties of Cobalt Particles Supported on Oxides by an in between Graphene Layer," *J. Phys. Chem. C*, vol. 120, no. 26, pp. 14130–14139, Jul. 2016.